HIGH-RESOLUTION MODELING AND VISUALIZATION OF DRAINED ROCK VOLUME AROUND HYDRAULICALLY FRACTURED WELLS IN HETEROGENEOUS RESERVOIRS

A Dissertation

by

KIRAN NANDLAL

Submitted to the Office of Graduate and Professional Studies of
Texas A&M University
in partial fulfillment of the requirements for the degree of

DOCTOR OF PHILOSOPHY

Chair of Committee,	Ruud Weijermars
Committee Members,	Thomas A. Blasingame
	Eduardo Gildin
	David S. Schechter
Head of Department,	Jeff Spath

August 2020

Major Subject: Petroleum Engineering

ABSTRACT

This study applies and further develops a new semi-analytical streamline simulator based on complex analysis methods (CAM) that creates high-resolution flow visualizations to identify the growth of the drained rock volume (DRV) in hydraulically fractured hydrocarbon reservoirs. This CAM tool is complementary to commonly used, computationally intensive finite-volume numerical reservoir simulators.

This body of research starts with an investigation of the effects on DRV when hydraulic fractures are represented as simple planar fractures or increasingly complex fractal networks. An algorithm based on the Lindenmayer fractal system was developed to model a variety of complex hydraulic fracture networks. Models show that complex hydraulic fracture networks are beneficial for reducing flow stagnation zones and will result in improved reservoir drainage. The subsequent introduction and modeling of natural fracture heterogeneity shows these natural fractures can have profound impact on flow and DRV shape and location in the reservoir. As such natural fractures must be properly taken into account to accurately model reservoir drainage.

Previous work done in 2D representations was then advanced to pseudo-3D models via the use of hydraulic fracture geo-mechanical propagation data to create DRV envelope plots. Pseudo-3D DRV envelopes were calculated by a new algorithm using hydraulic fracture conductivity data obtained from a commercial hydraulic fracture propagation simulator. This study showed that most of the distal length of hydraulic fractures remain undrained due to low conductivity. These developed methods were then

used to visualize the DRV and calculate recovery factors for Permian Basin wells. It is shown that recovery factors are poorly defined in unconventional reservoirs and requires new ways of thinking.

CAM models used to visualize the convective tracer fronts for outlining DRV were found to lag behind the often-used pressure depletion plots used by industry to represent drainage volume. The quantification of the time lag between the diffusive pressure front and convective tracer front shows that pressure plots are in fact poor proxies for DRV in ultra-low permeability shale reservoirs. Further work investigates the comparison between the diffusive time-of- flight calculated via the fast-marching-method (FMM) and the convective time-of-flight from CAM and presents avenues for future research.

DEDICATION

This work is dedicated first and foremost to my grandparents, Nandlal Roopchand and Boodhanie Nandlal, Dookie and Dhanmatie Chirkootsingh, who laid the foundation for the success and education of my parents who were then able to instill and foster in me a sense of dedication to learning and excellence. Without them none of this would be possible. To my parents, Dale and Rajdaye Nandlal, thank you for always guiding me along the right path and supporting me in all my endeavors. No amount of recognition can encapsulate all that you have sacrificed in helping me to get where I am now. I will be forever grateful for all that you have done for me. Finally, the last but in no way the least person this is dedicated to is Miss Shari Penelope Shantel Basdeo who has been a constant at my side through both the good and the most difficult of times. Thank you, Shari, for always being there for me and helping me to stay the path to complete this endeavor.

ACKNOWLEDGEMENTS

I would like to firstly acknowledge and immensely thank my committee chair Dr. Ruud Weijermars for his guidance and support throughout my Ph.D. studies and research thus far. His invaluable knowledge has been of immense help in moving forward with this research and I cannot begin to even count the number of hours he has spent mentoring me over the course of our numerous discussions.

Thanks also go out to my other committee members Dr. Blasingame, Dr. Gildin and Dr. Schechter for agreeing to sit on the committee for my Ph.D. dissertation. Their expertise and invaluable scientific insights have been crucial for the proper completion of this work

Finally, I would like to acknowledge the support of friends and colleagues in the department who have helped by making the time thus far at Texas A&M University a truly enjoyable experience both academically and socially. In particular I would be remiss to not acknowledge Dr. Aaditya Khanal who I have had the pleasure of working alongside with over the course of my Ph.D. studies and has been a constant source of assistance and positive feedback. I also wish to thank Dr. Sergei Parsegov, Dr. Murat Fatih Tugan and Dr. Chen Li who I have worked alongside with in some of these papers.

CONTRIBUTORS AND FUNDING SOURCES

This work was supported by funding from the Crisman Institute for Petroleum Research. Data was made available for this research by University Lands, Hawkwood Energy and Halcon Resources.

TABLE OF CONTENTS

Page

LIST OF FIGURES

Page

LIST OF TABLES

Page

1. INTRODUCTION AND LITERATURE REVIEW

1.1. Introduction

The massive shift in US oil and gas production, after the Millennium turn, from conventional to unconventional reservoirs, has seen the hydraulic fracturing of production wells become a crucial aspect of completion engineering. The productivity of shale wells is now primarily based on how effectively hydraulic fractures help to provide new pathways for flow towards the wells from the reservoir matrix with ultra-low permeability.

A proper understanding of the creation of hydraulic fractures and modeling of fluid flow near these fractures is needed for improvement of both the early well productivity and the ultimate recovery factor. The engineering of hydraulic fractures in unconventional hydrocarbon plays is a rapidly evolving art. Industry has moved to reduce fracture spacing from over 100 ft in 2010, to 50 ft in 2014, and less than 20 ft in 2018. The fracture spacing is designed using estimations of geomechanical rock properties from pilot wells in combination with fracture propagation models.

As we move from the early age of the shale revolution to a mature phase, more scientific insight is needed into the interplay between hydraulic fractures created (which are not the simple planar features represented in most models) and fluid flow in these subsurface reservoirs. The visual representation of where exactly in the reservoir is drained is the crux of this presented dissertation.

1.2. Literature review

1.2.1. Hydraulic fracture modeling

One of the earliest analytical models that described hydraulic fracture propagation is the KGD model put forward by Khristianovic and Zheltov (1955). This model was able to couple fluid flow from pumping with rock mechanics to describe the geometry of the created fracture in the 2D plane. The next model that gained traction and use was the PKN model as put forth by Perkins and Kern (1961). The major difference between both these 2D models is that the KGD assumes the creation of a fracture where the height is greater than length (short fracture) while the PKN model assumes the length is much greater than the heights (long fracture). Another major difference is the PKN model assumes an elliptical fracture cross-section with the KGD assumes a simple rectangular section.

From analytical solutions the next phase in hydraulic fracture modeling began with the use of numerical grid-based solutions. These numerical solutions allow the coupling of equations for fluid and proppant flow in the created fracture. The numerical solutions are termed as either pseudo-3D or planar-3D models, each with its own advantages and disadvantages. Variations in fracture geometry in 3D are often not considered in the pseudo-3D models. The planar-3D models tend to be more accurate than pseudo 3D but take up to twice as much computational time (Cohen et al., 2017). Other more complex methodologies in modeling hydraulic fracture propagation include

the uses of the Finite Element Method (FEM) as used by Smith et al. (2001) or the Finite Volume Method (FVM) coupled with a cohesive zone model (CZM) put forward by Yao et al. (2010).

The earliest attempts to compare hydraulic fracture patterns may be traced back to Warpinski et al. (1994), but today there is still no consensus regarding the relative merits of the various fracture propagation modeling platforms. The American Rock Mechanics Association (ARMA) initiated seven benchmark tests for 20 participating models (Han, 2017) with the intent to showcase recognized physics of hydraulic fracturing. Most platforms for modeling hydraulic fracture propagation are based on assumed homogeneous rock properties, which therefore uniquely favor the formation of planar, sub-parallel hydraulic fractures (Parsegov et al., 2018b). The way in which hydraulic fracture geometry is modeled has a great impact on any subsequent flow modeling as this is the only path through which fluid reaches the production well.

1.2.2. Reservoir flow modeling using numerical methods

For problems too complex for analytical methods the industry has turned towards the use of various numerical solutions for flow modeling. The majority of these numerical solutions rely on gridded methods that use discretization based on finite elements or finite volumes. These numerical methods allow for accurate reserve estimation, can be used to validate analytical models and optimize completion and

fracture designs (Olorode et al., 2013). For the modeling of naturally fractured porous media, which the majority of unconventional shale reservoirs fall under, the most commonly used methods are the dual porosity-dual permeability model and embedded discrete fracture models.

The use of both implicit and explicit finite discretization to model flow in naturally fractured reservoirs has been well documented in literature (Berkowitz, 2002; Neumann, 2005; Flemish et al., 2018). What is common in these methods is the need for grid refinement for the representation of natural or hydraulic fractures with differing permeability from the rock matrix. The main limitation of these local grid refinement (LGR) methods is the high computational costs incurred when using structured grids (Du et al., 2016). For complex fracture networks these structured grids become too cumbersome and one must then resort to using unstructured gridding such as Voronoi cells (Sun and Schechter, 2014).

The embedded discrete fracture model (EDFM) was first proposed by Lee at al., (2001) and further implemented in later work from Li and Lee (2008) for use in flow simulation in naturally fractured reservoirs. In this method the reservoir is subdivided into two domains, one representing the rock matrix and the other the fractures present, both hydraulic and natural. The matrix is represented by a structured grid while control volumes are used to represent the fractures that intersect the matrix grid. For interaction between the fracture control volumes and the matrix grid there is the definition of what

are termed non-neighboring connections (NNC). These NNC are what allow for fluid communication between grid-block to grid block (Moinfar et al., 2014). Various NNC are defined; Type 1 NNC between a fracture cell and a neighboring matrix grid-block, Type 2 NNC between two intersecting fractures, Type 3 NNC between two cells of an individual fracture line. The EDFM is much more accurate than the finite volume methods with the added drawback of being even more computationally expensive.

1.2.3. Reservoir flow modeling using complex analysis methods

1.2.3.1. Complex analysis method background

The present study developed numerous further advancements to CAM-based flow modeling methods, which allow particle tracking, time of flight computations and pressure modeling at high resolution. The use of streamlines and streamtubes to describe transport and the modeling of fluid flow in petroleum reservoirs was first introduced by Muskat (1937). Some of the fundamental work in streamline simulation can be traced back to the Pólya and Latta (1974) where streamlines were visualized by the mapping of complex contour integrals using the vector field representation of complex variables. Fundamental flow fields can occur in the form of vortices, sources, sinks, dipoles, doublets and uniform flows. This work of Pòlya and Latta (1974) was then extended for use in fluid mechanics by employing complex functions for a concise mathematical

representation of potential and stream functions (Batchelor, 1967; Weijermars and Poliakov, 1993; Kundu and Cohen, 2002).

For the application of complex flow functions to study subsurface flow in fractured petroleum reservoirs, this study uses a variety of established and newly developed flow elements. Potential flow theory has been used widely by numerous authors to model Darcy flow dynamics found in application of groundwater flow (Da Costa & Bennett, 1960; Strack, 1989; Holzbecher, 2005), geothermal wells (Holzbecher & Sauter, 2010; Holzbecher et al., 2011) and hydrodynamics (Milne-Thomson, 1962). From these basic fundamentals, advanced analytical flow descriptions based on complex analysis to obtain closed-form solutions for time-dependent flows were developed by Weijermars et al. (2014). Eulerian streamline tracking was used in complex analysis flow descriptions to visualize the competition for space in gravitationally driven lava streams. The modeling approach was then subsequently expanded upon to model hydrothermal circulation (Weijermars and Van Harmelen, 2016). The CAM model was also used to visualize sweep efficiency in hydrocarbon wells and time-of-flight in porous media, using closed-loop adjustment (Weijermars et al., 2016), gaining fundamental insights on flow in anisotropic porous media (Zuo and Weijermars, 2017), water flood tracking (Weijermars and Van Harmelen, 2017), and controlled water flooding with bounded domains in the Quitman Basin, Texas (Nelson et al., 2017).

In this dissertation I used the prior developed tools (briefly highlighted in the literature review above) as a starting point to further advance CAM solutions, with particular emphasis on flow in unconventional shale reservoirs. An important aspect of most shale reservoirs is their highly heterogeneous nature. This heterogeneity is due to these reservoirs typically possessing dense networks of natural fractures. As such the added capabilities developed by me, focus on the introduction of these natural fractures into the modeled reservoir space as discrete elements, and how to properly account for their impact on fluid flow in the subsurface.

1.2.3.2. Complex analysis model assumptions

CAM offer considerable advantages for modeling fluid flow, such as being grid-less, thus allowing for much faster computational times and nearly infinite resolution. These qualities are especially useful for studying flow in fractured porous media (distinguishing hydraulic and natural fracture behavior). For modeling Darcy flow in porous media certain assumptions must be made about both the reservoir as well as the fluid properties. In this study, the reservoir matrix was assumed homogenous, incompressible and uniform in thickness. Gravity and capillary forces are neglected. The fluid present in the reservoir space is assumed to be single phase and incompressible with flow being isothermal. The presence of natural fractures is accounted for by

discrete sets of fracture elements. Further, it was assumed that the boundaries of the reservoir are so remote that boundary effects on flow are negligible.

1.2.3.3. Complex analysis method formulation

The analytical formulations used start with the expression of the complex potential $\Omega(z)$ that links the potential function ϕ and the stream function ψ by:

$$\Omega(z) = \phi(x, y) + i\psi(x, y) \qquad [\text{m}^2.\text{s}^{-1}] \text{ (1-1)}$$

Writing the complex variable z as $z = x + iy$ with $i = \sqrt{1}$ the related complex function is given by the conjugate of the complex potential and is represented as:

$$F(\bar{z}) = \overline{\Omega(z)} = \phi(x, y) - i\psi(x, y) \qquad [\text{m}^2.\text{s}^{-1}] \text{ (1-2)}$$

Differentiation the complex potential ($\Omega(z)$) with respect to z and then conjugating gives the Pòlya vector field $\overline{V(z)}$ which has solutions in the Cartesian plane. We can also differentiate $F(\bar{z})$ with respect to $\bar{z}$. Using representations of $v_x = \frac{\partial \phi}{\partial x} = \frac{\partial \psi}{\partial y}$ and $v_y = \frac{\partial \phi}{\partial y} = -\frac{\partial \psi}{\partial x}$ gives:

$$\overline{V(z)} = \frac{\overline{\partial \Omega(z)}}{\partial z} = \frac{\partial \phi}{\partial x} - i\frac{\partial \psi}{\partial x} = v_x + iv_y \qquad [\text{m.s}^{-1}] \text{ (1-3)}$$

Thus, the complex velocity field is given by:

$$V(z) = \frac{\partial \Omega(z)}{\partial z} = \frac{\partial \phi}{\partial x} + i\frac{\partial \psi}{\partial x} = v_x - iv_y \qquad [\text{m.s}^{-1}] \text{ (1-4)}$$

This formulation can then be expanded upon to derive the complex potential for an interval-source with time-dependent strength *m(t)* along the real axis with the real interval [*a*,*b*] after Potter, 2008 as:

$$\Omega(z,t) = \frac{m(t)}{2\pi(b-a)}[(z-a)\log(z-a) - (z-b)\log(z-b)] \qquad [\text{m}^2.\text{s}^{-1}] \text{ (1-5)}$$

Once again, we differentiate with respect to *z* to get the velocity field as:

$$V(z,t) = \frac{m(t)}{2\pi(b-a)}[\log(z-a) - \log(z-b)] \qquad [\text{m.s}^{-1}] \text{ (1-6)}$$

Instead of representing the line interval by end points [*a*,*b*] we can use the center (x_c) and total length (L) to get:

$$V(z,t) = \frac{m(t)}{2\pi L}[\log(z - x_c + 0.5L) - \log(z - x_c - 0.5L)] \qquad [\text{m.s}^{-1}] \text{ (1-7)}$$

For a line interval at an angle (Fig.1-1) with endpoint of $z_a = (z_c - 0.5L \cdot e^{i\beta})$ and $z_b = (z_c + 0.5L \cdot e^{i\beta})$ the complex potential is now given by:

$$\Omega(z,t) = \frac{m(t)}{2\pi L}\{(z-z_a)\log[e^{-i\beta}(z-z_a)] - (z-z_b)\log[e^{-i\beta}(z-z_b)]\} \quad [\text{m}^2.\text{s}^{-1}] \text{ (1-8)}$$

Velocity expression now becomes:

$$V(z,t) = \frac{m(t)}{2\pi L}[\log(e^{-i\beta}(z-z_a)) - \log(e^{-i\beta}(z-z_b))] \qquad [\text{m.s}^{-1}] \text{ (1-9)}$$

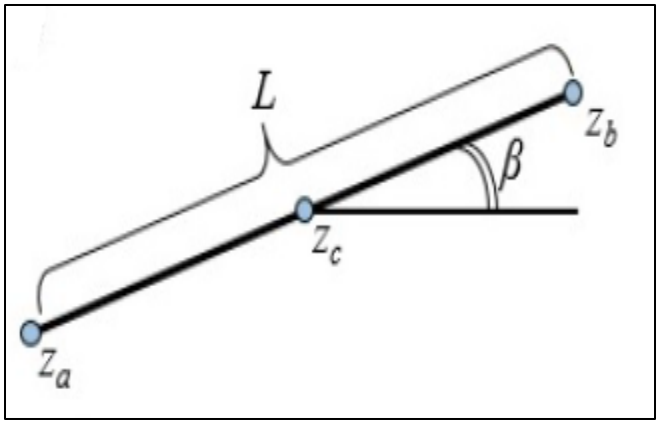

Figure 1-1Plan view of general fracture element with center location z_c, end-points z_a and z_b, total length L and angle β (After Weijermars et al., 2017)

The above Eqs. (1-8) and (1-9) can also be rewritten into generalized expressions for *N* interval sources as:

$$\Omega(z,t)=\sum_{k=1}^{N}\frac{m_k(t)}{2\pi L_k}e^{-i\beta_k}\{(e^{-i\beta_k}(z-z_{ck})+0.5L_k)\log[e^{-i\beta_k}(z-z_{ck})+0.5L_k]$$

$$-(e^{-i\beta_k}(z-z_{ck})-0.5L_k)\log[e^{-i\beta_k}(z-z_{ck})-0.5L_k]\} \qquad [m^2.s^{-1}] \text{ (1-10)}$$

$$V(z,t)=\sum_{k=1}^{N}\frac{m_k(t)}{2\pi L_k}e^{-i\beta_k}\cdot\left(\log\left[e^{-i\beta_k}\left(z-z_{c,k}\right)+0.5L_k\right]-\log\left[e^{-i\beta_k}\left(z-z_{c,k}\right)-0.5L_k\right]\right)$$

$$[m.s^{-1}] \text{ (1-11)}$$

Using the above formulas, we can calculate the specific velocity field solution at any point in time. We next couple this with a Eulerian scheme of $z_{n+1}\approx z_n+v(z_n)\cdot\Delta t$ to allow tracing of the streamline trajectories and definition of the time-of-flight-contours. We choose an initial point z_o for each assumed tracer particle that initially starts out

around the line interval. The position of the tracer at time t_1 after one-time step Δt, is denoted by $z_1(t_1)$ and can be calculated by:

$$z_1(t_1) = z_0(t_0) + v(z_0(t_0)) \cdot \Delta t \qquad \text{[m] (1-12)}$$

And in generalized form for any tracer particle at any time-step can be given by:

$$z_j(t_j) = z_{j-1}(t_{j-1}) + v(z_{j-1}(t_{j-i})) \cdot \Delta t \qquad \text{[m] (1-13)}$$

For pressure calculations, the pressure differential can be given by the real part of the complex potential when scaled by reservoir properties of permeability (k) and fluid viscosity (μ):

$$\Delta P(z,t) = -real(\Omega(z,t))(\mu / k) \qquad \text{[Pa] (1-14)}$$

Or in another form the real pressure-change in any location z at a given time t may be calculated analytically by:

$$\Delta P(z,t) = -\frac{\phi(z,t)\mu}{k} \qquad \text{[Pa] (1-15)}$$

The actual pressure field at any given time can be calculated if the reservoir initial pressure P_0 is known by:

$$P(z,t) = P_0 + \Delta P(z,t) = P_0 - \frac{\phi(z,t)\mu}{k} \qquad \text{[Pa] (1-16)}$$

1.3. Focus and novelty of dissertation

As this dissertation follows the Texas A&M University journal style format, the majority of the work put forward in this document has already been vetted and published by peer-reviewed journals and in industry conference proceedings. The following published papers are all stepwise contributions that greatly advance the CAM modeling capacity to solve for fluid flow in hydraulically fractured unconventional reservoirs, with and without natural fractures. In summary below are listed these papers, with a separate explanation of my novel contributions in each paper:

1) **Nandlal, K.,** and Weijermars, R., 2019a. Drained Rock Volume around Hydraulic Fractures in Porous Media: Planar Fractures Versus Fractal Networks. Springer Petroleum Science, https://doi.org/10.1007/s12182-019-0333-7.

   Original contribution*: Novel use of the Lindenmayer fractal system to create code to model increasingly complex branching hydraulic fracture networks. Fractal networks were coupled with CAM to obtain the drained rock volume (DRV). Models were constructed 1st, 2nd and 3rd generation fractals, for comparison with planar fractures.*

2) **Nandlal, K.,** and Weijermars, R., 2019b. Impact on Drained Rock Volume (DRV) of Storativity and Enhanced Permeability in Naturally Fractured Reservoirs: Upscaled

Field Case from Hydraulic Fracturing Test Site (HFTS), Wolfcamp Formation, Midland Badin, West Texas. MDPI Energies. 12(20), 3852, https://doi.org/10.3390/en12203852.

Original contribution*: Creation of new code to account for the heterogeneity created by natural fractures in an otherwise homogenous reservoir, with a sensitivity study of the altered porosity (storativity) and enhanced permeability within these natural fractures. I developed a new upscaling method for flow in naturally fractured reservoirs by combining object-based and flow-based upscaling methods, which was applied to field data from the Hydraulic Fracturing Test Site.*

3) Parsegov, S.G., **Nandlal, K.,** Schechter, D.S., and Weijermars, R., 2018a. Physics-Driven Optimization of Drained Rock Volume for Multistage Fracturing: Field Example from the Wolfcamp Formation, Midland Basin. SPE-URTeC: 2879159. Unconventional Resources Technology Conference, Houston, Texas, USA, 23-25 July 2018. DOI 10.15530/urtec-2018-2879159

Original contribution*: I devised a new production allocation algorithm programed to use hydraulic fracture conductivity inputs from a 3D hydraulic fracture propagation simulator. From this work, for the first time, the DRV has been visualized in pseudo-3D volume plots for a full hydraulic fracture stage.*

4) Khanal, A., **Nandlal, K.,** and Weijermars, R. 2019. Impact of natural fractures on the shape and location of drained rock volumes in unconventional reservoirs: Case Studies from the Permian Basin. SPE URTeC 2019 Denver Colorado 22-24 July, URTEC 1082.

Original contribution*: Application of the CAM model to accurately determine the impact of natural fracture clusters on the DRV extent. Based on newly devised flow velocity models and the associated DRV plots, I defined the inter-fracture and inter-well recovery factors.*

5) Weijermars, R., **Nandlal, K.,** Khanal, A., and Tugan, F.M., 2019. Comparison of pressure front with tracer front advance and principal flow regimes in hydraulically fractured wells in unconventional reservoirs. Journal of Petroleum Science and Engineering, Vol 183, 106407, https://doi.org/10.1016/j.petrol.2019.106407.

Original contribution*: I quantified and visualized the time lag between the diffusive pressure front and convective tracer front in unconventional reservoirs. This quantification reveals that the pressure front vastly overestimates the drained rock volume as compared to the convective time of flight (tracer front) visualized with CAM.*

6) Additionally, early results of a final, sixth paper (still in progress) are presented in Chapter 7 of this dissertation.

   Original contribution*: Comparison of convective tracer front propagation based on fast and grid-less CAM models, with diffusive time of flight fronts based on Fast Marching Methods (FMM).*

1.4. Coherence of research topics in this dissertation

One common theme in all six research papers presented in my dissertation is the development and application of new workflows for modeling fluid flow in hydraulically fractured reservoirs using the new semi-analytical streamline simulator based on complex analysis methods (CAM). All papers revolve around better accuracy of fluid flow calculations. The modeling capacity of my newly developed CAM codes were illustrated using multiple field data sources, such as production data, hydraulic fracture treatment data, and natural fracture diagnostics from core. These field data originated from a variety of hydrocarbon operations: 1) Hydraulic Fracturing Test Site (HFTS), Reagan County, 2) Eagle Ford Shale, Brazos County, 3) Wolfcamp Formation, Midland Basin, Upton County, and 4) Wolfcamp Formation, Delaware Basin, Ward County.

The CAM method for drained rock volume (DRV) visualization has unsurpassed high-resolution and is grid-less which reduces modeling time. The majority of my contributions include the expansion and development of original Matlab codes based on

CAM. I developed a new storativity module, branching fractal fracture network module and flux allocation algorithms. In addition, one major development was a new upscaling method for flow in a naturally fractured reservoir by combining object-based and flow-based upscaling methods. I also created a new pseudo-3D modeling method to compute the DRV around hydraulic fractures in a single fracture treatment stage using heterogeneous hydraulic conductivity maps, history matched with a commercial hydraulic fracture propagation simulator. Research work also resulted in the quantification of Pressure/Tracer front lag.

I integrated the CAM model with multiple data sources and several commercial software platforms (GOHFER hydraulic fracture simulation, CMG reservoir modeling). The CAM models are able to account for time-dependent flow in the reservoir making use of history matched production data. History matching was done using various DCA methods (Duong and Arps), as well as CMG based history matching of full-well performance.

In addition to initial literature review, developing workflows, writing code, creating visualizations, debugging code, integration with commercially available modeling tools, and application to field data, a considerable amount of time was spent on consolidating and preparing my research outcomes for publication in peer-reviewed journals and industry conferences. This required improvement of writing skills, embedding my research in concurrent and past literature, critical analysis of results,

professional formatting of graphs and plots, writing and rewriting concise figure captions, and validating all aspects of the manuscript before submission. The next phase in the publication process typically required handling reviewer comments in an apt and timely fashion, writing a response to reviewer report and completing revisions for the final manuscript.

2. DRAINED ROCK VOLUME (DRV) AROUND HYDRAULIC FRACTURES IN POROUS MEDIA: PLANAR FRACTURES VERSUS FRACTAL NETWORKS*

2.1. Introduction

2.1.1. Brief highlights

This chapter investigates the effects of using either a simple planar hydraulic fracture or a complex hydraulic fracture network on drained rock volume (DRV). My original contribution involved using the Lindenmayer system in conjunction with fractal theory to create branching hydraulic fracture networks, and adapting the complex analysis methods (CAM) code to model flow with branching hydraulic fractures. Branching of hydraulic fracture systems is coupled with CAM to obtain the DRV from a branching hydraulic fracture network which is then compared to the traditionally used planar hydraulic fractures.

The present study breaks new ground by modeling the flow around fractal fracture networks in porous media. The results have implications for fracture treatment designs required to maximize the drained rock volume. The flow analysis in this study uses branched fractals for describing the complex fracture networks that are present in the subsurface. A variety of branched fractal fracture networks are imported into a

*Parts reprinted with permission from "Drained Rock Volume around Hydraulic Fractures in Porous Media: Planar Fractures Versus Fractal Networks" by Kiran Nandlal and Ruud Weijermars, 2019, Springer Petroleum Science.

drainage model based on Complex Analysis Methods (CAM) to determine the flow response and pressure changes in the reservoir, for a given fracture geometry and fracture surface area. The major effect observed due to increasing fractal nature and branching of the fracture network (as outlined later in this study) is that the extent of dead zones between hydraulic fracture stages is suppressed. Instead, a more diffuse network of fractures drains the matrix between the fracture initiation points spaced by the perforation zones.

Depending on the geometry of hydraulic fractures, an otherwise non-fractured matrix with negligible spatial variation in permeability can be drained more or less effectively. Future work will need to determine when hydraulic fractures will develop as fractal networks. While the jury is still out on the prominent geometry of hydraulic fractures (planar vs. fractal), the models developed in the present study consider the effect on drained rock volume in a systematic investigation of hydraulic fracture geometry ranging from planar to multi-branched, higher order fractals.

2.1.2. Motivation of study

Although current fracture diagnostics can rarely resolve the detailed nature of the fractures created during fracture treatment of unconventional hydrocarbon wells (Grechka et al., 2017), recent empirical evidence suggests that deviations from planar fracture geometry may exist. Physical evidence from cores that were sampled from a

hydraulically fractured rock volume indicates that the generated fracture density far exceeds the number of perforation clusters (Raterman et al., 2017). The creation of fracture complexity in terms of deflection, offset and branching is possible at bedding surfaces and other naturally occurring heterogeneities, with pre-existing natural fractures not appearing necessary for the creation of complex, distributed fracture systems. In fact, this finding is not entirely new. Work by Huang and Kim (1993) from mineback and laboratory experiments showed that the common notion that hydraulic fractures are planar in nature and assumed to propagate linearly perpendicularly to minimum stress in simplified geo-mechanical models is not always correct. Clearly, empirical evidence suggests that fracture treatment may form fracture networks with branching fractal dimensions initiating from the perforation points (Fig. 2-1b), rather than planar hydraulic fractures (Fig. 2-1a). Thus, the practice of representing hydraulic fractures as single planar, bi-wing cracks in the subsurface may be an overly simplistic representation of what in reality are more complex, fractal structures.

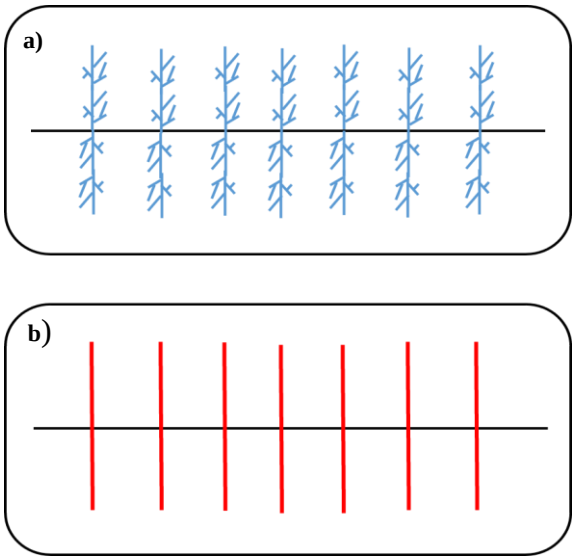

Figure 2-1 a) Plan view of bi-wing branched, hydraulic fracture networks. b) Plan view of idealized planar hydraulic fractures along horizontal wellbore.

The likelihood of complex fracture networks being created by the fracture treatment process (rather than mutually sub-parallel planar fractures) is further supported by evidence from microseismic monitoring (Fisher et al. 2002; Maxwell et al. 2002). In fact, most microseismic clouds generated during fracturing jobs show a poor correlation to the assumed planar, subparallel fractures. Therefore, we assume that the creation of complex hydraulic fracture networks may be more representative for many fracture treated wells, especially those that possess a network of natural fractures due to stress regimes varying over geological time. Such conditions are typical of most unconventional shale plays under exploration and development. Consequently, the use of planar hydraulic fractures for modelling reservoir depletion may not always

appropriately account for the actual reservoir attributes. The subsequent use of such over-simplified planar fracture geometries in flow models leads to unreliable calculations of important reservoir attributes such as the Drained Rock Volume (DRV) and flaws in the associated pressure response.

Current fracture representation methods that try to capture fracture complexity include discrete fracture network models and the unconventional fracture model (Weng et al., 2011; Zhou et al., 2012) and are reviewed later. These established fracture geometry models use block centered grids typically coupled with finite-difference discretization flow models, including compositional flow models to simulate reservoir performance (Yu et al., 2017b). The drawback of these finite-difference schemes is that they can be computationally intensive due to the necessity of fine meshing, especially at the fracture intersections. Other methods to model flow in fractured porous media include semi-analytical models to simulate and analyze the pressure change for complex well interference systems (Yu et al., 2016). The suitability of the dual porosity flow model (Warren and Root, 1963) for low permeability reservoirs has been questioned (Cai et al., 2015). Further work has led to the development of triple porosity models to model flow in fractured reservoirs (Sang et al., 2016). Zhou et al. (2012) proposed a semi-analytical solution for flow in a complex hydraulic fracture network model, which combined an analytical reservoir solution with a numerical solution on discretized fracture panels. The present study applies the analytical CAM flow model (Weijermars

et al., 2016, 2017a,b, 2018), which is computationally efficient, while being able to accurately model the flow near fractal fractures such as those observed in field tests (Raterman et al., 2017).

Planar, sub-parallel hydraulic fractures with a certain spacing will develop dead flow zones between them where no fluid can be moved due to the occurrence of stagnation point surrounded by infinitely slow flow regions in their vicinity (Fig. 2-2a). Such dead zones suppress well productivity, which may be remedied by plugging prior perforations and re-fracking into the dead flow zones by placing new perforations midway between the legacy perf zones after prior production wanes (Fig. 2-2b). However, the existence of dead zones is entirely premised upon the assumption that hydraulic fractures are planar and subparallel (Weijermars et al. 2017a, b; 2018).

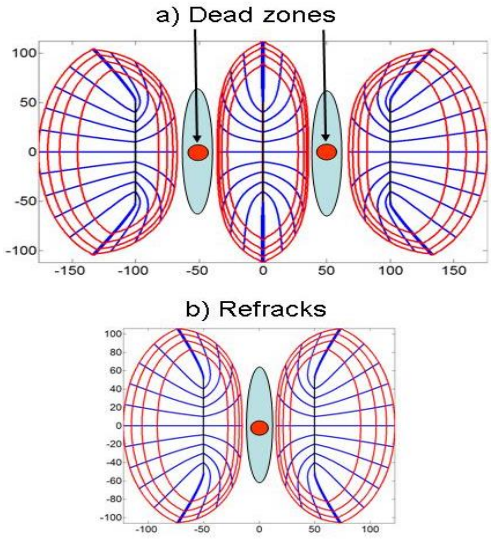

Figure 2-2 a) Time-of-flight visualizations showing drained rock volume (DRV, red contours) and dead zones (blue region, around flow stagnation point, red dot) between three parallel, planar hydraulic fractures. b) Refracks will tap into the dead zones.

2.1.3. Summary

This study applies the Lindenmayer system based on fractal theory to generate synthetic fracture networks in hydraulically fractured wells. The applied flow model is based on Complex Analysis Methods (CAM), which can quantify the flow near the fractures, and being grid-less, is computationally faster than traditional discrete volume simulations. The representation of hydraulic fractures as fractals is a more realistic representation than planar bi-wing fractures used in most reservoir models. Fluid withdrawal from the reservoir with evenly spaced hydraulic fractures may leave dead zones between planar fractures. Complex fractal networks will drain the reservoir matrix more effectively, due to the mitigation of stagnation zones. The flow velocities, pressure response and drained rock volume (DRV) are visualized for a variety of fractal fracture networks in a single fracture treatment stage. The major advancement of this study is the improved representation of hydraulic fractures as complex fractals rather than restricting to planar fracture geometries. Our models indicate that when the complexity of hydraulic fracture networks increases, this will suppress the occurrence of dead flow zones. In order to increase the DRV and improve ultimate recovery, our flow models suggest that fracture treatment programs must find ways to create more complex fracture networks.

2.2. Natural examples of hydraulic fractures

In addition to the cited examples of hydraulic fractures branching into closely spaced fracture networks (Raterman et al., 2017, Huang and Kim, 1993), manifestations of bifurcating fracture networks are commonly known from surface outcrops of hydraulic fractures formed by natural processes. For example, hydrothermal veins invaded and hydraulically fractured Proterozoic rocks from the Aravalli Supergroup in the state of Rajasthan, India (Pradhan et al., 2012; Kilaru et al., 2013; McKenzie et al., 2013). These hydraulic fractures formed under high fluid pressure deeper in the crust before being exhumed by tectonic uplift and erosion. Polished slabs containing the naturally created hydraulic fracture networks in Bidasar ophiolites are imaged in Fig. 2-3a. These rocks are exploited as facing stones and quarried near the villages of Bidasar-Charwas, Churu district (Fig. 2-3b). The quarries are confined to a 0.5 km wide and 2.5 - 3.5 km long belt of open pits dug below the desert plain. The rock in these pits has been described as the Bidasar ophiolite suite (Mukhopadhyay and Bhattacharya, 2009).

The precise natural pressure responsible for the injection of the hydraulic veins is unknown, but the pressure has exceeded the strength of the rock and was large enough to open the fractures at several km burial depth, thus being in the order of 100 MPa. The fluid was injected into the fractures as well as into a pervasive system of micro-cracks connected to the main fractures. Based upon the splaying of the fractures, one may reconstruct the provenance of the fracture propagation (Van Harmelen and Weijermars,

2018). Local heterogeneities in elastic properties may create conditions favoring the nucleation of fracture bifurcation points. More work is needed to determine the critical conditions required for creating fractal fracture networks in hydraulic fracture treatment programs.

Slabs like those shown in Fig. 2-3a may serve as a natural analog for flow into hydraulic fractures in shale reservoirs, with the limitation that shale may have different elastic moduli, different petrophysics, grain size and most crucially, the fracture aperture width from hydraulic fracturing is smaller than that in our natural analog presented here. Hydraulic fracture apertures in shale reservoirs are thought to be in the range of 1 to 5mm with the majority of created fracture apertures being less than 2mm (Gale et al., 2014, Zolfaghari et al., 2016, Arshadi et al., 2017). Natural fracture networks created in the rocks of Bidasar due to hydrothermal activity in the earth's crust bears similarity to

man-made hydraulic fracture networks that require the use of highly pressure fluids and proppants by fleets of pumps and trucks.

Figure 2-3 a) Examples of rock slabs from Bidasar with bifurcating, hydraulic injection veins. Image dimensions about 1 square meter (courtesy Dewan Group). b**)** Satellite image of quarry near Bidasar, Rajasthan, India (roads for scale). North is down in above image (Google Earth composite of 16 Dec 2015).

We content that the injection patterns of the hydrothermal veins exposed in natural outcrops and in quarries (of rocks exhumed by tectonic processes and subsequent erosion) provide a useful analog for hydraulic fracture networks created when fluid injection is applied to hydrocarbon wells. Figs. 2-4a, b shows an analysis of the principal

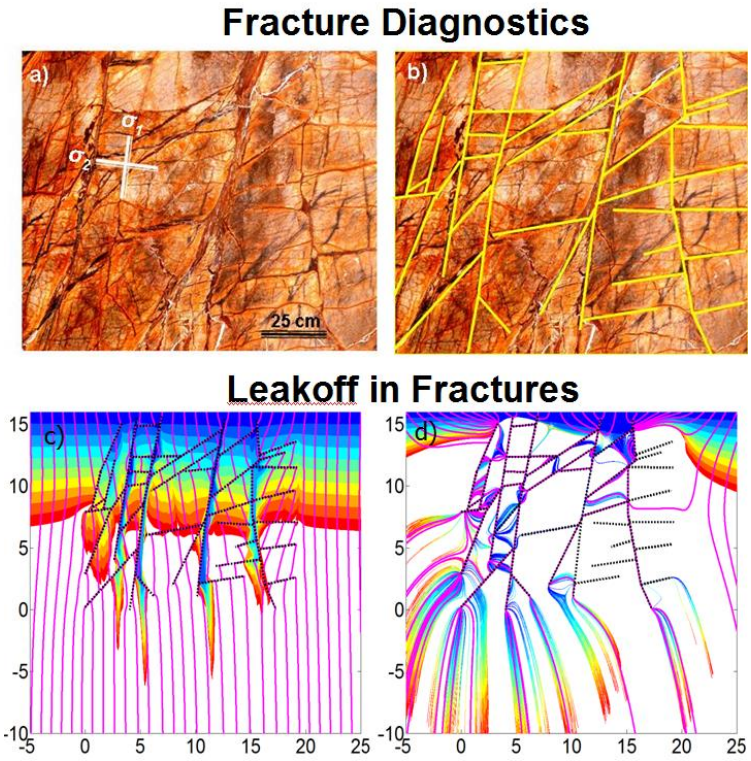

Figure 2-4 Orthogonal photograph of polished rock slab with injection veins. (a) Filled fracture veins with interpreted directions of the original largest (σ_1) and intermediate (σ_2) principal stress axes. Major veins open first normal to σ_1 and then normal to σ_2, which likely swapped with σ_1 after hydraulic loading of the main veins. (b) Interpreted principal fracture network (yellow lines). (c), (d): Fluid take by matrix and fractures in model assuming low permeability contrast (c), and high permeability contrast (d). Matrix blocks between the fractures in case d take less fluid than in case c. Rainbow colors give time of flight contours, and fluid injection is from the top. Flow lines are given by magenta streamlines. After Van Harmelen and Weijermars (2018, Figs10a, b).

hydraulic fractures in a rock slab from Bidasar. The corresponding flow front through the main fractures and matrix is modeled in Figs. 2-4c, d. The simulation does not account for the creation of the fractures, but instead assumes these have already developed and are subsequently flushed by the hydrothermal injection fluid. For details see a prior study from our research group (Van Harmelen and Weijermars, 2018).

2.3. Fracture and fractal theory

2.3.1. Prior models of complex hydraulic fractures

2.3.1.1. Fracture flow models

Various attempts have been made by researchers to develop new models to better represent complex hydraulic fracture network systems, in both geomechanical fracture propagation models and in production forecasting based on flow models in fractured reservoirs. For example, the geomechanical unconventional fracture model (UFM) was developed to simulate the propagation of complex fractures in formations with pre-existing natural fractures (Weng et al., 2011). The UFM simulates the propagation, deformation and fluid flow in a complex network of fractures. The model seeks to solve a system of equations governing parameters such as fracture deformation, height growth, fluid flow and proppant transport, while considering the effect of natural fractures by using an analytical crossing model. The Wiremesh model, consists of a fracture network with two orthogonal sets of parallel and uniformly spaced fractures (Xu et al., 2010;

Meyer and Bazan, 2011). Given fracture spacing, mechanical properties of the formation layers and pumping parameters, this shale fracturing simulator can be used to predict the growth of the hydraulic fracture network. Benefits of the Wiremesh model come in the form of increased surface area of the fracture network and mechanical interaction of fractures but is still only an approximation of the network's complexity. Limitations of this model include not being able to directly link pre-existing natural fractures to the hydraulic fracture network with regards to the fracture spacing used and that the network geometry is assumed to be elliptical in shape and thus symmetric. These assumptions do not always fit with fracture geometry indicated by microseismic. Alternative modeling attempts sought to create the complex fracture network by finding a full solution to the coupled elasticity and fluid flow equations using 2D plane strain conditions (Zhang et al., 2007). Other studies presented a complex fracture network capable of predicting the interaction of hydraulic fractures with natural fractures but did not consider fluid flow and proppant transport (Olsen et al., 2009).

Flow models of fractured reservoirs have also advanced by upscaling a discrete fracture network (DFN) model into a dual-porosity reservoir model or by enhancing the permeability of stimulated reservoir areas (Zhou et al., 2012). The fundamental discrete fracture network (DFN) solution methodology is based on satisfying continuity, mass conservation, constitutive relationships and momentum equations (Meyer and Bazan, 2011). For fracture representation in this method each fracture panel had to be manually

input with specific fracture parameters thus requiring prior knowledge of hydraulic fracture orientation. The model also assumes the intersection of individual planar fractures to create the complex fracture network with drained area represented by pressure depletion plots. These DFN are created using stochastic simulations based on probabilistic density functions of geometric parameters of fracture sets relating to fracture density, location, orientation and sizes based on measurements from field outcrops or borehole images. DFN requires an extremely fine grid at the scale of the fractures leading to complicated gridding and for multi-stage wells with large fracture numbers is very computationally expensive.

Recent advancements with DFN has now led to the embedded discrete fracture model (EDFM). EDFM allows for complex fractures to be implemented in conventionally structured matrix grids without using local grid refinement (Yu and Sepehrnoori, 2018). EDFM can be thought of as a hybrid approach where the dual porosity model is used for the smaller and medium size fractures and the DFN is used to model larger fractures (Li and Lee, 2008). Advantages of EDFM include the use of a structured grid to represent the matrix and fractures. EDFM was initially used for planar 2D cases but has developed to model in 3D (Moinfar et al., 2014). Though EDFM has overcome some of the problems of the traditional DFM method, it can still be computationally expensive in complexly fractured reservoirs.

2.3.1.2. Fracture geometry models

Beyond the modeling attempts outlined above to recreate and describe complex fracture networks, work has been done by various authors to characterize the created fracture complexity based on field data. Zolfaghari et al. (2016) proposed the use of flow-back salinity data to help characterize the fracture network complexity. The shape of the flow-back curves is used to define the aperture size distribution (ASD) for a particular well. A narrow ASD is correlated to a simple fracture network while a wider ASD is believed to match a fracture network that is more dendritic and complex in nature. Zolfaghari et al. (2017) looked at correlating total ions produced from chemical flowback to estimate fracture surface area for two wells that was validated against RTA values. Based on these results the authors postulated that greater production from one well was due to the larger fracture area calculated. This larger fracture area was attributed to a more complex fracture network in the subsurface but there was no indication of potential fracture geometry. Another attempt to characterize fracture complexity utilizes tracer flowback data. Li et al. (2016) made use of tracer flowback data to characterize fracture morphology into three general categories. Based on the tracer breakthrough curve (BTC) the hydraulic fractures are roughly classified as micro fractures, large fractures and their mix. These methods allow for qualitative descriptions of the subsurface fracture network but do not allow for quantitative description in terms

of surface area of the complex fracture network in contact with the reservoir matrix or fracture network geometry.

The majority of fracture flow methods all attempt to introduce discrete fractures to model explicitly the elastic fracture propagation, subsequent flow and evacuation of fluid from the reservoir. The importance of accounting for fracture network complexity is apparent from production and pressure transient responses (Jones et al., 2013). Properly modeling the complexity of the fracture network is crucial for accurate history matching in these reservoirs. In addition to the discrete fracture models based on geomechanical failure modes, another potential approach to model fracture complexity uses fractal geometry. Fractals have long been used to model naturally occurring phenomena including petroleum reservoir and subsurface properties and equations (Berta et al., 1994; Cossio et al., 2012). Early work by Katz et al. (1985) and Pande et al. (1987) showed that fracture propagation in nature was not irregular, and could be represented by various fractal models. Building forward on this work Al-Obaidy et al. (2014) and Wang et al. (2015) approached the fracture network problem by creating branched fractal models to capture fracture network complexity.

2.3.2. Fractal theory

Fractal theory was first put forth by Mandelbrot (1979) as “a workable geometric middle ground between the excessive geometric order of Euclid and the geometric chaos

of general mathematics". A fractal was defined by Mandelbrot as a rough or fragmented geometric shape that can be split into parts each of which is a reduced-size copy of the whole. For an object to be termed a fractal it must possess some non-integer (fractal) dimension (Frame et al., 2012). If this fractal dimension is an integer, we can obtain normal Euclidean geometry such as lines, triangles and regular polygons. Cossio et al. (2012) put into simple terms that a property of a given system can be termed a fractal if its seemingly chaotic, and unpredictable behavior with respect to time and space can be captured in a simple power-law equation. One of the basic principles underlying fractal geometry is the concept of self-similarity at various levels. If one zooms in on the represented object, a natural repetition of patterns and properties can be observed.

The abundance of fractals in our natural environment ranges from the fractal nature of coastlines to the growth and bifurcation of trees and plants. The use of fractals allows one to make mathematical sense from seemingly random and chaotic processes. Early use of fractals in petroleum engineering began with the work of Katz and Thompson (1985) to represent pore spaces in sandstone cores. The use of fractal theory to represent the pore space was verified by its accurate prediction of the core porosity. We now extend this approach of fractals to model complex hydraulic fracture networks.

One approach in fractal theory is to create a fracture network model by using the fractal addition of the Lindenmayer system (Wang et al., 2017). The Lindenmayer system (L-system) is widely used to describe the growth of plants which can be seen to

be bifurcating in nature as well as being fractal at some scale. The L-system is a rewriting system that defines a complex object by replacing parts of the initial object according to given rewriting rules which simulate development rules and topological structures well (Lindenmayer, 1968; Han, 2007). Wang et al. (2017) introduced the L-system into fracture characterization because a fracture has similar development rules as trees. Four key parameters are used to control the generation of the fracture network, and these parameters influence the performance of production wells (Wang et al., 2018):

1) Fractal distance (d), controls the extending distance of the fractal fractions, (can be thought of as a basic repeating pattern), and closely relates to half length of the fractures created.
2) Deviation angle (α), controls the orientation of the fracture branching once deviation from the base fracture pattern occurs and relates to the area of the stimulated reservoir.
3) Number of iterations (n), controls the growth complexity of the fracture network or in other words fracture network density. This parameter relates to the multi-level feature of the fractal branches; during each iteration, the fractal fractures will branch from the original nodes following the given generating rules to construct that part of the network.

4) Growth of the bifurcation of the fractures and irregular propagation mode of a complex fracture network are subject to fractal rules, which are an implicit means to account for geomechanical heterogeneities (Wang et al., 2015, 2017, 2018).

The branching fractal model used in our study makes use of a simple L-system growth rule, which along with the fractal distance parameter controls the branched hydraulic fracture network's half length, the deviation angle controls the branched fracture network width span and the iteration number controls the branching complexity or density. Though the fracture geometry created using the L-system is seemingly random, we use the branching of the hydraulic fracture in our models to capture and replicate the physical evidence seen in cores recovered from the Hydraulic Fracturing Test Site (HFTS). These cores show that hydraulic fractures "diverge with a projected line of intersection, or branch line, just out of the core" (Raterman et al., 2017). We acknowledge that due to uncertainty in the subsurface there are infinite possibilities that can be modeled by changing parameters such as branching angle, fracture length and iteration number. Our current model uses branching angles and other parameters (given in Table 2-2) that generate a fractal network span and half-length that matches with commonly observed values from fracture propagation modeling and micro-seismic data.

2.4. Flow models

2.4.1. Complex analysis method (CAM) tool

The effect of different fracture networks on drained areas, velocity profiles and pressure depletion are quantified and visualized using complex analysis methods. Introductions to analytical element method applications to subsurface flow are found in several textbooks (Muskat, 1949; Strack, 1989; Sato, 2015). Hydraulic fractures connected to a well act as line sinks (Weijermars and Van Harmelen, 2016). For multiple interval sources with time dependent strength $m_k(t)$ the instantaneous velocity field at time t can be calculated from:

$$V(z,t)=\sum_{k=1}^{N}\frac{m_k(t)}{2\pi L_k}e^{-i\beta_k}\cdot\left(\log\left[e^{-i\beta_k}\left(z-z_{c,k}\right)+0.5L_k\right]-\log\left[e^{-i\beta_k}\left(z-z_{c,k}\right)-0.5L_k\right]\right) \quad (2\text{-}1)$$

Traditional applications of CAM in subsurface flow models make use of integral solutions to model streamlines for steady state flows (Muskat, 1949; Strack, 1989; Sato, 2015). A fundamental expansion of the CAM modeling tool is the application of Eulerian particle tracking of time-dependent flows, which was first explored in Weijermars (2014; Weijermars et al., 2014) and then benchmarked against numerical reservoir simulations in Weijermars et al. (2016).

Most current studies use numerical reservoir simulation to create pressure depletion plots as a proxy for the drained regions in the reservoir after production. CAM can determine the drained rock volume (DRV) by constructing time-of-flight contours to

the well based on Eulerian particle tracking taking into account the changing velocity field (Weijermars et al., 2017a, b). This approach provides accurate determinations of the DRV (Parsegov et al., 2018a) with the added benefit of identifying flow stagnation zones. Such stagnation zones or "dead zones" are defined as regions of zero flow velocity (Weijermars et al., 2017a, b), which create undrained areas that can be targeted for refracturing (Weijermars and Alves, 2018; Weijermars and Van Harmelen, 2018). Another added advantage of CAM model is their infinite resolution at the fracture scale due to the method being gridless and meshless, resulting also in faster computational times as compared to numerical simulations.

Modeling flow in fractured porous media using analytical solutions generated with time-stepped CAM models also allows the determination of pressure changes in the reservoir. Pressure depletion plots are calculated by evaluating the real part of the complex potential to quantify the pressure change at any location z at a given time t by:

$$\Delta P(z,t) = -\frac{\phi(z,t)\,\mu}{k} \tag{2-2}$$

Here $\phi(z,t)$ is the potential function with pressure scaling based on fluid viscosity μ and permeability k of the reservoir. The actual pressure field at any given time can be computed from the following expression with P_0 accounting for the initial pressure of the reservoir:

$$P(z,t) = P_0 + \Delta P(z,t) = P_0 - \frac{\phi(z,t)\mu}{k} \quad (2\text{-}3)$$

The CAM solution basic premise is placing the produced fluid volume back into the reservoir to determine the areas drained and the pressure response corresponding to this fluid placement. From replacing production into the reservoir based on history matching using decline curve analysis, the corresponding pressure depletion is obtained by simply reversing the signs of the values on the pressure scale from positive to negative (Weijermars et al., 2017b). For the pressure depletion plots later in this study, the spatial pressure change $\Delta P(z,t)$ is shown.

2.4.2. Flux allocation and production modeling

This study assumes a synthetic production well of 8000 ft horizontal length and 80 transverse fractures with 100 ft spacing between them. This gives a total distance covered by the fractures of 7900 ft, leaving an untreated distance of 100 ft between the heel of the well and the first hydraulic fracture of the treatment plan. The flow simulation starts with a single fracture, using a base case model with a single planar fracture, expanded with branched iteration models of the fracture geometry. The fracture trees initiating from single perforations are then expanded to multiple fractal systems for fracture stages with variations in complexity to observe the impacts on the DRV, velocity field and pressure field. By assuming symmetry about the wellbore, we initially

look at only one half of the fracture (half-length x_f) to determine the effects on the flow velocities and pressure depletion for different fracture geometry models.

Current fracture propagation models that use simple planar fractures have the ability to predict proppant placement density which due to uneven placement can create zones of higher fracture conductivity (Parsegov et al., 2018a). Though work has been done on proppant placement in complex fracture networks (Shrivastava and Sharma, 2018) as we assume infinite fracture conductivity in our fractal network uneven proppant placement is not considered in this model.

Production data from a typical Wolfcamp well used in a companion study (Parsegov et al., 2018a) were used to produce a history matched type curve based on decline curve analysis. To match the production decline, the Duong decline method was used and found to give a total cumulative production over 30 years that is in line with forecasted EUR for wells in the Wolfberry play, Midland Basin which the Wolfcamp formation falls under. Forecasts give an ultimate per well recovery estimated at 100,000 to 140,000 barrels of oil equivalent (Hamlin et al., 2012). The production well used Duong decline parameters resulting in a cumulative production forecast of 102,069 bbls after a productive well life of 30 years.

Flux allocation was proportional to the relative surface areas of each branched fracture. For each successive iteration, the next generation of branches of the fracture network becomes progressively shorter, thereby automatically being allocated less of the

overall production. This allocation method based on fracture length allows for the main fracture branches having the highest allocated flux while the progressive iterations of the branched network will have less flux allocated. The flux allocation algorithm used is as follows:

$$q_k(t) = Z \cdot S(1+WOR) \cdot q_{well}(t) \cdot \left(\frac{h_k L_k}{\sum_k^n h_k L_k} \right) \qquad [ft^3/month] \ (2\text{-}4)$$

Z is a conversion factor of 5.61 to convert from barrels to ft^3. *S* is the prorated factor to scale the total well production, for example scaling for one half-length of one fracture;

$$S = (1/80) \text{ x } 0.5 = 0.00625$$

Once the flux algorithm has been properly calculated the next step is the creation of the time-dependent strength value to use in the velocity and pressure potential equations. This strength is scaled by reservoir properties such as the formation volume factor *(B)*, porosity *(n)*, residual oil saturation *(R_o)* (Khanal and Weijermars, 2019a) and fracture height *(H)* and is given as follows:

$$m_k(t) = \frac{B \cdot q_k(t)}{H_k \cdot n \cdot (1-R_0)} \qquad [ft^2/month] \ (2\text{-}5)$$

Table 2-1 Reservoir parameters used for modelling.

Porosity (n)	0.05
Permeability (k)	1 microDarcy
Water-Oil Ratio (WOR)	4.592
Formation Volume Factor (B)	1.05
Viscosity (μ)	1 centipoise
Residual Oil Saturation (R_o)	0.20
Fracture Height (H)	75 ft

2.4.3. Drained rock volume (DRV)

For the determination of drainage areas, the CAM process utilizes the concept of flow reversal. The produced fluid is essentially placed back into the reservoir at the same rate as produced to determine where the fluid has been drained from. As such the way in which the hydraulic fractures are represented will have a direct impact on the area which is drained, and the corresponding pressure gradient that drives the fluid flow back into the reservoir. The underlying assumption is that the larger the surface area of the hydraulic fracture the easier the flow into the matrix (and reverse), the narrower will be the width of the region drained around the fracture and thus the lower the pressure needed to achieve a given production rate. A fracture with smaller overall surface area (idealized planar hydraulic fracture, Fig. 2-5a) will need to have wider drainage width

whereas for the same production, a greater fracture surface area in contact with the matrix will mean a narrower drainage width (Fig. 2-5b).

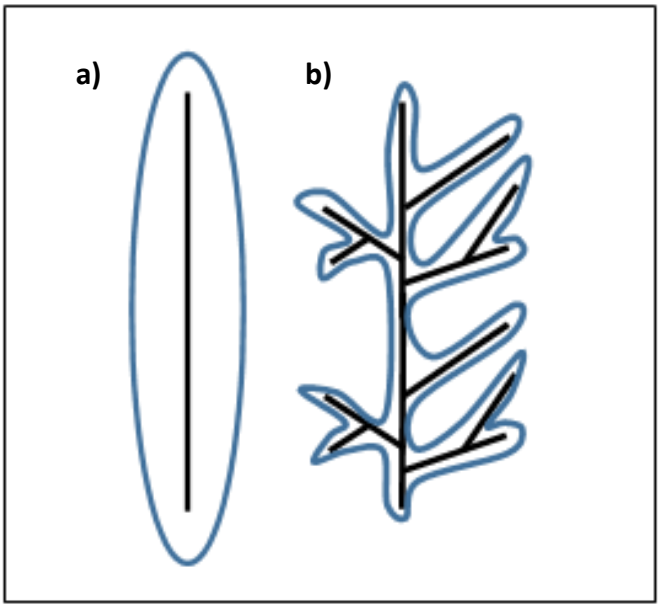

Figure 2-5 a) Plan view of drainage area around a planar fracture, b) drainage area around a branched fracture representative of our fracture network.

Initially, we expected that a larger fractal dimension with more surface area would increase the injectivity of the matrix and require lower pressures to evacuate the reservoir fluid. Our models however show that once a constant total fluid production is used the overall pressure change remains the same regardless of the fracture network complexity. The models confirm the expectation that more complex fractal networks cause smaller lateral drained areas away from the fractures with greater local pressure variations. The reason for the localized pressure depletion peaks is that denser fracture

networks with the same injectivity per fracture length will locally remove more fluid molecules from the matrix, thus resulting in larger pressure depletion locally.

The hydraulic fractal network is created and applied using an effective method of investigation by first modeling a small section of the horizontal wellbore. Because we use the method of fractals, a small sample of the well system should in fact be representative of the much larger drainage behavior of the well. This modeling strategy will also be beneficial in terms of computational and modelling time. Once the flow and pressure response have been determined based on individual fractal networks with increasing complexity, the investigation is extended to multiple fractal networks to investigate the possible effects of flow interference in fractured wells with numerous stages. Using this method both symmetrical and asymmetrical networks are modeled to determine changes in drained areas and flow response. The impact of fractal network complexity on reduction of flow stagnation zones is investigated to help determine the ideal fracture geometry to increase overall recoveries.

2.4.4. Model validation

The analytical solution to flow based on the complex analysis method has been validated against numerical simulators in previous work done. Weijermars et al. (2017a) compared the results of the analytical method for flow in planar fractures modeled as line sinks against a commercial simulator (ECLIPSE) that was augmented with a

validated streamline tracing algorithm. This allowed for the comparison of time of flight contours as well as streamline patterns. This validation against the numerical simulator was achieved via a three-step process. Flow simulation in the commercial simulator provided pressure and flow rates on the six faces for each finite cell. These results were then imported into a streamline algorithm to obtain streamline tracing data, which was then imported in Petrel to visualize the actual streamlines. For the simple planar fracture case the results from the numerical simulator matched well with the analytical complex analysis method proving validation of the complex analysis solution (Fig.2-6). Our current model can be thought of as an extension of this validated case where we replace the simple planar fracture by our complex fractal network that comprises numerous line sinks acting within our reservoir. For a more detailed look at the validation the reader is referred to the work by Weijermars et al., (2017a).

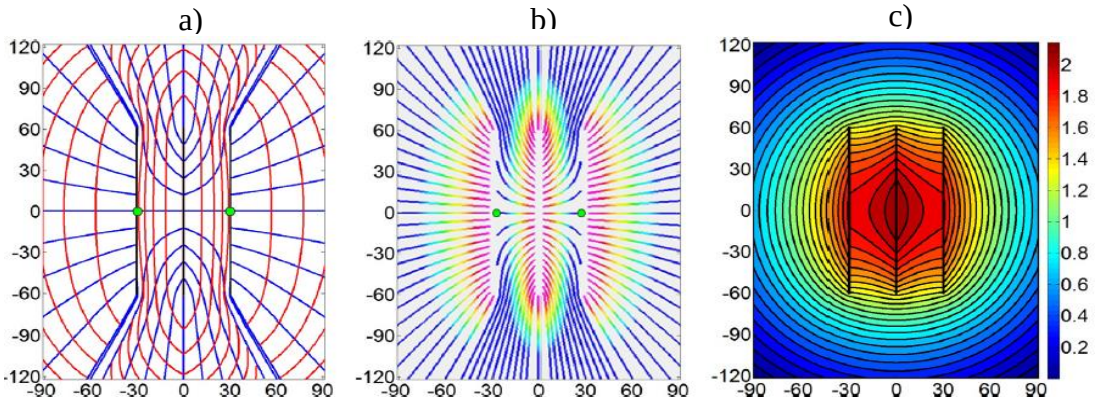

Figure 2-6 Streamlines with drainage contours: a) analytical solutions, b) commercial simulator, c) pressure field. a) Streamlines (blue), time of flight contours (red), stagnation points (green). b) Streamlines and time of flight contours (rainbow colors). c) Analytical pressure field. Fractures represented as black lines: Adapted from Weijermars et al., (2017a)

2.5. Results

2.5.1. Fractal network creation

The Lindenmayer (L-system) rewriting system based on fractals is used to construct numerous branching fractal networks. This system defines a complex object by replacing parts of the initial object according to given rewriting rules. The L-system, combined with information on fractal network geometry, fractal distance (d), deviation angle (α) and iteration number (n), allows the defining of rules for creating the overall network. A systematic workflow to investigate the effect of fractal network complexity is laid out in the subsequent sections.

The network structure is defined by a simple string or axiom using variables 'F' and 'G'. Using these variables, branching is represented by the use of square brackets with the '+' and '-' symbols denoting either clockwise or anticlockwise branching angles. The iteration number gives the replacement rules, changing the branching complexity and is referred to as different *fractal generations*. A simple fractal code written in Matlab from the M2-TUM group from the TU Munich was modified for our purpose of fractal network generation in 2D (available at http://m2matlabdb.ma.tum.de/author_list.jsp).

Axiom used for generation of the symmetrical fractal networks:

Symmetrical axiom rule = 'F [+G] [-G] F F [+G] [-G]'

Generated fractal networks using the above axiom and geometry parameters from Table 2-2 are shown below in Fig. 2-7:

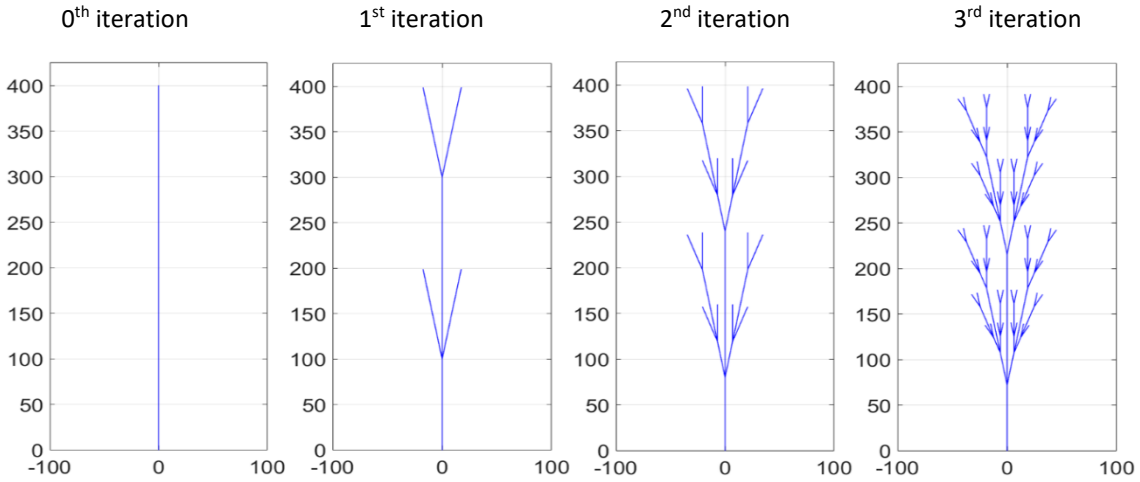

Figure 2-7 Fractal networks created using axiom rule and fracture geometry properties.

Table 2-2 Parameters used for creation of different fracture geometries.

Fracture model	Planar	1st generation fractal	2nd generation fractal	3rd generation fractal
F length (ft)	400	100	40	18
G length (ft)	-	100	40	15
Branching angle (degrees)	-	10	10	10
Created fracture half-length x_f (ft)	**400**	**398.5**	**398.2**	**391.1**
Created fractal network span (ft)	**-**	**34.7**	**69.04**	**89.44**

2.5.2. Drainage by single symmetrical fractal networks

The first scenario investigated uses symmetrical fractal networks. The L-system with given fractal geometry parameters (Table 2-2) were incorporated in the CAM model to determine flow and drained rock volume responses for a variety of fractal geometries, ranging from a single planar fracture to a 3rd generation symmetrical fractal network (Fig. 2-8). Moving from the planar fracture geometry towards higher fractal generations, an exponential increase occurs in the fracture surface area (Fig. 2-8). Even a simple branching hydraulic fracture is shown to have a much larger surface area than the planar fracture. Assuming the well production rate is fixed, total drained volume of fluid per fractal network stage stays constant. Higher fractal generations cover a larger areal extent but drain narrower matrix depth, whereas the planar fracture drains broader distances away from the fracture (Figs. 2-5 and 2-8).

The velocity contour plots show that when the fracture geometry evolves from planar to successive branched iterations results in a greater variability of the local velocities (Fig. 2-8, second row). As the branching complexity increases, individual fracture segments are spatially clustered close together, leading to small scale interferences resulting in higher flow velocities at the fracture network outer extremities, which is balanced by slower velocities between the branching fractures. The overall pressure change is found to be similar even as fracture complexity increases (Table 2-3). Pressure change is directly linked to the amount of production from the reservoir which

is kept constant for all simulations. What is observed from the pressure depletion plots is that the greatest local pressure response occurs in areas with the highest fracture density (Fig. 2-8, third row). Comparing the response from the velocity and pressure plots, the greatest pressure change does not correlate with where fluid flows fastest around the fractures. However, there is a clear correlation between the steepest pressure gradients (regions where the pressure contours are spaced tightest) and the regions of highest flow velocity.

Drained areas are outlined by the time-of-flight contours inferred from particle tracking, based on the production allocation due to the selected fracture strengths (Fig. 2-8, fourth row). Results for a planar fracture geometry show equal drainage around the entire fracture. As more complex fractal networks are simulated, the results show the total drained area stays constant (regardless of fracture complexity as a constant production is used). However, the DRV regions are not distributed equally around the fracture segments in the network, leading to some small undrained areas between the branches of the fractal network.

Table 2-3 Comparison of various parameters for different symmetric fracture geometry.

	Planar fracture	1st gen. fractal	2nd gen. fractal	3rd gen. fractal
Maximum velocity. (ft/month)	0.9477	1.1088	1.0087	1.0979
Maximum pressure change (10^6, psi)	1.3939	1.4547	1.4286	1.5035
Fracture surface area (10^4, ft^2)	6.0	10.501	20.403	37.04

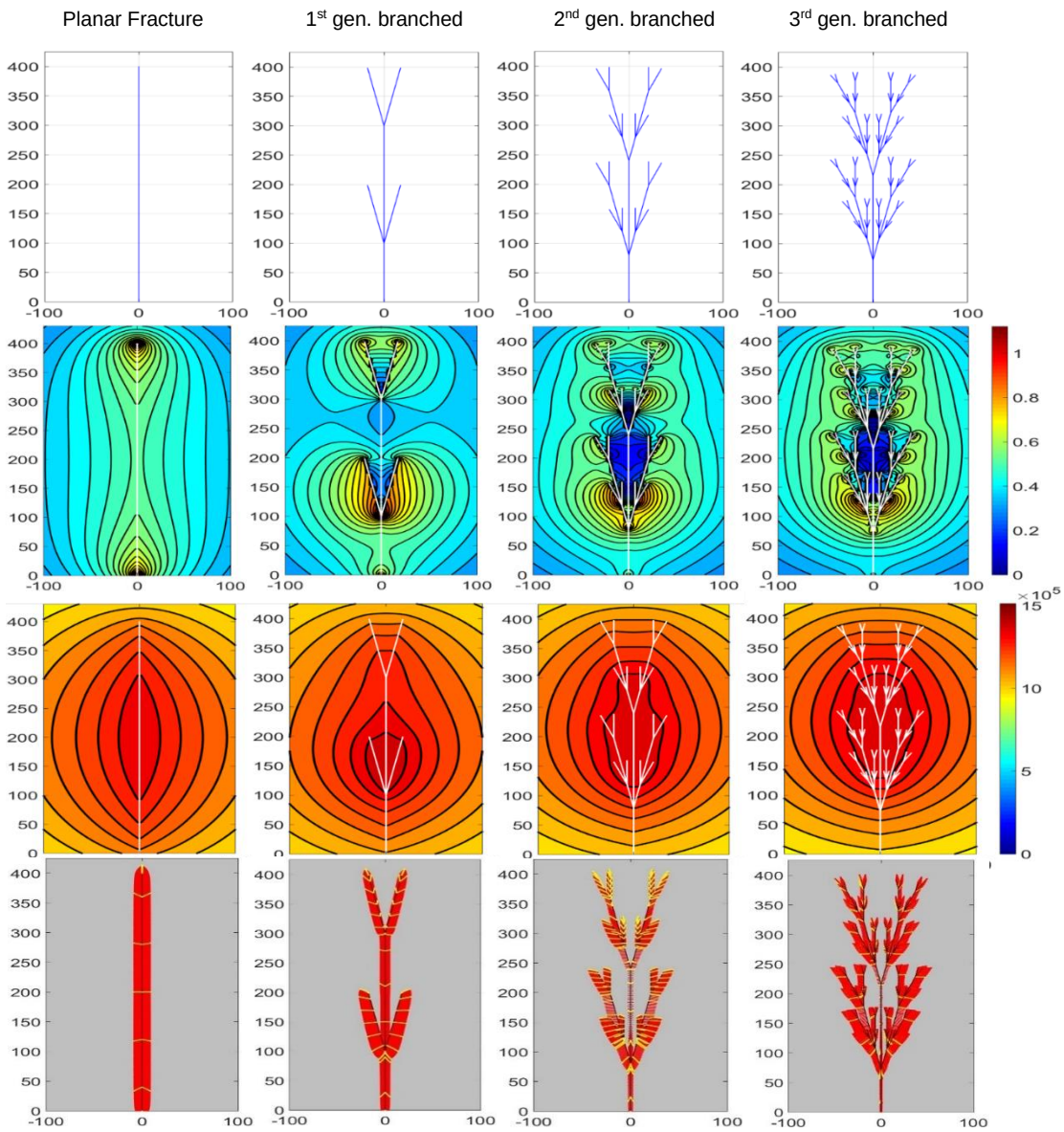

Figure 2-8 First row - Fracture geometry modeled with planar fracture, 1st generation symmetrical fractal network, 2nd generation, 3rd generation from left to right; Second row - Velocity contour plot (ft/month) after 1 month production; Third row - Pressure contour plots (drawdown in psi) after 1 month production; Fourth row - Drained areas after 30 years production (drained area highlighted in red with tracked streamlines in yellow). Length scale in ft.

2.5.3. Drainage by single asymmetrical fractal networks

Previous modeling assumed the generation of symmetrical fracture branches on both sides of the main branch. Due to the anisotropic nature of rocks there is a strong possibility that these branches in reality may form asymmetrically due to changing rock properties. Using the L-system, different generations of branched asymmetric fractures are modeled with the CAM to determine the impacts of asymmetry on flow and drained rock volumes (Fig.2-10). The axiom rule for this asymmetric fractal network is given as:

Axiom used for generation of the asymmetrical fractal network:

Asymmetrical axiom rule = ‘F [-G] F F [+G] [-G]'

Asymmetric fractal networks still effectuate an increase in fracture surface area for successive iterations when compared to the planar fracture but less than for the symmetrical fracture network (Fig. 2-9). The velocity plots again show greater variability in flow velocities as the fractal network complexity increases with the greatest variation coinciding with the region where fracture density is highest (Fig. 2-10, second row). The asymmetrical fractal network shows similarity to the symmetric fractal network in terms of overall pressure depletion and maximum/minimum flow velocities. The major difference with the asymmetric fractal network is the skewing of the highest pressure depletion contours to the area of highest fracture density (Fig. 2-10, third row). The premise that the steepest pressure gradients (areas where the pressure contours are tightest) correlates to areas of highest flow velocity is reinforced from these plots.

Drained areas are found to conform to the areas of highest flow velocity (Fig. 2-10, fourth row) with small scale stagnation areas found in between the highly branched areas as seen before in the symmetrical fracture network models (Fig. 2-8).

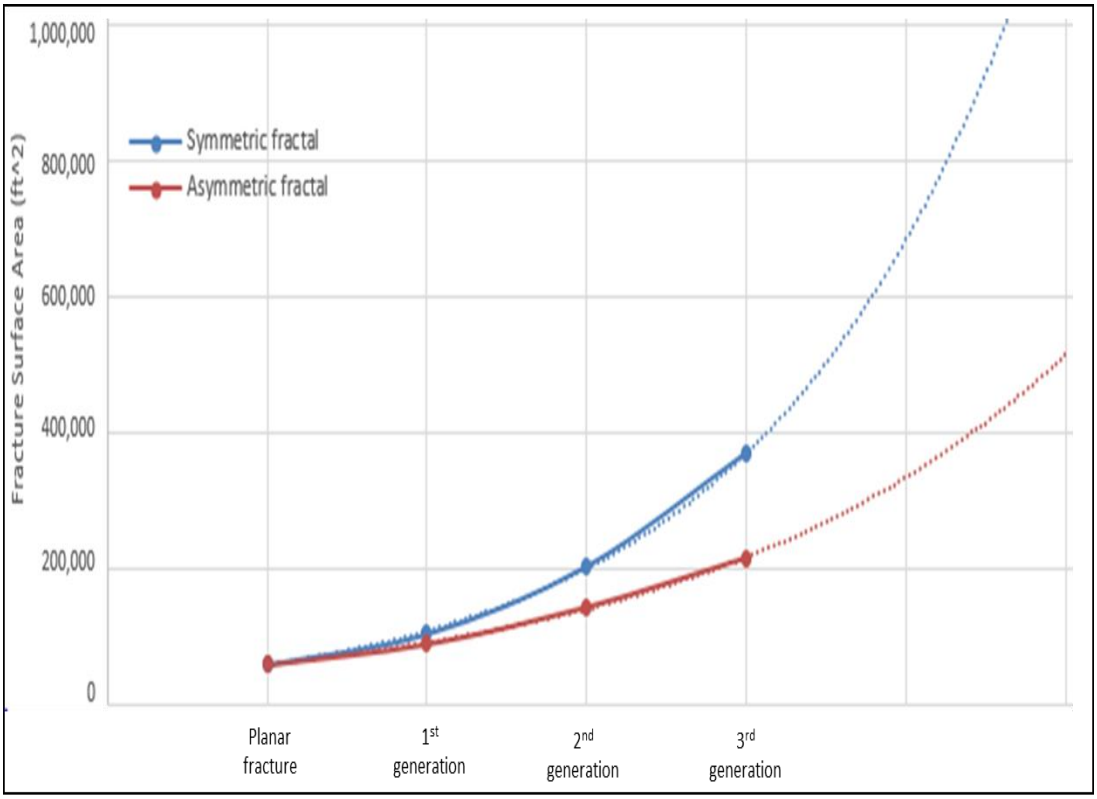

Figure 2-9 Graph of Surface area vs fracture geometry type for asymmetric and symmetric fractal networks.

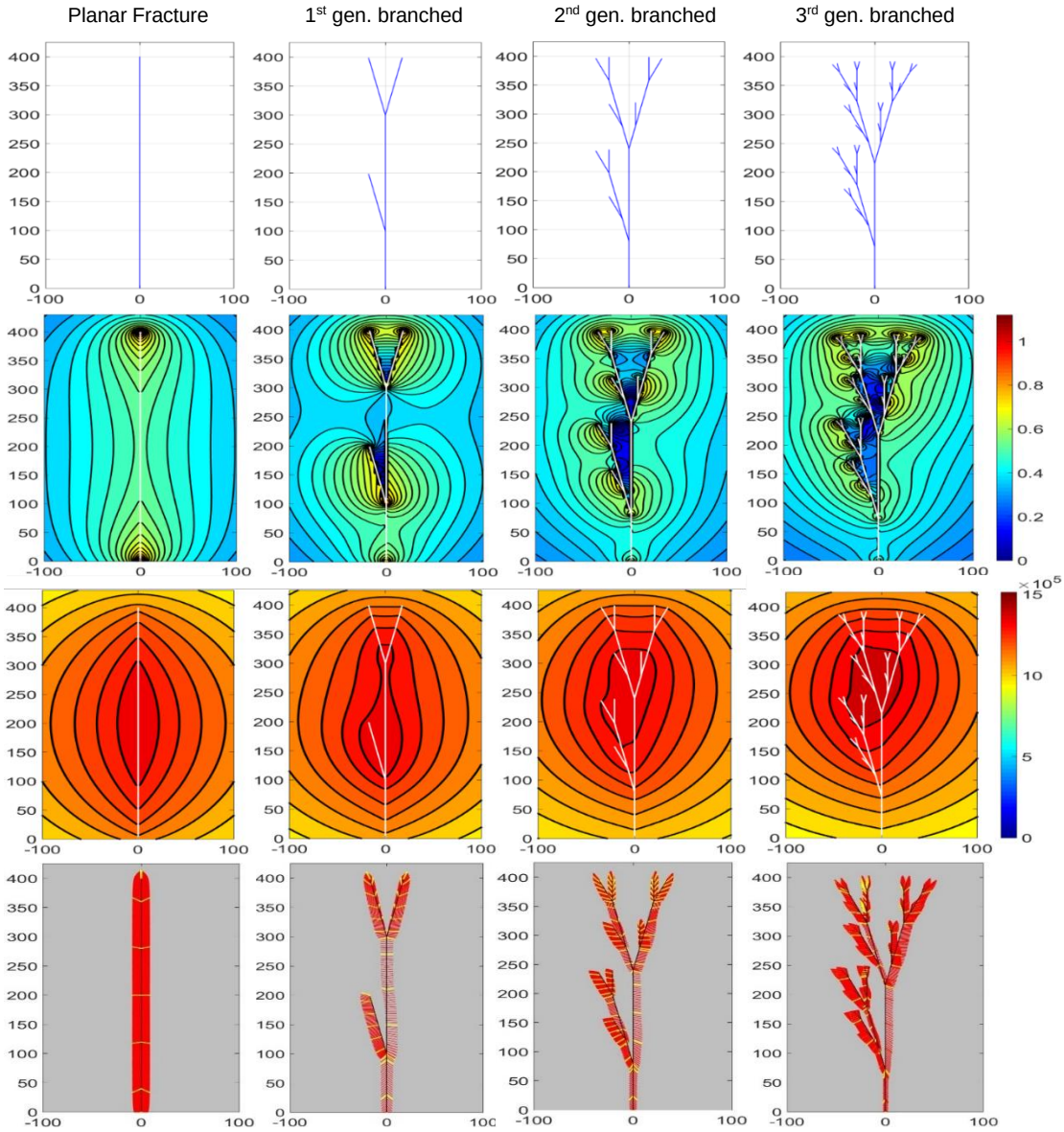

Figure 2-10 First row - Fracture geometry modeled with planar fracture, asymmetrical 1st generation asymmetrical fractal network, 2nd generation, 3rd generation from left to right; Second row - Velocity contour plot (ft/month) after 1 month production; Third row - Pressure contour plots (drawdown in psi) after 1 month production; Fourth row - Drained areas after 30 years production (drained area highlighted in red with tracked streamlines in yellow). Length scale in ft.

2.5.4. Interference effects of multiple fractal networks

Simulations in the previous section investigated the effect of moving from a single planar fracture to more complex symmetrical and asymmetrical branching fractal networks. Modeling of a single fracture is the most logical point to start from but is not truly representative of modern hydraulically fractured wells with multiple perforations per stage and multiple stages, resulting in several hundred fracture initiation points at the perforations. The typical hydraulically fractured well completion in 2017 and beyond can have 50 stages or more. The spacing of the fracture may have a crucial impact on flow interference and thus affects drained areas and estimated ultimate recovery. This section seeks to determine the impact of interference effects on flow velocity, pressure depletion and drained areas by simulating multiple fracture networks with different fractal network configurations. Using a base case of 3 planar fractures, comparisons of flow velocity, drained areas and pressure depletion are made for various combinations of 2^{nd} generation fractal networks (Fig.2-11).

The base case models the flow response of three planar fractures and shows with the given fracture half-length and fracture spacing, extremely low flow velocities occur between the central and outer fractures (Fig. 2-11, left column, top row). Flow stagnation zones are identified by velocity lows. These stagnation zones create areas in the reservoir that are left undrained due to the interference effect of the multiple fractures. The only way to drain these areas would be refracturing into the stagnation zones. The

pressure depletion plot (Fig. 2-11, left column, center row) shows the largest pressure drop occurs between the fractures however this coincides with our lowest flow velocities and stagnation zones. This reinforces the idea put forward in Weijermars et al. 2017b that the pressure plots are poor proxies to recognize the reservoir areas drained by the fractures. The drained region after 30 years is visualized by the time-of-flight-contours to the fractures (Fig. 2-11, bottom row) and shows the majority of the drained area is at the outer fractures where we also have the highest flow velocities. Flow interference between the fractures creates the stagnation zones that lead to undrained rock volumes.

The second scenario investigates the response to three symmetrical 2nd generation fractal networks (Fig.2-11, center column). Slower velocities are again found between the branched fractal areas but for this case are confined to a smaller area. This in turn means that branched networks create smaller stagnation zones, than with the planar fractures and thus the fractal network should be conducive to drain more of the reservoir space effectively (Fig. 2-11, center column, bottom row).

Better drainage coverage from the fractal network means less refractures are needed between the initial fractures. For branching fractal networks, too small a fracture spacing will result in draining the same reservoir areas due to overlapping fractal networks creating an inefficient drainage process.

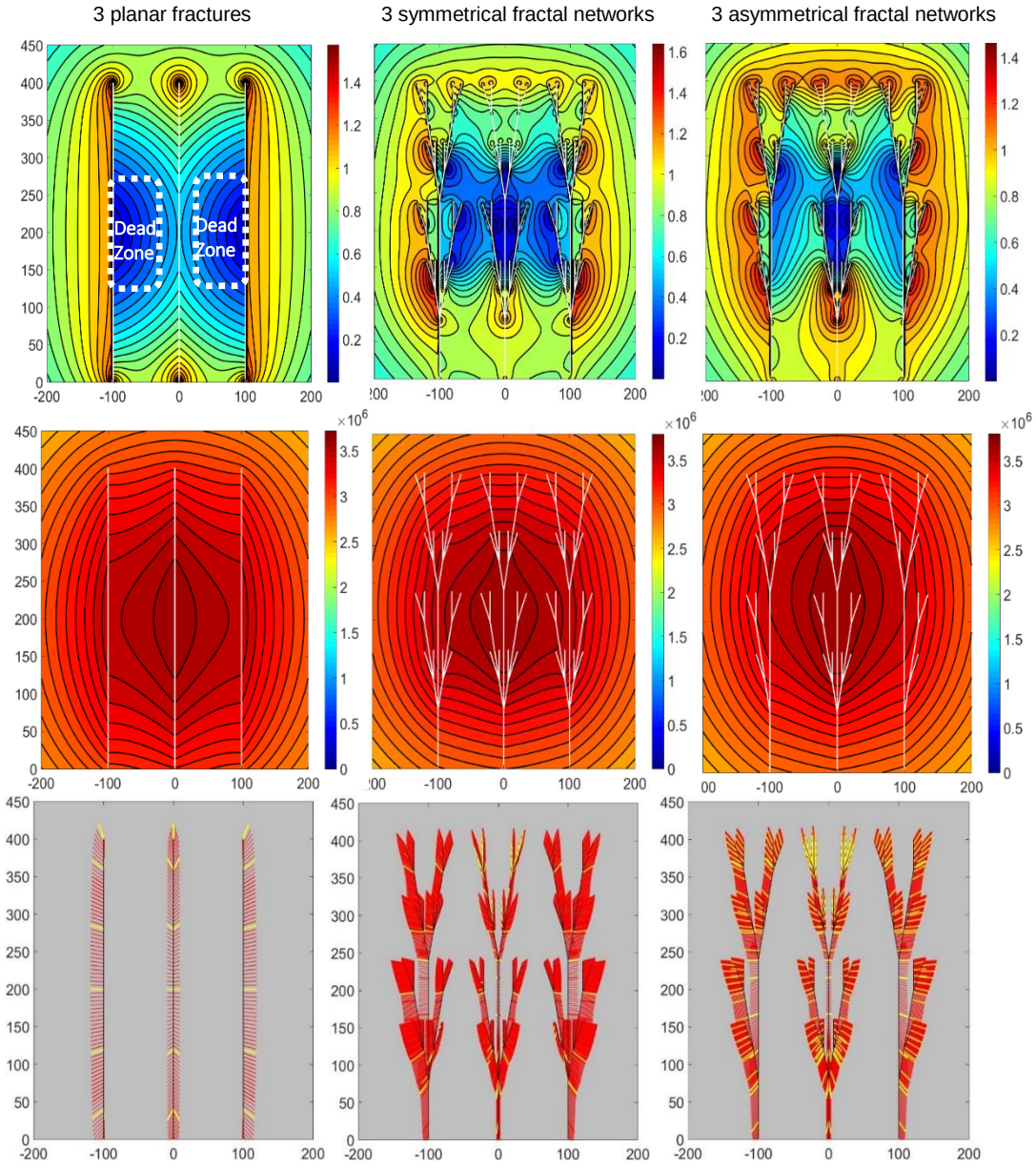

Figure 2-11 Top - Velocity contour plots (ft/month) after 1 month production; Middle - Pressure contour plots (drawdown in psi) after 1 month production; Bottom - Drained areas after 30 years production; Length scale in ft.

A third scenario looks at a central symmetrical fractal network flanked by two asymmetrical fractal networks (Fig. 2-11, right column). Again, the areas of highest velocity occur at the periphery of the fractures with the slowest flow between the fractal networks. From the various simulations there is a clear correlation between higher fractal network complexity and suppression in the areal extent of flow stagnation zones. Reduction in stagnation zones in turn means more efficient drainage of our rock and smaller undrained areas between fracture stages.

One interesting simulation case uses a symmetrical fractal network followed by two asymmetrical networks that grow away from the first symmetrical network (Fig. 2-12). This orientation is used to represent the effect of stress shadowing during sequential hydraulic fracturing from toe to heel. Stress shadowing is the concept that fractures in the subsurface will tend to propagate away from the direction of already fractured rock due to changes in the stress regime (Nagel et al., 2013). The introduction of a poroelastic model to capture stress shadowing is outside of the scope of this work but to recreate this effect we have the first hydraulic fracture network at the toe being symmetrical due to no stress shadowing. The subsequent hydraulic fracture networks towards the heel of the well (Fig. 2-12) will be influenced by stress shadowing and this is captured by no branching of the fractal network in the direction of the previous hydraulic fracture at the toe leading to an asymmetrical fractal network. Using this fracture geometry to mimic stress shadowing, the area of greatest pressure depletion becomes skewed toward the

initial fracture at the toe of the well (Fig. 2-12, center). Comparison of the velocity and pressure plots in Fig. 2-12 show the region with the largest pressure drop corresponds to the lowest flow velocities between the first toe fracture and the middle fracture. One would expect when the pressure drop is greater in a localized area, fluid velocity would be higher in that area of the reservoir. The physical explanation for the disparity between the regions with the largest flow rates and faster drainage being shifted with respect to the regions of highest pressure depletion as seen in our CAM model is as follows. Fluid moves fastest where the pressure gradients are steepest. The regions where fluid molecules are actively removed from the reservoir maintain the steepest pressure gradient. Adjacent regions with flow stagnation still will experience wider spacing between their fluid molecules leading to pressure depletion. This concept of the fundamental difference between pressure depletion and actual drained rock volume was first recognized in recent studies (Weijermars et al., 2017b; Weijermars and Alves, 2018; Weijermars and Van Harmelen, 2018), using the same model tools outlined in the present study. Most current models use pressure plots to show drained areas but conclusions from this study show that velocity plots (rarely visualized in other models) give a better indication of actual drained rock volume. The fracture configuration of Fig. 2-12 results in a less effectively drained area near the initial toe fracture, whereas areas drained by the fractal networks at the heel side with less pressure depletion and higher

flow velocities drain a slightly larger area, with a decrease in the size of the stagnation zone.

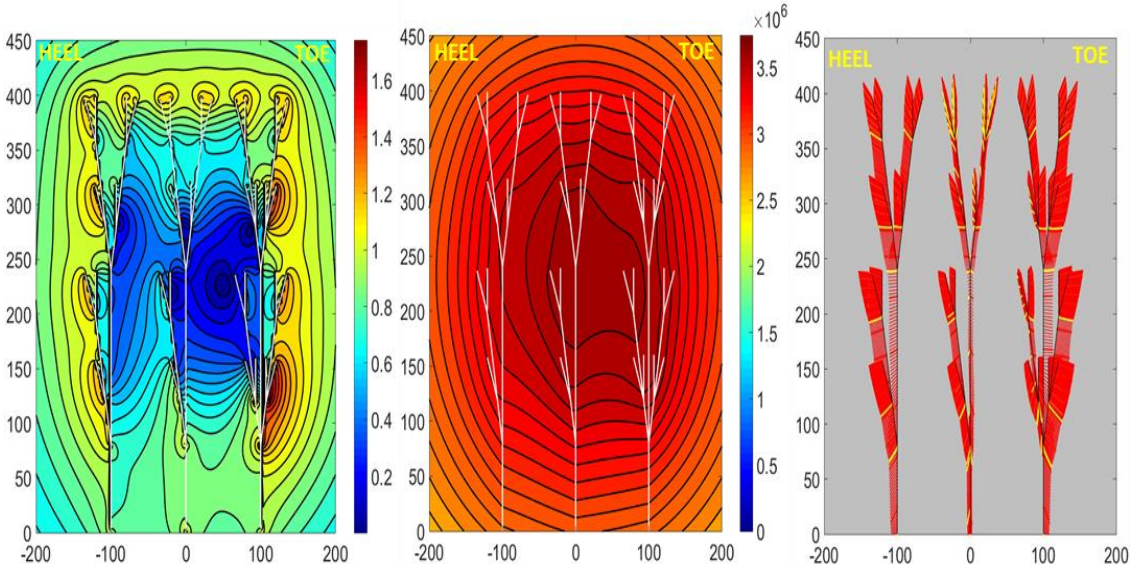

Figure 2-12 Left - Velocity contour plot for 3 branched fracture networks (ft/month) after 1 month production; Middle - Pressure contour plots (drawdown in psi) after 1 month production; Right - Drained areas after 30 years production; Length scale in ft; Surface area covered by symmetric/asymmetric 3 fracture networks is 4.9207 x10^5 ft^2.

Another configuration investigated was a single fracture stage with five fractures, each made up by a 2nd generation symmetrical fractal network (Fig. 2-13). This simulation mimics today's industry standard of five fracture clusters per stage. Typical fracture distance in horizontal wells can go as low as 20 ft between perforation clusters. For this model we maintain a fracture cluster spacing of 100 ft as used in previous simulations for ease of comparison and visual resolution. Similar to our base case with three symmetrical 2nd generation fractal networks (Fig.2-11, center column), we again

find slower velocities between the branched fractal networks, creating narrower flow stagnation areas. The stagnation regions are smaller than those created by planar fractures. A crucial take away from this simulation is that fracture interference effects, similar to those seen in other models, will equally occur for narrower spaced fractal networks. However, the much smaller fracture spacing used in the most recent well stimulation programs will only increase the intensity of local flow interference. Although more fractures increase the contact area with the matrix, the drained rock volume will not increase linearly with surface area increase due to the effect of increasing flow interference.

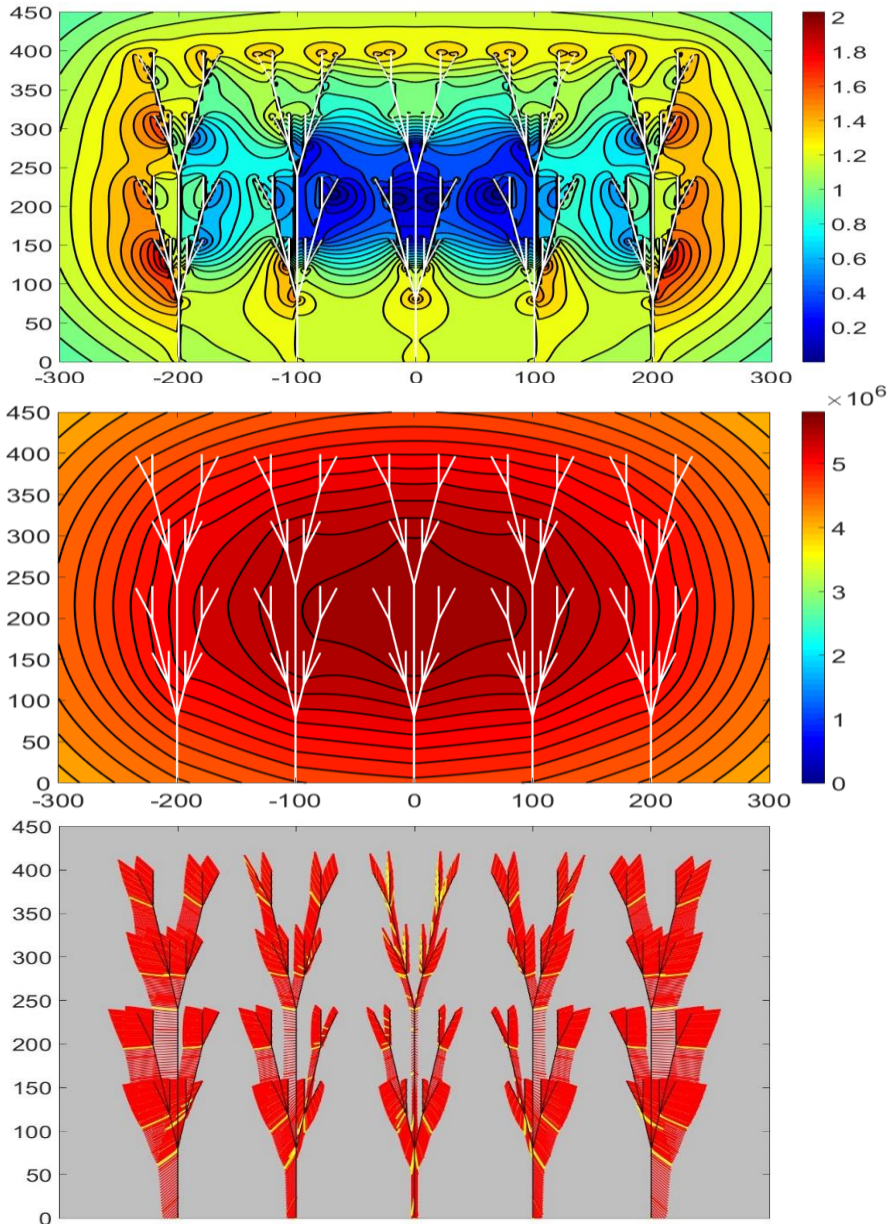

Figure 2-13 Top row - Velocity contour plot for 5 symmetrical branched fracture networks (ft/month) after 1 month production; Middle row - Pressure contour plots (drawdown in psi) after 1 month production; Bottom row - Drained areas after 30 years production; Length scale in ft; Surface area covered by 5 fracture networks is 1.0201 x10^6 ft^2.

2.5.5. Multiple full-length fractal networks

The preceding results all looked at half of the total fracture network length. The reason for this approach was the assumption of symmetry of the network on both sides of a horizontal wellbore. A final simulation looks at a full fracture length ($2x_f$) for a single fracture treatment stage with three perforation clusters, each generating fractal fractures (Fig. 2-14). Results show that the premise of flow symmetry about the wellbore is confirmed, as the velocity plots show contour patterns closely resembling those in Fig. 2-10 (center column). Flow stagnation points in Fig. 2-14 are shifted across the reservoir space to a location between the three fractures close to the wellbore, different from those seen in Fig. 2-11. The overall effect of a more complex fracture network is to reduce the spatial spread of flow stagnation zones, leading to improved efficiency of the DRV near the individual fractures.

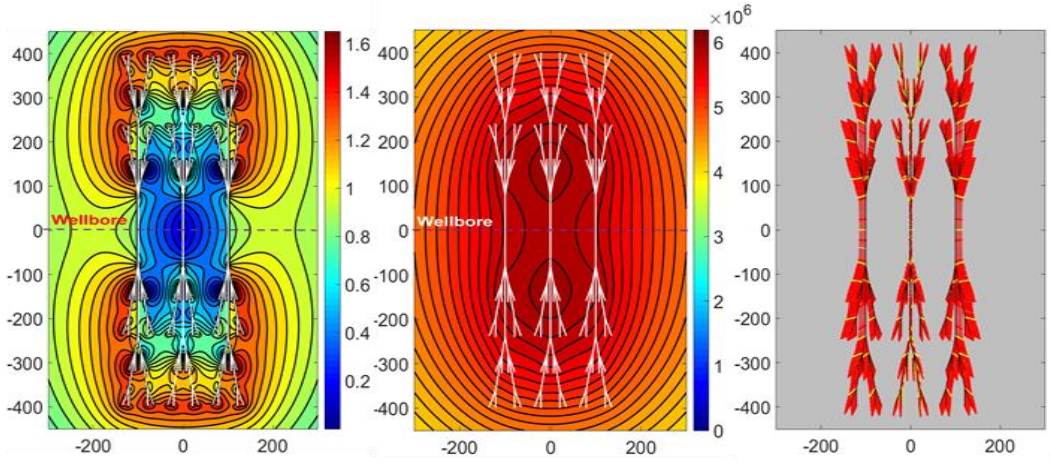

Figure 2-14 Left - Velocity contour plot for 3 full ($2x_f$) branched fracture networks (ft/month) after 1 month production; Middle - Pressure contour plots (drawdown in psi) after 1 month production; Right - Drained areas after 30 years production; Length scale in ft.

2.6. Discussion

2.6.1. Interference effects

The effect of fracture geometry on flow interference was investigated using a fractal fracture network description in combination with the complex analysis methods (CAM) to model drainage patterns and the resulting DRV near hydraulic fractures. Several series of simulations were conducted to determine the impact on drained areas and flow velocities when the fracture geometry varies, starting from a single planar fracture and evolving up to 3rd generation branching fractals. For greater fractal network complexity, the local area drained away from each individual fracture segment becomes smaller as compared to the area of drained regions near a single planar fracture. The difference occurs because fractals have a larger fracture surface area and we are putting back a constant amount of produced fluid (via the principle of flow reversal) in both the single and fractal models. Consequently, the fractal network shows more variations in flow velocities and pressure depletion peaks as compared to a planar fracture. These extreme changes in velocity lead to uneven drainage by the fracture network with the possibility of small undrained areas due to stagnation points occurring between the branches.

A planar fracture geometry based on our model's fracture spacing and half-length creates stagnation surfaces leading to relatively large undrained areas between the fractures. In contrast, the fractal network geometry shows a reduction in the effect and

areal extent of the stagnation zones (as seen from a comparison of the velocity and drained area plots, Fig. 2-11), due to a decrease in the interference effect on flow. The position of flow separation surfaces separating the drainage regions of individual fractures is controlled by the ratio of the fracture length and fracture spacing (Weijermars et al., 2018). When the fracture spacing is greater than a quarter of the fracture length, the flow stagnation points occur midway between the individual fractures. For complex fractal networks, each fracture branch has a smaller length compared to a single planar fracture. The smaller fracture branch lengths mean less flow interference will occur for an otherwise constant fracture cluster spacing.

2.6.2. Pressure depletion

Results show (Fig. 2-8, third row) that when the fracture surface area increases due to the more complex fractal networks, the average reservoir pressure change remains the same. One might expect that a greater fracture surface area to place fluid back into the reservoir model would result in smaller overall pressure changes. However, pressure peaks and lows show a larger spread where the fracture network complexity increases. The local variation in the pressure response is affected mostly by the fracture density. From the pressure plots (Fig. 2-11, second row) one can observe that areas with the highest fracture density give pressure contour depletion peaks. The current model uses a pre-fracture matrix permeability of 1μD giving pressure changes in the magnitude of 10^6

psi (Fig. 2-14). When permeability is changed to an after-fracture permeability of 1 mD the pressure change magnitude drops to the range of 10^3 psi, which is in line with field observations. We assume this after-fracture permeability change is due to the creation of a network of micro-fractures in the rock that is termed the enhanced after-fracture permeability region.

2.6.3. Model limitations

One aspect that the current model does not consider is the effect of various fractal iterations on fracture conductivity. Beyond the concept of fracture conductivity decreasing with time due to partial fracture closure following reservoir pressure decline (Daneshy, 2007), as we create successive iterations, each new branch will be less conductive due to fracture width reduction and the lesser ability for proppant placement. In the current model all fractures are given a constant flux, whereas in reality the shorter distal fracture branches may have less aperture and consequently less proppant placement, which may suppress fluid flux. The use of micro-proppant to help prop these smaller secondary and micro-fracture networks can retain fracture conductivity and is a field currently under research (Kim et al., 2018). The impact of fracture closure with time can be looked at in future work by the addition of a parameter to further decrease strength of flux into the fractal network. Water blockage to flow due to imbibed water during the fracturing job and subsequent soaking period is also not accounted for.

Another crucial point is that the current model ensured there was no overlapping of fractal branches either within a stage or by multiple stages. This may not always be true in nature and with very low current fracture spacing, there is a possibility of these fractal networks crossing. The possible crossing of the fractal networks from sequential fracture clusters can result in communication between stages that is regularly seen in the field (Barree and Misikims, 2015; Li et al., 2016).

2.6.4. Practical implications

The impact of fractal fracture geometries on the DRV and stagnation zones is investigated in this study. Our models indicate that when the complexity of hydraulic fracture networks increases, this will suppress the occurrence of dead zones. In order to increase the DRV and boost the associated well productivity (and thus improve ultimate recovery), our models suggest that fracture treatment programs must find ways to create more complex fracture networks. The generation of such complex fracture networks is currently not in included in concurrent fracture treatment design models, which limit the fracture development to mutually parallel planes. Because observational evidence from field experiments suggests that hydraulic fractures in hydrocarbon wells range from planar to multi-branched fractals (Huang and Kim, 1993; Raterman et al., 2017), fracture treatment propagation models need to be modified to more realistically account for the development of complex fracture geometries that predictably follows from local geo-

mechanical heterogeneities at the grain scale of rocks. The complex fracture geometry and fracture crossing provide a valid alternative explanation for the fact that tracer readings may overlap across fracture stages, which some commercial fracture propagation models presently attribute to the occurrence of longitudinal fractures parallel to the wellbore (Barree et al., 2015).

2.7. Conclusions

The aim of this project was to more accurately represent the detailed flow patterns and drained rock volume (DRV) in unconventional reservoirs for a range of complex fractal fracture geometries. Such fractal flow models may help reservoir engineers to improve the hydrocarbon recovery rates. The simulations in this work show that fracture geometry and complexity have a significant impact on the detailed hydrocarbon migration route near the fractures. Major conclusions realized from our study are as follows:

(1) A complex fracture network enhances the drained rock volume via two mechanisms. The first is that with more complex networks, the overall fracture surface area increases resulting in larger access to fluid stored in the reservoir matrix rock. The second mechanism is the suppression of stagnant flow zones when the complexity of the hydraulic fracture network increases.

(2) Hydraulic fracture treatment programs should stimulate the creation of bifurcating fractures as approximated by our fractal model. By reducing stagnant flow regions, the DRV will more effectively drain the reservoir. This will lead to improved drainage between the fractures, which will increase the estimated ultimate recovery from hydrocarbon wells.

(3) Using CAM, we are able to visualize in high resolution the effects of various fractal network geometries on flow and pressure response in the reservoir. We highlighted the fact that pressure plots, commonly used as proxies for drainage patterns, are poor proxies for the actual DRV. The DRV can be more accurate predicted using streamline tracking and time-of-flight contouring, as shown in our study.

(4) For planar fractures, stagnation zones in a three-fracture cluster occur close to the outer fractures, typically when the fracture spacing is less than a quarter of the fracture length (Fig. 2-11, left panel).

(5) Once fracture complexity is introduced in the form of fractal networks, the effect of the branching fractures leads to suppression of the flow stagnation areas, allowing for more efficient drainage (Fig. 2-11, center panel). The velocity plots for the fractal networks show a larger spread in the local variation of velocity than for the planar fractures.

(6) The highest velocities are still found at the periphery of the fractal networks for all cases. However, for asymmetrical fractal networks there is a tendency for the highest pressure and velocity response to skew towards the areas of highest fracture density (Fig. 2-11, right panel).

(7) It will be necessary to determine if the creation of complex fracture networks in the subsurface is solely dependent on the reservoir matrix properties (presence of natural fractures or matrix heterogeneities) or if fractal networks can be created by applying specific techniques during the hydraulic fracturing process. This requires the application of better diagnostic tools including the refinement of microseismic techniques to properly define and monitor created fractal network geometry.

(8) Improved capacity to engineer and model the propagation direction and control the generation of fractal geometries for hydraulic fractures are urgently needed in order to further increase the productivity of hydrocarbon wells by fracture treatment.

3. IMPACT ON DRAINED ROCK VOLUME (DRV) OF STORATIVITY AND ENHANCED PERMEABILITY IN NATURALLY FRACTURED RESERVOIRS: UPSCALED FIELD CASE FROM HYDRAULIC FRACTURING TEST SITE (HFTS), WOLFCAMP FORMATION, MIDLAND BASIN, WEST TEXAS*

3.1. Introduction

3.1.1. Brief highlights

This chapter introduces natural fractures into our flow models and how their heterogeneity can impact flow and the DRV shape and location in the reservoir. The CAM tool for flow modeling was adapted by additional coding in Matlab to account for the heterogeneity created by natural fractures in an otherwise homogenous reservoir. The natural fractures are modeled as line dipoles and can be given enhanced strengths to account for increased permeability. The research focuses primarily on the effect that altered porosity in these natural fractures will have on the DRV extent. The altered porosity is accounted for by defining the boundaries of the natural fracture domain and scaling flow based on the porosity ratio (R_n) of fracture and matrix rock.

Flow interaction in the reservoir space between natural fracture sets and hydraulic fractures is investigated, with an emphasis on how these fracture networks influence the development of the drained rock volume (DRV). A series of methodical

* Parts reprinted from "Impact on Drained Rock Volume (DRV) of Storativity and Enhanced Permeability in Naturally Fractured Reservoirs: Upscaled Field Case from Hydraulic Fracturing Test Site (HFTS), Wolfcamp Formation, Midland Basin, West Texas" by Kiran Nandlal and Ruud Weijermars, 2019, MDPI Energies Special Issue: Improved Reservoir Models and Production Forecasting Techniques for Multi-Stage Fractured Hydrocarbon Wells.

simulations allows us to understand how the natural fractures impact the DRV evolution. This work uses closed-form analytical solutions based on complex analysis methods (CAM) to model flow in a 2D model of both the natural and hydraulic fractures. The interaction of the natural fractures and the hydraulic fractures is modeled in CAM to determine the flow response and pressure changes in the reservoir. Based on these responses Eulerian particle tracking can then quantify the impact of natural fractures and hydraulic fractures on the DRV. Insights generated from the models can be used to optimize well production and recovery factors in unconventional reservoirs.

For the results, modeling begins with simple representative elementary volume (REV) models to show the impact of natural fracture with altered porosity and permeability. Subsequently, the models are extended to synthetic cases of flow effects of natural fractures around hydraulic fractures. A final case study makes use of natural fracture properties from the Hydraulic Fracturing Test Site (HFTS) in the Midland Basin to accurately model the DRV of an unconventional reservoir in the Wolfcamp Formation in West Texas.

3.1.2. Motivation for study

Numerous attempts have been made to properly model fractured reservoirs that can accurately account for flow in such fractured porous media. The earliest attempt was made by Warren and Root (1963) by using the dual-porosity model. Irregular natural fractures were modeled by using homogenous matrix blocks that are separated by orthogonal uniform natural fractures with fluid communication between the isotropic

and matrix blocks governed by the inter-porosity flow coefficient (λ) and fracture storage capacity ratio (ω). Starting with this model, Kazemi et al. (1976) introduced modifications that allowed for multiphase flow as well as the introduction of a new matrix shape factor. Beyond this work numerous other authors have tried to adapt the Warren and Root (1963) model to account for changes in matrix block geometry with new methods moving from double-porosity models to triple-porosity models (Huang et al., 2015; Sang et al., 2016). Drawbacks of dual and multi porosity-based fracture models are that discrete fractures are not included and actual fracture density is not accounted for. Dual-porosity models also do not account for the flow paths followed when the fluid exchange occurs between the matrix and fractures, which can thus lead to inaccurate modeling of complex flow behaviors and can result in the wrong calculation of pressure gradients (Weijermars and Van Harmelen, 2018).

Another method to model naturally fractured reservoirs has been the use of Discrete Fracture Networks (DFN). For this model fluid flow in the medium is represented through a system of connected natural fractures embedded within the rock matrix. This technique was first introduced by Long et al. (1982) and has evolved over the years and seen increased use to model flow in conventional and unconventional naturally fractured hydrocarbon reservoirs (Roger et al., 2010; Dershowitz et al., 2011). The DFN method is typically used when (1) simulations done on a small scale where fracture dominance would otherwise result in an invalid upscaled continuum approximation, (2) in simulations on a larger scale where fracture dominance is small and the upscaled continuum model with only the largest fractures accounted for is valid

(Jing and Stephansson, 2007). Drawbacks of DFN modeling comes from the lack of data for the detailed inputs needed for the model such as fracture orientation, length, aperture and transmissibility along the (natural) fractures. Use of field analogs in surface outcrops may help fill these data gaps but there is no consensus on how accurate these measurements from outcrops match the subsurface. To combat this downside, current modeling attempts use a stochastic approach based on probability density functions to determine parameters of interest. This stochastic realization method can be used to create multiple realizations of the natural fracture patterns with fracture lengths following a power-law distribution (Wu and Olsen, 2016). The DFN method is also computationally intensive (and therefore expensive) as it requires very fine grids, which is particularly the case for multi-stage wells in unconarpsventional reservoirs with numerous perforation zones per well. (Weijermars and Van Harmelen, 2018).

This work makes use of detailed core descriptions from the Hydraulic Fracturing Test Site (HFTS) for accurate natural fracture property and distribution data for our field case model. These descriptions come from six cores from a slanted well that sampled the rock volume around a hydraulically fractured well. These cores were located in the Upper and Lower Wolfcamp formation and this data (type based in origin, dip and dip direction of the fractures) was previously used to visualize fracture orientation, types of fracture and perforation clusters by Shrivastava et al. (2018). We make use of this data for a more realistic representation of the natural fracture system present in the subsurface in our flow models to determine the impact of this system on the DRV and its implication for well productivity. An essential corollary of our model is the introduction

of a new upscaling method for natural fractures, which reduces the number of fractures to the critical ones, while maintaining the same equivalent permeability as the prototype. The upscaled model still contains discrete fractures to reveal their key impact on the flow. The novel upscaling method makes use of a combination of object-based and flow-based upscaling techniques (Appendix A).

3.1.3. Summary

Hydraulic fracturing for economic production from unconventional reservoirs is subject to many subsurface uncertainties. One such uncertainty is the impact of natural fractures in the vicinity of hydraulic fractures in the reservoir on flow and thus the actual drained rock volume (DRV). We delineate three fundamental processes by which natural fractures can impact flow. Two of these mechanisms are due to the possibility of natural fracture networks to possess (i) enhanced permeability and (ii) enhanced storativity. A systematic approach is used to model the effects of these two mechanisms on flow patterns and drained regions in the reservoir. A third mechanism by which natural fractures may impact reservoir flow is by the reactivation of natural fractures that become extensions of the hydraulic fracture network. The DRV for all three mechanism can be modeled in flow simulations based on Complex Analysis Methods (CAM), which offer infinite resolution down to micro-fracture scale and is thus complementary to numerical simulation methods. In addition to synthetic models, reservoir and natural fracture data from the Hydraulic Fracturing Test Site (Wolfcamp Formation, Midland Basin) are used to determine the real-world impact of natural fractures on drainage

patterns in the reservoir. The spatial location and variability in the DRV is influenced more by the natural fracture enhanced permeability than enhanced storativity (related to enhanced porosity). A Carman-Kozeny correlation is used to relate porosity and permeability in the natural fractures. Our study introduces a groundbreaking upscaling procedure for flows with a high number of natural fractures, by combining object-based and flow-based upscaling methods. A key insight is that channeling of flow through natural fractures leaves undrained areas in the matrix between the fractures. Flow models presented in this study can be implemented to make quick and informed decisions regarding where any undrained volume occurs, which can then be targeted for refracturing. With the method outlined in our study, one can determine the impact and influence of natural fracture sets on the actual drained volume and where the drainage is focused. The DRV analysis of naturally fractured reservoirs will help to better determine the optimum hydraulic fracture design and well spacing to achieve the most efficient recovery rates.

3.2. Natural fracture and hydraulic fracture models

3.2.1. Natural fracture and hydraulic fracture interaction mechanisms

Numerous authors have stated that the presence of natural fractures will increase production in hydraulically fractured wells in unconventional reservoirs (Aguilera, 2008; Forand et al., 2017). Such a broad statement neglects the intricacies in natural fracture morphology, distribution and its ability to impact production. Gale et al. (2014) state that "*fracture systems in shales are heterogeneous; they can enhance or detract from*

producibility, augment or reduce rock strength and have the propensity to interact with hydraulic fracture stimulation". Of importance is whether the natural fractures are sealing or not, which depends on the degree of cementation in the natural fractures. For natural fractures lacking cement, with no natural proppant (as used in hydraulic fractures), significant reduction in permeability is possible but will not result in complete closure and thus permeability in the natural fracture would still be above that for the intact host rock (Gutierrez et al., 2000). Another factor to consider is the connectivity of the natural fracture system. Cross-cutting and abutting fracture systems of different ages may not be hydraulically connected, depending on the degree of sealing. Here it is possible that hydraulic fracturing can be beneficial for the reactivation of these natural fracture systems, which may lead to natural fracture networks becoming connected to the hydraulic fractures for the first time. In this study we model natural fracture systems with an enhanced conductivity, i.e. cementation is not a hindrance to the flow potential within the system.

Though some ambiguity remains on the true nature of natural fractures influence on well production, research using static, object-based permeability suggests that natural fractures would enhance well productivity (Aguilera, 2008). Three major mechanisms for the increase in productivity due to natural fractures have been put forward by Weijermars and Khanal (2019). These three production enhancement mechanisms related to natural fractures involve: 1) *equivalent permeability enhancement*, 2) *storage effects, due to enhanced porosity in natural fractures*, 3) *connection of hydraulic to natural fractures.* Each mechanism shall be further discussed below.

1) *Equivalent permeability enhancement:* The presence of a natural fracture system open to flow (uncemented) with higher permeability than the matrix, would increase the equivalent permeability of the overall reservoir. This enhanced equivalent permeability will result in a corresponding higher flow rate towards the hydraulically fractured well increasing the well productivity.
2) *Storage effects due to natural fracture enhanced porosity:* Natural fracture porosity may differ from the matrix either on initial formation of the fracture or due to later dissolution of precipitated minerals in the fracture space (Gale et al., 2014). Due to size dependent sealing patterns, larger natural fractures are believed to have greater porosity (Laubach, 2003) and as such porosity in natural fractures is thought to be underestimated in most models. A greater porosity in the natural fractures than in the matrix may affect the extent of the drained area because porosity is a major control on time of flight for particles traveling along streamlines (Zuo and Weijermars, 2017). If the porous fractures are more fluid-filled than the surrounding matrix, storage effects will affect the well productivity. Uncemented fractures with enhanced porosity will allow for storage of hydrocarbons that, when tapped by the hydraulic fractures, will flow readily towards the well.
3) *Connection of hydraulic fractures to natural fractures:* Hydraulic fractures will propagate preferentially along planes of weakness in the reservoir such as those created by natural fracture systems. If a hydraulic fracture reactivates and connects to the natural fracture system, this connection leads to the natural

fractures essentially becoming a direct extension of the hydraulic fracture pressure sink. The connection of both fracture systems correspondingly increases the total fracture surface area that is in contact with the reservoir matrix and will improve the production rate of such wells.

3.2.2. Natural fracture porosity and permeability

The effect of natural fractures on fluid flow is highly dependent on the reservoir type. Four major naturally fractured reservoir types have been identified by Nelson (2001) based on the extent that fractures have altered the reservoir characteristics. Type 1 reservoirs have natural fractures that provide the bulk of the reservoir storage capacity and permeability, and typically have very high natural fracture density. In Type 2 reservoirs, permeability is essentially provided by the fractures while the matrix is responsible for the bulk of porosity. For Type 3 the reservoir matrix has high permeability and porosity but the permeability is further enhanced by the natural fracture system and can result in very high flow rates. Type 4 naturally fractured reservoirs have fractures that provide no additional porosity or permeability enhancement due to the fractures being filled with impermeable minerals. Natural fractures in Type 4 reservoirs are actually detrimental to fluid flow as they create significant reservoir anisotropy, which acts as barriers to flow (Tiab et al., 2006).

Nelson's (2001) classification is mostly valid for conventional reservoirs and less applicable to shale reservoirs. Unconventional shale reservoirs have the majority of porosity contained within the rock matrix while hydraulic fracturing is needed to create

high enough permeability pathways for economical production. The majority of shale reservoirs also exhibit a high degree of natural fracturing. Due to the described attributes, unconventional shale reservoirs can be considered to range between Type 1 and Type 2 classification of naturally fractured reservoirs, with an example of Type 2 being the Spraberry reservoir in West Texas (Tiab et al., 2006). The extent to which the natural fracture systems in shale reservoirs affect hydrocarbon production due to enhanced storage and permeability is yet unclearly defined and remains nebulous (Gale et al., 2014). There is consensus that hydraulic fracture propagation needs to take into account the impact of natural fractures on this propagation (Zhang et al., 2007) but the impact that natural fractures have independently on production is not well constrained (Gale et al., 2014). This is because core observations tend to show cemented natural fractures giving lower permeability and porosity measurements. However, field tests indicate much higher values for both permeability and porosity of natural fractures. Soeder (1988) stated "*typical natural fractures that enhance reservoir permeability to the point of commercial production are probably not obvious lithological features, such as near-wellbore calcite mineralized joints"*. Description of natural fractures in the Barnett shale show completely cemented fractures before hydraulic fracturing that subsequently became open and might demonstrate stress sensitivity (Gale et al., 2007). The cited evidence shows that there is a strong possibility of natural fracture systems with enhanced porosity and permeability in shale reservoirs potentially high enough to impact fluid flow, which is crucial to accurately capture in any flow models.

Important characteristics of natural fractures include fracture length, aperture, orientation, density, spacing, porosity and permeability. Values for most of these parameters are difficult to obtain from the subsurface. Outcrops can give some indication of fracture length, density and spacing but reasons exist to believe that limited outcrop data do not give a proper representation of subsurface features that lie deeper within the earth (Gale et al. 2014). What we do know is that many shales exhibit a wide range of fracture sizes and properties. The larger the natural fracture the greater the porosity because of size-dependent sealing patterns (Laubach, 2003) and it is believed that underestimation of natural fracture porosity may have occurred (due to this phenomenon) in some case studies. A value of 2% or less for the porosity of a natural fracture system is considered typical, however field data from the Monterey shale Formation using samples from highly fractured parts, have shown values as high as 6% for natural fracture porosity (Nelson, 1985). Studies conducted by Weber and Bakker (1981) as well as Lee et al. (2011) give values of 2% to 7% for natural fracture porosities of the Marcellus shale (Gale et al., 2014).

3.3. CAM solution for hydraulic fractures and natural fractures

The line sink solution for modeling of hydraulic fractures in a given reservoir space was presented earlier in Section 2.4.1. This solution is utilized for modeling of flow in an unconventional shale reservoir. For the introduction of natural fractures as heterogeneities in the reservoir, we make use of a newly developed algorithm proposed by Van Harmelen and Weijermars (2018). To model natural fractures, the algorithm

makes use of a complex potential function created by the superposing of an infinite amount of line doublets and is:

$$\Omega(z,t)=\frac{-i.\upsilon(t).e^{-i\gamma}}{2\pi.h.n_m.L.W}[(z-z_{a2}).\log(-e^{-i\gamma}(z-z_{a2}))-(z-z_{a1}).\log(-e^{-i\gamma}(z-z_{a1}))$$
$$+(z-z_{b1})\log(-e^{-i\gamma}(z-z_{b1}))-(z-z_{b2})\log(-e^{-i\gamma}(z-z_{b2}))] \quad [\text{ft}^2/\text{day}] \quad (3\text{-}6)$$

Similarly to the solution for a line source, differentiation of the specific complex potential equation of Eq. 3-6 yields Eq. 3-7, which gives the instantaneous velocity field in the natural fractures at time *t*.

$$V(z,t)=\frac{-i.\upsilon(t).e^{-i\gamma}}{2\pi.h.n_m.L.W}[\log(-e^{-i\gamma}(z-z_{a2}))-\log(-e^{-i\gamma}(z-z_{a1}))$$
$$+\log(-e^{-i\gamma}(z-z_{b1}))-\log(-e^{-i\gamma}(z-z_{b2}))] \quad [\text{ft/day}] \quad (3\text{-}7)$$

Here $\upsilon(t)$(ft^4/day) is the strength of the natural fracture, which scales the permeability contrast with the matrix. The height, width and length of the natural fracture are denoted by *h, W* and *L* (ft) respectively, *n* is porosity, γ is the tilt angle of the natural fracture as

shown in Fig. 3-1. The variables z_{a1}, z_{a2}, z_{b1}, and z_{b2} give the corner points of the natural fracture domain.

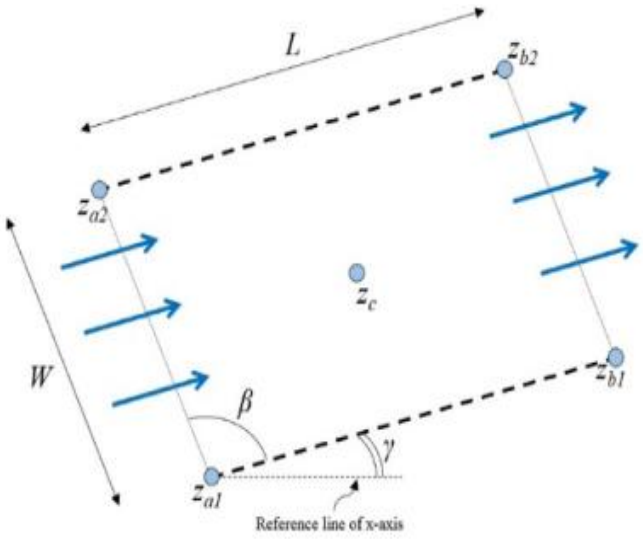

Figure 3-1 Natural fracture model. *L* and *W* are the length and width; z_c is the center; z_{a1}, z_{a2}, z_{b1}, and z_{b2} are the corners; β is the wall angles, while γ is the rotation angle of the natural fracture. Blue arrows give direction of flow (adapted from Van Harmelen and Weijermars, 2018).

As for boundary and initial conditions, CAM can be used to model both steady-state flow as well as transient flow as shown in our models. The initial REV models used to demonstrate the fundamental impacts of natural fractures on flow, use constant rate boundary conditions (using a constant far field flow of 2.5 ft/year). For the hydraulic fracture line sink models, we are able to introduce transient flow by the use of a declining flow strength based on the declining rate of the forecasted well production that is allocated back into each hydraulic fracture segment

3.4. Modeling of natural fracture interaction mechanisms

The major controls on fluid flow propagation in porous media are the porosity and permeability of the domain. For a naturally fractured reservoir, one may consider two domains for flow, the unfractured rock matrix and the natural fractures present within the reservoir. This assumes that the natural fractures are uncemented and allow for flow. For streamline simulations, the flow paths (FP) and time of flight (TOF) of fluids being transported in porous media due to pressure sources/sinks are calculated by the equation of motion which is intrinsically dependent on porosity and permeability in the reservoir. Work by Zuo and Weijermars (2017) led to the creation of two fundamental rules for FP and TOF in porous media. The first rule shows that an increase in permeability decreases the time of flight, and conversely an increase in porosity increases the time of flight. The second rule states that the permeability uniquely controls the flight path of fluid flow in porous media and local porosity variations do not affect the streamline path.

Armed with the above rules, we now proceed to explain the three principal mechanisms by which natural fractures may impact fluid flow in the reservoir. Natural fractures may result in localized discrete changes in both permeability and porosity or storativity in the reservoir domain, creating a direct impact on reservoir drainage patterns and drained areas. The third possibility is the reactivation and connection of natural fractures to the hydraulic fracture network, which functions as an extension of the hydraulic fracture pressure sink.

3.4.1. Equivalent permeability enhancement

This mechanism is due to the difference of permeability within the natural fracture and the surrounding rock matrix. In unconventional reservoirs, the natural fracture permeability (k_f) is typically greater than that of the rock permeability (k_m). Weijermars and Khanal (2019) show via explicit derivations how the permeability ratio (R_k) directly impacts the strength of flow in natural fractures as follows:

$$R_k = \frac{k_f}{k_m} \qquad [-] \quad (3\text{-}8)$$

The fracture hydraulic conductivity (C_f) is determined by the product of its fracture aperture (w_f) and its permeability (k_f):

$$C_f = k_f . w_f \qquad [\text{mD.ft}] \quad (3\text{-}9)$$

From this conductivity we are able to define and scale the strength of the natural fracture segment (υ_f) in terms of corresponding permeability contrast with the matrix as follows:

$$\upsilon_f = q_f L_f = v_f w_f h_f L_f = \frac{k_f}{k_m} v_m w_f h_f L_f \qquad [\text{ft}^4/\text{day}] \quad (3\text{-}10)$$

The length dimensions for the natural fractures (h_f – natural fracture height, L_f – natural fracture length, w_f – fracture aperture) are directly specified in the CAM models and matrix flow velocity (v_m) can be measured near the fracture in the simulation. By fixing the constituent parameters at time t the equation for R_k thus becomes:

$$R_k = \frac{\upsilon_f(t)}{v_m(t) w_f h_f L_f} \qquad [-] \quad (3\text{-}11)$$

Thus, from the above equation we can set the permeability ratio using an assigned strength in the natural fractures in our CAM model.

The most important aspect of the permeability enhancement mechanism is that natural fractures do not act as fluid sinks. Mechanism 1 assumes the natural fractures are not connected to the hydraulic fractures (unlike mechanism 3). Instead the natural fractures act as zones of flow acceleration and preferentially drain matrix fluid further away from the well at the end of the highly conductive natural fractures rather than from the nearby lower permeability matrix. Change in permeability in the natural fractures impacts both streamline patterns as well as time of flight. This mechanism was thoroughly modeled and investigated by Weijermars and Khanal (2019), using a variety of natural fracture parameters and readers are referred to this seminal work for further detail. Though prior studies (eg. Aguilera, 2008) that use static object-based permeability scaling also give results that natural fractures can enhance well productivity, the method employed by Weijermars and Khanal is based on dynamic, flow-based upscaling and is believed to be more accurate. Flow-based upscaling of permeability explicitly shows how for a fractured medium the equivalent permeability increases greatly when compared to similar porous media that are non-fractured. It is this overall increase in equivalent permeability (due to the enhanced permeability of the natural fractures) that leads to a higher flow rate towards the well and thus higher

recovery during the economic life of such wells. In this study, we extend this work to investigate the implications of equivalent permeability enhancement due to natural fractures on DRV in conjunction with porosity changes in natural fractures. A new upscaling method for discrete fractures is given in Appendix A, allowing for simultaneous changes to fracture permeability and porosity, which has not been investigated previously.

3.4.2. Natural fracture storativity effect

Besides effecting localized permeability changes, natural fractures have the ability to alter porosity. Shale reservoirs tend to exhibit a wide range of fracture sizes. Due to the industries limited data of natural fracture porosity, the effects of this on flow alteration in the subsurface has not been previously studied in any detail. We present a set of high-resolution simulations with altered porosity in the natural fractures to quantify how this parameter affects drainage in the subsurface.

As before with the change in permeability, we are now able to define a porosity ratio (R_n) for the porosity change inside of a natural fracture (n_f) compared to the matrix porosity (n_m) surrounding it given by the following equation:

$$R_n = \frac{n_f}{n_m} \quad [-] \quad (3\text{-}12)$$

For the CAM analytical solution, natural fracture alignment can be defined in relation to the hydraulic fracture. Equation 7 assumes that the porosity across both the fracture zone and matrix remains the same. If we remove this assumption, based on the evidence

presented on porosity differences in natural fractures when compared to the reservoir matrix, Equation 3-7 can be locally modified to take into account the altered natural fracture porosity as follows:

$$V(z,t) = \frac{-i.\upsilon(t).e^{-i\gamma}}{2\pi.h.n_m.L.W}[\log(-e^{-i\gamma}(z - z_{a2})) - \log(-e^{-i\gamma}(z - z_{a1})) + \log(-e^{-i\gamma}(z - z_{b1})) - \log(-e^{-i\gamma}(z - z_{b2}))] / R_n \quad \text{[ft/day] (3-13)}$$

This equation will now account for both the altered porosity and permeability within the natural fracture domain. As we manually define the boundaries of the natural fractures, the tracked particles that are displaced based on the time dependent strength of the flow in the reservoir will have velocity increased or decreased based on the porosity and permeability once the fluid particles enter the natural fracture domain. The trajectories of these particles are set by the permeability in the reservoir matrix and natural fractures (Zuo and Weijermars, 2017). Based on Rule 2 for flight paths and time of flight contours in porous media (Zuo and Weijermars, 2017). The time of flight will be slower in natural fractures with a higher porosity than the matrix (the streamline patterns will not be affected). Thus for a hydraulically fractured well, the presence or absence of natural fractures with different porosities (that may be in situ porosity or increased porosity due to natural fracture reactivation) will affect how far the matrix is drained (i.e., the shape and location of the DRV will be affected), which knowledge is relevant for fracture treatment design and well spacing decisions.

3.4.3. Natural fractures as extension to the hydraulic fracture network

The third mechanism that may cause natural fractures to increase well productivity occurs when natural fractures become extensions of the hydraulic fracture system. This can lead to the creation of complex fracture networks, defined as non-planar, branching fracture geometries that are caused by either strong stress shadow effects or by the interactions with natural fractures (Wu and Olsen, 2014). Wu and Olsen further state that the efforts to study interaction between natural fractures and hydraulic fractures have taken various forms of theoretical, experimental and numerical work. From this work they propose three possibilities due to the intersection of natural fractures and man-made hydraulic fractures. The first possibility is that the created hydraulic fracture propagates along its original directions and crosses the natural fracture with no change in orientation. A second possibility is that the hydraulic fracture could be arrested by the natural fracture and then continue to propagate along the natural fracture to finally exit at the tip of the natural fracture. Deflection of the hydraulic fracture into the natural fracture, followed by re-initiating out of the natural fracture at a point of weakness is given as the third possibility (Dahi-Taleghani and Olsen, 2013). No matter the propagation due to the interaction, the overall effect is that the natural fractures that intersect with the hydraulic fractures become extensions of the pressure sink imposed on the reservoir due to the connection of the fracture network to the wellbore. One way to model these interactions is via the use of fractal theory to replicate the branching fracture geometry that can then be modeled using CAM as presented in the previous chapter.

3.5. Results

Using the CAM approach, we investigated systematically the effects of porosity and permeability alterations within natural fractures on fluid flow using a range of model designs. The changes in these two crucial parameters were studied to determine the effect on the drainage area in the reservoir. Obviously, a proper understanding of the DRV development in naturally fractured reservoirs has implications for production from both conventional and unconventional oil and gas reservoirs.

We adjust the fracture strength and porosity ratio to determine the impact on drained areas in the reservoir. Modeling starts with a simple planar fracture with varying porosity ratios as well as different natural fracture configurations. The effects of natural fracture storativity and enhanced permeability on DRV are demonstrated and proved. We investigated the flow patterns near hydraulic fractures (modeled as line sinks using CAM), and how the presence of natural fractures and their corresponding porosity and permeability may change the drained rock volume (DRV). It should be noted that the CAM models used in these flow simulations assume hydraulic fractures of infinite conductivity.

These initial results are for synthetic models, intended to systematically demonstrate the effects of natural fractures via the natural fracture interaction mechanisms explained previously. The idealistic representative elementary volumes (REV) and simple fracture models assume porosity changes are independent of any permeability changes. In reality this may not be true and there are many established correlations that relate increases in porosity with corresponding increases in

permeability. We make use of field data for natural fractures to determine the DRV in an actual reservoir. Field data obtained from cores in the Hydraulic Fracturing Test Site (HFTS) as well as porosity-permeability correlations are used to determine the impact of natural fractures in the case study. By incorporating real data in our models, we can more accurately determine the impact of natural fractures on the DRV in the field. This is relevant to next propose methods for optimization of recovery in both highly fractured unconventional and conventional reservoirs.

3.5.1. Representative elementary volume (REV) models

To properly understand the effects on fluid flow, we start with the modeling of a simple representative elementary volumes (REV) that use a constant far field flow. A representative elementary volume (REV) is defined as a volume over which a measurement can be made that is representative of the whole. Using the REV allows for the understanding of the physics behind any changes in drainage patterns (before moving on to more complex situations). The first model provided is a base case which we use to compare all subsequent models. In this model (Fig. 3-2) we show a reservoir space in 2D with five natural fractures represented by discrete elements that have the same porosity and permeability as the reservoir space. Using Eulerian particle tracking we determine the flow path based on a constant far field flow. Flight paths (FP) are displayed in blue (Fig. 3-2, left image) with the corresponding time-of-flight contours (TOFC) shown in red (Fig. 3-2, right image). The base model represents a flow time of 30 years with each TOFC representing the fluid displacement after 3 years with reservoir porosity of 5%.

Referring back to the two fundamental rules for FP and TOF (Zuo and Weijermars, 2017) we observe that with no change in porosity and permeability in the natural fractures the FP and TOFC remain constant.

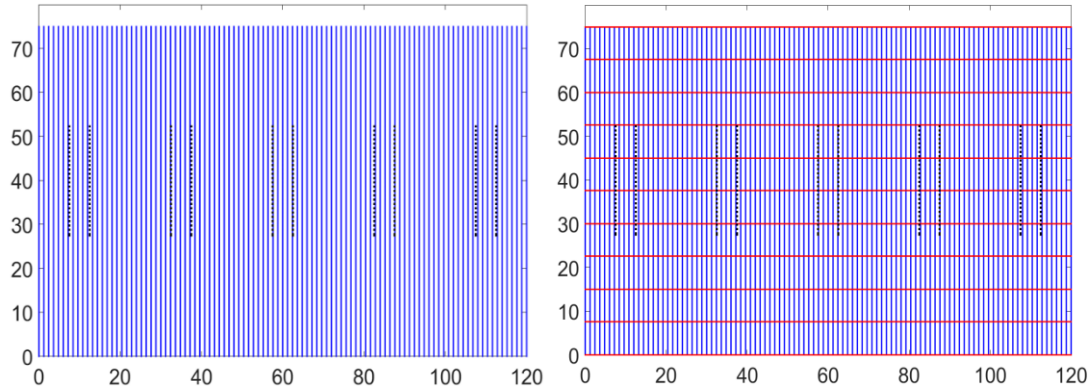

Figure 3-2 Base case model for homogenous reservoir space with 5 discrete natural fracture elements all having equal porosity and permeability. Left: Streamlines (blue) for uniform flow from bottom to top through reservoir space and natural fractures (black). Right: Time-of-flight (TOF) contours (red) shown every 3 years during a total simulated time of 30 years.

3.5.1.1. Porosity effects

The next REV model (Fig. 3-3) highlights the effect of systematically increasing the porosity in the natural fractures. As stated previously, fracture system porosities of 2% or less are considered typical (Nelson, 1985), but values as high as 7% for natural fracture porosity in shale formations have been reported (Lee et al., 2011; Gale et al., 2014). With numbers still based on very limited datasets, it is possible that porosity changes in natural fractures can be higher than the values reported thus far. Therefore, we model porosity changes up to 15% to observe the impact on flow. The initial models decouple the correlation between increased porosity and permeability and such that there

is no permeability change in the natural fracture relative to the matrix. When we use the term porosity, we mean connected porosity.

Fig. 3-3 shows the effects, of increasing NF porosity, on the FP and TOFC in the reservoir space. The reservoir porosity is kept at 5%, while NF porosity changes incrementally from being equal to the reservoir space to a high of 15%. The results clearly show that the change in porosity within the natural fracture has no effect on the streamline flow paths but does affect the time-of-flight contours. In NF 1 the porosity is the same as the reservoir and as such there is no slowdown in the TOFC. From NF 2 to NF 5 we progressively increase the porosity to 6%, 8%, 10% and finally 15%. The model shows that for each successive porosity increase in the natural fractures, the FP stays constant but the TOF increases. As we are using a constant run time for all models, the increase in TOF results in flow not reaching as far into the reservoir space for the natural fractured with higher porosity. With no porosity change, flow reaches out to approximately 75 ft in the reservoir space. With a porosity change from 5 to 15% in the natural fractures, flow is retarded and reaches only approximately 44 ft out into the reservoir space. Thus a 10% increase in natural fracture porosity results in a 40% reduction in lateral flow extent. This result can have great implications for accurately

determining the DRV in the subsurface when the reservoir rock has a high density of natural fractures with variable porosity.

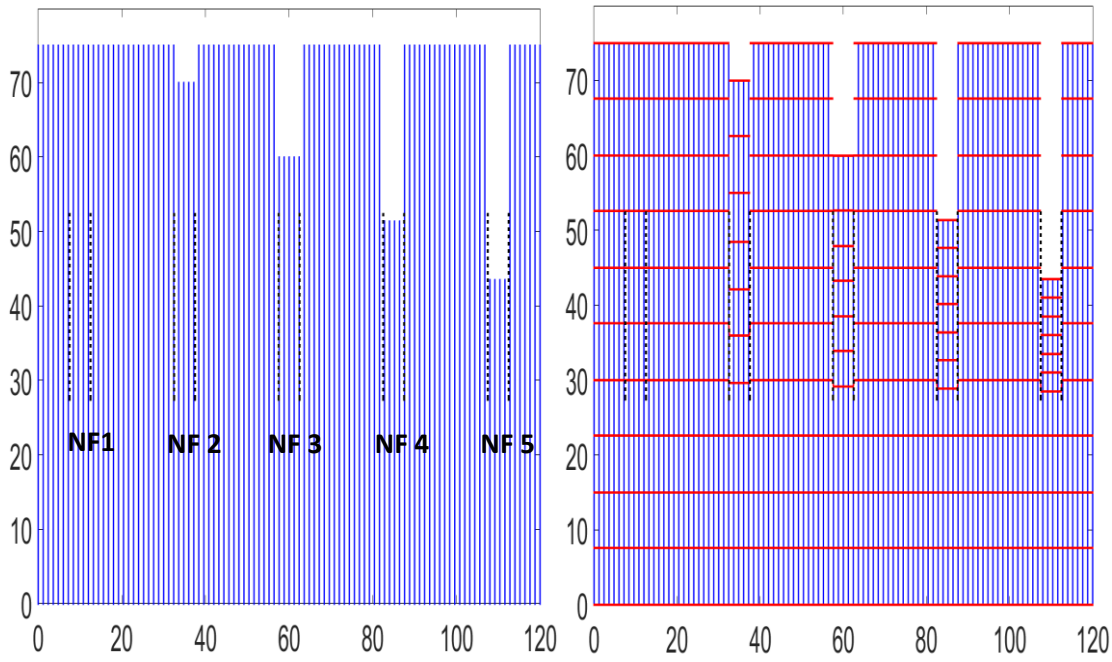

Figure 3-3 REV model showing impact of different natural fracture (NF) porosity on FP and TOF in a reservoir space of 5% porosity. NF porosity from left to right: NF 1 = 5% (NF 1 porosity same as reservoir), NF 2 = 6%, NF 3 = 8%, NF 4 = 10%, NF 5 = 15%. Streamlines in blue (left side) and TOF in red (right side). Far field flow of 2.5 ft/year scaled by reservoir porosity is used in all REV models.

3.5.1.2. Permeability effects

Our next REV model investigates the impact of change in natural fracture permeability on the FP and TOFC after simulation for 30 years. For this model the porosity in the natural fractures are kept constant with the reservoir to allow for detailed investigation of the flow effects due to only the permeability change in the fractures. Using CAM, we model higher permeability in the natural fractures by assigning (scaling with) a particular fracture strength [Eq. (3-10)]. An increase in strength can be related

back to the natural fracture permeability using the permeability ratio R_k. The REV model (Fig. 3-4) uses a far field flow of 2.5 ft/year (after being scaled by the reservoir space porosity of 5%). The strengths for NF 1 to NF 5 are increased, respectively, from 0.1 ft^4/year to 40, 160, 500, and 1000 ft^4/year.

Results in Fig. 3-4 show that keeping porosity constant in the natural fractures while increasing the natural fracture strength (and thus NF permeability), leads to a change in both the FP and TOF. This is in line with what is expected from the first fundamental rule for FP and TOFC (Zuo and Weijermars, 2017): permeability changes affect the FP and thus the path of the streamlines is altered. Fluid is seen funneled into the higher permeability natural fractures while the TOF correspondingly decreases. Using the constant run-time of 30 years, this decrease in TOF results in fluid flow reaching further out into the reservoir space. As more of the fluid flow is funneled into the NF due to increasing strength, less of the fluid is transported in the inter-fracture domain (space between the natural fractures). In the space between NF 2 and 3 (though the FP are altered due to the increased NF permeability), fluid still flows in the inter-fracture space as shown by the streamlines. However, in the space between NF 4 and 5 (which are assigned much greater strengths) almost all the fluid flow is funneled into the natural fractures, with most of the inter-fracture space receiving no fluid.

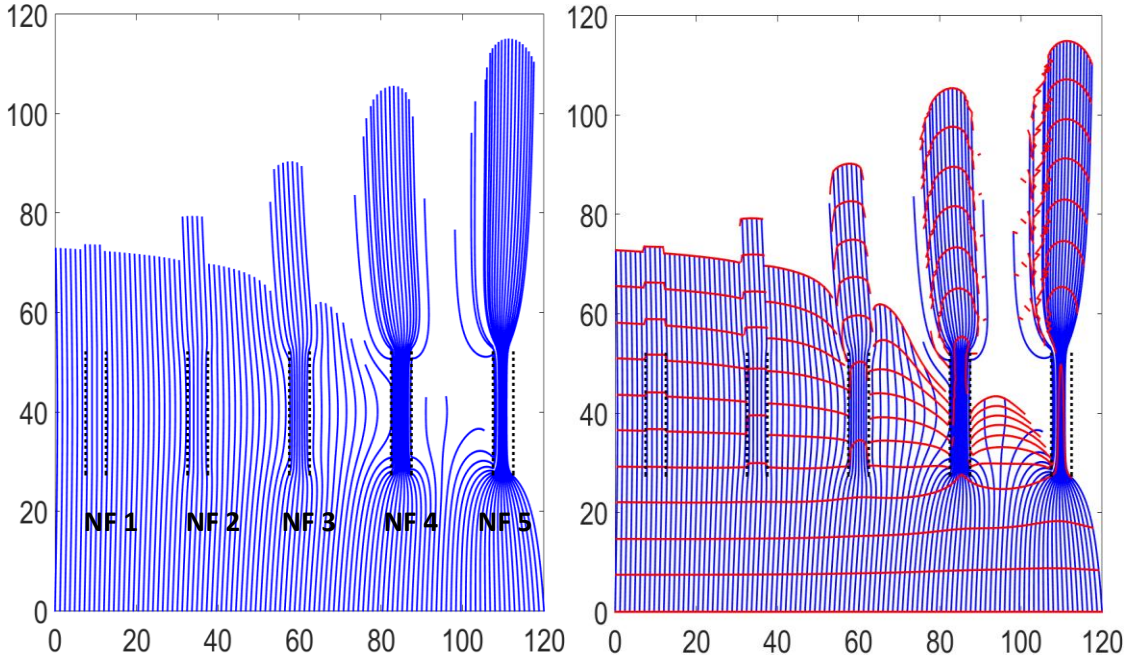

Figure 3-4 REV model showing impact of different natural fracture (NF) permeability on FP and TOF in a reservoir space of 5% porosity. NF strengths from left to right: NF 1 = 0.1 ft^4/yr, NF 2 = 40 ft^4/yr, NF 3 = 160 ft^4/yr, NF 4 = 500 ft^4/yr, NF 5 = 1000 ft^4/yr. Streamlines in blue (left side) and TOFC in red (right side).

The relation between the natural fractures input parameters used in Fig.3-4 and the approximate equivalent natural fracture permeability (based on Eq. 3-11) are given in Table 3-1. Fracture input properties used in all subsequent flow models with enhanced natural fracture permeability in this study are included in Table 3-1.

Table 3-1 List of natural fracture input properties for models with enhanced permeability

Figure number		Natural Fracture Strength (ft^4/yr)	Natural Fracture Length (ft)	Natural Fracture Width (ft)	Natural Fracture Height (ft)	Matrix Flow Rate (ft/yr)	Permeability Ratio (R_k)	Natural Fracture Permeability (nD)
3-4	NF1	0.1	25	5	1	2.5	-[a]	-[a]
	NF2	40	25	5	1	2.5	0.13	12.8 [a]
	NF3	160	25	5	1	2.5	0.51	51.2 [a]
	NF4	500	25	5	1	2.5	1.60	160
	NF5	1000	25	5	1	2.5	3.20	320
3-5b		1000	25	5	1	2.5	3.20	320
3-6		500	25	5	1	2.5	1.60	160
		(ft^4/day)				(ft/day)		
3-8	a	2500	20	10	60	0.1693	1.23	123.06
	b	5000	20	10	60	0.1693	2.46	246.11
	c	10000	20	10	60	0.1693	4.92	492.22
3-9		5000	20	10	60	0.1693	2.46	246.11
3-10b		155	20	0.5	60	0.1693	1.53	152.59
3-11		155	30	0.5	60	0.1693	1.02	101.73

[a] R_k formulation gives an approximate natural fracture permeability and does not hold well for very low strengths. A matrix permeability of 100 nD is assumed. R_k is calculated from Eq. 3-11 with natural fracture permeability then back-calculated from Eq. 3-8 using the assumed matrix permeability

3.5.1.3. Open fractures

A final scenario investigated with the REV model was the effect of a natural fracture with 100% porosity. Theoretically this can be thought of as an open fracture in the subsurface. We artificially separate the effects of porosity and permeability to investigate each parameter individually. Fig 3-5a shows the result for completely open natural fractures set within a reservoir space of 5% porosity. The FP is unchanged but the TOF in the fractures increases dramatically. The fluid drawn from the open fracture does not require long travel paths (due to 100% fluid fill), and drawing the same amount of fluid from the inter-fracture matrix regions requires much longer travel paths in those regions outside the NF.

Fig. 3-5b shows the effect of natural fractures with very high permeability as compared to the reservoir space. The natural fractures in this model have a strength of 1000 ft^4/year (while porosity is kept the same as that of the reservoir matrix) and fluid flow is simulated for a run-time of 30 years. The marked effect of the change in permeability is seen in the alteration of the FP as well as the decrease in TOF. With such a high fracture strength (high R_k) almost all flow is funneled through the natural fractures with no fluid being transported via the inter-fracture domain.

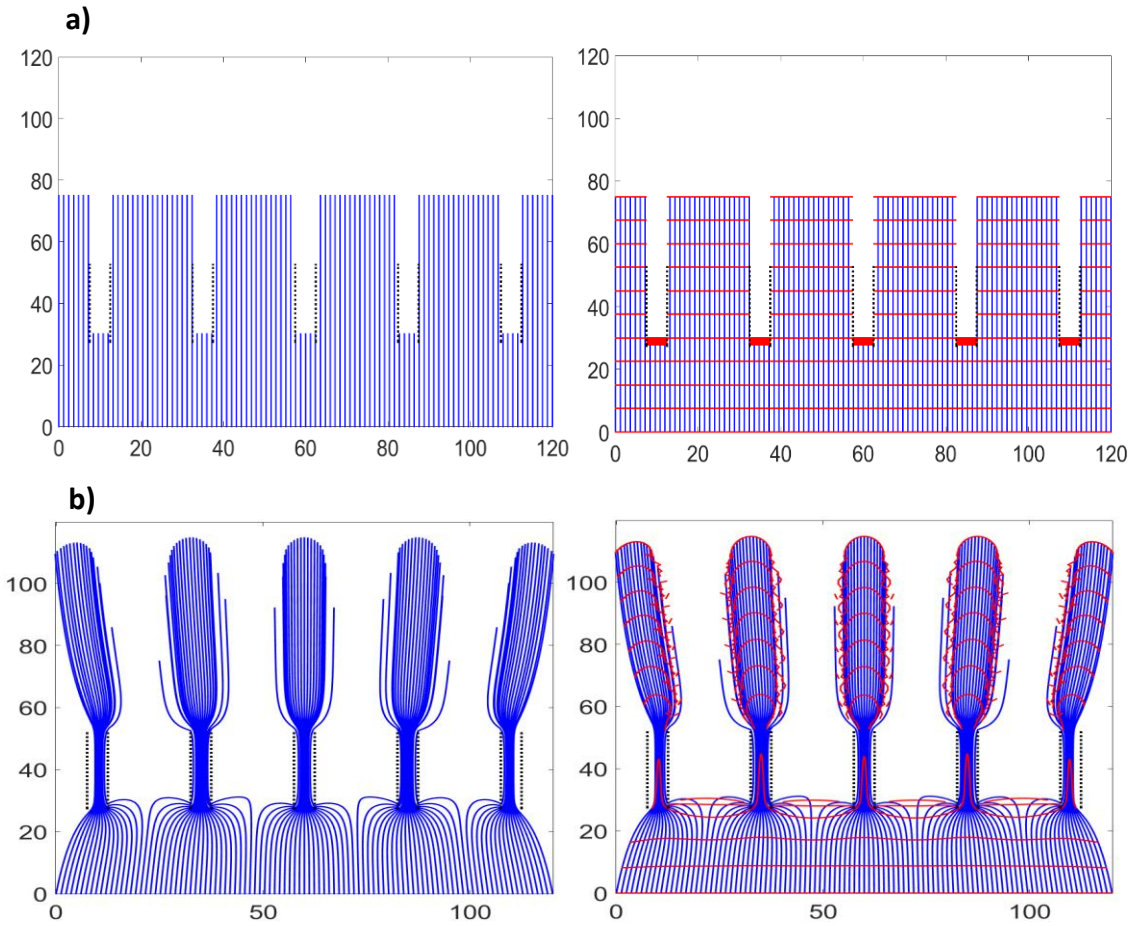

Figure 3-5 a) REV model showing effect of a natural fracture (NF) porosity of 100% (open fracture) in a reservoir space of 5% porosity with no permeability change. b) Natural fractures with increased strength of 1000 ft^4/year. Streamlines in blue (left side) and TOFC in red (right side). Natural fractures in black.

All previous REV models have considered the varying effects of porosity and permeability independently of each other. Fig. 3-6 investigates the effect of simultaneous changes of natural fracture porosity on flow, while the permeability contrast with the matrix exists (R_k>1). In this model we systematically change the porosity within the NF from initially being equal to that of the reservoir space of 5% (Fig. 3-6a) to a high of

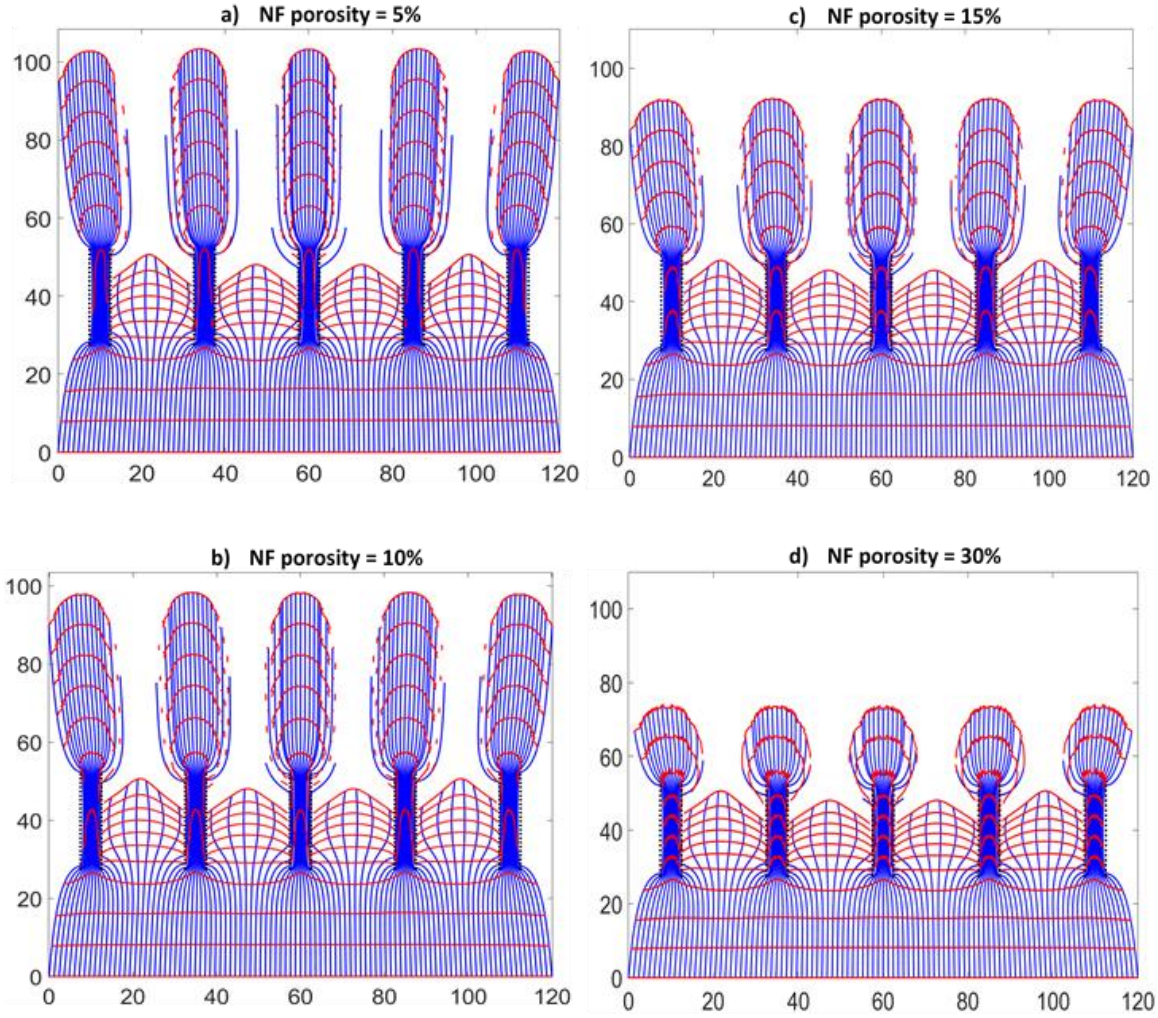

Figure 3-6 REV model showing effect of various natural fracture (NF) porosity changes in a reservoir space of 5% porosity with enhanced strength in the NF of 500 ft^4/yr. Streamlines in blue and TOFC in red. Natural fractures in black.

30% (Fig. 3-6d), all the while keeping a constant enhanced permeability in the natural fractures.

The results from the models in Fig. 3-6 show the competing effects between porosity and permeability as defined in the fundamental rules for FP and TOF by Zuo and Weijermars (2017). Fig. 3-6a shows the alteration in FP and decrease in TOF (fast travel times via the fractures) due to the enhanced natural fracture permeability. The successive models (Fig. 3-6b-d) with gradually increasing porosity in the natural fracture conversely increase the TOF and thus reduce the lateral distance reached by the fluid flow in the given run-time. Although the porosity change negates the effect of the enhanced permeability in terms of lateral distance reached, the alteration of the FP by the permeability still occurs. This proves that permeability is responsible for the particle paths while both the permeability and porosity inversely affect the TOF (as stated in Zuo and Weijermars, 2017).

3.5.2. Synthetic hydraulic fracture models

Using the CAM model, hydraulic fractures can be modeled as either line sinks or as line sources, which is used in this study applying the principle of flow reversal. Line sinks can show fluid withdrawal contours being forward modeled by line sources (a simple sign reversal in our equations). The effects of fluid flow of enhanced permeability and porosity in natural fractures of an otherwise homogenous reservoir space was modeled in the previous section using a constant far field flow. Models are now presented to demonstrate how natural fracture will alter fluid flow around a single

hydraulic fracture. Time-dependent production data from a well completed in the Wolfcamp Formation is used in these models and prorated for fluid allocation produced by a single hydraulic fracture stage. The relatively wide zones (10 ft) of altered permeability and porosity used in these models represent the effect of upscaling numerous smaller individual natural fractures (a detailed upscaling procedure is given in Appendix A). The effect of such altered zones can be clearly demonstrated visually. Each naturally fractured zone has dimensions of 10 ft width by 20 ft in length and the zones are angled at values of 45^{o} and 135^{o} from the hydraulic fracture.

The first model looks at the effect of a synthetic, single hydraulic fracture surrounded by six natural fracture zones having a higher porosity than the reservoir matrix (Fig. 3-7). For this model the natural fracture zones are not attributed any additional permeability change, only porosity enhancement. Fig. 3-7a to 3-7b has a progressively increasing porosity in the natural fracture from left to right, starting with a NF porosity of 10% in 8a, and increases to 15% and 20% in Figs. 3-7b and 3-7c. The models show that as porosity increases in the natural fracture zone there is a decrease in the distance drained. In other words, as porosity increases the time-of-flight also increases. The major observation from these models is that the presence of naturally fractured zones with increased porosity (and assumed fluid storage in those fractures) will decrease the distance drained away from the hydraulic fracture.

The next property investigated is the effect of increased permeability (by changing the strength of the natural fractures as compared to rest of the reservoir matrix) (Fig. 3-8). The porosity in the NF zones is kept the same as for the reservoir matrix so

we can focus solely on the permeability effect. From left to right the strength in the natural fracture zones is progressively increased from 1,000 ft^4/day in Fig. 3-8a to 5,000 ft^4/day and 10,000 ft^4/day respectively in Figs. 3-8b and 3-8c. The streamlines converge into the high permeability zones and lead to larger drainage regions in the direction of the higher permeability zones. One additional point of note is that the direction of the angle of these zones in conjunction with the streamline direction, influences how much effect there is on the drainage. If the naturally fractured zones are angled in the same direction as the streamlines, the effect is more pronounced than if they occur at a larger angle to the principal flow direction induced by the hydraulic fracture.

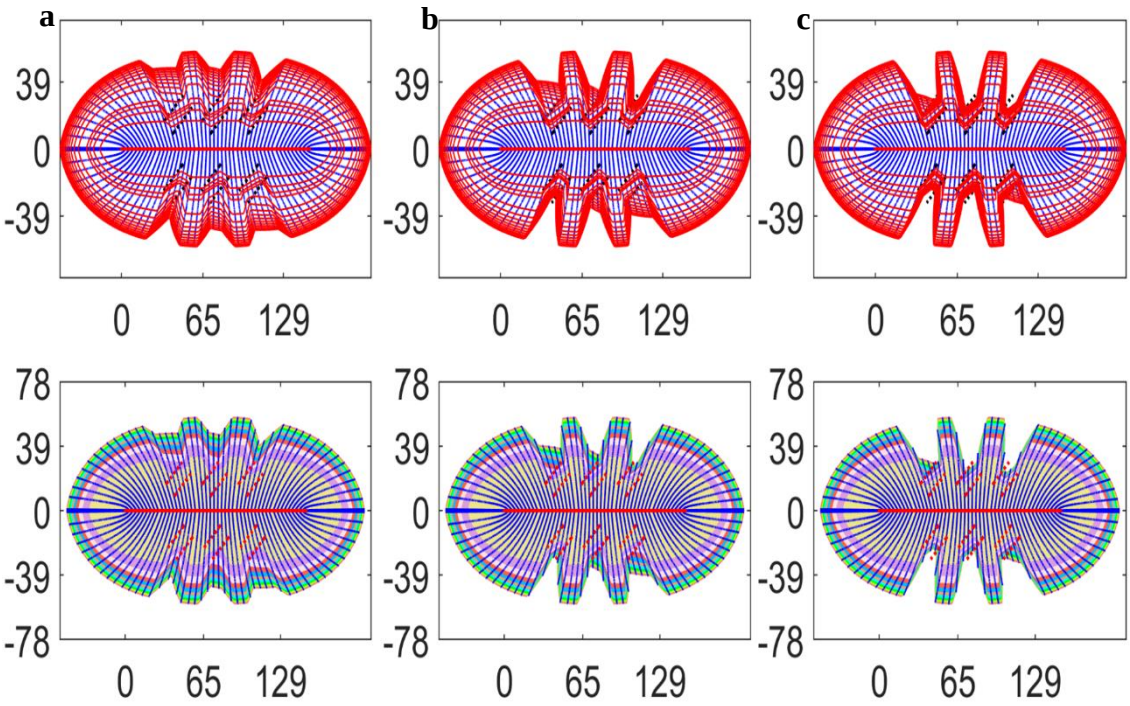

Figure 3-7 Hydraulic fracture model showing effect of various natural fracture (NF) porosity changes in a reservoir space of 5% porosity with enhanced porosity in the NF of a) 10% b) 15% c) 20%. Streamlines in blue and TOFC in red. Natural fracture zones in dashed lines. Bottom plots use rainbow colors to show drained areas after 3-year time periods.

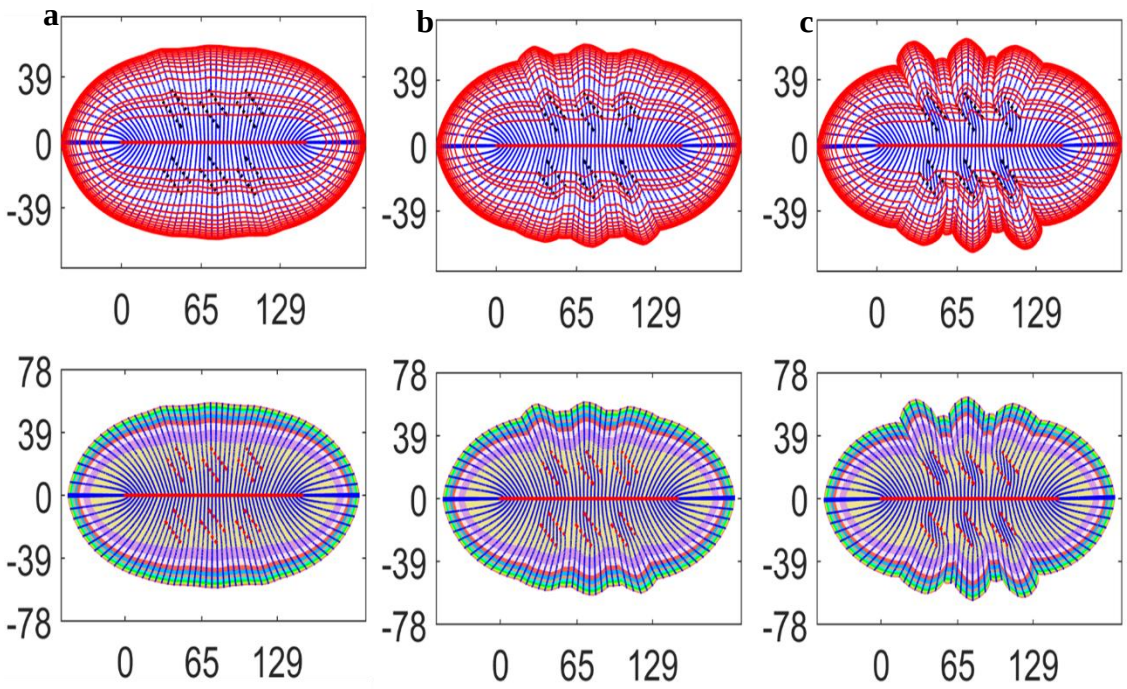

Figure 3-8 Hydraulic fracture model showing effect of various natural fracture (NF) permeability changes in a reservoir space of 5% porosity with enhanced permeability strengths in the NF of a) 2,500 ft^4/day b) 5,000 ft^4/day c) 10,000 ft^4/day. Streamlines in blue and TOFC in red. Natural fracture zones in dashed lines and have same porosity as reservoir. Bottom plots use rainbow colors to show drained areas after 3-year time periods.

The previous models investigated the effect of altered porosity and permeability in naturally fractured zones around a hydraulic fracture independently. Fig. 3-9 looks at the competing effects of altered porosity and permeability together. Fig. 3-9a shows the case with an enhanced permeability in the natural fractured zones, while the porosity is kept the same as the reservoir porosity of 5%. The results show the convergence of the streamlines into these zones resulting in a lateral extension of the DRV beyond. As we progress from left to right, Figs. 3-9a-c show the effect of increasing porosity in the NF zones while also having an enhanced permeability. Fig. 3-9b has the same enhanced

permeability as in Fig. 3-9a, but now the porosity in the natural fractured zones is increased from 5% (same as the reservoir matrix) to 10%. This model shows that although the streamlines converge into the zones of higher permeability, the lateral extent of the DRV is now slightly reduced due to the increased porosity. The enhanced DRV from Fig. 3-9a has now been reduced in Fig. 3-9b to an extent smaller (due to the porosity effect) than if there were no natural fractures. If the natural fracture porosity is increased further to 20%, the extent of the drained area shrinks much further (Fig. 3-9c). The large changes in lateral extent and the spatial location of the DRV due to natural fractures may have significant implications for fracture and well spacing for optimum drainage. The limiting factor for improving models is the lack of fracture diagnostics for field cases (in particular the fracture permeability and porosity values). In the next section, detailed field data abstracted from the Hydraulic Fracture Test Site will be used to constrain fluid withdrawal patterns near the hydraulic fractures that drain the Wolfcamp reservoir space.

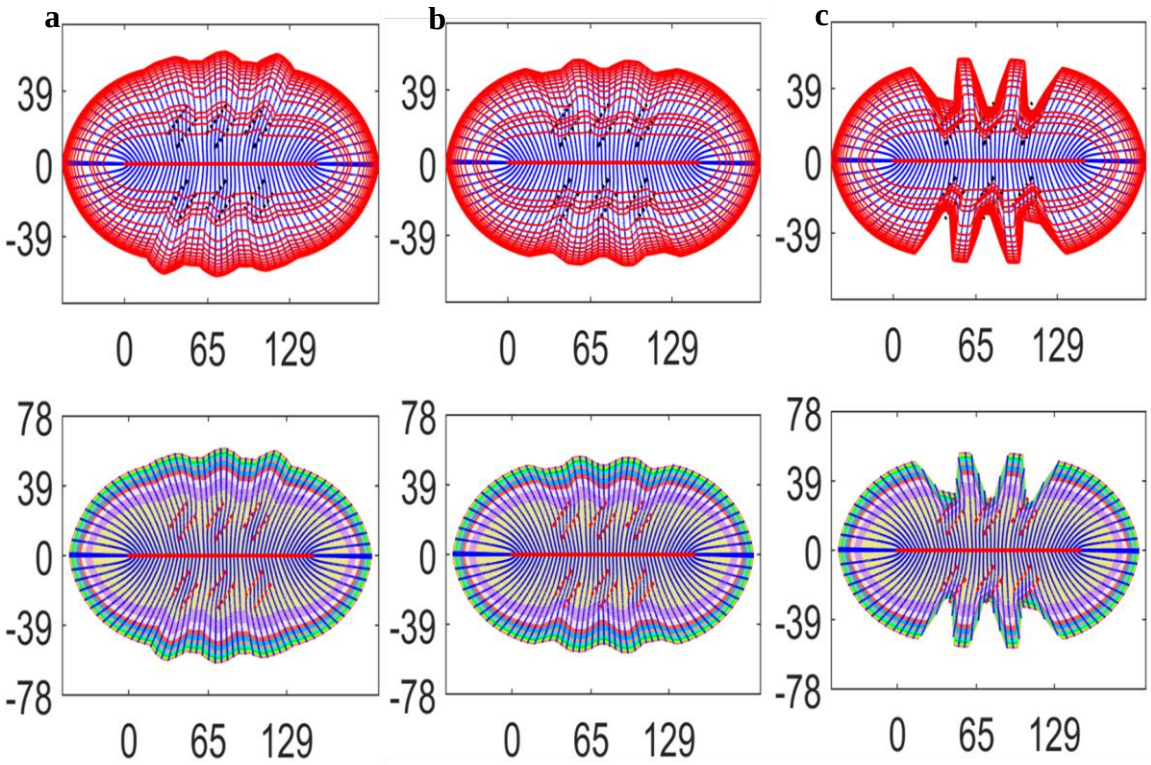

Figure 3-9 Hydraulic fracture model showing effect of competing changes in natural fracture (NF) porosity and permeability changes in a reservoir space of 5% porosity. a) NF porosity same as reservoir (5%) and enhanced strength of 5,000 ft^4/day b) NF porosity of 10% and enhanced strength of 5,000 ft^4/day c) NF porosity of 20% and enhanced strength of 5,000 ft^4/day. Streamlines in blue and TOF in red. Natural fracture zones in dashed lines.

3.5.3. Field models using data from the Hydraulic Fracture Test Site (HFTS)

Data from the Hydraulic Fracture Test Site (HFTS; Midland Basin, West Texas) is used because the natural fracture network present in the subsurface has been characterized in prior studies for this real field case (Shrivastava et al., 2018; Kumar et al., 2019). Six cores obtained from the Wolfcamp Formation within the Stimulated Rock Volume (SRV) near to a hydraulically fractured well were studied in detail (Shrivastava et al., 2018). One of the aims of the core description was to understand the primary

origins of fractures in terms of hydraulic, natural and reactivated natural fractures. The density of the individual types of fractures along the core depths, and the dominant orientations of the fractures obtained by Shrivastava et al. (2018) are used in our study for a field-based simulation of the impact of natural fractures on the DRV development.

For the present study, certain mean values for natural fracture lengths and aperture were assumed in our models, because natural fracture length and aperture values from the HFTS core samples were poorly constrained (Shrivastava et al., 2018). In their approximation, the latter authors used a power-law relation to generate a range for natural fracture lengths, and the fracture apertures were estimated using a geomechanical fracture propagation simulator. In the present study, we constrain the fracture length to 30 ft (Table 3-1), corresponding to the maximum value used by Shrivastava et al. (2018). Additionally, the DRV model requires inputs, for every natural fracture, of permeability and porosity. However, almost no data is present in literature for relating in situ natural fracture porosity with permeability in the subsurface, which is why a Carman-Kozeny (CK) relation is used, in our study (Appendix B).

An example of the impact of the Carman-Kozeny porosity-permeability correlation in the natural fractures, but for a still unscaled model, is given in Fig. 3-10. The effect of the enhanced permeability in the natural fractures (Fig. 3-10b) as compared to a single hydraulic fracture without any natural fractures nearby (Fig. 3-10a) is to channel fluid flow faster through these high-speed zones. The effect of the enhanced permeability for this synthetic case completely outweighs any impact of the increased

porosity in the natural fracture, which actually increases the time of flight (TOF) and leads to narrowly spaced TOF contours.

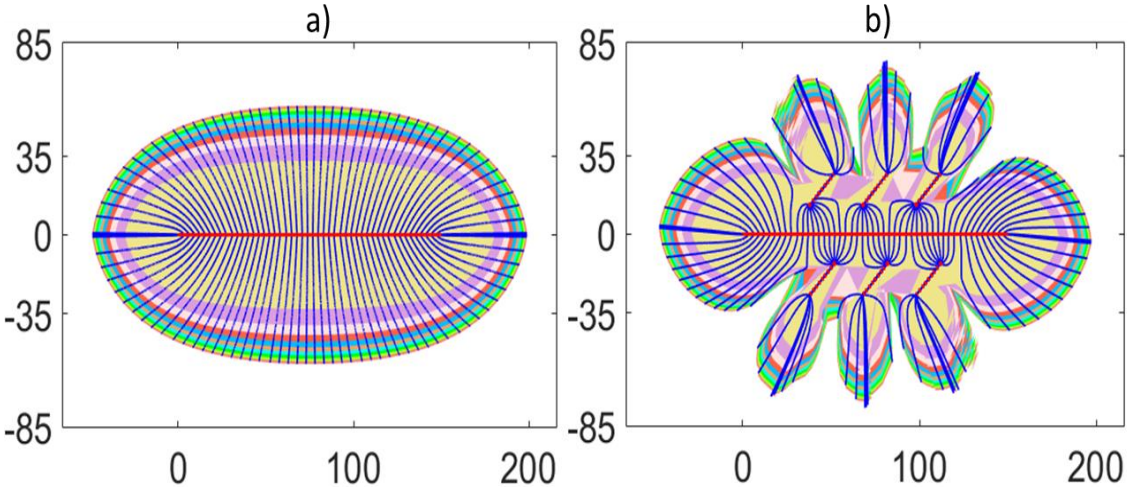

Figure 3-10 a) DRV around a single hydraulic fracture with no natural fractures around, b) DRV around a single hydraulic fracture with 6 natural fractures with porosity of 8.4% and corresponding strength of 155 ft^4/day from CK correlation after 30 years production. Hydraulic fracture in red, Streamlines in blue, Natural fractures in dashed red lines. Rainbow colored fill shows drained areas after 3-year time periods

Analysis of the HFTS natural fracture field data suggests that a dense network of natural fractures occurs around the hydraulic fractures (Shrivastava et al., 2018). The natural fracture density model based on HFTS field data generated by a discrete fracture network contained over 40,500 individual natural fractures distributed over a domain of 300 m by 300 m (Kumar et al., 2019). For tractable run times with our smaller model, the number of natural fractures can be reduced by upscaling. A similar approach was used by Kumar et al. (2019) where the permeability tensor for the entire stimulated rock volume was determined from flowback for input in a discrete fracture network model.

The upscaling method used in the present study seeks to reduce the overall number of fractures to be modeled by upscaling the natural fracture widths and fracture permeabilities (strengths) for a dense natural fracture network. Original natural fracture apertures in the subsurface were assumed to be 5 mm (0.2 inches), which follows from core observations that kinematic apertures are estimated to have been more than 1 mm wide (Gale et al., 2018). A combination of object-based and flow-based upscaling was developed for this study, with an in-depth discussion of this topic given in Appendix A. The proposed upscaling method was applied to produce field models for DRV around a single hydraulic fracture with a representative, upscaled natural fracture distribution of the HFTS. Using the data input ranges (Table 3-2) for natural fractures in conjunction with the Carman-Kozeny correlation, the final model was simulated to determine the real life impact of natural fractures on the DRV.

Table 3-2 Natural fracture data from HFTS used for model simulations

Natural fracture orientation (to hydraulic fracture)[a]	-55° and 55°
Natural fracture length[b]	30 ft
Original natural fracture density[c]	0.042 fractures/ ft^2
Assumed original natural fracture aperture	0.2 inches
Upscaled natural fracture aperture[d]	6 inches
Number of natural fractures [d]	12
Natural fracture porosity	7.32%
Natural fracture strength	155 ft^4/day

[a] Core data obtained values
[b] Use of maximum value from Shrivastava et al.(2018)
[c] From Shrivastava et al.(2018)
[d] Values obtained from upscaling (Appendix A)

From the upscaling of the original natural fracture density the outcome is a model with 12 natural fractures around the single hydraulic fracture. These 12 natural fractures are stochastically placed around the hydraulic fracture using the relevant field data all other

parameters needed. The CK correlation is used to relate natural fracture permeability to porosity. Simulation of this model in CAM gives the representative DRV when affected by natural fractures (Fig.3-11a).

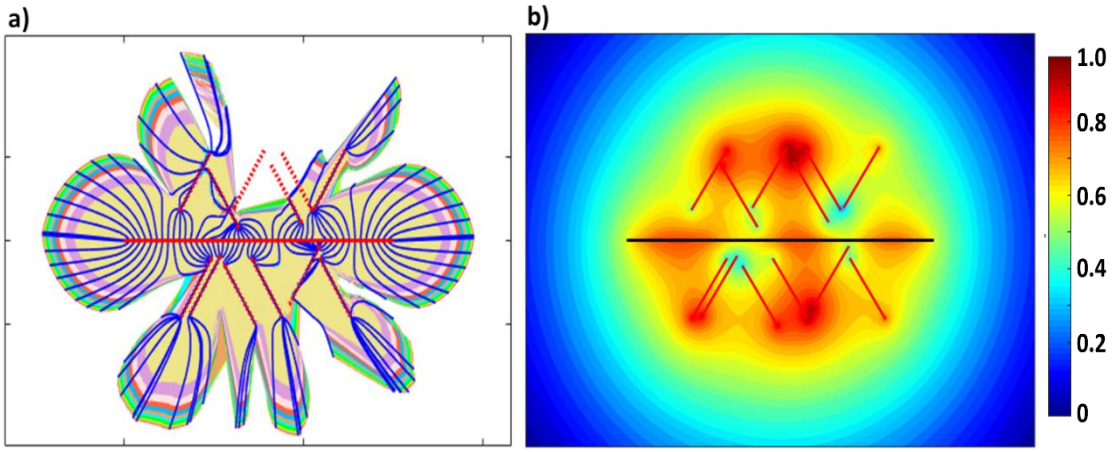

Figure 3-11 a) DRV generated with upscaled natural fractures using field data from HFTS; hydraulic fracture in red; streamlines in blue; natural fractures in dashed red lines. Rainbow colored fill shows drained areas after 3-year time periods. b) Pressure plot after 1 month production generated from CAM around single hydraulic fracture with HFTS upscaled natural fractures; hydraulic fracture in black; natural fractures in red; pressure scale normalized by highest pressure value.

Fig.3-11a shows that fluid is preferentially channeled through the natural fractures for the HFTS field case models. The DRV in the upscaled HFTS model is highly convolute (Fig. 3-11a) with numerous undrained matrix zones occurring between the upscaled natural fractures created from field data. Any storativity effects of the enhanced porosity in the natural fractures remains obscured by the enhanced flow due to the enhanced permeability of the natural fractures. For comparison, the pressure plot after 1 month production is generated using CAM (Fig. 3-11b). Pressure is calculated in

CAM by extracting the potential function from the complex potential and normalizing by the ratio of reservoir permeability and fluid viscosity (Khanal et al., 2019a). For the plot presented the pressure scale is normalized by the maximum pressure present in the reservoir at 1 month production. The lowest pressures occur near the hydraulic fractures. We utilize the process of flow reversal, which means the highest pressures occur at the hydraulic fractures (which can be simply corrected by flipping the scale in Fig. 3-11b). Anomalous high pressures at the tips of the natural fractures are due to singularities and associated branch cut effects occurring when high permeability contrasts (Rk) are used. The progressive distortion of the pressure field near a hydraulic fracture due to the presence of natural fractures is further discussed in Section 3.6.2 (see also Figure 3-14).

The overall pressure field is greatly altered by the presence of natural fractures due to their impact on the flow pattern. The results presented here confirm that the calculated DRV do not conform 1:1 to the pressure field, making the use of pressure plots very poor proxies for reservoir drained areas.

3.5.4. HFTS full well model and implications

The previous section analyzed the impact that natural fractures modeled from field data have on the DRV around an individual hydraulic fracture. This concept is now expanded upon to determine the impact of natural fractures on DRV across multiple fracture stages representative of an entire hydraulically fractured well. The Wolfcamp production well used in these models had 22 stages with each stage spanning 300 ft with a total of 131 individual fracture clusters along the entire lateral. Our modeled DRV

around a single hydraulic fracture is assumed representative of the collated drainage for all the fracture clusters per stage. Each stage has 6 fracture initiation points (clusters) with 50 ft spacing. The results thus show the total drainage of these 6 clusters when upscaled to one single hydraulic fracture.

The first model investigates the drainage based on the given 50 ft cluster spacing (corresponding to the stage spacing of 300 ft) with the assumption of a homogenous reservoir with no natural fractures (Fig. 3-12a). Based on this stage spacing and from the DRV calculated, the multi-stage plot shows large undrained areas in between the existing DRV's after 30 years forecasted production. Results indicate that a maximum distance of 50 ft is drained perpendicularly away from the hydraulic fractures, which represents the drainage of all 6 fracture clusters. The plots (Fig. 3-12a, b) show this stage spacing was sub-optimal due to the large undrained areas that can be targeted for refracs. For comparison, we model the same number of stages but now including the impact of reservoir heterogeneity using the HFTS field data on natural fractures (Fig. 3-12b). When compared to the case with no natural fractures, the maximum area drained perpendicular to the hydraulic fracture increases from 50 ft to approximately 80 ft. Fig. 3-12b shows that even though there is a shift in the spatial location of the DRV due to the natural fractures, this increase in lateral drainage is not enough to efficiently drain in between the fractures at this stage spacing.

Assuming a modified initial fracture cluster spacing of 25 ft, down from 50ft (which corresponds to a stage spacing of 150 ft instead of the field value of 300 ft), the DRV's are modeled using CAM to investigate cases of a homogenous reservoir and

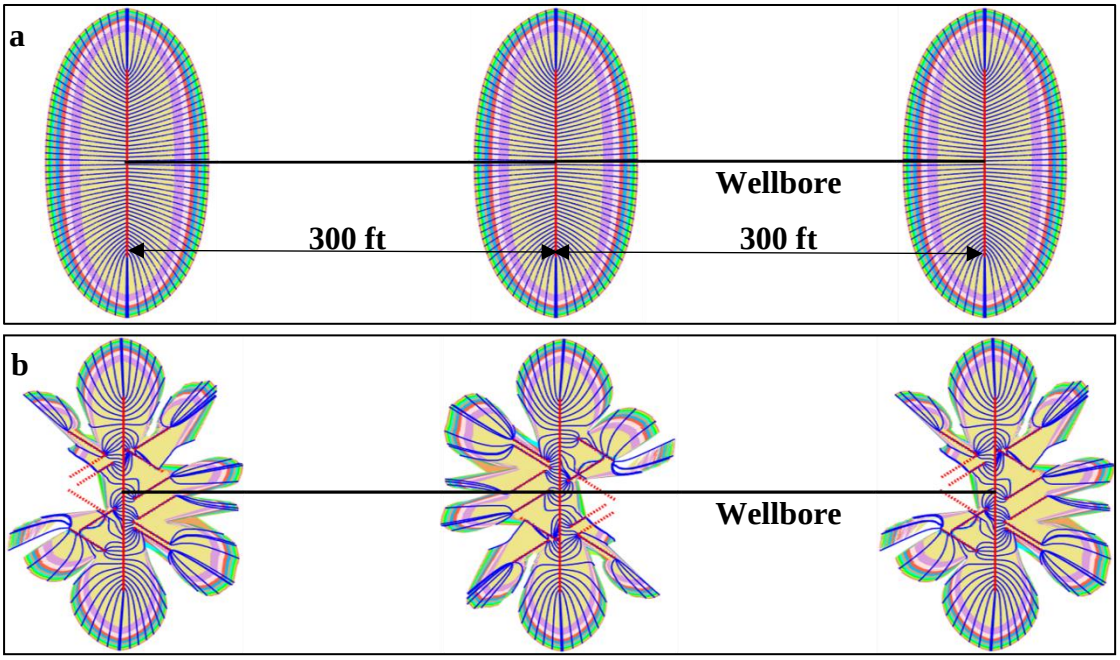

Figure 3-12 a) Plan view of DRV for modeled well using current stage spacing of 300 ft assuming homogenous reservoir b) Plan view of DRV for multiple stages using current 300 ft spacing with the impact of natural fracture modeled using HFTS data. Hydraulic fracture in red line; natural fractures in dashed red line; streamlines in blue. Rainbow colored fill shows drained areas after 3-year time periods.

heterogeneous reservoir with natural fractures (Fig. 3-13a, b). The first case for a homogenous reservoir (Fig. 3-13a) suggests that the reduction of the cluster spacing based on the upscaled DRV for a single stage, allows for more efficient drainage along the length of the lateral. This decrease in spacing to a more optimal value would lead to enhanced well productivity. Our method visualizes the exact DRV and the new spacing does not create adverse flow interference. In fact, the model shows that the spacing can be further optimized to slightly less than 150 ft per stage due to there still being undrained areas between the hydraulic fractures. The introduction of natural fracture heterogeneity reveals a different finding when the stage spacing is decreased to 150 ft. Natural fractures with enhanced permeability when properly oriented to the hydraulic

fracture extend the lateral drained areas as shown in our models (Fig. 3-13b). Though the natural fractures extend the drained areas, at the new stage spacing of 150 ft there is now nearly an overlapping of the DRVs from each stage (shown by dashed black ellipses in Fig. 3-13b). The proximity of these DRVs implies that reduction of the stage spacing to less than 150 ft will lead to flow interference that will reduce the overall recovery from the well. The conclusion from this being that when natural fractures are present, fracture stage treatment with a spacing of less than 150 ft will now be sub-optimal. These results show the importance of accounting for - and properly modeling of -- natural fractures, particularly in flow simulations for unconventional reservoirs.

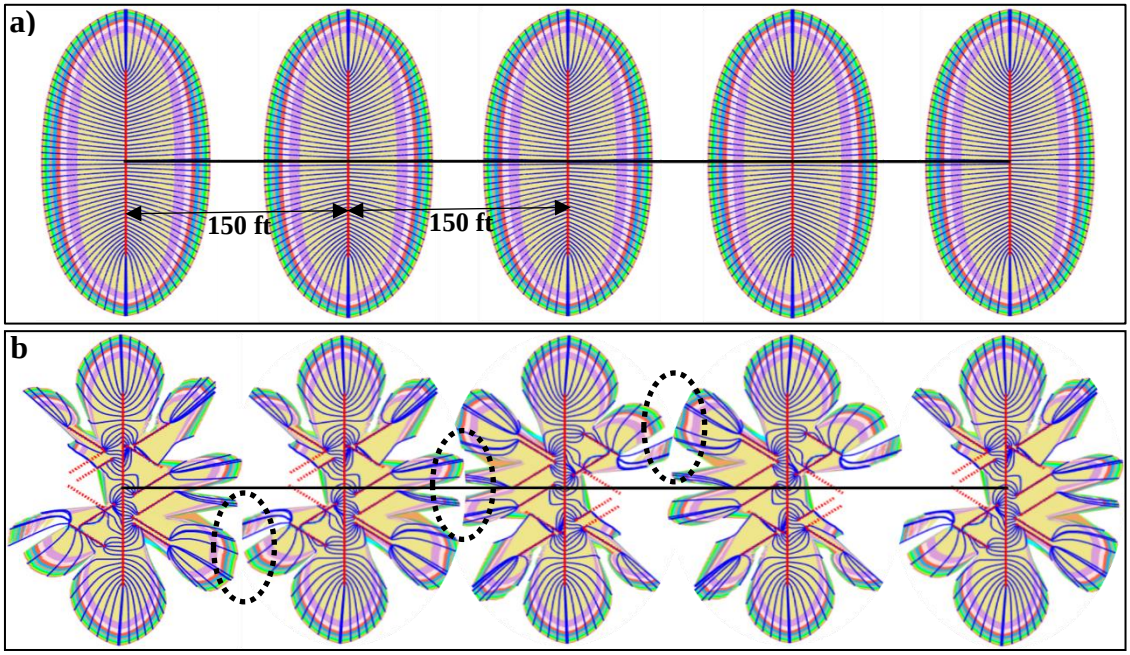

Figure 3-13 a) Plan view of DRV for modeled well using a possible stage spacing of 150 ft assuming homogenous reservoir b) Plan view of DRV for multiple stages using 150 ft spacing with the impact of natural fracture modeled using HFTS data. Hydraulic fracture in red line; natural fractures in dashed red line; streamlines in blue. Rainbow colored fill shows drained areas after 3-year time periods. Dashed ellipses in black show overlapping of DRV's that can cause unwanted flow interference.

3.6. Discussion

Proper modeling and forecasting of production from unconventional reservoirs need to take into account important reservoir heterogeneity such as the presence and the impact of natural fractures. Numerous authors have noted the possible impact that natural fractures can have on production and well-performance (Aguilera, 2008; Forand et al., 2017), but very few seek to succinctly delineate and differentiate the ways in which this is possible. The present study puts forward three major mechanisms by which natural fractures can impact well productivity. Natural fractures present in the subsurface can affect well productivity via: 1) enhanced permeability, 2) enhanced storativity, and 3) reactivation of natural fractures as extensions to the created hydraulic fracture network. By the use of a simple analytical streamline simulator, based on complex analysis methods (CAM), we visualize the drainage patterns around hydraulic fractures by Eulerian particle tracking. The effects of natural fractures, in particular, the enhanced permeability and storativity are investigated systematically and results show that the drainage patterns (DRV) can be greatly altered by the presence of these reservoir heterogeneities.

3.6.1. Storativity impact of natural fractures

Natural fractures present in the subsurface show a range of measured porosity from 2% to 7 % (Gale et al., 2014) but these measured data sets are very limited in sample size and it is believed that porosity ranges may include even higher values. The altered mineralogy in these natural fractures can lead to a porosity and permeability that

is vastly different to that of the unfractured reservoir matrix. With regards to natural fractures present in the Permian Basin, Forand et al. (2017) stated that "*despite natural fractures having a calcite fill, the permeability contrast between the fracture and matrix is likely high enough that the healed fractures may be preferential hydrocarbon pathways. Combining this dominant character with the orientation of natural fractures to maximum horizontal principal stress has the potential to affect the efficiency of hydraulic fractures and the size of the total connected and stimulated rock volume.*" The change in permeability will also result in an increased porosity, which we see as a cause of enhanced storativity for reservoir fluids.

Enhanced storativity can contribute to better well performance as these naturally fractured regions will have a larger hydrocarbon fluid supply that may last longer (Weijermars and Khanal, 2019). The impact of enhanced storativity in natural fractures on the drainage area around a well is for the first time visualized in our results. Starting with a simple REV model (Fig. 3-3), the effect of increased porosity is seen to slow the time-of-flight (TOF) in the natural fracture as compared to the matrix. This proves that porosity changes do not affect streamline patterns but only the time-of-flight (Zuo and Weijermars, 2017). When applied to naturally fractured zones around a hydraulic fracture (Fig. 3-7), the increase in the TOF results in a slower expansion of the DRV in the natural fracture zones compared to the rest of the matrix with a lower porosity. This leads to a decrease in the lateral distance drained away from the hydraulic fracture and can thus impact the optimum fracture cluster spacing distance. For a highly naturally fractured reservoir with higher storativity, the well spacing could be decreased compared

to a reservoir with no natural fractures, as the drained area laterally would be smaller. This ability to increase the number of wells without introducing interference effects (by draining the same area with multiple hydraulic fractures) will lead to higher recoveries per acreage.

3.6.2. Enhanced permeability vs enhanced storativity

For natural fractures with higher permeability, fluid moves preferentially through these high-velocity conduits. REV models for natural fractures with various permeabilities (Fig. 3-4), modeled by individually specified natural fracture strengths in our CAM simulation, show that as fluid moves via the natural fractures some of the matrix areas between the natural fractures are bypassed or left undrained. When applied to flow around a single hydraulic fracture (Fig. 3-8) the preference for flow through the higher permeability zones creates enhanced lateral drainage in the areas where the drainage plumes near the tips of the natural fractures reach deeper into the lateral reservoir space. Our results show that altered permeability impacts both the streamline patterns (convergence into natural fractures) and TOF. For a greater permeability the TOF reduces in the natural fractures as compared to the TOF in the matrix. Thus, natural fractures with enhanced permeability can lead to greater lateral drainage with the caveat that there is the possibility of bypassed areas between the natural fractures that can still contain hydrocarbons.

The synthetic models all assumed variations in the porosity being possible independent of permeability changes. In reality, this is not the case as an increase in the

effective porosity commonly correlates to an increase in permeability. Nonetheless, the synthetic examples clearly highlight that increased porosity leads to an increase of the TOF (i.e. flow is slowed down in the higher porosity region), whereas increased permeability reduces the TOF (i.e. flow if quickened). The latter also alters the flow paths in the reservoir. This leads to a competing effect of higher porosity reducing the lateral DRV, with greater permeability increasing the lateral DRV assuming otherwise similar production (as used in our models).

The key questions now become: *"(1) Which parameter (permeability vs. porosity) has the more dominant impact on the drainage pattern? and (2) How can one correlate any increases in porosity with permeability, and vice versa?"* Data for natural fracture porosity values is very limited and any natural fracture permeability values are for typically reactivated fractures that connect directly to the hydraulic fracture. Due to this paucity of data, this paper made use of the commonly used Carman-Kozeny (CK) correlation for determining permeability based on a given natural fracture porosity. Results show (Fig. 3-10) that using this correlation with a limited number of natural fractures, the permeability effect far outweighs the storativity of the enhanced porosity.

The HFTS case (Fig. 3-11), using field data for natural fracture representation (based on natural fracture upscaling), shows that once the CK correlation is used, the impact of the natural fracture enhanced permeability (lateral extension of DRV and undrained matrix between natural fractures), vastly outweighs the storativity effect of said natural fractures. The DRV and pressure field distortion for the HFTS (Figs. 3-11a, b) provide a specific example of what is a generic effect. For example, Figs. 3-14a-d

show the pressure field around a single hydraulic fracture without any natural fractures present (Fig. 3-14a) and the stepwise distortion of the associated pressure field due to the presence of one, two and six natural fractures (Figs. 3-14b-d).It should be noted that our models have the highest pressures at the hydraulic fracture due to the flow reversal modeling used (whereby fluid is placed back into the reservoir via the hydraulic fractures at the same rate as produced).

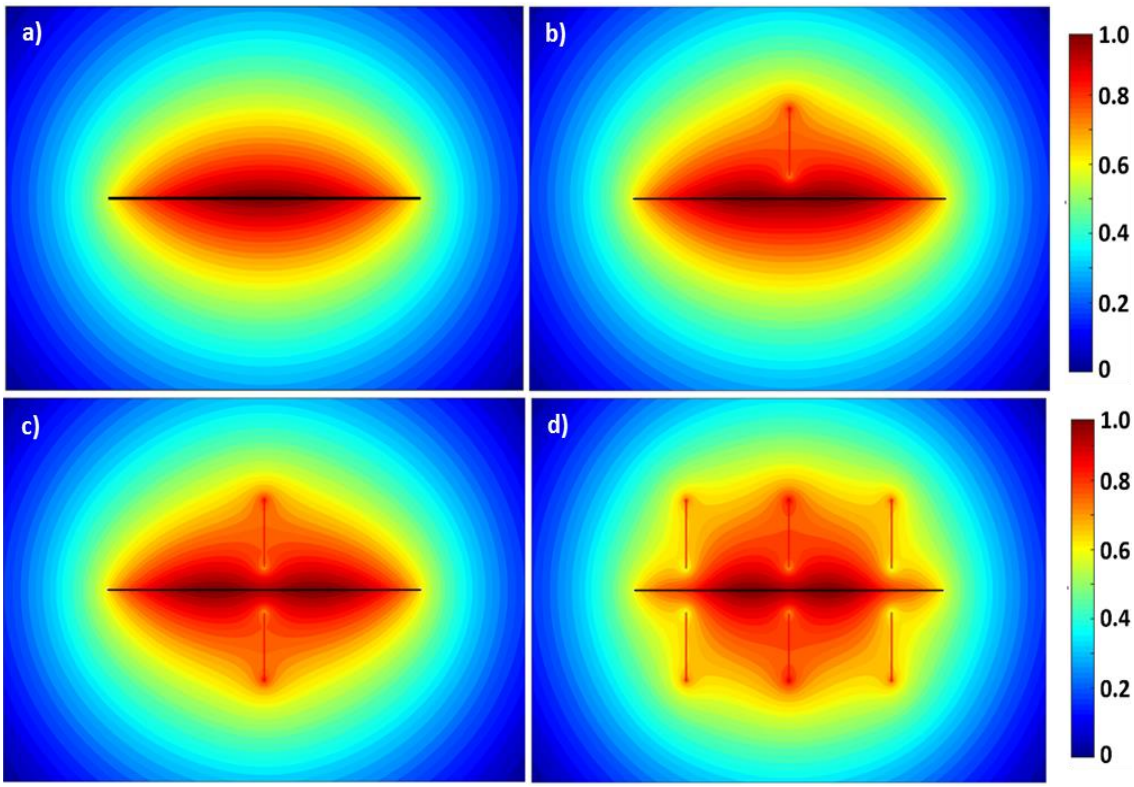

Figure 3-14 a) Pressure field around a single hydraulic fracture in a homogenous reservoir with no natural fractures b) Pressure field with the presence of 1 natural fracture c) Pressure field with 2 natural fractures on either side of hydraulic fracture d) Pressure field with 6 natural fracture with 3 on either side of the hydraulic fracture. Hydraulic fracture in black, natural fractures in dashed red line. Pressure scale was normalized.

3.6.3. Model strengths and limitations

The CAM models presented here are grid-less and meshless unlike the more often used numerical methods in industry. Due to being grid-less, CAM is much less computationally intensive than finite-volume/difference numerical methods with the added advantage of high resolution at the scale of the hydraulic and much smaller natural fractures. Other strengths of the CAM model to accurately determine the impact of natural fractures on drained rock volumes comes in the form of this analytical method having closed form solutions as well transparency in all steps of the methodology (Weijermars and Khanal, 2019). The present study is limited to flow in 2D as well as only modeling single phase fluid flow. As the natural fractures are modeled as individual discrete elements, the model would become cumbersome to use and computationally expensive if large scale, stochastically generated natural fracture networks are taken as inputs. This is the rationale behind the use of upscaling methods to represent natural fractures used in the field scale models. In reality the geometry of both the natural fractures (in terms of inclination angle in 3D) and the hydraulic fractures (as fractal networks instead of simple bi-planar features) are much more complex that represented here. In spite of these simplifying and reductionist model assumptions (as all other models also have), the CAM tool developed in this paper to include the impact of natural fractures can be used as a quick and simple method to screen optimum hydraulic fracture spacing and to support and direct well spacing decisions in naturally fractured reservoirs. What the 2D studies provide are very valuable systematic insight that will benefit the improvement of 3D model studies as well. Accounting for 3D dimensionality

may make for more realistic models, but when coupled with flow also may disguise some of the systematic effects visualized in our 2D models of flow in hydraulically and naturally fractured reservoirs.

3.6.4. Practical implications

Impacts of natural fractures on production in unconventional wells are still debated. However, the interaction of the in-situ stress, hydraulic fractures and natural fractures could be leveraged to optimize well path planning and completions designs (Forand et al., 2017). In this study, we distinguished three major mechanisms via which natural fractures may impact flow and, implicitly, acreage productivity. Flow models based on CAM show that enhanced natural fracture permeability and porosity can alter the DRV shapes and spatial location greatly. This can have implications for the spacing of both hydraulic fractures and wells, once the nature of the natural fracture network in the subsurface has been accurately characterized. For formations with highly permeable natural fractures, well spacing should be slightly increased to avoid interference as the DRVs would otherwise overlap.

However, this assumes the spacing is based on DRV modeling. If based on pressure interference models only, our previous work (Weijermars and Van Harmelen, 2018; Khanal and Weijermars, 2019a) argues that such pressure interference occurs for much larger well spacing and fracture spacing. However, such pressure interference should not be used as the sole criterion for well and fracture spacing decisions, because

of the over one order of magnitude time-lag between the pressure front and the tracer front propagation in ultra-low permeability reservoirs (Weijermars et al., 2019).

The models presented emphasize how the spatial orientation, location and lateral extent of the DRV are vastly impacted by the presence of natural fractures. Fluid flows preferentially through the highly conductive natural fractures, altering the shape of the DRV around hydraulic fractures. Any undrained matrix zones that have been bypassed due to flow channeling into the natural fractures with high flow rates can then be preferentially targeted for refracturing. For rock formations where the stress regimes preferentially allow for reactivation of natural fractures to form an extension of the hydraulic fracture, cluster spacing can be decreased to allow for the creation of the largest, most complex fracture network that gives greatest access to the hydrocarbons trapped in the low permeability reservoir rock (Nandlal and Weijermars, 2019a).

3.7. Conclusions

Natural fractures present in the subsurface are a major form of heterogeneity in both conventional and unconventional hydrocarbon reservoirs. Highly conductive natural fractures may provide preferential pathways for fluid withdrawal to the production wells, which is why natural fractures are highly crucial for well design decisions (especially in unconventional reservoirs). The major conclusions from our analysis on the impact of natural fractures on subsurface flow are:

1) Natural fractures can affect reservoir flow through three major mechanisms: (i) by enhancing permeability, (ii) by altering the porosity in the fractures, leading to

increased storativity, and (iii) by becoming extensions of the hydraulic fracture network due to reactivation.

2) Enhanced permeability in natural fractures creates high velocity flow zones which preferentially channel fluid flow through them. At high enough permeabilities (or natural fracture strengths as used in our models), this preferential pathway to flow leads to bypassed regions in the matrix blocks between the natural fractures, which are left undrained. These undrained matrix regions can then be targeted by refracturing to improve recovery factors from hydraulically fractured horizontal wells.
3) Altered porosity or enhanced storativity (due to natural fractures with a higher porosity than the reservoir matrix as investigated in synthetic models) leads to a decrease in the lateral extent of the DRV. The impact of both natural fracture storativity and permeability greatly affect the shape and extent of the DRV around the hydraulic fractures.
4) The Carman-Kozeny (CK) relation was used to determine the relative impacts of the correlated porosity and permeability in natural fractures on the DRV development. Results based on the CK correlation show that the enhanced flow due to permeability far outweighs any storativity effects (even if natural fractures were to have a higher porosity than the reservoir matrix).
5) Use of a hybrid object-based and flow-based method for upscaling allows for the modeling of a high density natural fracture network. Upscaling is needed to

reduce the number of natural fractures modeled while keeping the equivalent permeability the same.

6) Field data on in-situ natural fracture characteristics such as porosity and permeability is sparse and lacking in literature. Industry needs to ensure collection of such data for use in reservoir models to accurately determine subsurface flow and drainage volumes.
7) Proper analysis of natural fracture data and the predominant mechanism by which it will affect flow will lead to accurate DRV calculations in the subsurface. From these determined DRV (based on a well type curve) fracture cluster spacing and well spacing could possibly be optimized.

4. PHYSICS DRIVEN OPTIMIZATION OF DRAINED ROCK VOLUME FOR MULTISTAGE FRACTURING WITH FIELD EXAMPLES FROM THE WOLFCAMP FORMATION, MIDLAND BASIN*

4.1. Introduction

4.1.1. Brief highlights

This chapter makes use of hydraulic fracture propagation data to move from the 2D plane to 3D and create DRV plots for a single fracture stage in a well from the Midland Basin. For this project I was able to devise a new allocation algorithm that is programed to use hydraulic fracture conductivity to allocate fluid production to accurately determine DRV. From this work, for the first time ever we are able to visualize the DRV in pseudo-3D realizations.

In this chapter, we use the conductivity attribute obtained from a history-matched hydraulic fracturing model to build a reservoir drainage model that uses streamline tracing and time-of-flight contours and identifies the locations of the drained rock volume. We demonstrate our workflow by the *retrospective analysis* of a field case from the Wolfcamp Formation, Midland Basin, Texas. However, the methodology developed in our study can be equally applied to the *field development planning stage* using pilot hole logs and offset well data for the fracture propagation model and type curves for flux

* Part of the data reported in this chapter is reprinted with permission from "Physics-Driven Optimization of Drained Rock Volume for Multistage Fracturing: Field Example from the Wolfcamp Formation, Midland Basin" by Parsegov, S.G., Nandlal, K., Schechter, D.S., and Weijermars, R. in Proceedings of the 6th Unconventional Resources Technology Conference. Copyright 2018 by American Association of Petroleum Geologists and by Society of Petroleum Engineers.

allocation to the drained rock volume (DRV) in the reservoir simulation. The DRV can be estimated by coupling a calibrated hydraulically fracturing model with a fluid flow model near the fractures based on history matching of production data.

4.1.2. Motivation of study

Physics-driven flow models in hydraulically fractured rock volumes make significant progress in completion design possible. Such models attempt to solve a coupled problem of rock mechanics, fluid flow, and proppant transport during fracturing and fluid flow to the wellbore. The key problem here is to integrate all information available about rock properties (Izadi et al. 2017; Kresse et al. 2013, 2011; Niu et al. 2017; Parsegov and Schechter 2017; Weng 2015; Weng et al. 2011), and reconstructed reservoir depletion (Weijermars et al. 2017b, 2017a, Yu et al. 2018, 2017a, 2017b, 2016). A common objective of the models is the maximization of the recovery of original hydrocarbon from the acreage by minimizing unstimulated and undrained regions, which prompts for the tightest possible well spacing while avoiding adverse effects due to well interference.

Prior work (Ajani and Kelkar 2012; Kurtoglu and Salman 2015) shows that the intensity of well interference increases when the well spacing decreases. In particular, fracture hits may negatively affect well performance and play an essential role in optimizing well spacing to maximize overall recovery (Malpani et al. 2015; Yaich et al. 2014). Tighter well spacing in multi-well pads may intensify well-to-well interference

causing fracture hits (King and Valencia 2016; Lawal et al. 2013; Yu et al. 2017a, 2017b). Such fracture hits may involve connecting hydraulic and natural fractures.

With fracture treatment leaving significant portions of the near-wellbore region unstimulated (Parsegov et al., 2018a) and the production flux not draining dead zones between the fractures and between interfering wells (Weijermars et al. 2017b, 2017a; Weijermars and Nascentes Alves 2018) there is room for improvement of completion designs

4.1.3. Summary

This chapter presents a new workflow comprised of using hydraulic fracture modeling outputs (effective length, height, and conductivity) for the next step – a discrete fracture flow model which visualizes the drainage pattern in 3D based on history matched production data.

This study shows the process of import and conversion of 2D fracture conductivity maps for further use in fluid flow allocation to the individual fractures. The 3D Drained Rock Volume (DRV) is rendered based on 2D streamline and time-of-flight maps for drainage, velocity and pressure depletion with 5 ft vertical resolution layers representing the reservoir. Instead of using a grid-based numerical simulation, we apply a meshless flow model based on Complex Analysis Methods (CAM) to solve linear differential equations. The fluid velocity field is computed for narrowly discretized time steps, which allows high-resolution visualization of hydrocarbon flow near and into each of the discrete fractures.

Honoring critical physical interaction of fracture fluid, rock mechanics, proppant transport, the fracture propagation model coupled with the flow model for discrete fractures, provides a powerful tool to pinpoint the drained rock volume. Our systematic study highlights trade-offs between fracture design inputs and the total drained rock volume. Field data from the Wolfcamp Formation, Midland Basin in West Texas, provides a real-world case to demonstrate our workflow.

4.2. Drainage and pressure depletion models

The starting point for this modeling workflow is output from the commercially available "GOHFER3D" hydraulic fracture simulation software. Using the necessary geomechanical subsurface properties for the Wolfcamp Formation in the Midland Basin Texas, the creation of hydraulic fractures are simulated with the main output being fracture conductivity maps for each cluster along the horizontal wellbore.

We seek to model drained areas and pressure depletion using the novel CAM solution described in previous chapters for modeling hydraulic fractures as line sinks. The workflow to complete our objective is as follows:

- Creation of 3D fracture model with appropriate inputs.
- Determination of total well production using Duong decline curve.
- Discretization of 3D fracture and assigning of fracture conductivity per node.
- Allocation of production per fracture based on flux allocation algorithm.
- Modeling of velocity and pressure depletion per discretized reservoir layer drained by the fracture.

- Modeling of drained area realized in each discretized layer.
- Interpolation of drained area per layer to create a 3D envelope of the drained rock volume (DRV).

4.2.1. Production forecasting

We assume radial flow toward the wellbore in the fracture plane and 2D flow perpendicular to the fracture plane in the reservoir (Al-Kobaisi et al. 2006). Justifications for this 2D flow idealization comes from Weijermars et al. (2017b) by assuming matrix flow is confined between an upper and lower finite boundary which thus imposes a 2D flow geometry in the matrix. Production data is history matched with the Duong's Decline Curve Model (Duong 1989) to generate a type curve for the given well. For oil production the equations used are:

$$q_{well}(t) = q_i \cdot t(a,m) + q_\infty \tag{4-7}$$

with time exponent:

$$t(a,m) = t^{-m}\, e^{\frac{a}{(1-m)}(t^{1-m}-1)} \tag{4-8}$$

and cumulative oil production $N_p(t)$ is given after integration as:

$$N_p(t) = \frac{q}{a}\, t^m \tag{4-9}$$

Based on historical production data parameters a, m, $q_{\infty,}$ and q_i can be determined using the least squares fit method. The parameters are used to forecast production for Well 46H **(**Fig. 4-1**)**. For the well modelled the parameters obtained from curve fitting the monthly production data were: q_i = 7,713 STB/month, q_∞ = 0 STB/month, a = 1.81

month^{-1} and m = 1.5. Our curve fitting shows a good correlation to actual produced cumulative production values. With these parameters, we forecast production for the well for 40 years life.

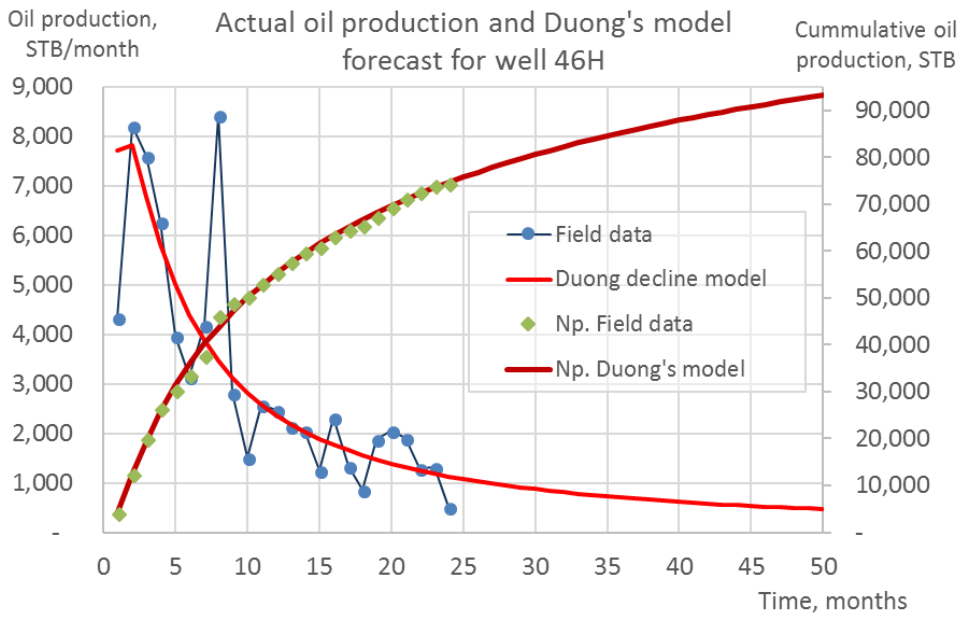

Figure 4-1 Well 46H actual production and type curve forecasts used for the flow model

4.2.2. Production matching stage-by-stage

Weijermars et al. (2017a, 2017b) introduced analytical solutions for the visualization of flow interference between hydraulic fracture clusters based on Complex Analysis Methods (CAM). The CAM code was used to devise an analytical streamline simulator, which can be used to produce high-resolution plots of the areas drained around hydraulically fractured wells for comparison with pressure depletion plots and velocity fields around the fractures. From this work, new insights were developed such as the fact that areas of high flow are better illustrated by velocity plots rather than the

pressure plots that are currently used as a proxy for drained regions. Another significant insight was the recognition of so-called dead zones due to flow interference between the fractures.

Previous CAM-based flow models assumed the hydraulic fractures were planar features with uniform height and length as determined from micro-seismic events. The fracture surface area was used as the control on the amount of production each fracture was contributing. The present study assigns properties to the 3D fractures making use of a greater dataset than just the micro-seismic events. By importing the fracture conductivity from the 3D fracture model with a high resolution of the propped fracture variability a more accurate representation of the fluid flow around individual fractures becomes possible.

The CAM flow model initially used a simple flux allocation algorithm that allocated well production rates to the individual fractures in the drainage model. The amount of flow allocated to each fracture from the total type curve output was based on the surface area of each fracture, labeled {1, 2, 3,…, k}, and the fracture height and length were inferred from micro-seismic data available for 13 stages. A scaling term was used to prorate the total production output of the sample Well 314H to just 13 out of the 33 fractures:

$$q_k(t) = (1 + WOR) \cdot \ q_{well}(t) \frac{13}{33} \frac{H_k \ . \ X_{f,k}}{\sum_k H_k \ . \ X_{f,k}} \qquad (4\text{-}10)$$

To account for the oil formation volume factor (*FVF*) and reservoir porosity, the following expression was used in the complex potential solution, where $m_k(t)$ represents the strength of the interval source at a time *(t)*:

$$m_k(t) = \frac{FVF \cdot q_k(t)}{H_k \cdot PORO} \tag{4-11}$$

This original method utilized flow reversal to help define the drained regions around the fractures. Production data was analyzed using the Duong's Decline Curve method (Duong 1989) to forecast long-term production. The production was allocated back to individual fractures based on the production allocation algorithm. The initial algorithm prorated production based on idealized planar, fracture height and length based on, for example, the micro-seismic interpretations. Though this is a reasonable assumption, recent work shows that actual productive fracture half lengths and heights may not exactly correlate to these micro-seismic events. That is why, in this study, we make use of the result of a planar-3D hydraulic fracturing modeling to allocate production to the individual fractures.

4.2.3. Discretization of 3D fracture and fracture paneling

The adapted flux algorithm makes use of fracture conductivity data from the 3D geomechanical fracture model. 3D baseline fracture conductivity from the 3D geomechanical model takes into account corrections for proppant pack degradation and imperfect fracture cleanup as proposed by Parsegov et al. (2018b). The improved flow allocation algorithm can better capture the physics of the producing hydraulic fracture

network and thus gives a better representation of drained regions and the location of stagnation zones. Such detailed flow models may help to improve well and fracture treatment design to achieve higher EUR and improve recovery factors.

The fracture model uses a grid of 5 ft by 10 ft nodes to represent the created hydraulic fracture (Fig. 4-2). Due to this, we can discretize the fracture height into 5 ft thick layers, and fluid flow in each layer was modeled based on the conductivity (C_k) of the grid blocks in that layer (Fig. 4-3). The conductivity within one layer can at times vary by several orders of magnitude, which is captured by panels within each layer averaging the conductivities of grid blocks that are relatively within the same order of magnitude. Each of these panels is used for flux allocation in the CAM code to model fluid flow into the individual layers. For Stage 2 the paneling procedure represents the five fractures discretized into 15 individual layers with on average five different conductivity panels. The actual number of panels in each layer is not constant but depends on the range of conductivity values for that particular layer.

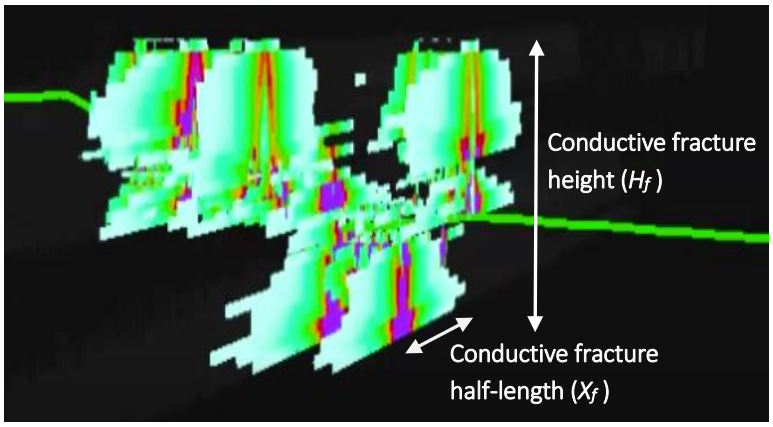

Figure 4-2 Snapshot of evolved fractures of the Stage 3 well 46 with effective conductivity indicated by the color (purple - high conductivity, green - low conductivity).

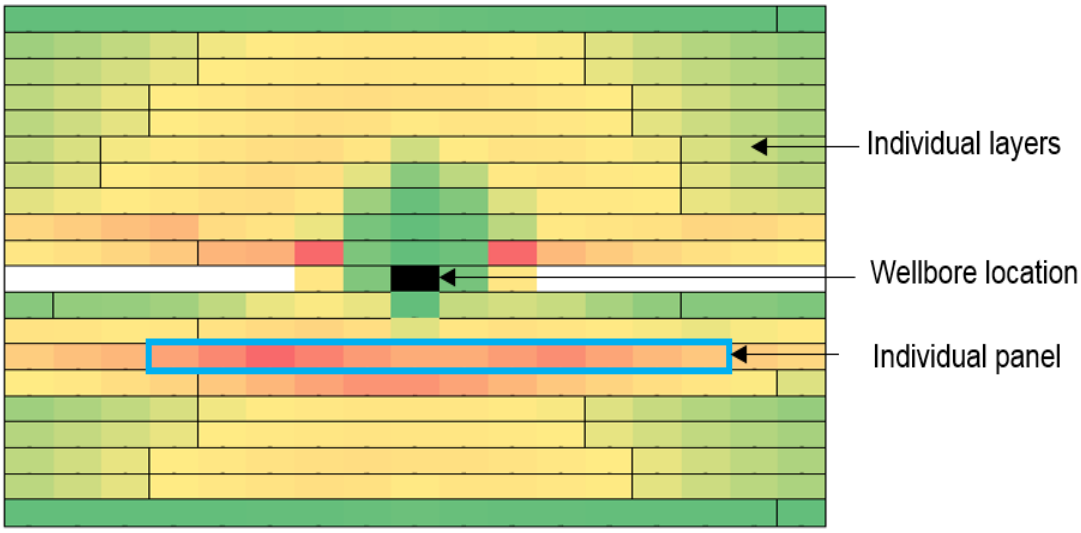

Figure 4-3 Discretized Fracture front view; warmer colors indicate higher conductivity

4.2.4. Flux allocation

Next, the average fracture conductivity, $\overline{C_k}$, of each panel is calculated based on the individual node values for C_k and the number of nodes in that particular panel:

$$\overline{C_k} = \frac{\sum_{k=1}^{N} C_k}{N} \tag{4-12}$$

Where N is the number of nodes in the panel and $\sum C_k$ is the sum of the conductivities of the individual nodes in the panel. This approach is followed for all panels in all 15 layers for all 5 fractures in our modeling of Stage 2 in this well. From this we propose a conductivity-based flux algorithm:

$$q_k(t) = Z(1 + WOR) \cdot q_{well}(t) \cdot S \cdot \frac{\overline{C_k} . H_k . 2 \cdot X_{f,k}}{\sum_k^n \overline{C_k} \cdot H_k . 2 \cdot X_{f,k}} \tag{4-13}$$

The algorithm takes into account the fracture panel conductive surface area when allocating flow into the individual fractures. A conversion factor Z = 5.61 accounts for conversion of input units of $q_{well}(t)$ in STB/day into output units of $q_k(t)$ in ft^3/day.

Scaling factor S in Eq. (4-13) depends on the allocated production for the stage as determined from the tracer data. Tracer data (Table 4-1) allow us to allocate total production to each fracture stage. Stage 2 is part of the traced segment "5-2" (Stages 2-5), which shows a contributing percentage of 13.1% from normalized oil-soluble tracer flowback. Based on this percentage of flow over these four stages we can average the portion of the production allocated to Stage 2 as 3.28% of total well production.

Table 4-1 Oil soluble tracer data for fracture stages.

	Oil Frac Tracer Concentration, ppb						
Traced Segment	30-26	25-21	20-17	16	15-11	10-6	5-2
Stim Date	7/30/14	7/27/14	7/24/14	7/24/14	7/22/14	7/20/14	7/18/14
OFT Injected (gr)	1,250	1,250	1,000	250	1,250	1,250	1,000
% Injected	17.2%	17.2%	13.8%	3.4%	17.2%	17.2%	13.8%
Sample Type	OFT 5800	OFT 5300	OFT 15010	OFT 15110	OFT 15000	OFT 5100	OFT 5500
Oil (Produced)	42.3	63.6	28.0	8.8	68.4	17.3	2.4
Oil (Produced)	33.6	49.8	26.1	8.5	58.2	13.0	2.6
Oil (Produced)	34.6	53.4	27.1	8.7	65.9	14.3	2.3
Oil (Produced)	38.5	57.7	27.8	8.4	63.5	15.3	2.7
Oil (Produced)	37.1	59.7	28.8	8.7	66.9	19.1	4.5
Oil (Produced)	40.1	65.0	28.6	8.5	69.5	24.1	5.2
Oil (Produced)	41.6	62.1	29.1	8.9	68.9	17.1	2.9
Oil (Produced)	28.8	52.0	24.5	8.0	60.0	20.5	9.7
Oil (Produced)	32.1	64.2	21.9	7.1	60.8	16.1	10.8
Oil (Produced)	39.7	64.1	30.1	9.4	76.4	23.8	12.3
Oil (Produced)	42.0	68.6	32.9	10.8	89.0	34.7	25.6
Oil (Produced)	35.3	56.3	27.6	9.3	72.8	28.3	32.3
Oil (Produced)	38.8	59.3	28.8	8.9	72.0	31.0	32.1
Oil (Produced)	39.0	43.2	21.2	13.0	70.2	21.8	28.9
Oil (Produced)	37.6	41.1	19.3	12.6	64.9	20.6	28.2
Oil (Produced)	44.5	48.6	18.6	11.6	61.2	24.8	28.2
Oil (Produced)	48.0	52.0	19.0	10.9	69.2	26.0	33.1
Oil (Produced)	24.2	27.0	15.9	6.4	52.6	15.2	49.6
Time Weighted Avg, ppb	36.8	47.7	21.5	9.2	64.5	21.8	30.3
% total ppb from Stage	15.9%	20.6%	9.3%	4.0%	27.8%	9.4%	13.1%

4.3. Drainage visualization

The rock volume drained by the five fractures of Stage 2 in Well 46H has been reconstructed after quantifying the flux allocations for 15 horizontal layers in the stage. For the creation of a 3D envelope of the drained rock volume (DRV), we stack the individual 2D drainage shapes for each layer in the z-direction to visually represent the area drained out by the fracture stage. Hydraulic fractures are modeled as line sinks with varying strengths to visualize fluid flow near the fractures, pressure depletion and the velocity field in 2D flow planes based on the complex analysis. The drained rock volume (DRV) can be computed based on the corresponding time-of-flight contours from the particle tracking of streamlines. The 3D fracture model discretized each fracture into individual flow layers (Fig. 4-4), which intersect all fractures in each plane. By combining the drainage areas per layer we can create a 3D visualization of the drainage envelope for Stage 2.

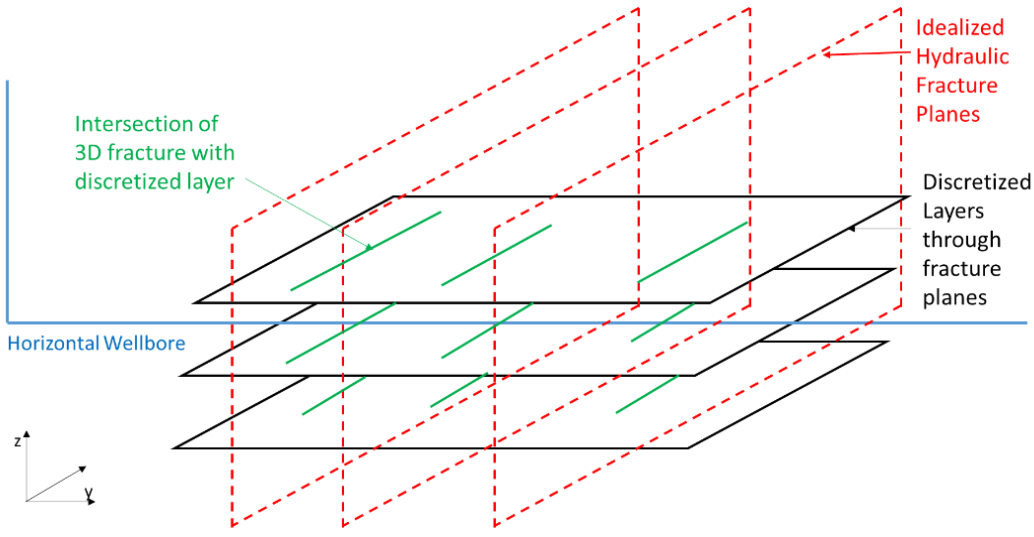

Figure 4-4 Schematic of discretization of 3D fracture plane into layers for modeling.

4.3.1. Flow visualization and pressure change realization

With calculated total well output and the algorithm for flow allocation, we can now visualize flow based on the prorated flux into discretized fracture layers using our method of complex potential. The velocities contours $|V(z,t)|$, for a specific time *t* and layer *l* of the discretized hydraulic fracture, are plotted using the equation:

$$V(z,t)=\sum_{k=1}^{N}\frac{m_k(t)}{2\pi L_k}e^{-i\beta_k}\cdot\left(\log\left[e^{-i\beta_k}\left(z-z_{c,k}\right)+0.5L_k\right]-\log\left[e^{-i\beta_k}\left(z-z_{c,k}\right)-0.5L_k\right]\right) \tag{4-14}$$

The calculated $q_k(t)$ accounts for the strength of flow near the fractures in our model layer of thickness H_k by adjusting for formation volume factor *(FVF)* and reservoir porosity (*PORO*) as follows:

$$m_k(t)=\frac{FVF\cdot q_k(t)}{H_k\cdot PORO} \tag{4-15}$$

We apply the principle of flow reversal, and local pressures are calculated relative to an initial reference reservoir pressure P_0 at the time of injection (Weijermars et al. 2017b):

$$P(z,t)=P_0+\Delta P(z,t)=P_0-\frac{\emptyset(z,t)\mu}{k} \tag{4-16}$$

Where μ is fluid viscosity, *k* is the reservoir permeability, and $\emptyset(z,t)$ is the potential function representing pressure change ΔP. We can model the flow of fluid into the hydraulically fractured well, and the corresponding pressure declines due to the drainage by the producing well. For the visualization of drainage contours we assume the following: *PORO* = 5%, *k* = 100 μD, *FVF* = 1.05 RB/STB, μ = 1 cP, and WOR = 4.6.

4.3.2. Results of visualization

This section shows the flow modeling results for Stage 2 taking into account the spatial variation in conductivity along each hydraulic fracture discretized into 15 individual layers (Fig. 4-5). The drained region for each layer is determined from the time-of-flight contours over the productive life of the well. We present the 2D drainage areas as well as velocity and pressure contour plots for key individual layers (Layers 4, 6, 8, 10, 12 and 14). From our results (Fig. 4-5 and Fig. 4-6) it is clear just how much of the actual fracture length is unproductive. In fact, regions drained after 40 years are still confined to the proximity of the fracture surfaces.

Pressures in the model are calculated using Eq. (4-16) with the potential function representing the pressure change based on the initial reservoir pressure as the reference pressure P_0. The potential function is scaled by the fluid viscosity (μ), and reservoir permeability (k), and $\Delta P(z, t)$ is quantified, efficiently rescaling initial reservoir pressure P_0=0. Actual reservoir pressure can be obtained at all times by adding back in P_0 = 5,850 psi (based on vertical pressure gradient). Assuming a reservoir permeability of 100 μD (0.1 mD) after fracturing, the potential function of Eq. (4-16) associated with the flow rates near the hydraulic fractures give pressure changes $\Delta P(z, t)$ on the order of 10^3 psi. The pressure contour plots (Fig. 4-5, right column) are scaled with the absolute pressure change ΔP, which represents the pressure drawdown of the fractured well. Velocity peaks in each layer of the model coincide with regions where pressure contour spacing is narrowest. Pressure drawdown is highest near the central region of the fractures. By comparison, the velocity contours show highest velocities of the fluid occur at the

fracture tips and particularly at the outer fractures where there is less flow interference between fractures.

The permeability used in the flow model 100 μD (0.1 mD) to match the actual reservoir production with realistic pressure changes differs 3 orders of magnitude from the matrix permeability used in the initial fracture propagation model, which has a mean permeability of 0.1 μD. The low pre-frac permeability of 0.1 μD cannot be reconciled with the productivity and corresponding pressure depletion rate in history matching, which requires the use of 0.1 mD in the flow model. A possible explanation for the inferred difference in matrix permeability before and after the frac treatment could be the existence and/or creation of secondary fracture systems near the main hydraulic fractures (enhanced permeability region).

The time of flight contours (Fig. 4-5, middle column) outline the area drained after 40 years of production. Commonly, pressure depletion plots are used as a proxy for drainage. Indeed, pressure plots in our study indicate where the fluid is moving fastest in the reservoir due to a pressure gradient, namely where pressure contour spacing is tightest. However, not all moving fluid will reach the fractures within the time scale of the well. Time-of-flight contours give a more accurate estimation of the drained reservoir region as visualized by the CAM model. Therefore, we conclude that in unconventional, ultra-low permeability reservoirs, pressure plots are less reliable for representing the drained rock volume.

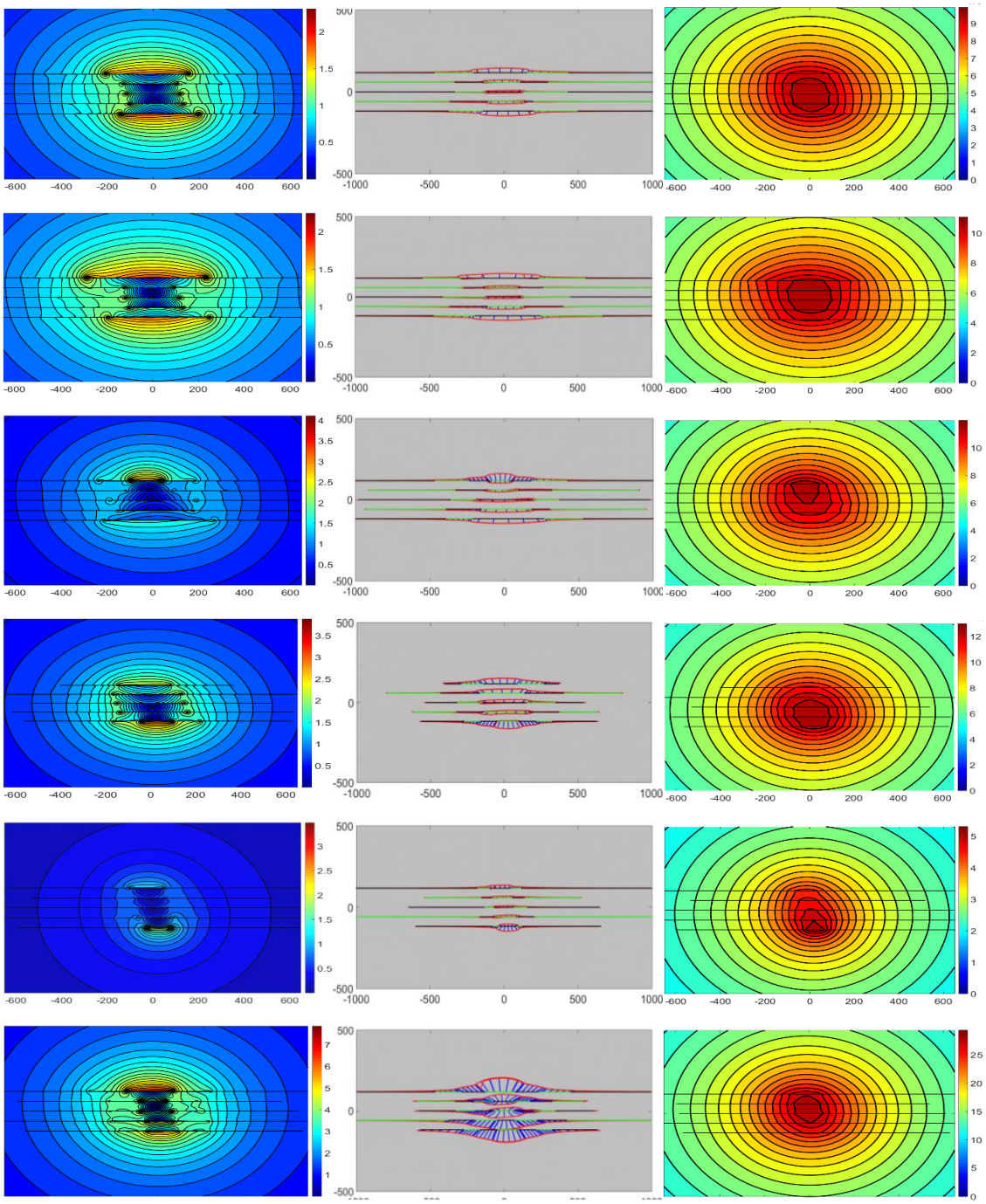

Figure 4-5 Top to bottom: Flow data for Layers 4 (top panel), 6, 8, 10, 12, and 14 (bottom panel). Left column - Velocity contour plots (ft/month); Middle column - Drained area after 40 years production outlined by red time of flight contours. Streamlines in blue and fracture segments with variable conductivity marked by alternating blue and green line segments; Right column - Pressure contour plots (drawdown in psi). Velocity and pressure plots are shown after one-month production. Length scale is in ft.

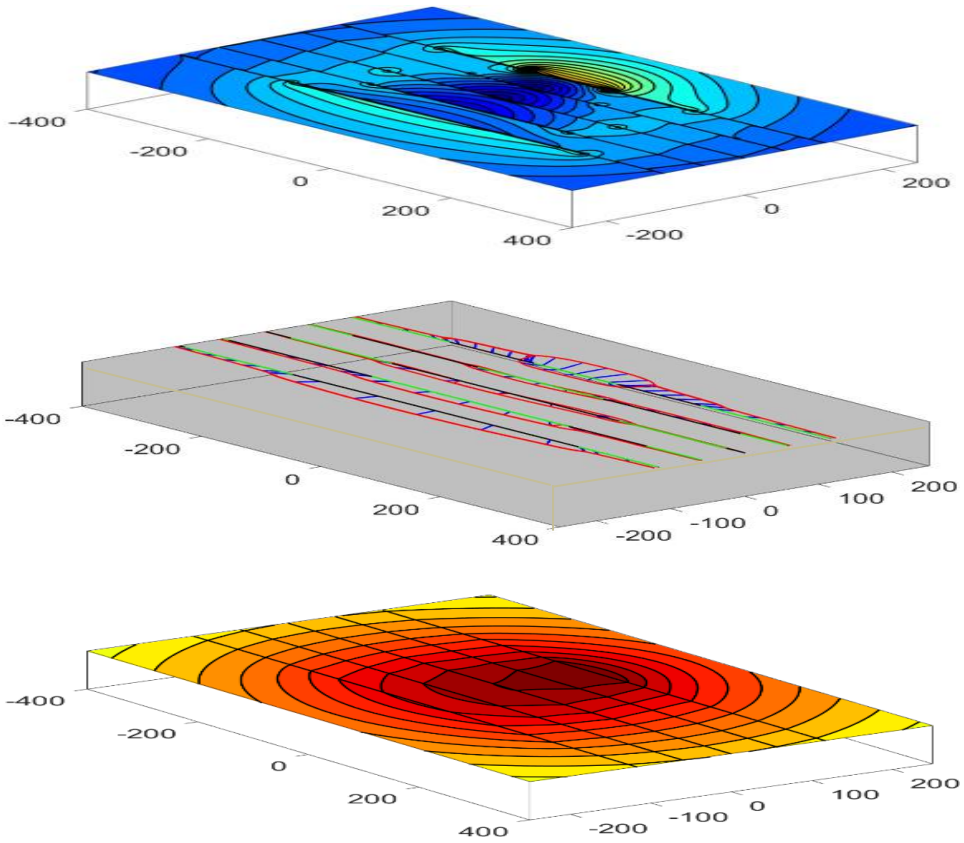

Figure 4-6 Zoom on Layer 8 for velocity contour plot, drained area, and pressure contour plot. Length scale is in ft

For the first time, we are able to visualize the 3D drained rock volume (DRV) for Stage 2 after 40 years of production **(**Fig. 4-7**)**. Between the fractures, there are still undrained regions that can be targeted for refracturing. One observation is that the lower layers have a larger drained area than the upper layers of the fractured zone showing the non-uniform flow from the reservoir into the fracture at different depths. Outer fractures have higher hydraulic conductivities and therefore drain the adjacent matrix region more effectively. Additionally, the external fractures in Stage 2 show hydraulic conductivities

increasing from the top to the bottom layer, which is why the drained region is the largest accordingly near the bottom of the outer fracs.

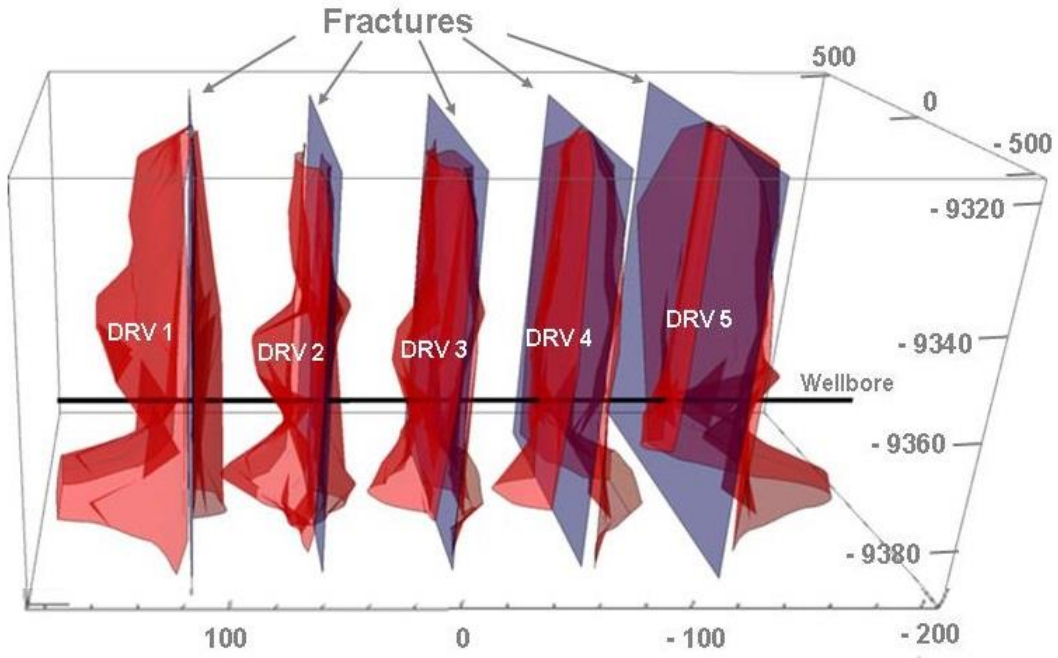

Figure 4-7 Drained Rock Volumes (DRVs) for five clusters for Stage 2. DRVs after 40 years of production are in red shades; idealized fracture planes are in blue. Length scale is in ft.

4.3.3. Fracture interference

Above we demonstrated our discretization method on a single stage case (Stage 2). However, the well has 29 active stages and as such flow interference between stages is to be expected. While full intensive modeling of each stage by the discretization method to observe flow visualization is outside the scope of this paper, a simple scenario is modeled to investigate flow interference effects between the toe stages (Fig. 4-8).

From the modeled results for Stages 2 to 9 (Fig. 4-9), the extreme ends of fracture stages appear to have higher velocities, due to less interference with adjacent fractures.

The highest velocities are confined to the near-axial region n of the wellbore, again emphasizing how much of the created fracture length away from the near-wellbore area is unproductive. The pressure plot (Fig. 4-9) suggests a large depletion region, while the time-of-flight contours after 40 years of production show the actual area drained is very small when compared to the areas that show marked pressure changes. Actual areas drained are much smaller than inferred from pressure contour plots, which concurs with previous work (Weijermars et al., 2017b).

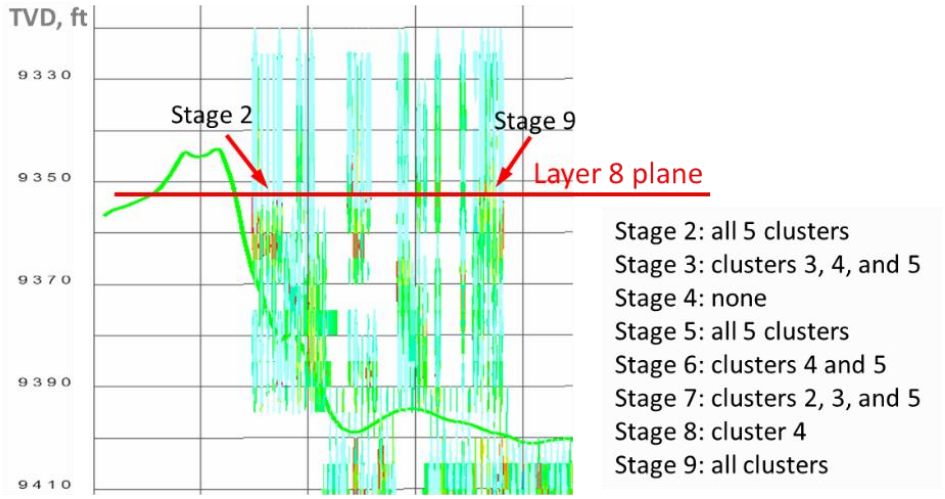

Figure 4-8 Side view of well, showing Stages 2 to 9 crossed by the Layer 8 flow plane (Fig. 4-9). The slope of the well is negligible and appears steep due to horizontal length being compressed by a factor of 30.

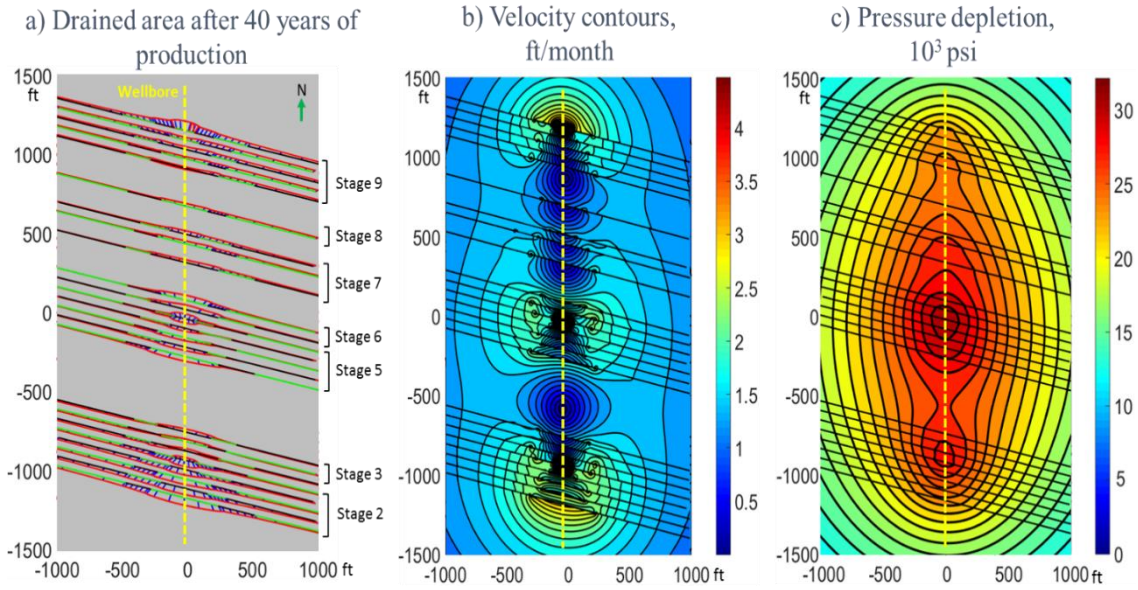

Figure 4-9 Top view for Stages 2 to 9 crossed by Layer 8. Drained area is shown after 40 years of production; Velocity contours and Pressure depletion are shown after one month of production.

4.4. Discussion

The methodology used in this chapter allowed us to model flow near to the fractured wells at high resolution and was used to generate flow velocity field solutions, pressure depletion plots and visualize the Drained Rock Volume (DRV) near to the fractures. The method allocates flow of individual fractures using fracture properties determined by a planar-3D fracturing simulation, which takes into account stress shadowing on the fracture propagation and also rock permeability enhancement. The results reinforce the notion that pressure plots are poor proxies for the DRV, because the drained volume remains very limited (and much smaller than suggested by the pressure plots) even after 40 years of production.

4.5. Conclusions

A critical insight gathered from our modeling is the unevenness in the drainage volumes around each hydraulic fracture in Stage 2 (Fig. 4-7). The lower layers (13, 14, and 15) of the fractures have the highest drained regions and correspondingly also the highest fracture conductivities, which may be a direct result of proppant settling, as while pumping, more proppant settles into the lower layers creating higher proppant placement and thus higher conductivity nearer to the base of the fractures. From the estimated DRV, we seek to provide a schedule for refracturing that targets undrained regions to improve the overall recovery of the wells. Further recommendations are summarized below:

1) Based on results of the fracture propagation and CAM models, a significant section of the distal fracture length has hydraulic conductivity so low that no significant contribution is made to the DRV.
2) The outer fractures of modeled Stage 2 have the highest hydraulic conductivity and therefore greater DRVs.
3) However, all DRVs remain quite narrow when visualized using the time of flight contours.

5. IMPACT OF NATURAL FRACTURES ON THE SHAPE AND LOCATION OF DRAINED ROCK VOLUMES IN UNCONVENTIONAL RESERVOIRS: CASE STUDIES FROM THE PERMIAN BASIN*

5.1. Introduction

5.1.1. Brief highlights

In this chapter, the previous methods are combined and applied to additional wells from the Permian Basin. This research has led to the development of a CAM model that is able to accurately determine the impact of natural fracture clusters on the DRV extent. Based on newly devised flow velocity models and the associated DRV plots, I was able to define recovery factors using a new method based on the actual area drained. This has led to newly coined terms for what we have defined as inter-fracture and inter-well recovery factors.

Production data from three Permian Basin wells (two from the Midland Basin and one from the Delaware Basin), are used to study the DRV development around hydraulic fractures with, and without natural fractures. The models use compact CAM algorithms developed to study the impact of natural fractures on fluid flow. The Permian Basin wells used to identify the plausible reservoir properties by history-matching the field production data.

* Part of the data reported in this chapter is reprinted with permission from "Impact of Natural Fractures on the Shape and Location of Drained Rock Volumes in Unconventional Reservoirs: Case Studies from the Permian Basin" by Khanal, A., Nandlal, K., and Weijermars, R. in Proceedings of the 7th Unconventional Resources Technology Conference. Copyright 2019 by American Association of Petroleum Geologists and by Society of Petroleum Engineers.

5.1.2. Motivation of study

Natural fractures, even if non-conductive, may profoundly affect the sweep pattern near vertical hydrocarbon well arrays (Weijermars and van Harmelen, 2018). In shale reservoirs, natural fractures may interact with hydraulic fractures, altering the flow and geomechanical properties by enhancing the fracturing fluid leak-off (Gale et al., 2014; Khoshgahdam et al., 2015, 2016; Pankaj and Li, 2018). Thus, systematic modeling of fluid flow near hydraulic fractures and the interaction with natural fracture networks remains important to better understand the effects of fluid withdrawal patterns on well interference. The impact of natural fracture networks on well performance depends on several factors, such as natural fracture density, conductivity, and connectivity with the hydraulic fractures (Olson 2008; Cipolla et al., 2011; Kang et al., 2011).

Previous modeling methods used to describe the flow through heterogeneous porous media with natural fractures primarily focused on dual porosity models (Warren and Root; 1963; Kazemi et al., 1976), discrete fracture network models (Long et al., 1982; Elsworth, 1986; Andersson and Dverstorp, 1987; Dershowitz and Einstein, 1987) or a combination of DFN and dual porosity models such as embedded discrete fracture network models (Yu et al., 2017a). Several other analytical (Brown et al., 2011; Stalgorova and Mattar, 2013) and semi-analytical methods (Chen and Raghavan, 1997; Valko and Amini, 2007) have been developed to model the flow in multi-fractured horizontal wells, with and without natural fractures.

The CAM tool has been previously applied in fundamental studies of the equivalent tensor concept (Weijermars and Khanal, 2019), and of pressure gradients

during fluid flow in fractured porous media (Khanal and Weijermars, 2019a, b). Additionally, the CAM model can visualize the DRV, by tracing particle paths and time-of-flight contours. Such an approach is particularly useful for studying hydraulically fractured parent and child wells as previously shown in the Eagle Ford shale (Weijermars and Alves, 2018). The inclusion of natural fractures in CAM models (Van Harmelen and Weijermars, 2018; Khanal and Weijermars, 2019a, b, c, d) has revealed that attributes of the fractures may profoundly affect the shape and location of a well's drained rock volume (DRV). More accurate determinations of the DRV shape and location are required to establish the optimal well-spacing design and avoid undue pressure communication among adjoining horizontal wells.

5.1.3. Summary

This work in this chapter investigates the still insufficiently understood complex interaction of natural fracture networks with hydraulic fractures, which impacts the estimation of the drained rock volume (DRV), and fracture spacing for optimal production. Flow in natural fractures is modeled at high resolution using recently developed algorithms, which enable fast, grid-less, Eulerian particle tracking based on Complex Analysis Methods (CAM). Publicly available production data from the Permian Basin were used to visualize the DRV with time-of-flight contours and particle paths, initially assuming a homogeneous reservoir without any natural fractures. Next, the distortion of the DRV, by including natural fractures with different conductivity in the proximity of the hydraulic fractures, is visualized and compared to the homogeneous

reservoir without any natural fractures. The shape and location of the DRV in shale wells will be profoundly impacted by the overall location, density, and hydraulic conductivity (strength) of the natural fractures. High-resolution contour plots of (1) drained rock volume, (2) pressure depletion, and (3) spatial velocity variations are presented to compare the fluid migration paths near hydraulically fractured wells with and without natural fractures. Detailed case studies of several wells completed in Wolfcamp landing zones from the Permian Basin (i.e. Midland Basin and Delaware Basin wells) are included. The impact of the natural fracture networks, which are assumed to occur in clusters at various distances from the hydraulic fractures, on wells with different production characteristics, is modeled. Wells in reservoir sections with numerous natural fractures develop DRV, pressure and fluid velocity patterns that are more complex as compared to wells in reservoir sections without natural fractures. The results highlight that the impact of natural fractures on fluid withdrawal patterns (DRV) needs to be considered to make better completion decisions and optimize fracture spacing in naturally fractured reservoirs

5.2. Reservoir and well data

5.2.1. The Permian Basin

The Permian Basin is a complex sedimentary system located in the foreland of the Marathon–Ouachita orogenic belt covering an area of more than 75,000 square miles and extending across 52 counties in West Texas and Southeast New Mexico (Gardiner, 1990). The basin consists of several sub-basins: the eastern Midland Basin, the Central Basin, and the western Delaware Basin (Fig. 5-1a). The Permian Basin currently is one of the most active shale plays in the US, accounting for over 20% of the total crude oil production and about 9% of the total dry gas production in 2017 (EIA, 2018). Our present study focuses on the Wolfcamp shale, which occurs in both the Midland Basin and the Delaware Basin. The Wolfcamp Formation, a Wolfcampian-age organic-rich shale sequence, extends in the subsurface under all three sub-basins of the Permian Basin. Being the most productive tight oil and shale gas-bearing formation in the Permian Basin, the Wolfcamp Formation is divided into four sections known as the Wolfcamp A, B, C, and D (with A and B being the most widely targeted sections; EIA, 2018). The Wolfcamp Formation in the Midland Basin harnesses an estimated 20 billion bbls of oil, 16 trillion ft^3 of natural gas, and 1.6 billion bbls of natural gas liquid, which consists of undiscovered and technically recoverable resources according to USGS (Gaswirth et al., 2017). The Wolfcamp thickness ranges between 800-7,000 ft in the Delaware Basin, 400-1,600 ft in the Midland Basin, and 200-400 ft in the adjacent Central Basin Platform (EIA, 2018).

The Wolfcamp Formation has a complex lithology consisting mostly of organic-rich shale and argillaceous carbonates. The porosity of the Wolfcamp Formation varies across the individual benches or sections (A-D) from 2% to 12%, with an average of 7% (Blomquist, 2016; Walls et al., 2016; EIA, 2018). The absolute horizontal permeability calculated from core analysis was reported to range between 40 and 1,900 nD. However, an average permeability of 10 mD is also reported in the literature (Blomquist, 2016; EIA, 2018). The TOC ranges from 2% to 8%, indicating the formation is a good source rock (Kvale and Rahman, 2016). Oil production from the Permian Basin has steadily increased from 710 Mbbl/d in 2008, to 2,362 Mbbl/day in 2018 (with only a slight dip to 2,011 Mbbl/day in 2019) (TRRC, 2014). Although the first wells were drilled in the Permian Basin as early as 1920, the rapid increase in production from 2008 to 2019 can be wholly attributed to horizontal wells with hydraulic fracturing.

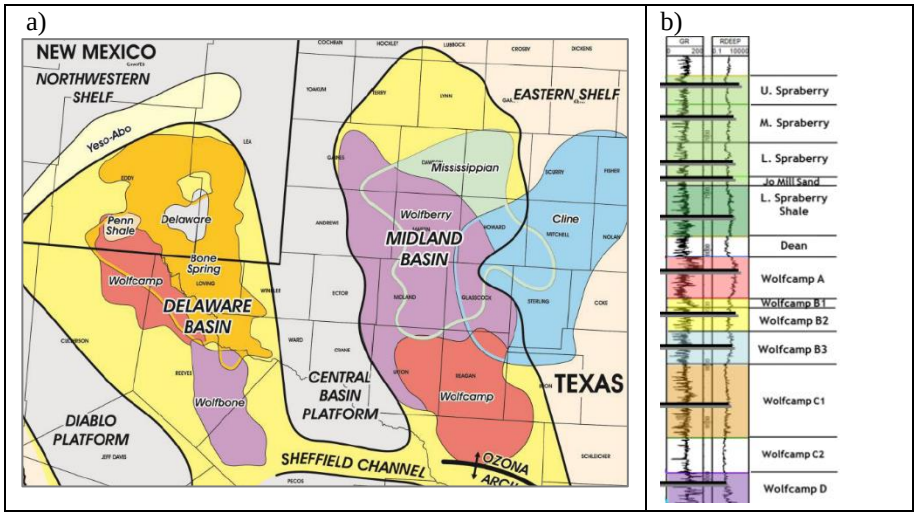

Figure 5-1 a) Permian Basin showing the Delaware Basin, the Central Basin and the Midland Basin (USGS). b) Stratigraphic units and drilling targets in the Midland Basin (adapted from Parsegov et al., 2018a).

5.2.2. Issue of high water cut

Various of the Midland Basin wells considered for this study (Neal 344H, 345H and 346AH, for which a fracture treatment description was given in Zakhour et al., 2015) showed extremely high water-cut throughout the available production history. Appendix C shows the water and gas production history for Neal 346AH, and other wells analyzed. At the end of 53 months, Neal 346AH produced approximately 500 Mbbl of water and 75 Mbbl of oil, with an average water cut of 87% and average water to oil ratio (WOR) of 5.6. The average WOR for wells in the Midland Basin has been previously reported to be around 2.6-2.8 based on regional production data from 2005-2015 (Scanlon et al., 2017). The WOR in the Delaware Basin was reported to be higher than that for the Midland Basin by a factor of 1.5-1.7 (based on 2015 data; Scanlon et al., 2017). The production data till the first month of 2019, for close to 10,000 horizontal wells were obtained from Drillinginfo to calculate the average WOR for wells in the Midland Basin and Delaware Basin. The histograms of WOR distributions for wells in the Midland and Delaware Basin are compiled in Figs. 5-2a and b, respectively. The average WOR was 3.6 (Fig. 5-2a) and 4.4 (Fig. 5-2b), respectively.

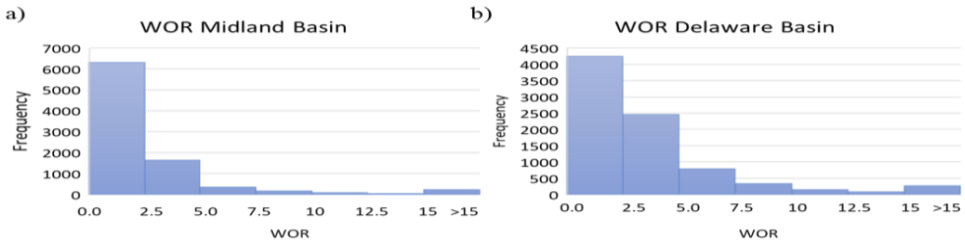

Figure 5-2 WOR calculated based on public production data from numerous wells in several completion zones. a) Midland Basin b) Delaware Basin.

5.2.3. Well characteristics and field data

For our analysis, we use one of the three stacked horizontal wells drilled in Wolfcamp shale-oil play drilled in a chevron pattern (Fig. 5-3a). Two of the wells, Neal 344H and 345H, were drilled in the Wolfcamp B, whereas Neal 346AH was landed in the Wolfcamp A. The horizontal spacing between the Wolfcamp B wells (Neal 344H and 345H) is about 500 ft (Figs. 5-3a, b). The oblique distance between the horizontal laterals in the Wolfcamp A and Wolfcamp B is approximately 350 ft. A schematic of the well trajectory for Neal 346H in a vertical cross-section is shown in Fig 5-3c. The TVDs for Neal 344H, 345H, 346AH are 8,835 ft, 8,779 ft, and 8,557 ft, respectively. Each of the wells was completed towards the beginning of 2014, and monthly production data is available for about 5 years. The historic production data show that only Neal 346AH produced any discernible volume of oil after the first year. Neal 344H and 345H produced some oil during the first year of operation, but then switched to almost exclusively produce water and gas.

The fracture treatments for all wells considered in this study were largely similar, with identical pump schedules, using slickwater fluid with 100 mesh sand and 40/70 white sand. Each well had an average propped fracture height of 220 ft (Zakhour et al., 2015). Wells 344H and 345H were completed with five clusters per stage, and 30 stages with a cluster spacing of 50 ft. Neal 346AH had a slightly different completion with 26 stages and 4 clusters per stage with a spacing of 60 ft. The completed well lengths for Neal 344H, 345H, and 346AH were 7,528 ft, 7,562 ft, and 6,524 ft respectively. Additional completion details and geomechanical properties for Neal 344H, 345H, and

346AH are given in Zakhour et al. (2015). A fourth well studied in this chapter, Neal 322H, is assumed to have been landed in the Wolfcamp B (based on the TVD). The well trajectory of Neal 322H runs opposite to the direction of Neal 344H, 345H, and 346AH (antiparallel). The shortest distance between Neal 346AH and 322H is 3,400 ft. For this study, the completion, geomechanical and reservoir properties for Neal 322H were assumed to be identical to those of Neal 346AH.

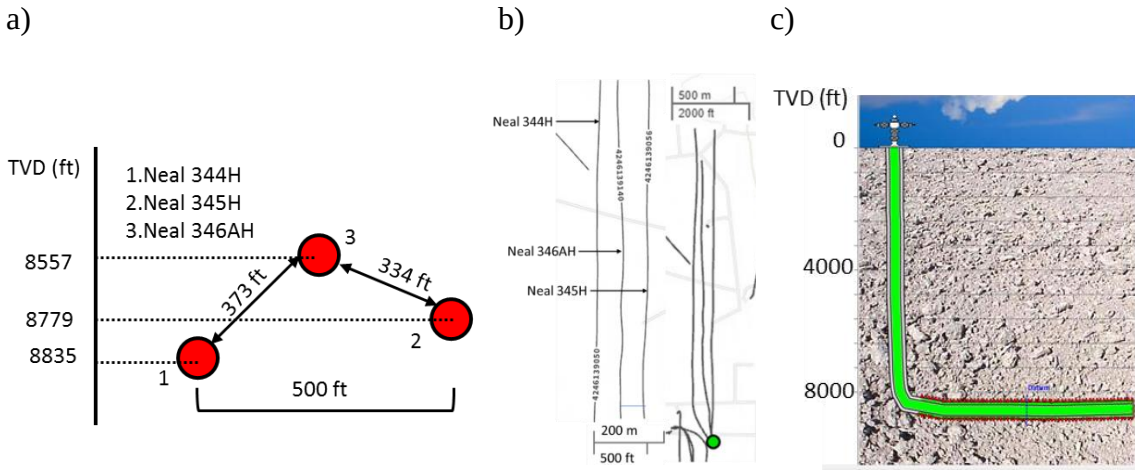

Figure 5-3 a) Gunbarrel view (looking north) of three Wolfcamp production wells (Neal 344H, 345H, and 346AH). b) Map view of the wells showing the well spacing. c) Lateral view of Neal 346AH.

5.2.4. Production forecasting using decline curve analysis (DCA) history matching

In this study, the fluid rates in the CAM model are allocated to individual stages and fractures based on the production rate of the well over the course of its productive life. The flow rate of the well at each time-step is first constrained by applying decline curve analysis (DCA). Reservoir properties and completion attributes (fracture half-

lengths etc.) are subsequently estimated by history matching with a numerical reservoir simulator.

The production decline method proposed by arshadi (1945) is the most widely used procedure in the industry to forecast the EUR for both oil and gas reservoirs. The relationship used for the Arps hyperbolic decline model is:

$$q = q_i \frac{1}{\left(1 + bD_i t\right)^{\frac{1}{b}}} \tag{5-1}$$

Where q is the production rate at time t, q_i is the initial production rate, b is the hyperbolic decline parameter ($0<b<1$, or $b>1$) and D_i is the initial decline rate defined as follows:

$$D_i = -\frac{dq}{dt} \times \frac{1}{q} \tag{5-2}$$

Unconventional reservoirs with low permeability are unique in that b-values greater than 1 can be used to obtain the best fit for historic production data. However, such b-values can result in over-prediction of the EUR when used to forecast longer periods (such as 30 years). Robertson (1988) suggested that hyperbolic decline should be converted to exponential decline at a predetermined decline rate to constrain the possibility of unrealistically high production forecast. Over the years, several other DCA methods have been suggested such as multi-segmented/hybrid approaches, where each flow regime is forecasted by different decline curves (Khanal et al., 2015a, 2015b; Khoshghadam et al., 2017). The latter methods require the identification of the proper flow regimes and other involved processes, which is outside the scope of the current

study. For this reason, we use the Duong model (Duong, 2011), which was specifically developed for unconventional reservoirs with ultra-low permeability. The Duong DCA model is appropriate for wells exhibiting long-term linear transient flow which leads to a more conservative and realistic estimate of the EUR as compared to Arps decline with b>1. The DCA equations for the Duong model are:

$$q = q_i t_m + q_\infty \tag{5-3}$$

$$t_m = t^{-m} exp\left(\frac{a}{1-m}\left(t^{1-m} - 1\right)\right) \tag{5-4}$$

$$N_p = \left(\frac{1}{a}\right) t^m q \tag{5-5}$$

where q is the production rate at time t, q_i is the initial rate, a and m are empirical constants, t_m is "modified" time, N_p is cumulative production and q_∞ is the intercept of a plot of q vs. t_m. Figs. 5-4a and 5-4b show the Arps history match and Duong history match, respectively, for well Neal 346AH. For this study, 57 months of monthly production data was available for the well Neal 346AH. The first three months of data were discarded due to negligible production. The Duong parameters generated by DCA matching the field data were used for the CAM model of the DRV for 30 years.

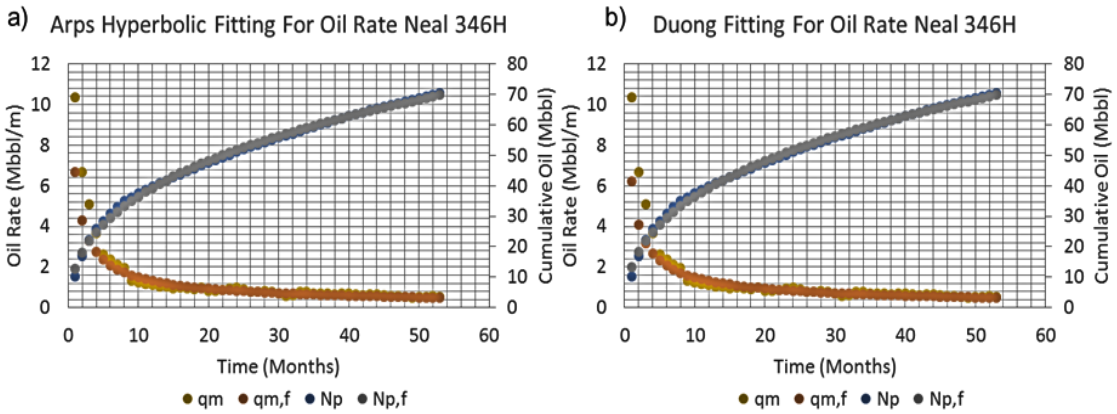

Figure 5-4 DCA history matching the production data of Neal 346AH. a) Arps decline fitting, with DCA parameters for best curve fit: q_i = 41379 bbl/month, D_i = 115/y, and b =1.5. b) Duong decline fitting with DCA parameters for best curve fit: q_i = 6195 bbl/ month, a =0.46 / month, m = 1.05, q_∞ = 0.

5.2.5. Determination of reservoir properties

A commercial reservoir simulator was used to constrain the combination of matrix permeability, porosity and fracture half-length (Table 5-1), which results in a close match to the production history for Neal 346AH. Most of the completion parameters were reported by the operator (Zakhour et al., 2015), except for the hydraulic fracture half-length, which is here assumed to be around 220 ft (based on the fracture height). The reservoir porosity is assumed to be 7% based on the average values reported in the literature (Blomquist 2016; EIA, 2018). Different values of reservoir permeability are reported in the literature from as low as 10 mD (Blomquist 2016; EIA 2018) to 40-1,900 nD based on core analysis (Walls et al. 2016) and 20-200 nD (Gas Research Institute (GRI) permeability; Parsegov et al., 2018b). Based on these values, we assumed an initial reservoir permeability of 500 nD. The Wolfcamp Formation in Upton County has an estimated effective pore pressure gradient, based on diagnostic fracture injection

tests (DFIT), of around 0.6 psi/ft (Loughry et al., 2015; Rittenhouse et al., 2016; Wang and Weijermars, 2019). Based on the TVD of 8,557 ft, the initial reservoir pressure is assumed to be 5,134 psia. The geothermal gradient in the Permian Basin is reported to be 1-1.5 °F/100 ft (Ruppel et al. 2005).

For this study, the mean value of 1.25°F/100 ft was used to calculate the initial reservoir temperature of around 110 °F. The oil API is reported to be around 46.8° (Drillinginfo), which corresponds to very light oil. The oil viscosity is around 0.5 cP for the assumed flowing bottomhole pressure of 1,000 psia, based on the live oil viscosity correlations from Beggs and Robinson (1975). Although Neal 34AH produces water and gas, we make no attempt to history match all phases due to the absence of any detailed fluid property information required for inferring reliable relative permeability curves. The principal goal of this study is to analyze the DRV, with and without natural fractures, by assuming a 2D single phase flow. The water production in our study is scaled by including the WOR during the allocation of the flux to individual hydraulic fractures. The best history matching result is shown in Fig. 5-5, and the final properties used to generate the match are summarized in Table 5-1.

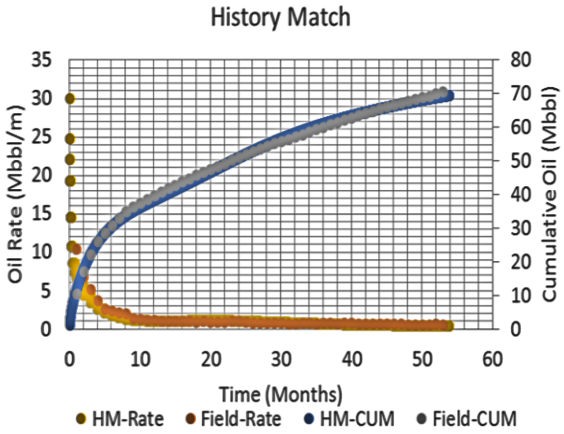

Figure 5-5**:** Comparison of historic production data for Neal 346AH history-matched by DCA curves (Field-Rate and Field-CUM) and by a physics-based reservoir model (CMG). Matches are excellent for both oil production rate (Mbbl/ month), and cumulative oil (Mbbl).

Table 5-1 Reservoir properties obtained from history match for Neal 346AH.

Parameters	**Values**	**Units**
TVD	8557	ft
Well Length	6524	ft
Number of Fractures	109	
Fracture Stages (no.)	26	
Fracture Width	0.01	ft
Fracture Spacing	60	ft
Fracture Height	220	ft
Fracture Half-length	105	ft
Fracture Permeability	6000	mD
Initial Reservoir Pressure	5,161	psia
Reservoir Temperature	110	°F
Total Compressibility	$3x10^{-6}$	psi^{-1}
Permeability	100	nD
Porosity	4.2	%
Initial Oil Saturation (1/WOR)	0.15	
Residual oil and/or water	0.25	
Oil API	46.8	°API

The pressure depletion in the Wolfcamp production zone along the full length of the Neal 346AH lateral can be predicted by the history-matched CMG model (based on the best fit parameters of Table 5-1). Figs. 5-6a-f shows the progressive drop in reservoir

pressure due to an imposed BHP of 1000 psi and an initial reservoir pressure of 5,161 psi for various production times up to the estimated end of the well life of 30 years. Figs.5-6a-f can be compared to the DRV obtained from particle tracking (Section 5.3). After 30 years, the pressure depletion front has advanced to almost 600 ft away from the horizontal wellbore.

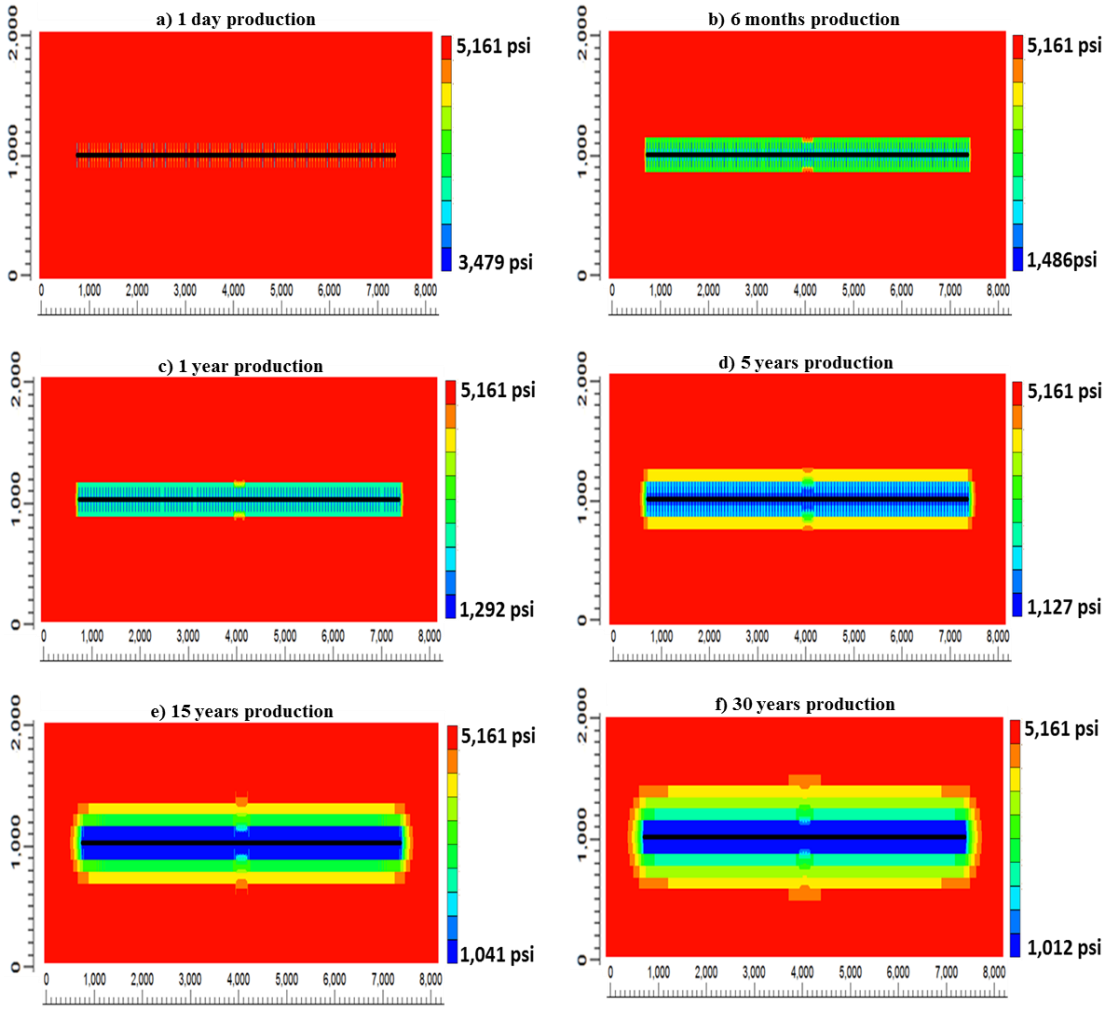

Figure 5-6 Numerical simulation of pressure depletion for the Neal 346AH production well (Wolfcamp, Midland Basin). a-f) Pressure field at various production times: 1 day, 6 months, 1 year, 5 years, 10 years and 30 years.

5.3. Application of CAM to determine DRV

We assume homogeneous reservoir properties and a reservoir with a large lateral extent, such that the reservoir can be assumed to be infinite-acting, without any lateral flow boundaries and fluid flow stays confined between the upper and lower boundary of the pay zone. The fluid is assumed to be incompressible, immiscible and isothermal with constant viscosity and density, and stays in single phase flow without any relative permeability effects. Other forces, such as gravitational effects and capillary pressure, are assumed negligible.

A major advantage of CAM models is the grid-less nature which enables the computation of the drained rock volume (DRV) with an infinite resolution, which is faster and more practical than with discrete numerical methods. The flow of fluid in porous media is depicted by particle paths and time of flight contours. In addition to this, CAM allows for an instantaneous computation of the fluid velocity at any point in the reservoir. The hydraulic fractures are modeled by a communicating array of interval sources (line sources) in CAM formulation (Weijermars et al., 2017a,b; 2018), whereas the natural fractures (shown later in the study) are modeled by an infinite array of line doublets (so-called areal doublets) (Van Harmelen and Weijermars, 2018; Khanal and Weijermars, 2019c). The flux (strength) of each of the line-sources is calculated based on the fluid flux allocated to each of the fractures using history matched production data. The so-called flow reversal principal is applied, where the produced fluid is injected back into the reservoir via the hydraulic fractures, based on the dimensions of each hydraulic fracture. The flux of each hydraulic fracture, scaled by production allocation

based on fracture dimensions, diminishes with time analogous to the history matched production rate

5.3.1. Determination of DRV for Neal 346AH (Midland Basin)

Figs. 5-7 a-c show the particle paths for each of the 26 fracture stages represented by single hydraulic fractures of 105 ft half-length, which are modeled in CAM formulation by a communicating array of line sources. The particle paths (blue lines) show the drained fluid and outline the region occupied by the final DRV after 30 years of production. The central three stages (Fig. 5-7b), show that only a limited rock volume is drained after the 30-year production period. The infinite resolution offered by CAM can be used to calculate the exact extent of the fluid volume that contributes to the DRV in the reservoir (Fig. 5-7b). The time of flight contours (TOFC) show the incremental growth of the DRV for each 3-year period (Fig. 5-7c) and that the DRV growth declines rapidly. Even after 30-year long production period undrained regions remain between the hydraulic fractures, which indicate the need to either re-stimulate the existing fractures or create new infill fractures after the first few years of production.

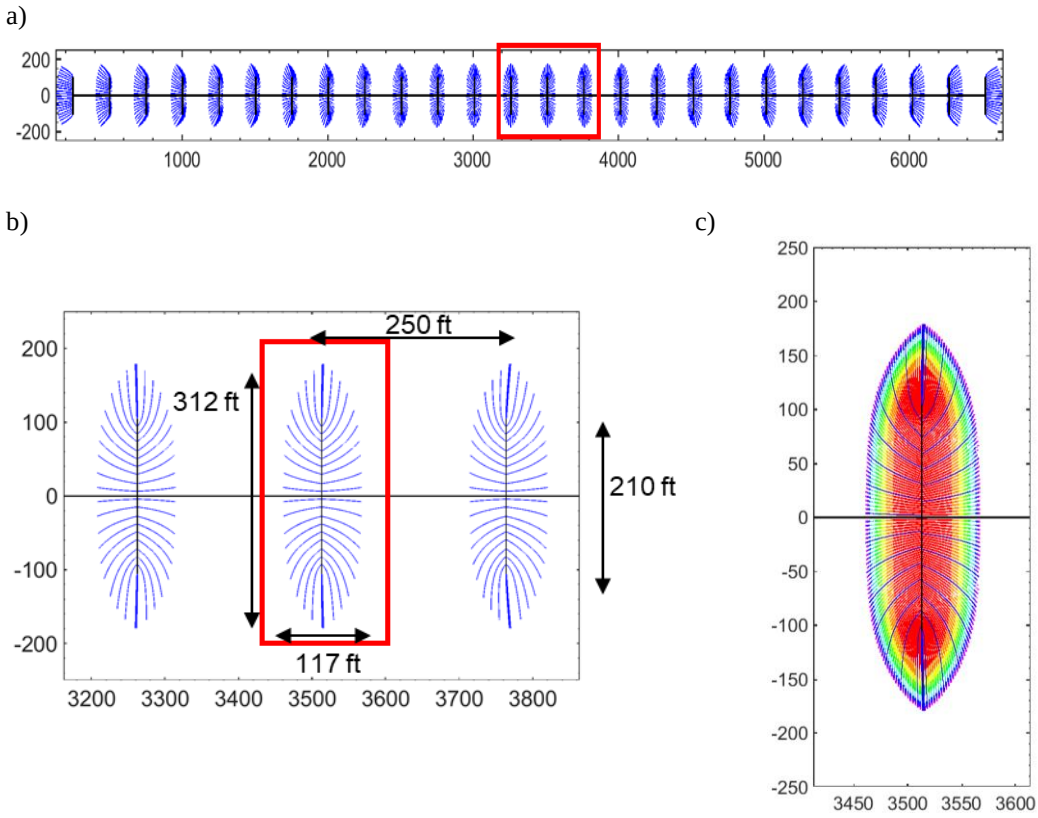

Figure 5-7 CAM model of fluid withdrawal patterns (oil and water, accounting for 25% residual oil and water) near the hydraulic fractures in Neal 346AH, a Wolfcamp A well, Upton County, Midland Basin. a) Particle paths (blue) toward 26-line stages represented as single hydraulic fractures. The actual fracture stages each comprise four perf clusters. Hydraulic fracture stages are spaced at 250 ft, and each hydraulic fracture has a half-length of 105 ft. b) Enlarged view of the three central stages, showing the particle paths and the final DRV outline after 30 years of production. c) DRV outlined by TOFCs (rainbow colors) around the central fracture stage. Each color band represents the DRV growth for 3-year production increments. All dimensions are true to scale.

In Fig. 5-7, the DRV for Neal 346AH was calculated by including the produced water in the flux allocation, scaled by the average WOR. The well has produced significant amounts of water (WOR of 5.7), as shown by the water production data in Appendix C. If water production for this well would be ignored, the DRV would be

proportionally smaller (Fig. 5-8a). The TOFC for each of the 3-year periods show that the DRV remains small, even after a 30 year well life (Fig. 5-8b).

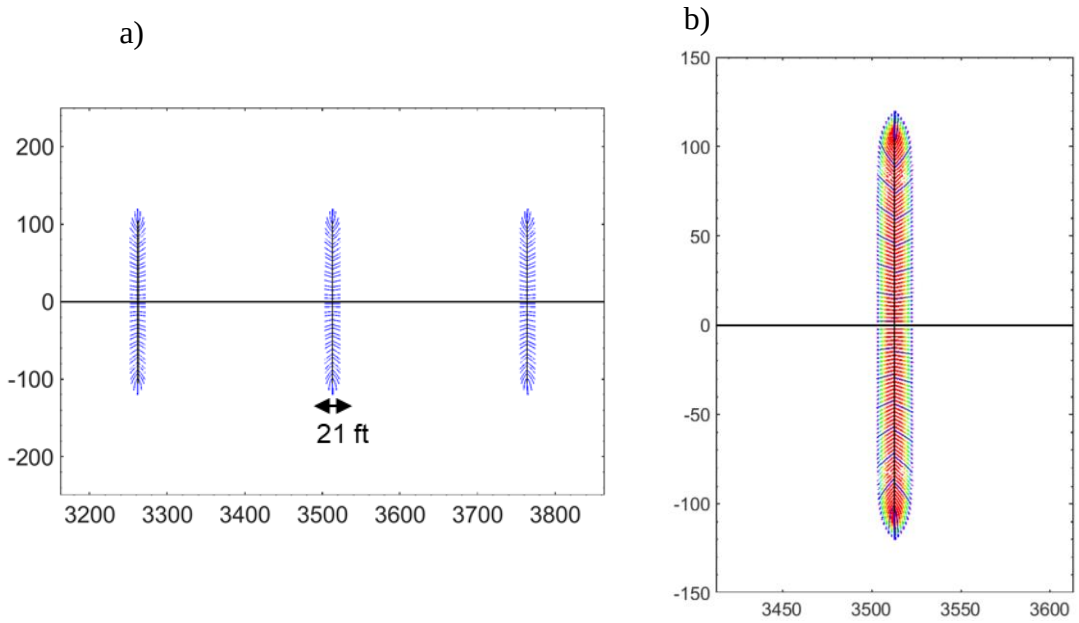

Figure 5-8 CAM model of fluid withdrawal patterns (oil only, assuming 25% residual oil) near the hydraulic fractures in Neal 346AH, Midland Basin. a) Enlarged view of the DRV near the three central stages. The particle paths and the DRV after 30 years of production (excluding water production). b) DRV as marked by TOFC (rainbow colors) around the central fracture stage. Each color band represents the DRV growth for 3-year periods. All dimensions are true to scale.

5.3.2. Determination of DRV for Neal 322H (Midland Basin) and for Autobahn 34-117 1H (Delaware Basin)

Next, we analyze the production data from two wells with a comparatively lower water cut (low WOR) from respectively the Midland and Delaware Basins.

5.3.2.1. Midland Basin

Neal 322H was landed in the Wolfcamp B, Spraberry Field, Upton County, Midland Basin. The well depth (TVD) is 8,776 ft (Wolfcamp B) with a lateral length of 7,924 ft. Six years of production data are available for water, oil, and gas, starting from the end of 2013. The cumulative water production of the well at the end of six years of production is 70 Mbbl compared to 820 Mbbl of oil, which corresponds to the WOR of 0.08 and water cut of just 8% (water production data shown in Appendix C). The reservoir properties for Neal 322H were assumed to be the same as for Neal 346AH, because the wells are located fairly close to each other (3,400 ft), and were completed in the same formation (Wolfcamp) by the same operator in the same year (2014). The stage spacing of 250 ft for Neal 322H is assumed the same as for Neal 346AH.

5.3.2.2. Delaware Basin

Autobahn 34-117 1H is located in the Ward County at a TVD of 11,899 ft (lower region of the Wolfcamp A) and has a lateral length of 4,235 ft. Despite its relatively short lateral, Autobahn 34-117 1H is an excellent oil producer during the first five years. The initial cumulative oil production from the well is just over 1 million bbl at the end of

six years. The WOR for the well is 0.1 with the cumulative water production of 140 Mbbl at the end of its 2018 production history (shown in Appendix C). Delaware Basin Wolfcamp, which is deeper, is thermally more mature than the Midland Basin Wolfcamp (EIA, 2018). As a result of higher thermal maturity, the Delaware Basin Wolfcamp has numerous nanopores and has higher pressure compared to the Midland Basin Wolfcamp. The Delaware Basin also has higher TOC values compared to the Midland Basin (CITI, 2018). Despite these differences, the wells in both Basins are completed in a similar fashion (CITI, 2018). The wells completed in the Delaware Basin in 2016 and 2017 had a stage spacing of 200 ft with a cluster spacing of 33 ft (CITI, 2018). However, at the time frame when Autobahn was completed (end of 2013), the wells were still completed with a stage spacing of 240-260 ft and a cluster spacing of 50-65 ft (CITI, 2018), which is why we assume the completion properties for Autobahn to be same as that of Neal 322H and 346AH (250 ft stage spacing). The completion data for all the wells analyzed in detail in this study are summarized in Table 5-2.

Table 5-2 Completion data for Midland Basin and Delaware Basin wells used.

Parameter	Neal 322H	Neal 346AH	Autobahn 34-117 1H
Basin	Midland	Midland	Delaware
Formation	Wolfcamp B	Wolfcamp A	Wolfcamp A
TVD (ft)	8,776	8,557	11,899
Well length(ft)	6,524	7,924	4,235
Stage spacing (ft)	250	250	250
Cluster spacing (ft)	50	60	50
Number of Stages	26	32	17
Number of clusters/stages	5	4	5

The production data for Neal 322H and Autobahn 34-117 1H are DCA matched with Arps hyperbolic decline curves (Figs. 5-9a, b). The initial 12 months of production data were not used in the history match for either of the wells, due to noise in the production data. The production data for Neal 322H show that the oil rate declines rapidly after the first 18 months from 50 Mbbl/month to 10 Mbbl/month (Fig. 5-9a). However, the total EUR after 30 years of well life is about 800 Mbbl. Autobahn 34-117 1H shows a relatively flat decline which results in a higher EUR of about 1 million bbl at the end of the forecasting period (Fig. 5-9b).

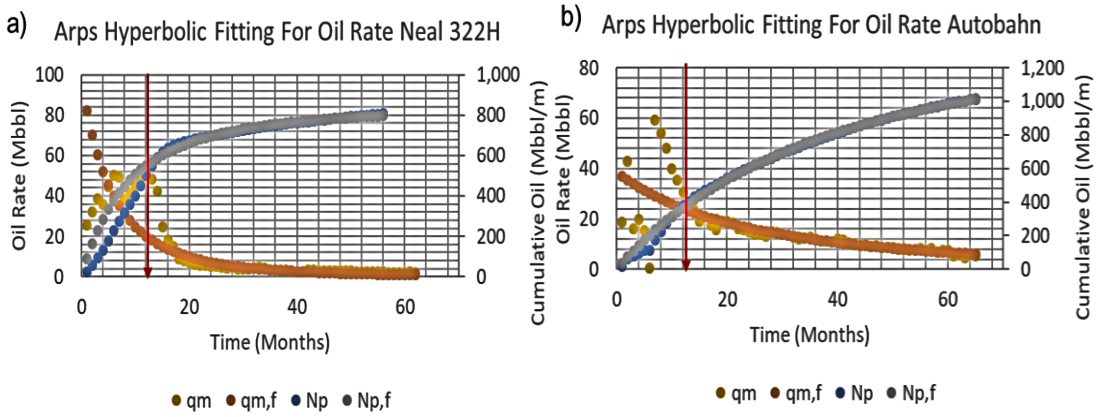

Figure 5-9 a) Arps decline fitting for the production data for Neal-322H (Midland Basin), with DCA parameters for best curve fit: q_i = 96,781 bbl/month, D_i = 2.04/y, and b =0.33. b) Arps decline fitting for the production data from Autobahn 34-117 1H (Delaware Basin), with DCA parameters for best curve fit: q_i = 38,350 bbl/month, D_i = 0.51/y, and b =0.41. For both wells, only the production data after the first 12 months (shown by the red arrows) was used for the history match.

5.3.2.3. DRV for Neal 322H (Midland Basin)

The CAM model was used to visualize the DRV for the well after 30 years of production (Fig. 5-10a-c). The particle paths are represented by blue lines (Fig. 5-10a, b), whereas the TOFC for 3-year periods are represented by the rainbow colors (Fig. 5-10c). Fig. 5-10b shows the extent of DRV after 30 years of production. Compared to Neal 346AH (Fig. 5-7a-c), fluid in Neal 322H is drained further away from the hydraulic fracture tips (345 ft vs 312 ft). However, the width of the drainage region for Neal 322H is narrower than for Neal 346AH (97.5 ft vs 117 ft). The EUR calculated by summing the individual DRVs of each fracture stage will be higher for Neal 322H, which has six more fracture stages than Neal 346AH. Fig. 5-10c shows that the increase in DRV is negligible after the first three years of production due to the rapid decline of the well rate. The DRV development shown in Figs. 5-10a-c for Neal 322H, with the WOR of less than 0.1, mostly reflects the cumulative oil production. A residual oil factor of 25% was assumed to remain in place in the DRV region.

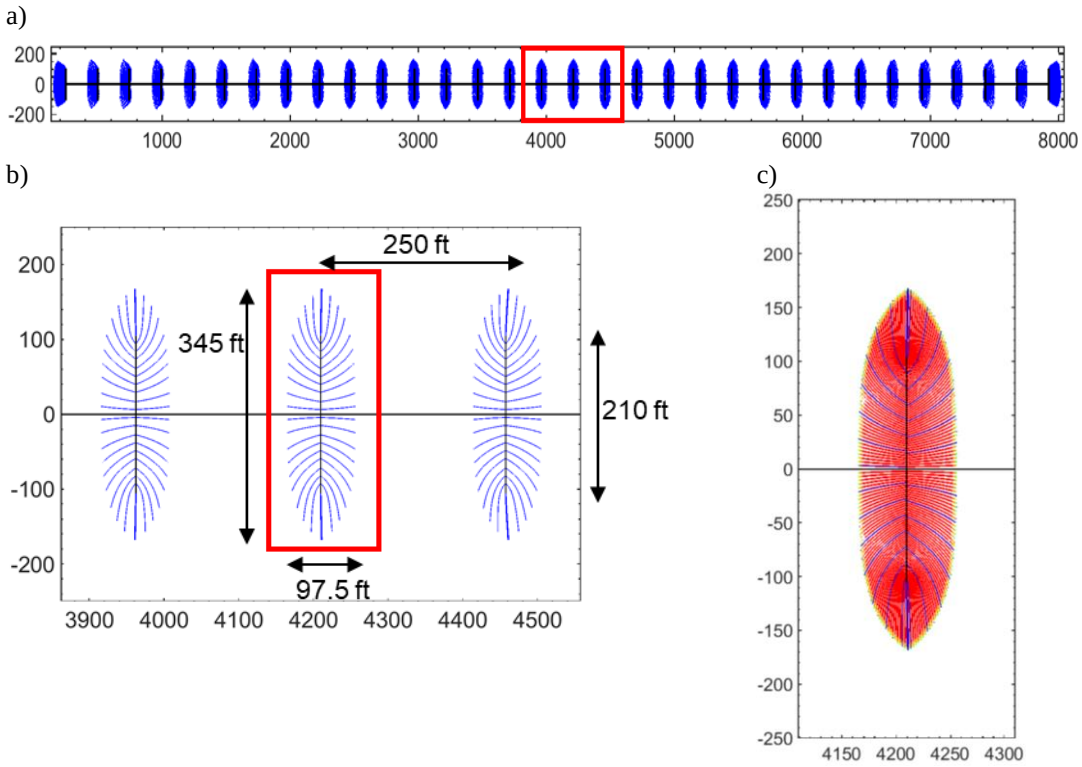

Figure 5-10 CAM model of fluid withdrawal patterns for Neal 322H (Midland Basin), which has 32 fracture stages based on the stage spacing of 250 ft and well length of 7924 ft. a) Particle paths (blue), b) Enlarged view of the three central stages, showing the final DRV drained by particle paths after 30 years of production. **c)** DRV outlined by TOFCs (rainbow colors); each color band represents 3-year production increments. All dimensions are true to scale.

5.3.2.4. DRV for Autobahn 34-117 1H (Delaware Basin)

The inputs from the DCA generated in Fig. 5-9b for the Autobahn well in the Delaware Basin were used in the CAM model to determine the DRV after 30 years of production. The extent of the particle paths in Fig. 5-11a, b shows that Autobahn has a significantly larger DRV as compared to the wells in the Midland Basin (Neal 322H and 346AH). The DRV measured from the tips of the hydraulic fractures reaches approximately twice as far in Autobahn (Figs. 5-11a-c) as compared to the Midland

Basin wells (Figs.5- 7a-c, 5-9a-c). The higher cumulative production of Autobahn 34-117 1H is due to a high well rate with production allocation to a fewer number of hydraulic fractures. Unlike Neal 322H, the decline in Autobahn 34-117-1H is not as drastic, and a significant increase in DRV is observed even in the final years of the 30 years production period (compare the TOFCs of Figs. 5-10c and 5-11c).

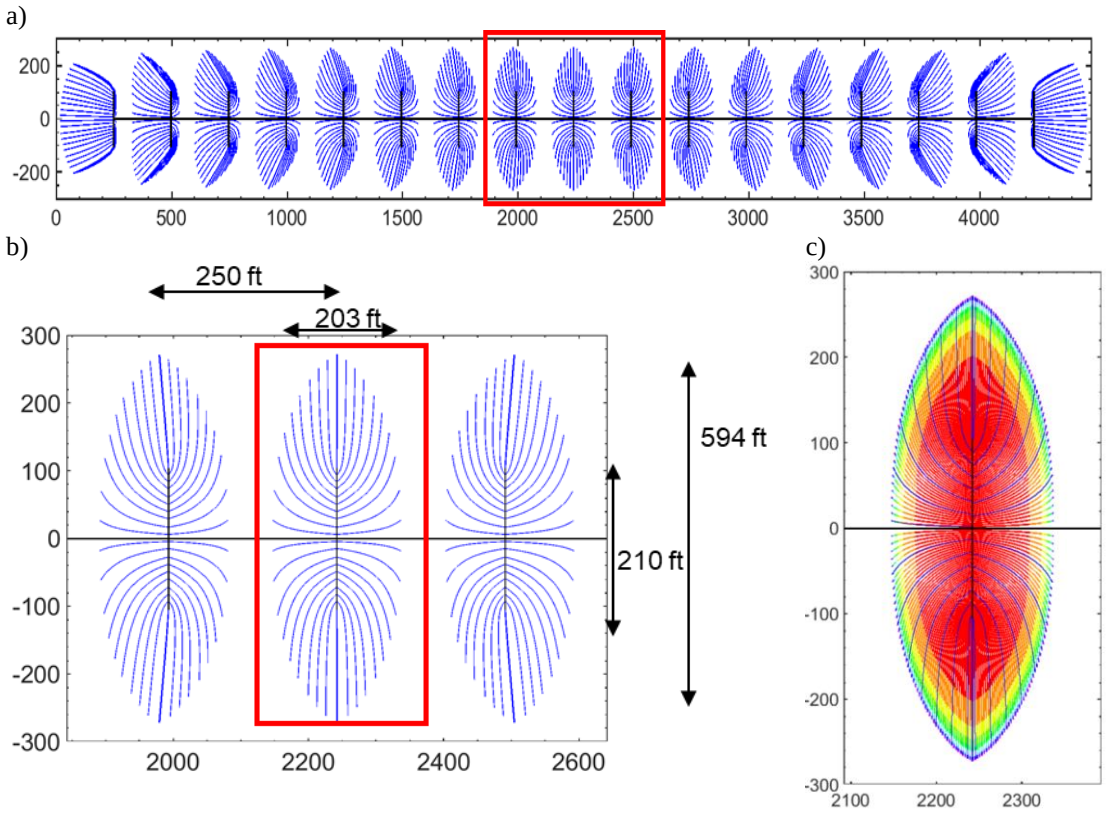

Figure 5-11 CAM model of fluid withdrawal patterns for Autobahn 34-117 1H (Delaware Basin), which has 17 fracture stages based on the stage spacing of 250 ft and well length of 4235 ft. a) Particle paths (blue), b) Enlarged view of the three central stages, showing the final DRV drained by particle paths after 30 years of production. **c)** DRV outlined by TOFCs (rainbow colors); each color band represents 3-year production increments. All dimensions are true to scale.

5.4. Impact of natural fractures on DRV

In this section, we introduce heterogeneity in the reservoir by adding two random clusters of natural fractures on either side of the central hydraulic fractures. We rank the wells in this section into two classes: wells with moderate DRV around their hydraulic fractures (Neal 322H and Neal 346AH, Midland Basin), and a well with a larger DRV around its hydraulic fractures (Autobahn 34-117 1H, Delaware Basin). The two Midland Basin wells are similar in terms of DRV (Figs. 5-7a-c, 5-10a-c); hence only one of the two Midland Wells (Neal 346AH) is further analyzed below. The properties of natural fractures in an unconventional reservoir are highly uncertain and extremely difficult to characterize. Although tests are available to characterize natural fractures in the field and laboratory (e.g., identification of closure stress, porosity reduction due to compaction, hardness test, and several others), the results can be uncertain as they are affected by other reservoir properties in a non-unique fashion (Olson, 1997).

Thus, in the present study, the natural fracture properties used in our models are stochastically generated, as follows. The width (aperture) of the individual natural fractures varies between 0.1 and 0.5 ft, length between 8 and 20 ft. The flux (strength) of the natural fractures is indexed to the flux of the hydraulic fractures and randomly assigned to vary between 0.02 and 1 [ft^4.$month^{-1}$].The strength dimension of the natural fractures is a measure of the permeability contrast with the matrix (for details see Weijermars and Khanal, 2019). Thus, the flow through the natural fractures wanes with time, as the flow toward the hydraulic fractures declines. Other properties are summarized in Table 5-3.

Table 5-3 Parameters for the randomly generated natural fracture clusters used in the DRV sensitivity study.

Parameter	Symbol	Value	Unit
Reservoir height	*h*	220	
Number of natural fractures		10	per cluster
Number of clusters		2	
Natural fracture length	*L*	8-20	ft
Natural fracture width	*W*	0.1-0.05	ft
Natural fracture angle	*γ*	-π/2 to π/2	Radians
Reservoir porosity	*n*	4.2	%
Strength of natural fractures (*)	*υ*	0.02-1(*)	$ft^4.month^{-1}$

(*) Strength of natural fractures is indexed by hydraulic fracture strength

5.4.1. Natural fractures close to the hydraulic fractures with moderate DRV (Neal 346AH, Midland Basin)

In this section, the effect of short natural fractures, located close to the hydraulic fractures, is analyzed. The fluid flux is allocated to the hydraulic fractures based on the production history of Neal 346AH. The flux of the natural fractures is stochastically varied as a sensitivity analysis parameter. Each cluster of natural fractures is placed about 23 ft away from the central hydraulic fracture (at 3,513 ft). Since the maximum length of the natural fractures was constrained to 20 ft, none of the fractures is directly connected to the hydraulic fractures.

Figs. 5-12a and b show the effect on the DRV shape and location of two randomly generated natural fracture clusters located at either side of the hydraulic fractures. After 30 years of production, the particle paths and TOFC patterns become highly distorted due to the presence of the natural fractures. Compared to the cases without natural fractures (Figs. 5-7a-c), the DRV patterns change shape and the DRV location shifts from the original location to a new location. One may conclude that

natural fractures facilitate production from a different region of the matrix. Results from Fig. 5-12 also show that the effect of natural fractures is highly localized, and the maximum impact of the natural fractures on the fluid withdrawal paths is seen mostly in close vicinity of the natural fractures. In our study, the DRVs in both the homogenous reservoir (Fig. 5-7) and the heterogeneous reservoir (Fig. 5-12) remain equal due to scaling of the flux by the history matched well rate. The natural fractures are relatively short and placed close to the hydraulic fractures, resulting in only minor distortions of the DRV. The natural fractures do not show any direct interference with the flow in the adjacent hydraulic fracture stages.

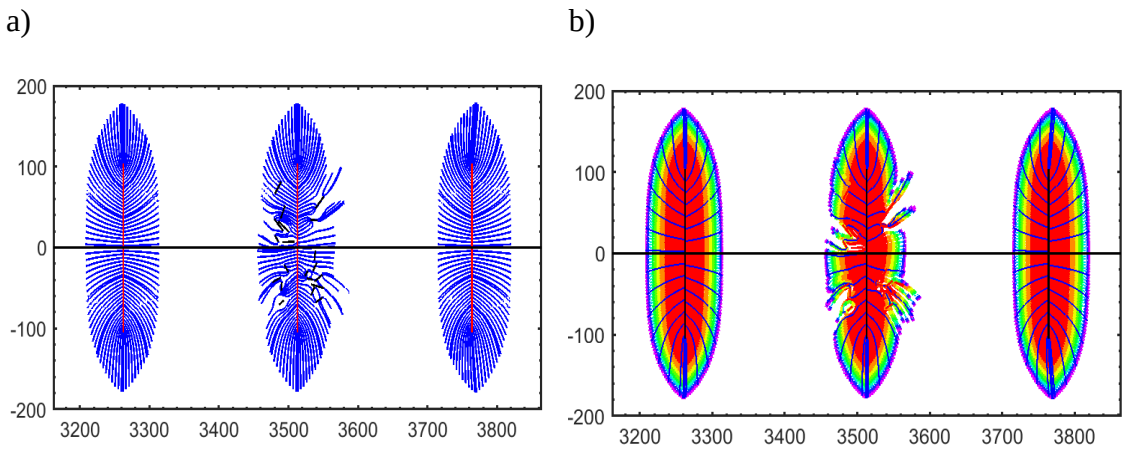

Figure 5-12 CAM model for Neal 346AH (Midland Basin) showing the impact of assumed natural fractures near the fracture stages. Each row shows the DRV with a different set of natural fractures. a) Flow simulation for three central hydraulic fracture stages with two clusters of natural fractures (black) in the nearby matrix. Each natural fracture cluster has 10 discrete fractures. Particle paths (blue) after 30 years of simulation. b) The TOFC for three central hydraulic fractures. Each color band represents 3-year production increments.

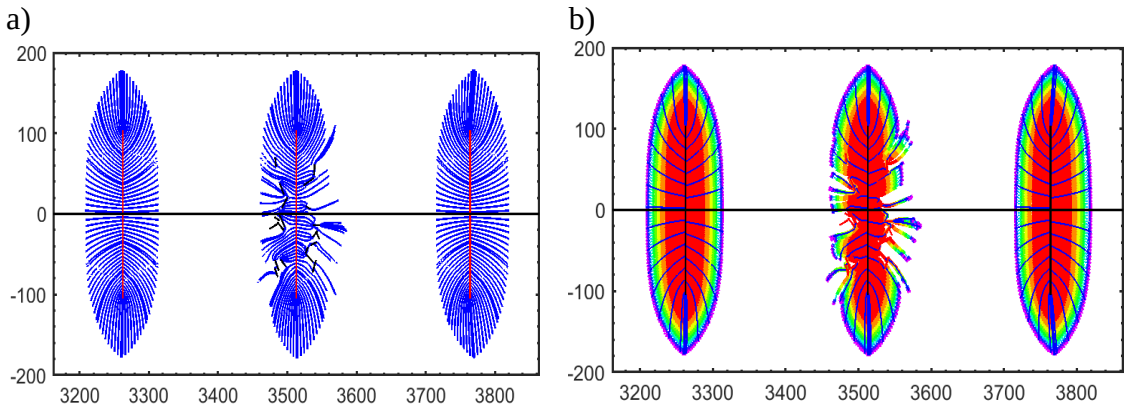

Figure 5-12 Continued

5.4.2. Natural fractures further away from hydraulic fractures with moderate DRV (Neal 346AH, Midland Basin)

In this section, we place the natural fractures further away from the hydraulic fractures and increase the permeability (strength) of the natural fractures by a factor of 5-20 [ft^4.$month^{-1}$]. The flux strength of the natural fractures is again scaled proportional to the flux allocated to the hydraulic fractures. Fig. 5-13 shows examples where two clusters of randomly generated natural fractures are placed on either side of the central hydraulic fracture. The length of the natural fractures is increased from 8 to 80 ft, with length distributions randomly generated with a constraint that natural fractures are not connected to the hydraulic fractures. If natural fractures were to connect to the hydraulic fractures, the former would start to behave as pressure sinks and essentially become part of a complex hydraulic fracture network. Increasing fracture network complexity may lead to increased recovery due to greater fracture surface area and suppression of stagnation zones (Nandlal and Weijermars, 2019a). The fundamental difference between

natural fractures and hydraulic fractures is further highlighted in a systematic study by Weijermars and Khanal (2019).

The DRV shapes in Figs. 5-13b become highly distorted and shift to drain slightly different reservoir regions if highly conductive natural fractures were to occur in the vicinity of the hydraulic fractures. The effect of the natural fractures remains localized and only affects the flow near the hydraulic fracture in close proximity. If we assume the hydraulic fractures stages to be a proxy for a hydraulic fracture, Figs. 5-13 a-c show that the shift in DRV could potentially result in flow interference between the adjoining fractures. Thus, the presence of natural fractures should be accounted for when fracture spacing is selected to minimize fracture interference.

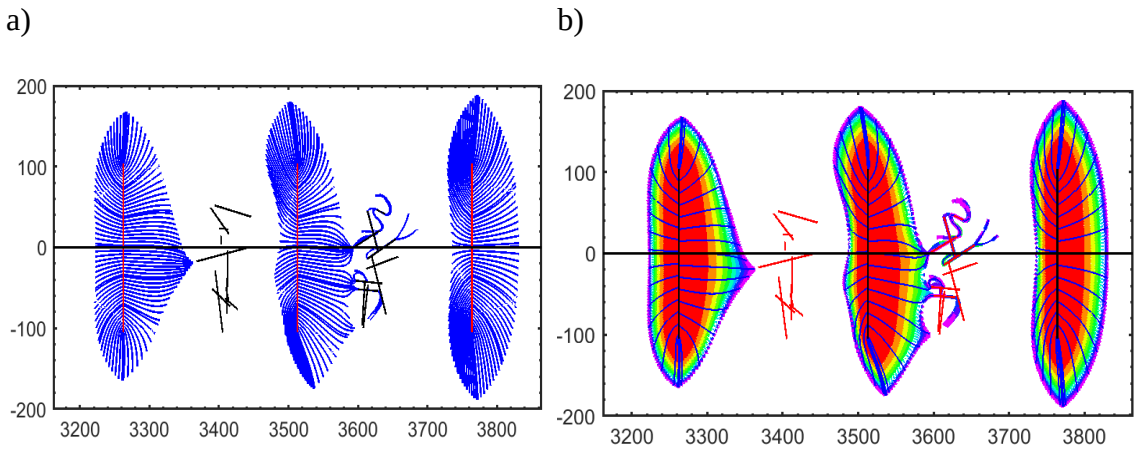

Figure 5-13 CAM model for Neal 346AH (Midland Basin) showing impact of assumed natural fractures near the fracture stages. Each row shows the DRV with a different set of natural fractures. a) Flow simulation for three central hydraulic fracture stages with two clusters of natural fractures (black) is located far from the hydraulic fractures. Each natural fracture cluster comprises 10 discrete fractures. Particle paths (blue) after 30 years of simulation. b) The TOFC for three central fractures; each color band represents 3-year production increments.

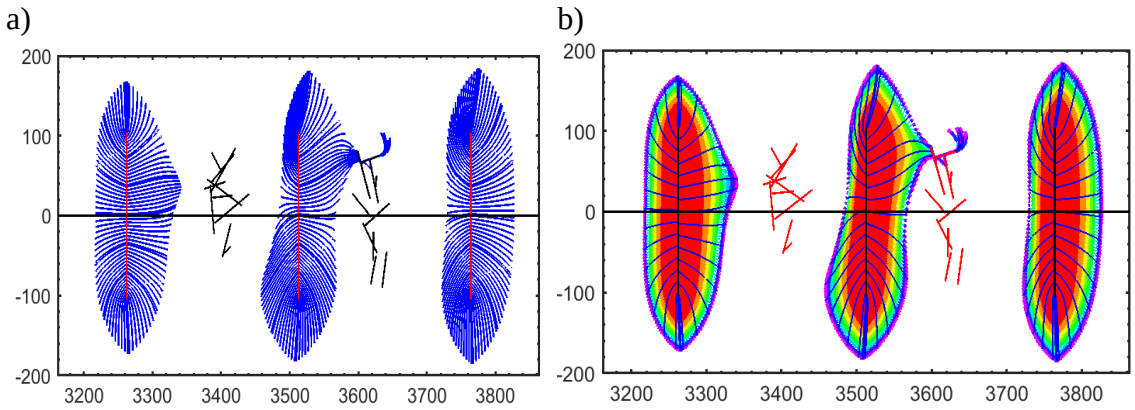

Figure 5-13 Continued

5.4.3. Natural fractures near hydraulic fractures with large DRV (Autobahn 34-117 1H, Delaware Basin)

The effect of the presence of natural fractures near hydraulic fractures with a relatively large DRV is analyzed in some detail, using the production data from the Autobahn well in the Delaware Basin (Fig. 5-9b). Figure 5-14 shows that natural fractures may have a significant impact on DRV growth (shape and location). Two different, random sets of natural fracture clusters were assumed in the top and bottom rows of Fig. 5-14. The strength of the natural fractures varies between 2.5-15 [ft^4.$month^{-1}$], which is a measure of the permeability contrast with the matrix (Weijermars and Khanal, 2019). The length varies between 8 and 80 ft, and the natural fractures do not directly connect to the hydraulic fractures. Figure 5-14 shows that the DRV shape becomes consistently distorted (due to the assumed presence of the natural fractures) as compared to the homogeneous reservoir assumption (Fig. 5-10). The natural fractures cause direct flow communication with the hydraulic fractures in the two adjoining stages, which may be classified as the beginning of flow interference between hydraulic

fractures due to the natural fractures. Our analysis shows that natural fractures could potentially result in flow interference with the adjacent hydraulic fractures. During well planning, the natural fractures need to be accounted for as much as fracture diagnostics can identify their relevant attributes. The fracture spacing can be optimized based on the desired DRV shapes and locations and must be communicated to fracture treatment engineers responsible for executing the field operations.

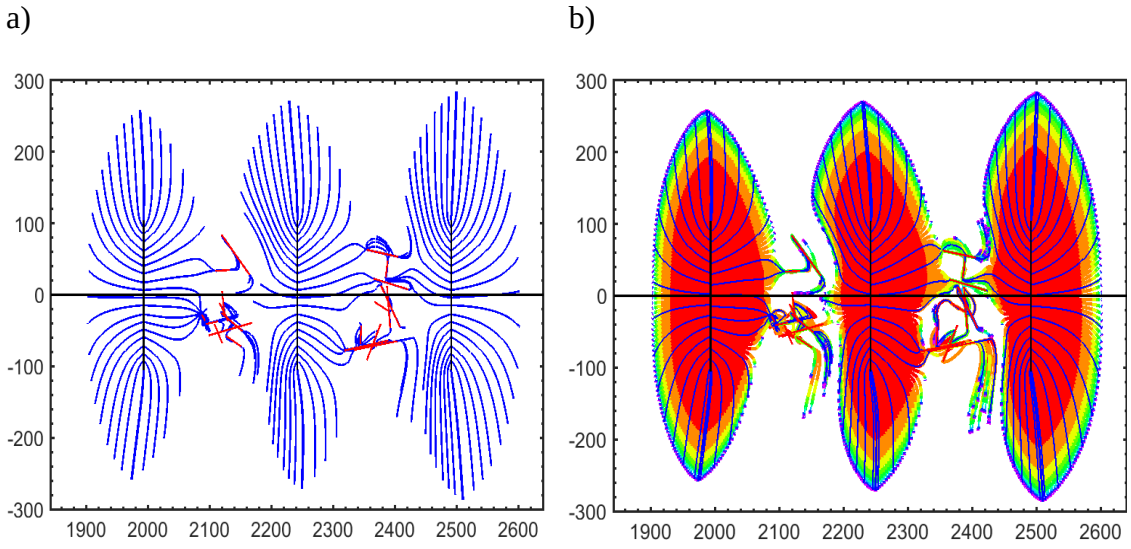

Figure 5-14 CAM model for Autobahn 34-117 1H (Delaware Basin) showing the impact of assumed natural fractures near the fracture stages. Each row shows the DRV for a different set of assumed natural fractures. a) Flow simulation for three central hydraulic fracture stages with two clusters of natural fractures (black) near the hydraulic fracture stages. Each natural fracture cluster comprises 10 discrete fractures. Particle paths (blue) after 30 years of simulation. b**)** The TOFC for three central three fractures; each color band represents 3-year production increments. The presence of natural fractures shifts the DRV and results in hydraulic fracture interference.

a) b)

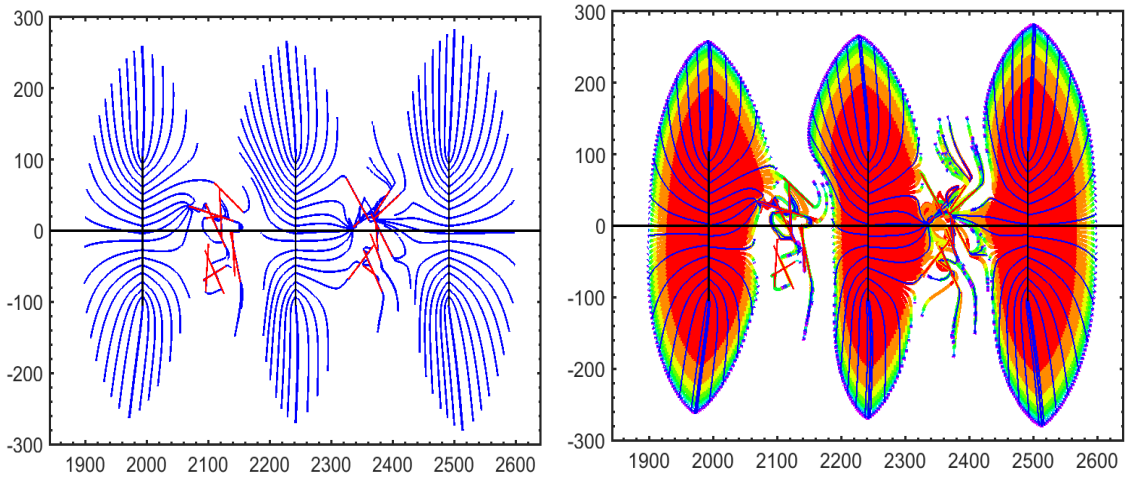

Figure 5-14 Continued

The preceding results highlight that natural fractures may have a significant impact on the DRV shape and location in a horizontal well. The natural fractures may also result in increased flow interference between the adjoining fractures. Thus, the hydraulic fracture treatment plan for shale wells should take the natural fractures into account.

5.5. Pressure depletion and spatial velocity changes

We further assess the development of the DRV in the Delaware Basin well (Autobahn 34-117 1H) by analyzing in further detail the pressure depletion history and velocity field evolution. Such analyses are useful to better understand how both the local pressure gradients and the related velocities will spatially vary and change over time when the flow due to the hydraulic fractures is affected by the presence of natural fractures (with a permeability higher than the matrix).

5.5.1. Pressure depletion analysis

The pressure in the CAM model is calculated by extracting the potential function from the complex potential and normalizing the value by the ratio of the reservoir permeability and fluid viscosity. More details on the calculation of pressure in CAM models are found in our earlier studies (Weijermars et al., 2017a,b; Khanal and Weijermars, 2019a,b). Figs. 5-15a-d show the pressure plots at different times, normalized by the maximum pressure at the onset of production for a homogeneous reservoir without any natural fractures. One should remember that our CAM models compute the DRV by applying the flow reversal principle using history-matched production data, which is why the highest pressures occur at the hydraulic fractures.

The early pressure plot (Fig. 5-15a) confirms that the pressure gradients in the regions close to the hydraulic fractures and the matrix are maximum at the beginning of the production, which results in an extremely large initial production rate. After the first

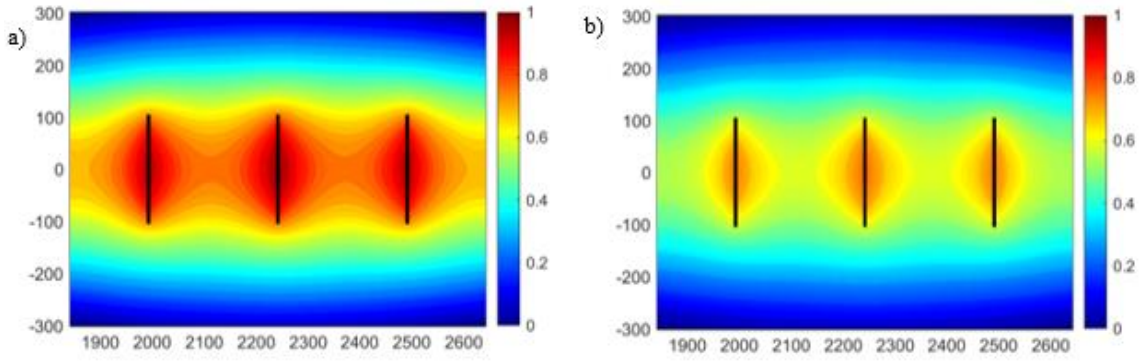

Figure 5-15 Pressure contour plots calculated from the CAM model for Autobahn 34-117 1H (Delaware Basin, without natural fractures) for the following times: a) Onset of production, b) after 6 months of production, c) after 1 year of production, and d) after 5 years of production. The pressure is normalized in each case by the maximum pressure at the onset of production. The pressure around the fractures is highest at the beginning resulting in maximum flow during the initial time.

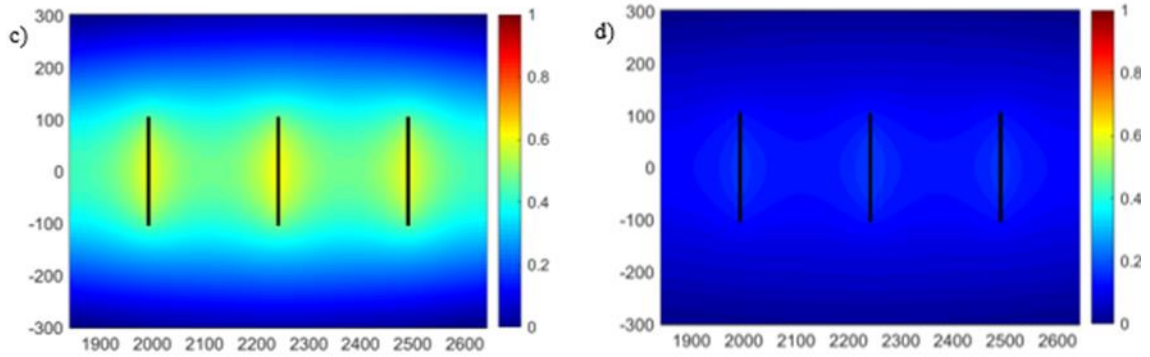

Figure 5-15 Continued

year of production (Fig. 5-15c), the pressure around the fractures reduces to almost half of the initial pressure. The pressure gradient between the fractures and matrix becomes negligible at later times as shown by Fig. 5-15d (5 years), which results in a much lower production rate. This observation is consistent with the TOFC growth in Fig. 5-11c, which shows that most of the reservoir depletion due to withdrawal of produced fluid from the reservoir, occurs in the first three years of the well life.

Figure 5-16 shows the evolution of the pressure contour patterns for the reservoir case with natural fractures (corresponding to the DRV cases shown in Fig. 5-14) for day 1 (top row), after 6 months (middle row) and after 12 months (bottom row) of flow simulation. The pressure contours for the initial time (Fig. 5-16a, top row) that were symmetric for a homogeneous reservoir (Fig. 5-15a) now become distorted. The maximum pressure is no longer confined to the hydraulic fractures, as was the case for the homogeneous reservoir (Fig. 5-15a), but become stretched in the direction of the natural fractures clusters. The directions of the pressure gradients are changed by the presence of the natural fractures (with high permeability relative to the matrix), which

explains why the DRV of Fig. 5-14b (with natural fractures) is distorted as compared to Fig. 5-11c (no natural fractures).

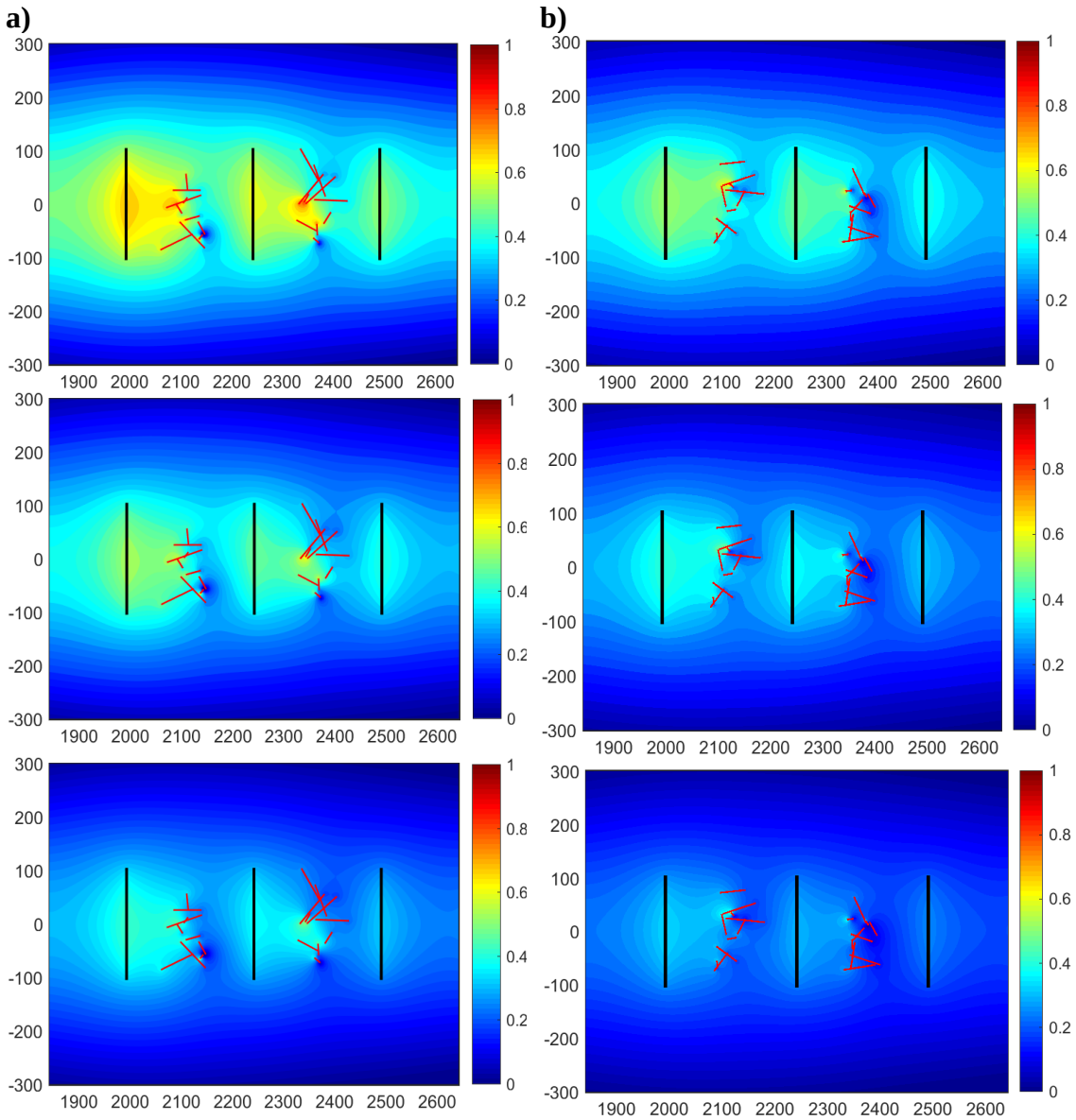

Figure 5-16 Pressure plots calculated from the CAM model for Autobahn 34-117 1H (Delaware Basin) with natural fractures as in: a) Fig. 5-14 (top row), b) Fig. 5-14 (bottom row). Top row: pressure at onset of production. Middle row: after 6 months. Bottom row: after 12 months of production.

5.5.2. Velocity field analysis

The velocity field contours for the Delaware Basin well (Autobahn) are evaluated, first without and then with natural fractures. Figure 5-17 shows the fluid velocity at different time-frames around the middle three fracture stages for the case that no natural fractures were to occur (corresponding to the DRV visualization of Fig. 5-11c and pressure field of Figs. 5-15a-d). The maximum fluid velocities occur near the tips of the hydraulic fractures, and stagnation points occur centrally between each pair of fracture stages. After the first year of production (Figs.5-17c, 1 year) the fluid velocity decreases significantly (Fig. 5-17d, 5 years of production). The high velocity near the fracture tips ensures that drainage in the regions around the fracture tips keeps up with drainage of the matrix regions between the hydraulic fractures. Similar high flow rates near the fracture tips were highlighted in earlier well studies using CAM (Weijermars et al., 2017b, 2018; Weijermars and van Harmelen, 2018). The velocity plots in Fig. 5-17 also show that the rock volume between the fractures cannot be drained effectively when natural fractures are absent, because stagnation points are surrounded by concentric regions of very low flow rates.

The velocity plots for the Autobahn well in a reservoir section with natural fractures (Fig. 5-18) correspond to the particle paths and DRV visualization of Fig. 5-14a,b and the pressure contour plots of Figs. 5-16a,b. The flow velocity in the natural fractures are extremely high, but flow velocities in the matrix outside the natural fractures will only be slightly enhanced due to the presence of the natural fractures.

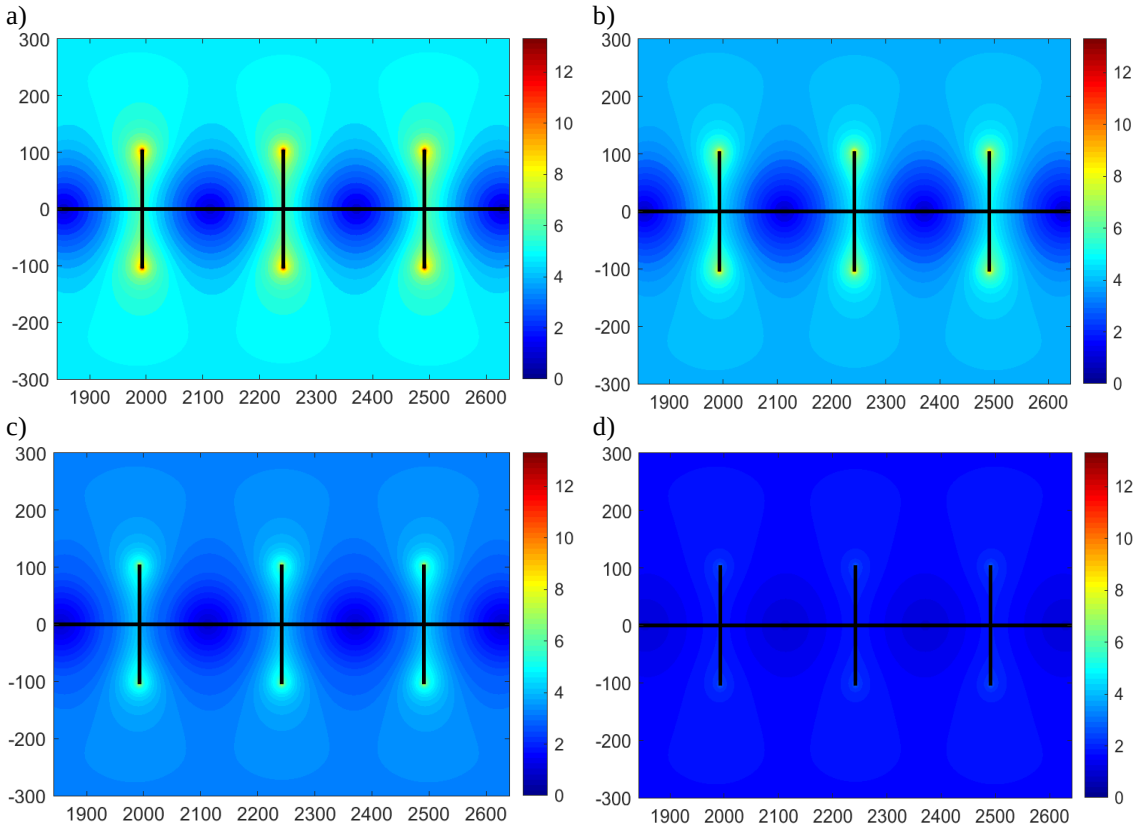

Figure 5-17 Velocity plots calculated from the CAM model for Autobahn 34-117 1H (Delaware Basin) without natural l fractures (Figs. 5-11 and 5-15) for the following times: a) Onset of production, b) after 6 months of production, c) after 1 year of production, and d) after 5 years of production. For each time, the velocity is maximum in the regions near the tips of the hydraulic fractures.

Multiple scattered regions with low velocities occur between the natural fracture clusters (Fig. 5-18), unlike the homogeneous reservoir case without natural fractures where we see only a single stagnation point (Fig. 5-17).

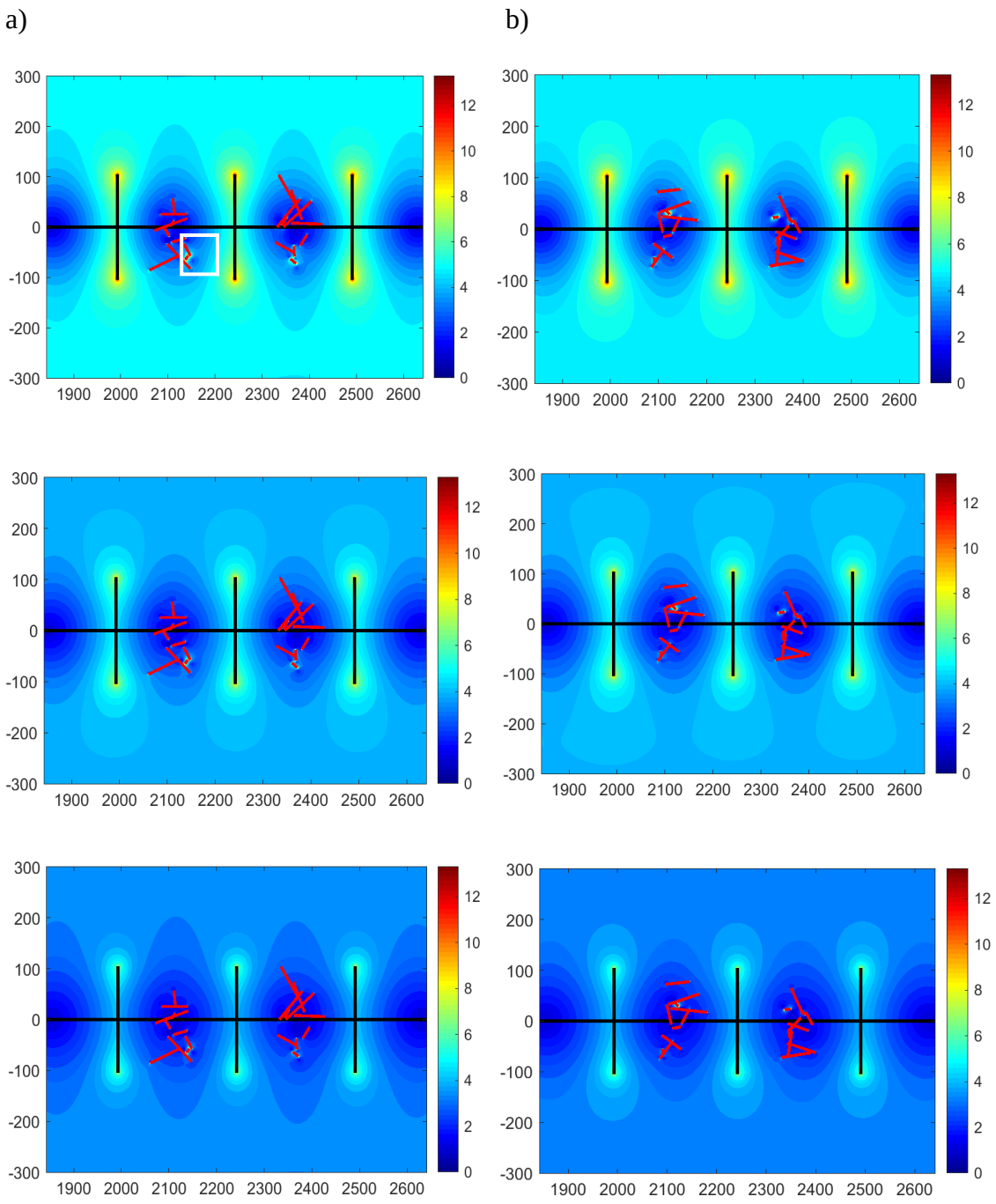

Figure 5-18 Velocity plots calculated from CAM model for Autobahn 34-117 1H (Delaware Basin) with natural fractures (as shown in Figs. 5-14 and 5-16. a) Fig. 5-14 (top row). b) Fig 5-14 (bottom row). Top row: Onset of production, Middle row: after 6 months of production, and Bottom row: after 1 year of production. For each time, the velocity is maximum in the regions near the tips of the hydraulic fractures (inset white box shows the area of high velocity due to the natural fracture effect).

5.6. Discussion

The principal goal of this project was to study in considerable detail the growth of the DRV around hydraulic fractures in shale wells. A CMG pressure depletion model was constructed based on history-matched production data for a 2014 well completed in the Wolfcamp Formation (Midland Basin). The DRV of the history matched well was constructed based on CAM algorithms. Production forecasts used to allocate and attribute produced fluids to individual hydraulic fractures were obtained using DCA history matching methods, based on the Arps and Duong equations. The accuracy of the DCA production forecasts was validated by numerical simulation using commercial software (CMG) and the appropriate reservoir and completion parameters (Table 5-1).

For a reservoir with no natural fractures (homogenous reservoir space), the DRV is uniform and elliptical in shape around the hydraulic fractures of the central stages. Towards the outer hydraulic fractures, interference effects result in slight asymmetry of the DRV (Fig. 5-11a). If conductive natural fractures were to occur near the study wells (introduction of heterogeneity) the particle paths become distorted, and the matrix around the hydraulic fractures is no longer drained uniformly. The variability in DRV due to the natural fractures is also reflected in the corresponding velocity and pressure plots from CAM. The impact of natural fractures on the DRV between hydraulic fractures is further expounded upon in the following sections.

5.6.1. DRV alteration due to impact of natural fractures

In the absence of natural fractures, DRV shapes around hydraulic fractures will develop as seen in Figs. 5-7, 5-10 and 5-11 for the three wells under investigation. For such assumed uniform reservoir properties, the major controls on the extent of the DRV will be the occurrence of any enhanced permeability zone around the hydraulic fracture (referred to as the SRV which is distinct and different from the DRV) as well as hydraulic fracture properties such as fracture half-length and fracture height. From our models, it is observed that after 30 years of production there are still large undrained regions between the hydraulic fractures for these wells. Common between all three wells is that the majority of the DRV is established within the first 3 years of production with the additional 27 years adding relatively little to the overall EUR (Fig .5-7c.).

A detailed analysis of the velocity field for the Autobahn well (Delaware Basin), in the assumed absence of natural fractures (Fig. 5-17a), shows that the undrained regions correlate to the low velocity regions around stagnation points occurring between the hydraulic fractures. The low velocity zones near the stagnation points correspond to regions with shallow pressure gradients (Fig. 5-15a). An important takeaway from this observation is that to maintain and maximize production, re-stimulation of the existing hydraulic fractures or re-fracturing between the original fracture clusters will be necessary. Our models provide high-resolution visualizations of where precisely in the reservoir space these undrained areas occur and where to best position the new infill fracture clusters for maximum increased recovery.

The natural fracture cases were modeled for three scenarios. The first two scenarios involved the modeling of natural fracture clusters with varying distances, closer and farther, from the three central hydraulic fractures for the Neal 346AH well (Wolfcamp, Midland Basin). The third case used the production and completion parameters from the Autobahn 34-117 1H well to model the impact of natural fracture clusters near to the three central fractures in the well. The Autobahn well (Wolfcamp, Delaware Basin), due to its high production, had a greater overall DRV after 30 years production than the Neal 346AH well. Our aim was to compare the impact of the natural fractures on a low DRV situation (Neal 346AH) with a high DRV case (Autobahn 34-117 1H).

For the first Neal 346AH case, the natural fractures were placed close to the central hydraulic fracture (Fig. 5-12). Some distortion of the particle paths occur due to the preference of flow through highly permeable natural fracture conduits, rather than through the reservoir matrix. The overall lateral extent of the DRV is only slightly distorted and does not cause any interference between the hydraulic fracture stages. The total area drained with and without the fractures remains unchanged as a constrained production profile was assumed based on the DCA/CMG history-matches.

For the second Neal 346AH case, the natural fracture clusters were placed further away from the central hydraulic fractures (Fig. 5-13) but given a higher strength than the previous model (Fig. 5-12). Due to the increased flow impact of the natural fractures, a greater distortion of the particle paths occurs with the DRV migrating towards the naturally fractured zones. The shift in the DRV occurs because of natural fractures and

for reservoirs with a high density of natural fractures, the possibility of fracture interference on flow must be taken into account when deciding fracture spacing. A reservoir with no natural fractures should have a smaller fracture spacing (due to a low chance of interference effects), while a highly naturally fractured reservoir may suffice with a larger fracture spacing (as the stagnation regions between the hydraulic fractures are penetrated by enhanced flow via the natural fractures).

A final case considered the impact of the natural fractures on the Autobahn well which has the greatest DRV extent of all the three wells modeled. Due to the natural fracture clusters now being located within the reach of the DRV, there is a large impact on the particle paths and the spatial area drained by the hydraulic fractures. For the Autobahn well with natural fracture clusters (Fig. 5-14), we see direct flow communication between the adjoining hydraulic fractures which can be classified as the onset of major flow interference between hydraulic fractures. Communication between adjacent hydraulic fractures may reduce the undrained regions between the hydraulic fractures as compared to the case with no natural fractures present (Fig. 5-11c).

The velocity field (Fig. 5-18) shows that the presence of natural fractures reduces the size of the flow stagnation regions. Due to the high-resolution of CAM models, one can observe that regions of locally increased velocity occur between the natural fractures (inset white box Fig. 5-18a) that allow fluid to flow to the hydraulic fracture from the otherwise low velocity region of flow stagnation. The results emphasize the relationship between the DRV extent and recovery efficiency, and how these two mechanisms are dependent on the impact on drainage by natural fractures. Only by adequately assessing

the impacts of natural fractures (as done in our CAM drainage models) can fracture spacing be optimized and the undrained areas visualized be targeted by refracturing.

5.6.2. Pressure front depth of investigation vs tracer front depth of investigation for DRV

One of the most crucial outcomes from the work done in this chapter was the recognition of how the calculated DRV differs from the commonly used pressure depletion maps which are used as a measure of production effectiveness. A distinction is made between the depth of investigation from a propagating pressure front in the reservoir (referred to as the diffusive time-of-flight, DTOF), and the tracer time-of-flight (TrTOF) due to the tracking of tracer particles released at the source/sink in the reservoir. It is this tracer front that is used to define the computed DRV. The implications of this difference are so crucial that the next chapter of this dissertation is solely devoted towards this topic.

5.6.3. Effect on estimated recovery factors

For unconventional reservoirs very low recovery factors are usually given in the literature as ranging from 8% to 13% (Sinha et al, 2017; Khanal and Weijermars, 2019a). Recovery factor (RF) is defined as the ratio between the estimated ultimate recovery (EUR) and the oil originally in place (OOIP). Of importance is what region we define as the OOIP, especially in the case of unconventional reservoirs. Conventional reservoirs assume OOIP to be the extent of the reservoir volume from where

hydrocarbons can be recovered and is typically limited by rock type and petrophysical parameter cutoffs. The RF definition becomes somewhat diffuse when applied to unconventional reservoirs because production from unconventional reservoirs originates only from stimulated areas, which occupies only a fraction of the OOIP region.

The question arises whether one should consider the entire acreage as the OOIP or just the extent of the SRV from which production is possible. If one were to use the entire acreage as OOIP, recovery rates drop to as low as 1% or less (Weijermars and Alves, 2018). An alternative approach proposes to use the inter-fracture recovery factor (Khanal and Weijermars, 2019a), defined as the ratio of the DRV ($A_{DRV}(t)$) and the limited OOIP volume (A_{OOIP}) confined to the reservoir region penetrated by the hydraulic fractures. The recovery factor (RF) is calculated by Eq. (5-6) (Khanal and Weijermars, 2019a):

$$RF(t)(\%) = \frac{Produced\_volume(t)}{OOIP} = \frac{A_{DRV}(t)(1-R_s)}{A_{OOIP}} \tag{5-6}$$

A residual fluid saturation (R_s) of 0.25 as given previously for this reservoir is used. Using Autobahn 34-117 1H as an example, the inter-fracture RF is given by the region drained by a single facture at the end of 30 years production, compared to overall region between the fractures available for drainage (Fig. 5-19a). The inter-fracture recovery for Autobahn is 42.6%. If the well spacing is used as the OOIP volume (Fig. 5-19b), the RF of 21.37% is obtained for the Autobahn well. This further emphasizes the importance of the OOIP volume used in the calculation of recovery factors.

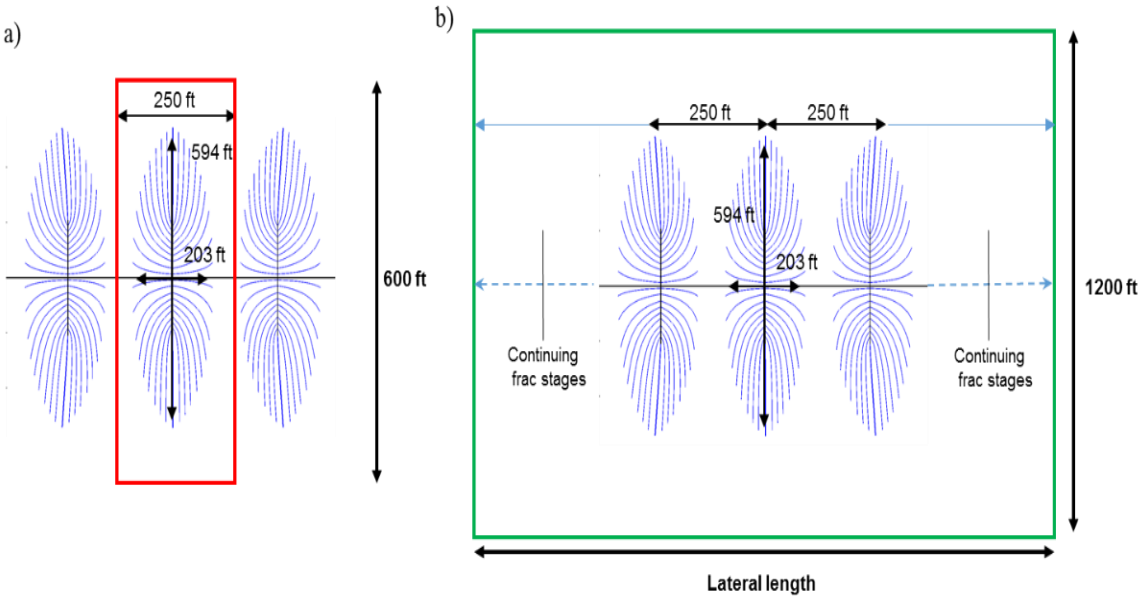

Figure 5-19 OOIP regions given for a) Inter-fracture recovery factor by red box and b) Well spacing recovery factor by green box (which represents the entire well length) for Autobahn 34-117 1H (dimensions not to scale).

Applying the methodology of Eq. (5-6) to all the wells in this study (Neal 346AH, Neal 322H and Autobahn 34-117 1H), gives the inter-fracture RF of 2.15%, 11.88%, and 42.6%, respectively. The low RF for the Neal 346AH can be attributed to its extremely high water-cut (WOR= 5.6). If we use the OOIP drainage area as being the well spacing area, different RF's will result as each of the three wells studied have different well spacing. With a well spacing of 350 ft as the OOIP drainage area, the Neal 346AH RF now becomes 3.67%. Neal 322H with a well spacing of 850 ft gives a RF of 8.47%. The Autobahn well with a spacing of 1,200 ft as calculated in the example gives a RF of 21.37%. The Autobahn well gives the highest recovery factor and this correlates to the greatest well spacing. With the largest well spacing, the Autobahn well suffers the least impact of any well interference and thus has the highest recovery. The well spacing

based RF estimates for our study wells cover a wider range than the 8-13% given by other researchers (Sinha et al., 2017). For example, Neal 346AH has an exceptionally low RF of 3.67% due to the high water-cut.

5.6.4. Model strengths and weaknesses

The CAM model for visualizing flow in the reservoir provides a practical tool with numerous advantages but does possess some minor weaknesses. The basic model does not take into account possible changes in hydraulic fracture conductivity along the hydraulic fracture length, although when used in combination with conductivity data for fracture sections from a fracture simulator, CAM can be adapted to account for hydraulic conductivity variations (Parsegov et al., 2018a). One of our assumptions is that the hydraulic fractures in the present study are of infinite conductivity. Also, not accounted for are any changes in conductivity with time due to fracture closure due to declining reservoir pressure. As we assume a single-phase, incompressible reservoir fluid, the impacts of multi-phase flow as well as other factors such as water blockage due to imbibed water during the process of creating the hydraulic fractures is not modeled. One other weakness of this approach is that we assume a homogenous reservoir space except in the areas where we directly place natural fractures to introduce heterogeneity in the reservoir. Also, gravity and capillary effects are assumed to be small enough to be ignored. In terms of strengths, this model as being analytical in nature is gridless and meshless and allows for infinite resolution at the fracture scale and with faster computation times than any other known method. Using CAM allowed for high quality

visualization of the DRV, pressure and velocity fields. For example, due to its high resolution, we have been able to identify the occurrence of high velocity areas that are related to the presence of natural fractures. Our model is unique in that it is a simple tool that provides information of crucial importance for determining where in the reservoir occur regions that are left undrained. Based on this new knowledge about DRV behavior, we can begin to develop practical engineering solutions to optimize fracture and well spacing for the most efficient recovery.

5.7. Conclusions

In this study we have effectively made use of the CAM formulation to model the development of the drained rock volume near individual hydraulic fractures, using production, reservoir and completion data from three study wells in the Permian Basin. Additional insight is also presented about the impact of conductive natural fractures on the DRV and associated interference effects. The following conclusions can be drawn:

1) The CAM model due to being meshless and gridless allows us to create high-resolution visualization at both the hydraulic fracture and the smaller natural fracture scales. For our models, the computational runtimes are much faster than intensive numerical simulation models.
2) For all three wells studied even after a forecasted production life of 30 years, there are still undrained regions between the hydraulic fractures.
3) Natural fractures can be seen to have a large impact on the shape of the DRV, depending upon their density, location, orientation and hydraulic conductivity.

Highly conductive natural fractures may lead to flow rates that lead to interference between hydraulic fractures in the same well.

4) The presence of natural fractures leads to changes in the velocity field by the reduction of stagnation zones between individual hydraulic fractures. Due to this reduction, fluid now flows in areas where without the natural fractures it did not. This has the major implication that we will now produce from areas between the hydraulic fractures which were previously undrained leading to better recovery factors.
5) We highlight the difference between the depth of investigation due to the propagating pressure front and the depth of investigation from the tracer front, which is used to calculate the extent of the DRV.
6) The limited growth of DRVs in the shale wells studied here shows that there is considerable potential for undrained regions between the hydraulic fractures that can be accessed by either restimulating the existing hydraulic fracture or by creating new ones by refracturing.
7) The recovery factor (RF) depends heavily on the rock volume used for the OOIP calculation, and for the wells considered in this study the recovery factors were 3.67% (Neal 346AH), 8.47% (Neal 322H), and 21.37% (Autobahn 34-117 1H), when well spacing is used as the OOIP rock volume.

6. COMPARISON OF PRESSURE FRONT AND TRACER FRONT ADVANCE IN UNCONVENTIONAL RESERVOIRS AND EFFECTS ON GROWTH OF DRAINED ROCK VOLUME (DRV)*

6.1. Introduction

6.1.1. Brief highlights

The chapter presents new insight based on the detailed analysis of DRV, that pressure plots are poor proxies for the actual DRV in shale reservoirs. Instead we should use tracer fronts for DRV which is what CAM enables and has been highlighted over the series of chapters in this dissertation. Using the analytical CAM tool, I was able to track individual tracer particles around the hydraulic fracture with time. This allowed the creation of a plot of depth of investigation by tracer front which can then easily be compared with the depth of investigation from the pressure front. With these two plots, the final plot shows the lag between the pressure front and tracer front depth of investigation.

The factors controlling the DOI-DRV time lag and their different propagation distances at any given time are quantified in an explicit formulation in our present study, for use in shale field development planning. Study wells from the Permian Basin (as described in Chapter 5) are used to illustrate the DOI of the pressure front and that of the

*Part of the data reported in this chapter is reprinted with permission from "Comparison of pressure front with tracer front advance and principal flow regimes in hydraulically fractured wells in unconventional reservoirs" by Ruud Weijermars, Kiran Nandlal, Aadi Khanal, Murat Fatih Tugan, 2019, Journal of Petroleum Science and Engineering.

tracer front at various times and stages in the well life. The time-lag between the pressure depletion depth and drained rock volume radius is quantified and analyzed.

6.1.2. Motivation of study

An often overlooked, or poorly recognized phenomenon is the lag, typically occurring in unconventional reservoirs, between the depth of investigation (DOI), which limits the pressure depletion zone and the drained rock volume (DRV), which is the fluid zone drawn into the well. In conventional reservoirs with a permeability of milliDarcy or higher, the DOI is established very quickly throughout the reservoir space after pressure is lowered in a point source, due to the presence of one or more production wells. The pressure depletion plot can be successfully used as a proxy for delineating the drained area in hydrocarbon reservoirs.

For practical production engineering in *conventional oil and gas reservoirs*, no special consideration needs to be given to DOI calculations. The DOI remains mostly a theoretical concept, useful in the context of short-lived well tests. The pressure front depth of investigation is commonly used by industry in various calculations as the DOI propagates fast enough for reservoir properties to be determined by very short flowing times needed for pressure build up and drawdown tests. The propagation rate of the pressure front is also used in the calculation of changes in flow regimes (bi-linear to transient to pseudo-steady state etc.; Vasco et al., 2000).

However, in *unconventional oil and gas reservoirs*, which are developed by closely spaced vertical and/or horizontal wells, the DOI needs to be monitored very

closely as highlighted in recent studies (Weijermars and Alves, 2018; Khanal and Weijermars, 2019a). The reason is that the ultra-low permeability causes a large disparity to occur between the propagation of a pressure depletion front, which outlines the drainage area of the well (and its potential interference with adjacent wells), and the rock volume that is actually drained (DRV). The DOI of the advancing pressure front is the extent in the reservoir at which the fluid feels the effect of the pressure sink imposed. The existence of a regional pressure gradient, however, does not mean that all of the moving fluid will reach the hydraulic fractures during the productive time scale (well life). In fact, the rock volume that is actually drained is much smaller than the drainage area affected by pressure depletion (Weijermars et al., 2017a,b; Weijermars and Alves, 2018; Khanal and Weijermars, 2019a). The DRV occupies only a fraction of the rock volume affected by the pressure depletion as outlined by the DOI. Consequently, in unconventional reservoirs, the DOI of pressure depletion gives an unrealistic representation of the actual rock volume drained.

6.1.3. Summary

Pressure depletion patterns in ultra-low permeability shale reservoirs occupy a much larger region than the regions where fluid has been removed from the reservoir as outlined by fluid withdrawal contours near hydraulically fractured wells. When used for reservoirs with moderate or high permeability (say k>1 mD), industry never needed to caution using pressure depletion plots as a proxy for fluid removal or drained rock volume (DRV). Fluid that moves from the margins of a pressure front, indicative of the

so-called depth of investigation, will reach the well on the time-scale of the economic life of the well. However, a whole new way of thinking is required when studying fluid migration paths and the associated drained rock volumes in shale reservoirs. In ultra-low permeability shale (nanoDarcy range), a large gap may occur between the extent of the pressure depletion zone and the region of fluid that is actually drained by the well. Therefore, when producing from ultra-low permeability reservoirs, the distinction between pressure depletion zones and the region where recovered fluid originated from becomes crucial in order to truly understand which factors control the hydrocarbon recovery process. Our detailed analysis compares the depth of investigation (DOI), of the leading edge of the pressure depletion front, and that of a tracer front (equivalent to the DRV outline). The pressure depletion pattern vastly overestimates the reservoir zone from where produced fluid originated.

6.2. Propagation of pressure depletion and drained rock volume

A 2014 study well (Neal 346AH, Upton county, West Texas), a 6524 ft long lateral landed and completed in the Wolfcamp Formation, Midland Basin, was history matched and analyzed as outlined in chapter 5 of this dissertation. The well is hydraulically fractured, with 60 ft perf cluster spacing assumed to originate 109 discrete hydraulic fractures with enhanced fracture conductivity (Zakhour et al., 2015). The history-matched reservoir simulation model for Neal 346AH (Khanal et al., 2019) is used here to generate pressure depletion maps and pressure depletion profiles for different times during the assumed 30-year production life of the well. Although the

entire well is simulated, our analysis focuses on the pressure changes near the three central fractures (no. 54-56). Focusing on the central fracture stage allows studying of the pressure depletion, at high resolution, in both the matrix blocks between the individual fractures and in the matrix away from the fracture tips.

6.2.1. Propagation of pressure depletion in year 1

The initial reservoir pressure in the Wolfcamp Formation (before any production) was 5,161 psi, as determined in our prior history match (Khanal et al., 2019). In the present study, we identify the pressure front as the distance where a first change/perturbation/drop in pressure occurs. Figs. 6-1a-f show the pressure front propagation at six different times during the first year of production. Fig. 6-1a shows the pressure decline at the first day of production due to an imposed bottomhole pressure (BHP) of 1000 psi. Figs. 6-1b-f display the pressure front advance and local pressure depletion after 1, 2, 4, 6 and 12 months of production. Fig. 6-1b shows that it takes only one month before adjacent fractures begin to communicate with each other, in the sense that their respective pressure fronts meet. After the pressure fronts of adjacent fractures make first contact, the pressure decline around the hydraulic fractures accelerates (Figs. 6-1c-f).

Pressure readings are based on refined grid blocks in a vertical strip across the central three fractures (no. 54-56). The left column in Fig. 6-1a-f shows map views of the pressure front advancement around the three fractures (note that the full well was modeled) and associated pressure decline in the immediate vicinity of the three central

fractures. The central column shows the pressure change in a depth section perpendicular to the well, close to the central stage (0 ft) between the 54th and 55th fractures. The pressure front normal to the wellbore travels rapidly within the first month (Fig. 6-1b, central column) toward the imaginary boundary of the rectangular box outlined by the tip of the hydraulic fractures (105 ft on either side). Overall, the pressure front normal to the wellbore continues to advance very slowly after the first month and reaches only about 200 ft on either side after the first year (Fig. 6-1f, central column). During this time, the pressure inside the 60 ft wide regions bound by the spaced fractures, decreases relatively rapidly as shown in Figs. 6-1c-f (right column).

The pressure front advancement and depletion in the matrix blocks between the hydraulic fractures is detailed in depth cross-sections parallel to the well and normal to the hydraulic fractures (Figs. 6-1a-f, right column). The pressure front from the central fracture travels outward, towards the adjoining fractures, until an imaginary flow boundary is reached, located halfway each fracture pair, after the first month of production. Pressure gradients facilitate fluid flow toward the central fracture from either side (Figs. 6-1b, right column). The pressure near the hydraulic fractures decreases at each subsequent time, reducing the initial pressure in the matrix blocks between the fractures by 2,500 psi or more within the first year of production (Figs. 6-1f, right column). Most of the well's first year production is supported by the pressure drop in the matrix blocks between the hydraulic fractures (Figs. 6-1a-f). The matrix outside of the fracture tips, judging from the slow propagation of the pressure front, appears to contribute only little to the well's first year production. One should realize that the

pressure gradient at the fracture tips is steep (Figs. 6-1a-f, central column), but due to the narrow apertures of the hydraulic fractures, the flux into the well from the fracture tips is negligible as compared to the flux into the hydraulic fractures from the matrix regions between the fractures, at least during the first year of production.

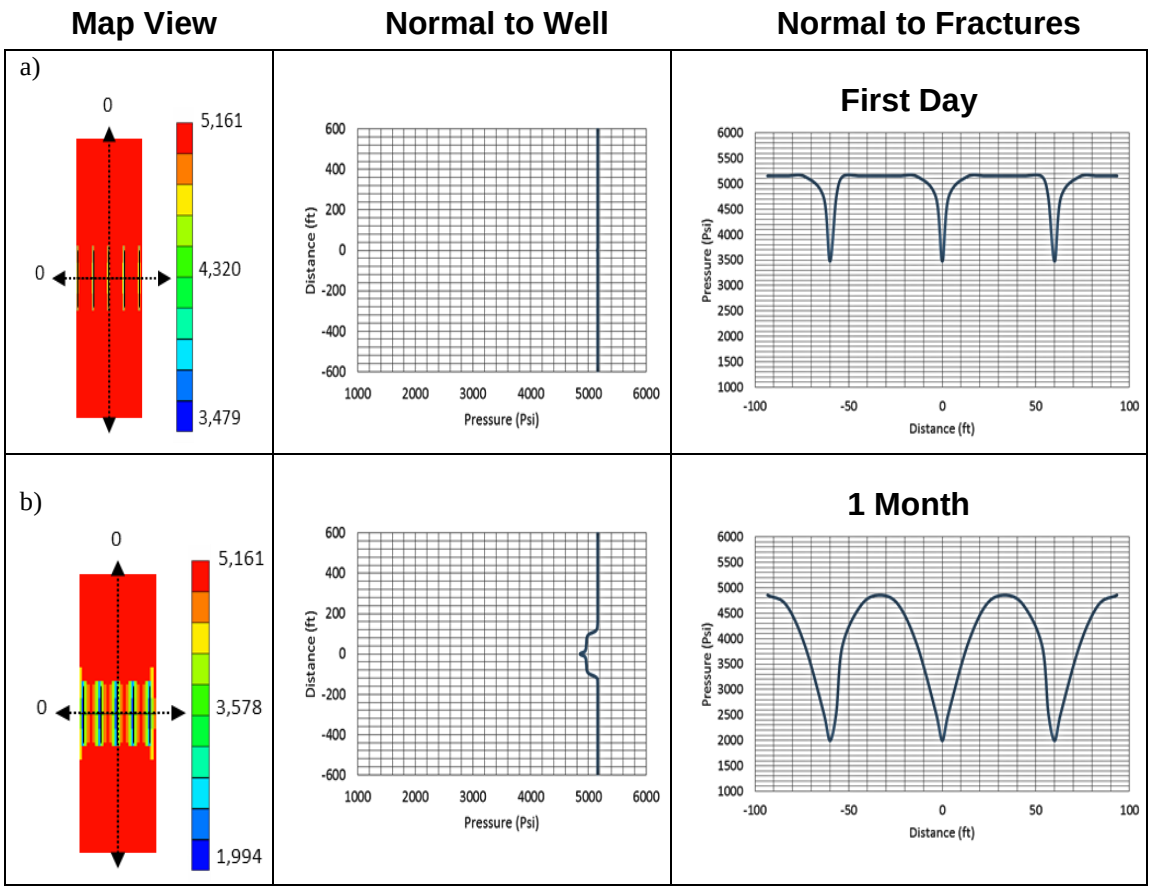

Figure 6-1 First year pressure depletion (psi) progression for the central 3 fractures in Neal 346AH, a Wolfcamp shale well (Midland Basin, West Texas) constructed using a production history-matched CMG model. Left column: Map views of pressure depletion in production bench with wellbore horizontal in image and transverse fractures sets spaced at 60 ft. Central column: pressure gradient in the direction normal to the well. Right column: pressure gradient normal to the fractures. (a)- (f) Time shots for day 1 and, next, after 1, 2, 4, 6, and 12 months respectively.

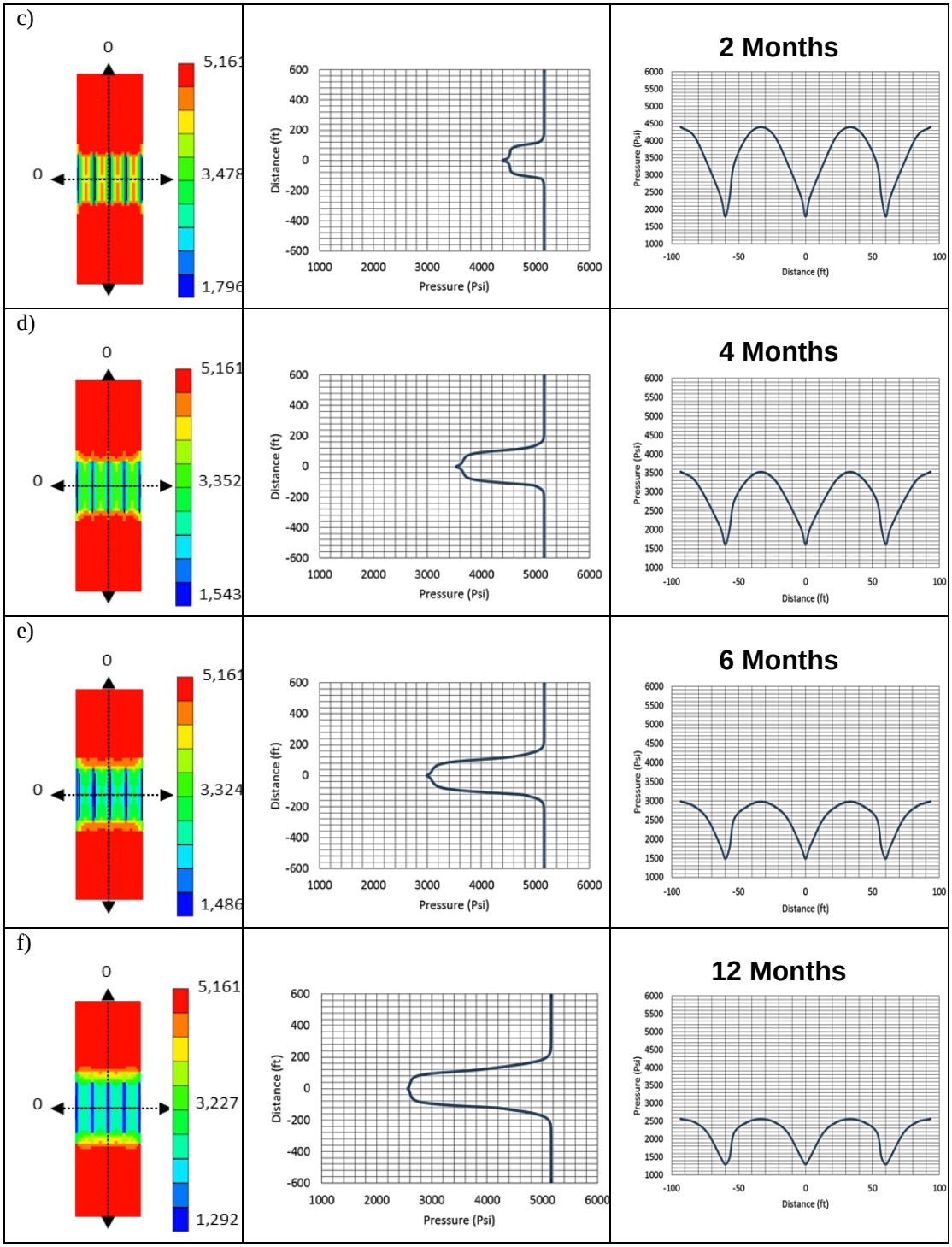

Figure 6-1 Continued

At the end of year 1, the bottomhole pressure (BHP) is nearly established in the hydraulic fractures and is close to 1000 psi (Fig. 6-1f, right column). The pressure in the matrix blocks between the hydraulic fractures has been reduced to 2500 psi (Fig. 6-1f, right column), or about half the original reservoir pressure (5161 psi). The reduced pressure in the matrix between the fractures indicates that some fluid has been removed from the reservoir. However, only a small fraction of the original hydrocarbons in place (OHIP) in the region between the hydraulic fractures will reach the well after 1 year of production.

6.2.2. DRV during the first year of production

Let us now examine the development and advance of the drained rock volume (DRV) during the first year of production. Fig. 6-2 shows the DRV around the three central fractures of our study well (Neal 346AH, Midland Basin; Zakhour et al., 2015; Khanal et al., 2019) after 6 months and 1 year of production, as constructed using CAM algorithms and Eulerian particle tracking methodology (see Weijermars et al., 2017b, 2018; Khanal et al., 2019). All fluid in the matrix region between the fractures is moving after 1 month of production, according to the pressure gradient in Fig. 6-1b (right column). The pressure decline in the matrix blocks between the fractures (Figs. 6-1a-f) is due to the fluid migration toward the well. However, at the same time, the fluid is traveling very slowly and only a small fraction of the matrix fluid will have reached the well via the hydraulic fractures after one year of production. The fluid withdrawal paths in Figs. 6-2a,b outline the DRV extent after 6 months and 1 year of production,

respectively. The flow normal to the hydraulic fractures is obviously quite slow, whereas draining of reservoir fluid by the fracture tips occurs slightly faster. The actual velocity field will also be analyzed in detail below.

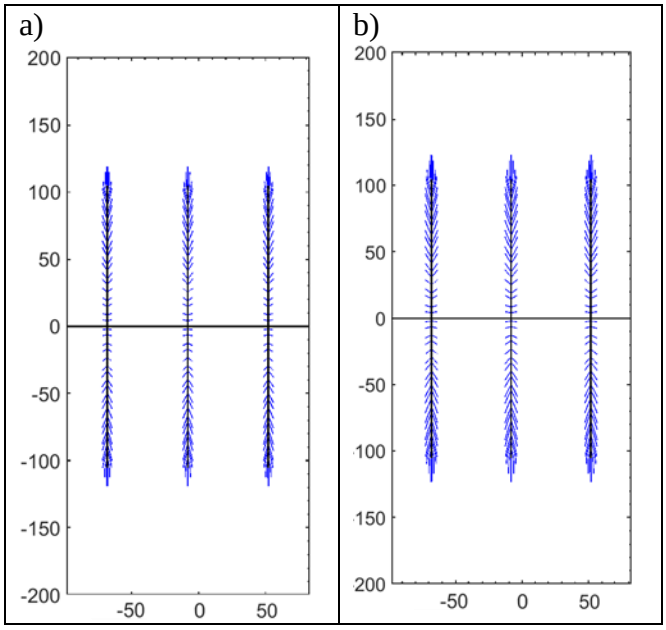

Figure 6-2**:** Particle paths (blue) around the three middle fractures (54-56) of Neal 346AH for two different times: a) after 6 months, and b) after 12 months of production. There are 109 fractures spaced at 60 ft from each other over a lateral well length of 6524 ft. Map views of reservoir with length scale marked in ft.

The particle paths in Figs. 6-2a,b are relatively short and deliberately track only fluid particles that made it all the way to the well, in order to know how the DRV develops after 1 year of production. However, all non-residual fluid stored in the matrix between the fractures will be moving (already after the first month of production) as can be inferred from the pressure gradient in Fig. 6-1b (right column). So while it is true that the majority of the OHIP volume is no longer in its original place (apart from the residual oil fraction, given by R_s in Eq. (6-5), see later), only a tiny fraction of the moving fluid will actually contribute to first year production. The reason is that a large

proportion of the fluid body that is moving toward the well (ultimately via its hydraulic fractures), will never reach all the way to the well. Although the pressure has been significantly depleted between the matrix blocks after the first year of production, the central sections will still have (mobile) oil that moved too slow to reach the well, and henceforth remained undrained (white zones in Figs. 6-2a,b).

Figs. 6-3a-c highlight the fluid velocity field in the producing layer after the first month of production (when the pressure gradient is fully established in the matrix between the hydraulic fractures (e.g., Fig. 6-1b). Although the maximum velocity at the fracture tips is initially close to 4 ft/month (Fig. 6-3a), the flow rate wanes in step with the pressure gradient decline seen in Figs. 6-1a-f. After 1 year, the fluid moves to the fracture tips at a much lower rate of 0.77 ft/month (Fig.6- 3c) and continues to decline. Also note that the matrix regions between he hydraulic fractures develop so-called dead zones (a term first coined in Weijermars et al., 2017a), due to the occurrence of flow stagnation points surrounded by zones where fluid moves less than 0.5 ft/month, even in month 1 of production. The explanation for the low flow rate in the matrix blocks between the hydraulic fractures is the occurrence of the pressure saddles (Figs. 6-1a-f, right column), at the apex of which a pressure gradient, required to drive the fluid flow, does not exist.

We have now explained in part why much of the OHIP will never reach the well on a practical time scale. This assertion has been highlighted in our prior studies (Weijermars et al., 2017a,b; Weijermars et al., 2018), but is here systematically documented for the first time. The lagging growth of the DRV is not limited to the first

year of production (Fig. 6-2b). DRV growth continues to decline rapidly even after the first year of production.

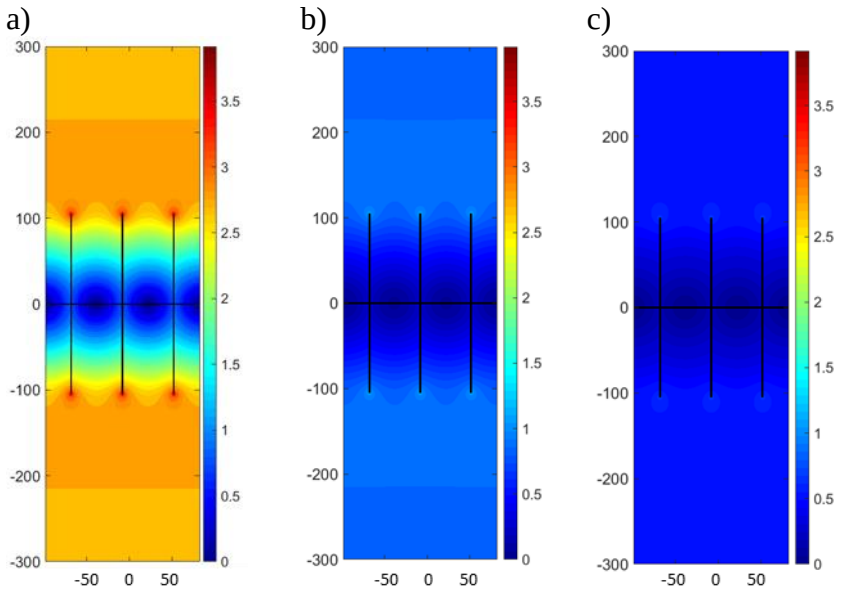

Figure 6-3 Contour plots (of reservoir section in map views) showing the fluid velocity (scaled in ft/month) around the three middle fractures (54-56) of Neal 346AH (Midland Basin, Upton County) for three different times: a) 1-month, b) 6 months, and c) 12 months. The scale in each figure is between 3.92 ft/month and 0 ft/month. The maximum velocity is seen around the tips of the fractures. The maximum velocity depletes from 3.92 ft/month to 0.77 ft/month from 1 month to 12 months. Length scale is in ft.

6.2.3. Propagation of pressure depletion front in later years (5-30 years)

Next, we analyze the pressure depletion development of Neal 346 AH at 5-year intervals. After 5 years of production, the pressure front has advanced into the ambient matrix normal to the wellbore up to 400 ft away from the well (Fig. 6-4a, central column). Compare the 400 ft advance for year 5 to the 200 ft for year 1 (Fig. 6-1f, middle column). The pressure in the grid blocks between each pair of the central fractures at year 5 (Fig. 6-4a, right column) has nearly reached the minimum bottom-

hole pressure (1000 psi). One may infer that the matrix region between the fractures no longer contributes in any significant way to the production in year 5 of the well life. Slow velocity components occur in the direction normal to the hydraulic fractures, because the pressure gradient (or pressure differential) has flattened fast. After a decade of production, the pressure transient still propagates outward, but very slowly and mostly in the direction perpendicular to the wellbore (Fig. 6-4b, middle column). The pressure gradients normal to the hydraulic fractures have all but vanished in year 10 (Fig. 6-4b, right column).

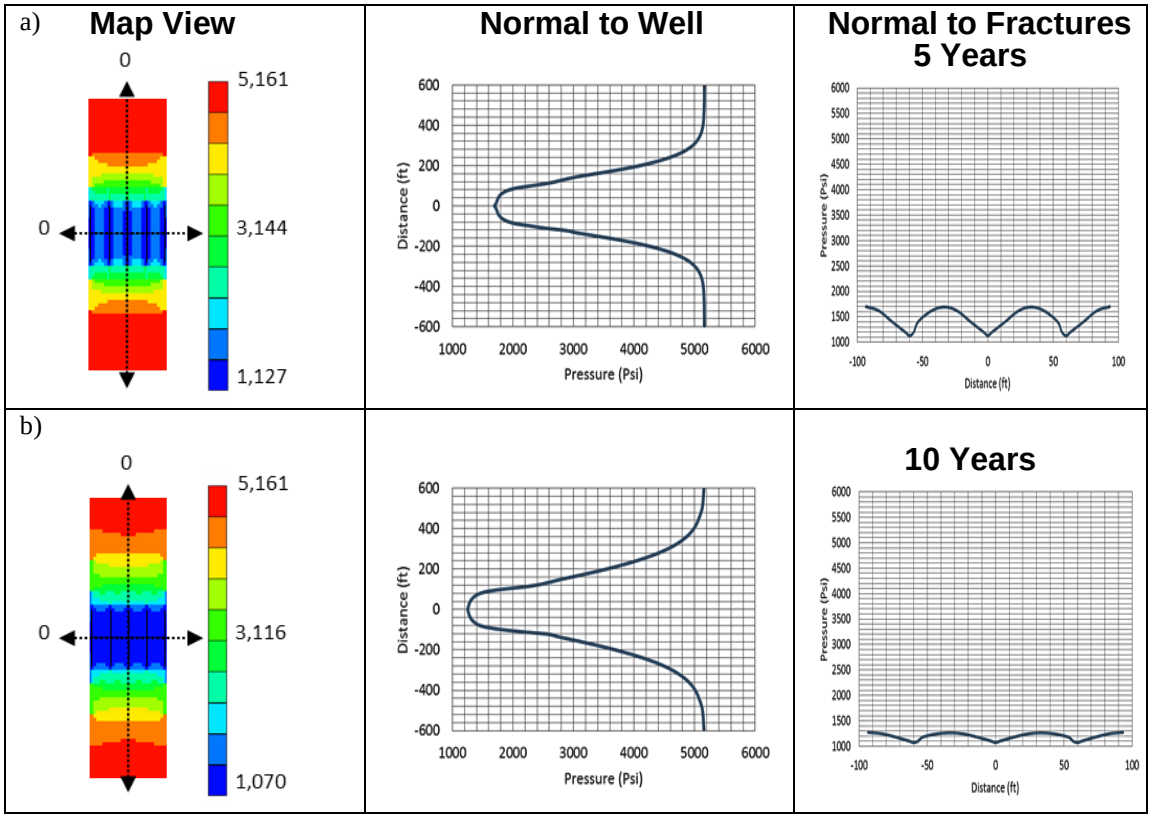

Figure 6-4 Late life (5-30 years) pressure depletion (psi) progression for the central 3 fractures in Neal 346AH. *Left column:* Map views of pressure depletion in production bench. *Central column:* pressure gradient in the direction normal to the well. *Right column:* pressure gradient normal to the fractures. (a)-(f) Time shots for 5, 10, 15, 20, 25, and 30 years, respectively.

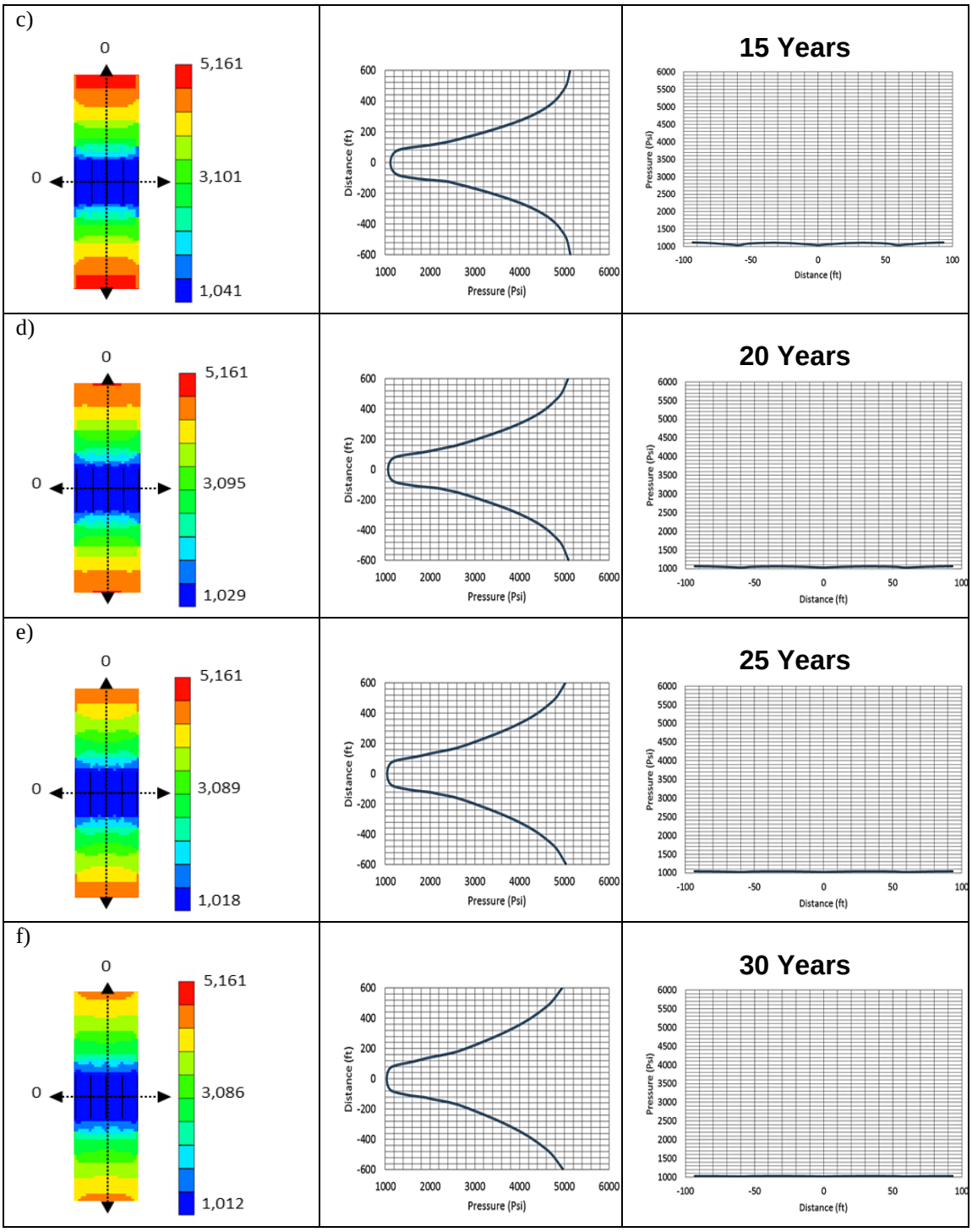

Figure 6-4 Continued

After 15 years of production (Fig. 6-4c), the produced fluid is entirely sourced from the matrix region outside the fracture tips, because there no longer remains any discernable pressure differential in the matrix between the hydraulic fractures (as evidenced by the flat horizontal pressure gradient plots; Figs. 6-4c-f, right column). However, there is still a large fraction of OHIP trapped in the dead fluid zones between the hydraulic fractures (as can be inferred from the limited DRV outline modeled before). Meanwhile, the pressure front continues to advance, but the advance slows down. Fluid is mostly drained from a direction normal to the well (away from the fracture tips), but the declining velocity explains the extremely low well rate after 15 years of production. The pressure plots in Figs. 6-4a-f reveal that the DOI migration, and pressure gradients that must drive production in unconventional reservoirs, evolve very slowly.

Figs. 6-5a-d show a full well simulation by a history-matched CMG well model (Khanal et al., 2019). The simulations confirm that the rectangular region outlined by the fracture tips of the full well has become largely pressure depleted after the first year of production (Fig. 6-5a). The pressure front continues its advance in a direction normal to the wellbore (Figs. 6-5b-d), and the pressure gradient supports continued fluid flow to the tips of the hydraulic fractures along the full length of the well. The flow rate to the tips of the hydraulic fractures is always faster than the fluid rate received from the matrix regions between the fractures (Figs. 6-3a-c). However, after year 1, the overall drainage speeds will decline faster and further growth of the DRV continues at an extremely slow

pace, because the well is mostly fed by fluid drained via the fracture tips, as the pressure gradient in the matrix blocks between the fractures wanes (Fig. 6-1f, right column).

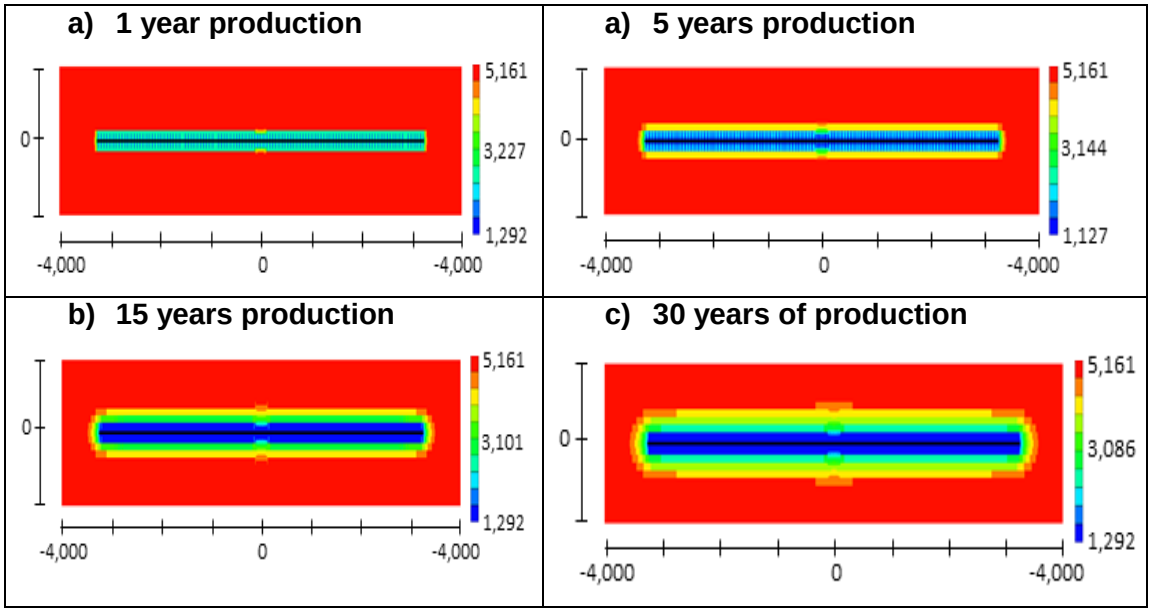

Figure 6-5 Pressure depletion round well (Neal 346AH) in the Wolfcamp production bench A using full well model at different times: (a)-(d) for 1, 5, 15, and 30 years, respectively; pressure in psi (after Khanal et al., 2019). Length is in ft.

6.2.4. DRV after 30 years of production

After 30 years of production, the pressure front or DOI has propagated to only about 600 ft away from the wellbore (Fig. 6-4f, middle column). Beyond 600 ft, the reservoir pressure is still pristine (Fig. 6-5d), close to the original pressure before first production started. *So how much of the fluid in place will have reached the well after 30 years?* Figs. 6-6a,b give the particle paths and DRV around the hydraulic fractures after 30 years of production, reconstructed using a history-matched CAM model. Amazingly, large non-drained regions remain between the hydraulic fractures. The DRV remains modest and extends to only 165 ft away from the wellbore (Fig. 6-6b), and thus lags far

behind the DOI of 600 ft that is due to the pressure front (Figs. 6-4f, 6-5f). Thus, the wells should be stimulated further to improve the production after a certain time interval (based on economics). An advisable approach is to use pressure enhancing EOR methods like gas injection, as is already being done by several operators.

After 30 years of production, fluid has only been drained up to 62 ft away from the fracture tips (measured from the fracture tips outward in a direction normal to the well orientation). The DRV depth in a direction normal to the hydraulic fractures is only 15 ft. After 30 years of productive well life, the lag between the DOI (600 ft away from the well) and the slow advance of the DRV (165 ft away from the well) has now been quantified and explained. A subsequent section will show how we quantify the advance of (and increasing lag between) the DOI and DRV over the full life-time of the well. However, the close relationship between the pressure depletion pattern, implied pressure gradient directions, and the consequent spatial changes in the magnitude and direction of fluid flow rates is illustrated in a later section.

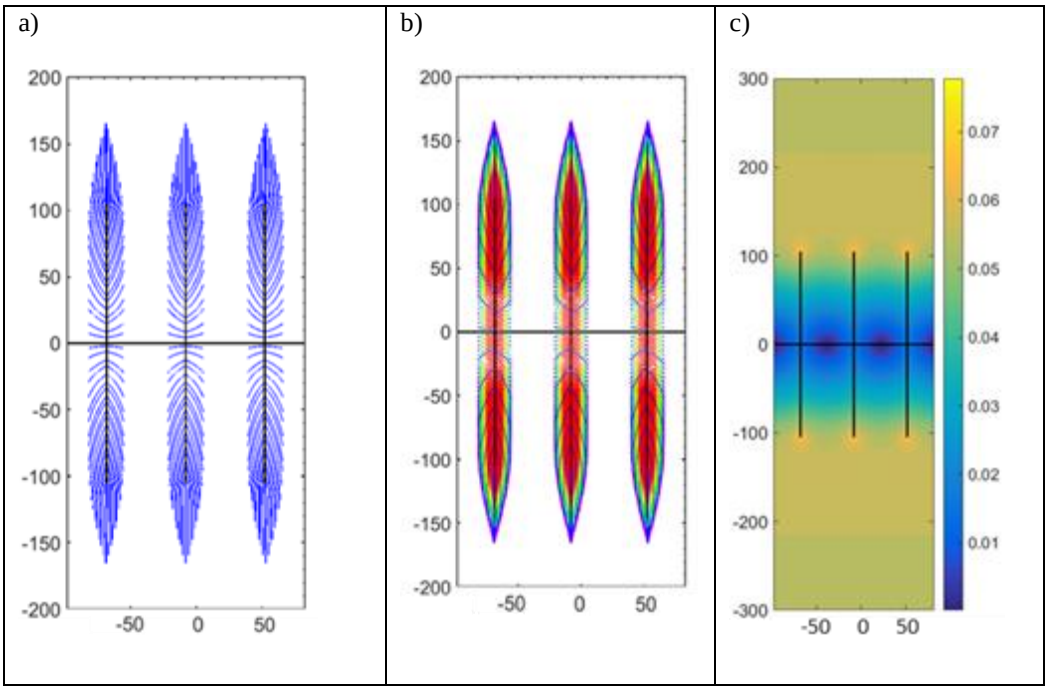

Figure 6-6 Map view of fluid motion near three central hydraulic fractures (54-57) in production layer after 30 years of production. a) The particle paths (blue) for the fluids originating from the fractures, b) The TOFC (rainbow colors) for the DRV around the fractures. Each color represents the DRV for 3-year interval. c) Corresponding velocity plot (scaled in ft/month). The maximum velocity after 30 years is 0.079 ft/month around the fracture tips.

6.2.5. Pressure gradients and velocity field

A prior study has analyzed the DRV of another hydraulically fractured Wolfcamp well in considerable detail (Weijermars et al., 2018). A summary of the principal results is merited here, because of the illustrative correlation between fluid rates, pressure gradients and the occurrence of flow stagnation zones between the hydraulic fractures. Figs. 6-7a,b show the pressure contour pattern near the fracture stages in the well, constructed using CAM algorithms and flow in the reservoir scaled by the history-matched production profile of the well (Weijermars et al., 2017b). Typical

pressure saddles/troughs occur in between the fractures. When the well draws down, the pressure profile flattens (Fig. 6-7c). The position of the apex of the pressure gradient profile does not shift. Note that these pressure saddles develop in a similar fashion as those given in Fig. 6-1 (right column), which is for a nearby Wolfcamp well, also located in Upton County (West Texas). In Fig. 6-7c, pressures go up over time, because the model reverses fluid flow; produced fluid is injected back into the reservoir via interval sources that represent the fractures.

The velocity field plots given in Figs. 6-8a,b correspond to the pressure field plots of Figs. 6-7a,b. The velocity profile of Fig. 6-8c is for the same reservoir section as covered by the pressure profiles in Fig. 6-7c. Careful comparison of Figs. 6-7c and 6-8c reveals that the flow stagnation points coincide with the reservoir locations between the hydraulic fractures where the pressure gradient vanishes. Also instructional is that the highest flow velocities occur at the fracture tips (Fig. 6-8c) The explanation of the peripheral zone at the fracture tips with the higher flow velocities (Fig. 6-8a) lies in the fact that the pressure contours are closer spaced in the same peripheral zone (Fig. 6-7a), thus the steepest pressure gradients perfectly coincide with the belt of higher fluid flow rates. The study of Weijermars et al. (2018) also concluded that the DRV leaves behind large undrained regions between the hydraulic fractures.

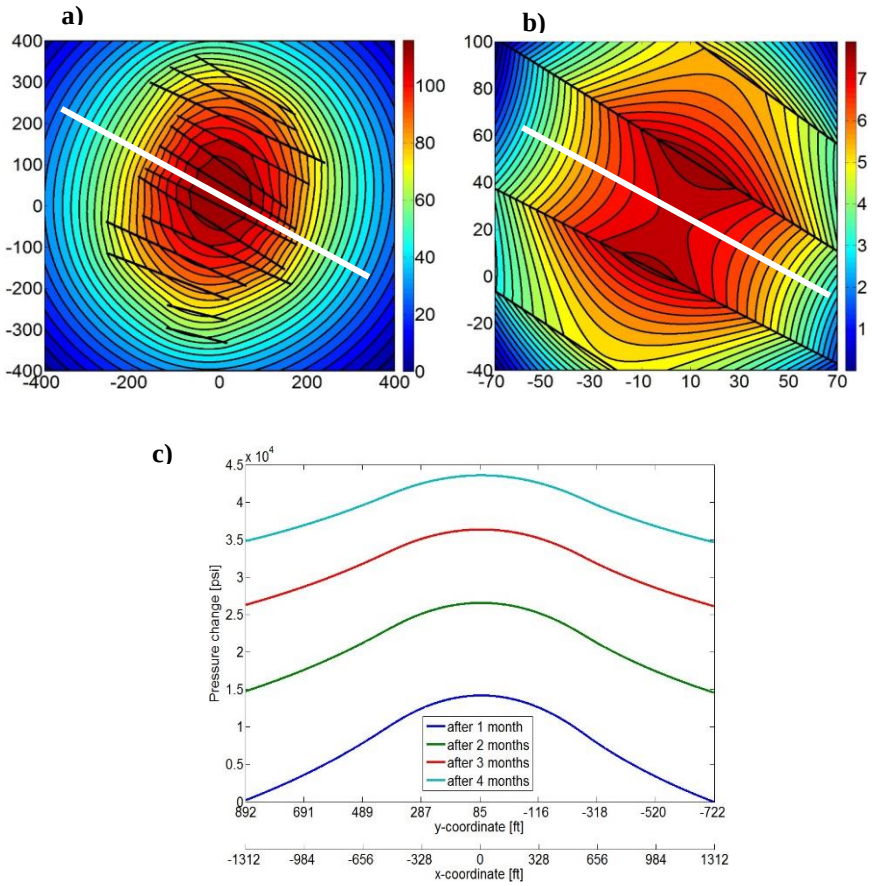

Figure 6-7 Pressure depletion of a hydraulically fractured well in the Wolfcamp Formation (Upton County, West Texas). The wellbore is vertical in the image (due North), with the hydraulic fractures oblique to the wellbore, trending NW-SE. **a:** Pressure field (10^2 psi) after 1 month of production. Length dimensions in ft. **b:** Detail of central pressure depletion zone. **c:** Progressive pressure changes obliquely across the central depletion zone in (a). Note that pressure scale is inverted due to the application of the flow reversal principle in our model (after Weijermars et al., 2017b).

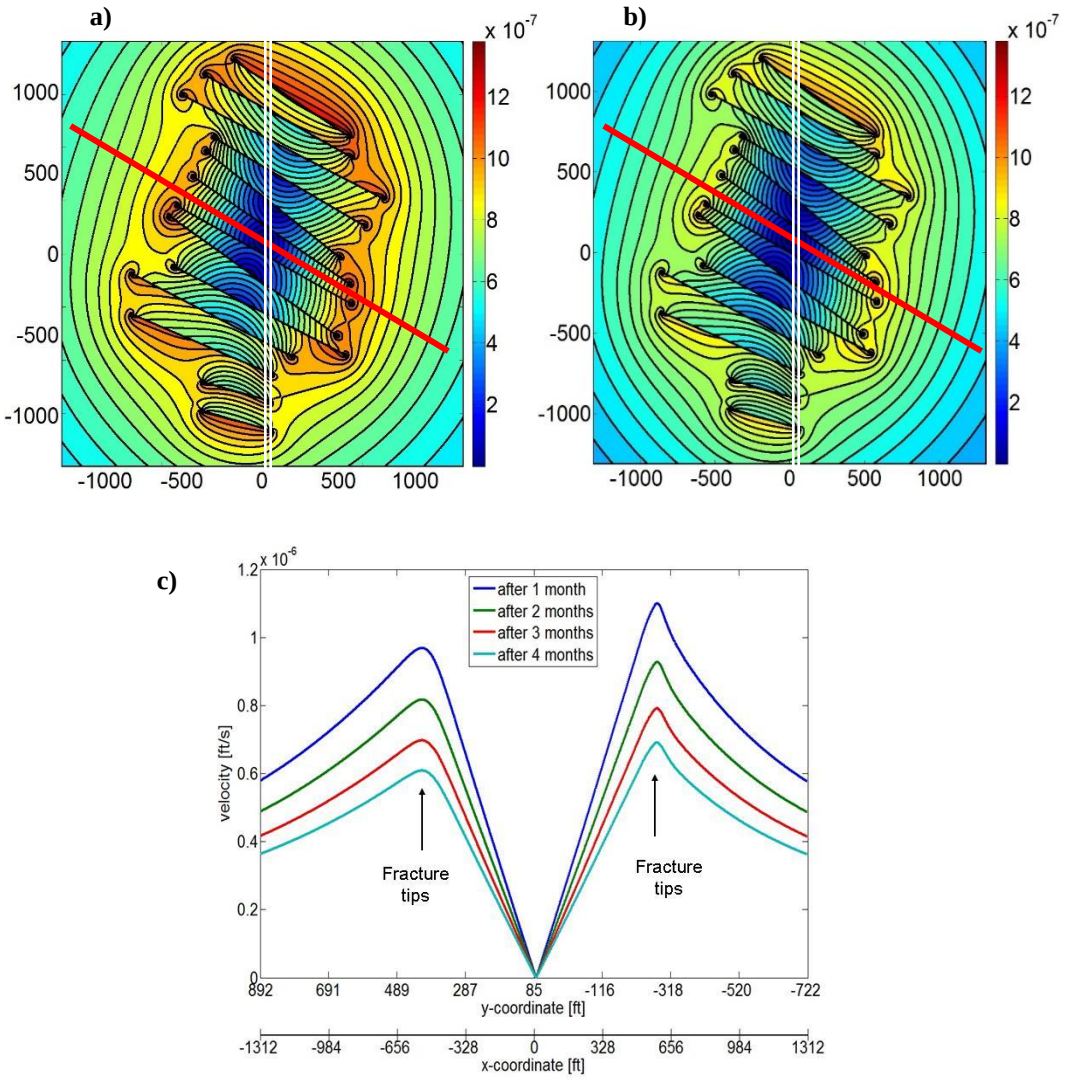

Figure 6-8 Flow in fracture treatment zone of horizontal well, represented by double white lines with oblique fractures. Length dimensions in ft. Velocity field (ft/s) **a:** after 1 month, **b:** after 2 months. **c:** Velocity profiles across the red line in a and b show that the largest velocities at any one time occur near the fracture tips (where the pressure gradient is steepest, see Fig. 7c). (after Weijermars et al. 2017b).

6.3. Time-of-flight for pressure fronts and tracer fronts

An important distinction needs to be made when discussing time of flight (TOF). The reason for this is that TOF is used to refer to either the distance traveled by a propagating pressure wave or the displacement of neutral tracers from a pressure source or sink. The importance of this distinction is made clear in Figs. 6-9a-d. The studied reservoir section has a heterogeneous permeability, with red zones indicating higher permeability and blue zones a lower permeability (Fig. 6-9a). A vertical well (central star) will drain the region via the visualized particle paths (Fig. 6-9b). Figs. 6-9c and d emphasizes the major difference in the TOF for the pressure front and the tracer front. The pressure wave travels several orders of magnitude faster (Fig. 6-9c) than the tracer front (Fig. 6-9d), shown by the vastly different scales for the time of flight contours.

The disparity in the rates of propagation of the pressure front and the tracer front warrants a detailed explanation. The present chapter expounds upon each topic in turn to further support the interpretation of the field data presented in the preceding section. The lag between the moving pressure front and the areal extent to which molecules are removed from the reservoir space by drainage are quantified below.

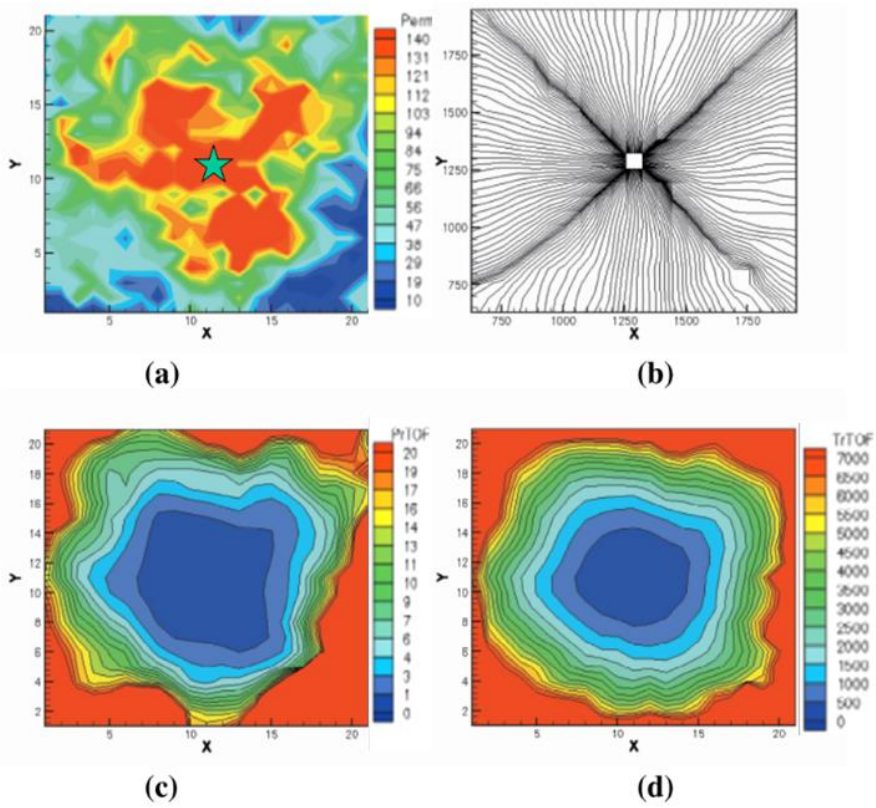

Figure 6-9 a) Permeability field, b) particle paths to central vertical well, c) diffusive or pressure time of flight (PrTOF in days), and d) tracer time of flight (TrTOF in days). (after Datta-Gupta and King 2007, Fig. 10.18).

6.3.1. Depth of investigation (DOI) of pressure front

In the discipline of streamline simulation (more correctly particle path tracking, as the flow is commonly transient and not steady-state), there is an inherent link between the time of flight and what is termed the depth (or radius) of investigation. The radius of investigation (r_i) refers to the advance of the pressure drawdown front, which expands from the well outward. The transient radius of investigation is given by Weijermars and Alves (2018):

$$r_i(t) = \sqrt{\frac{kt}{1688.7 n \mu c_t}} \qquad \text{[ft]} \qquad (6\text{-}1)$$

Eq. (6-1), formulated in field units, shows the importance of permeability (k) and porosity (n) of the reservoir in determining the radius of investigation. The time required for the pressure front to reach a given depth of investigation at location r_i is (Weijermars and Alves, 2018):

$$t = \frac{1688.7 r_i^2}{\alpha} \qquad \text{[hours]} \qquad (6\text{-}2)$$

The term α(x) is known as the hydraulic diffusivity:

$$\alpha(x) = \frac{k(x)}{\phi(x) \mu c_t} \qquad (6\text{-}3)$$

The TOF to establish a certain depth of investigation is solely dependent on the reservoir parameters contained within the hydraulic diffusivity term (Eq. (6-3)). Assuming an incompressible fluid with very little change in viscosity, the major control of the diffusive time of flight to establish the DOI for a propagating pressure front are the porosity, permeability and fluid viscosity; the compressibility is relatively invariant. Figs. 6-10a,b show plots for the changes in the DOI rate of advance for a range of permeabilities in two reservoirs of 8% and 2% porosity respectively. The analytical results of Figs. 6-10a,b can be benchmarked against the DOI propagation rate for the 100 nD Wolfcamp reservoir (penetrated by Neal 346AH).

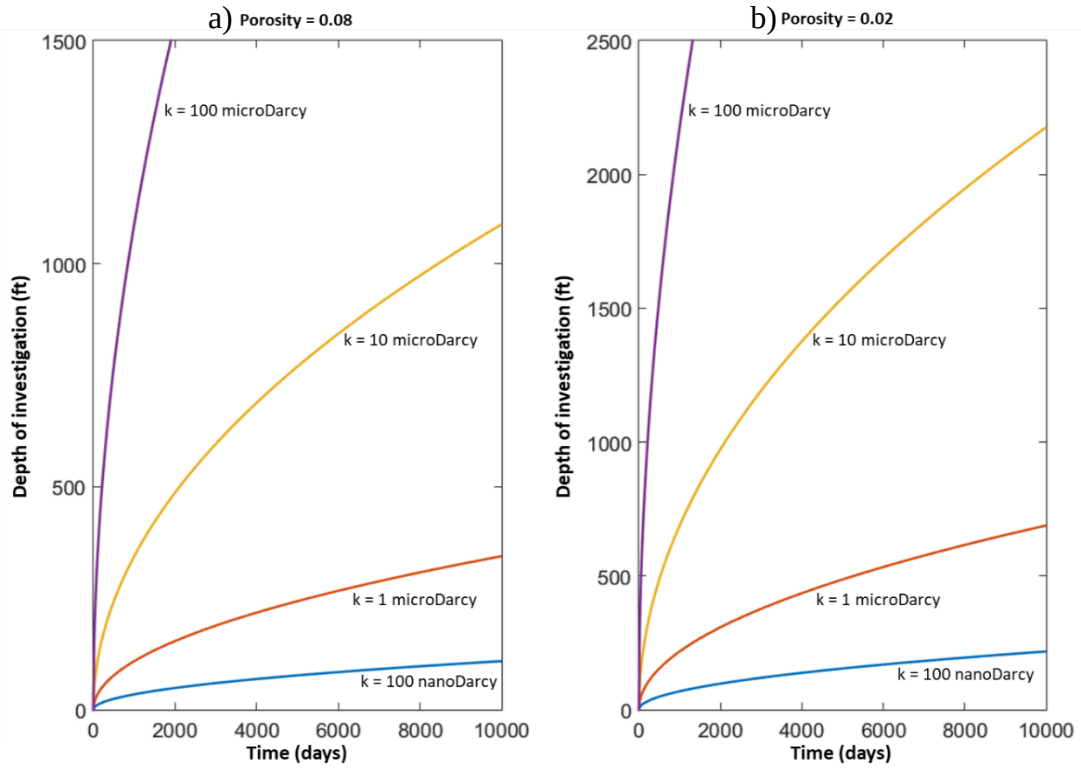

Figure 6-10 Growth of the DOI with time, calculated from Eq. (6-1) for various reservoir permeabilities. (a) is for a porosity of 8%, (b) for 2%; fluid viscosity is 1 cPoise in both (a) and (b).

Fig. 6-11 shows the propagation rate of the pressure front based on the CMG model of Fig. 6-5. Two different pressure differentials were selected to denote the CMG DOI propagation front: (1) pressure front marked by a 10% drop from initial reservoir pressure (561 psi drop), and the analytical DOI for the pressure transient front are almost identical (Fig. 6-11).

Fig. 6-11 also investigates the range of depth of investigation due to different total compressibility values, as in most simulation studies this parameter is often poorly constrained due to lack of field data. The DOI for this reservoir after 360 months

production ranges from 861ft for a c_t of $1x10^{-6}$ psi^{-1} to 497ft for a higher c_t of $3x10^{-6}$ psi^{-1}. Also plotted in Fig. 6-11 is the DOI using two different pressure drops as marking the start of the pressure front in the producing reservoir. Pressure drops from the initial reservoir pressure of 5161 psi, of 100 psi and 561 psi are used. The value of 561 psi represents a 10% drop from the initial reservoir pressure and is modeled here as this value falls in line with the pressure drop used by other authors to denote the volume/depth in the reservoir contributing to production (Kim et al., 2019).

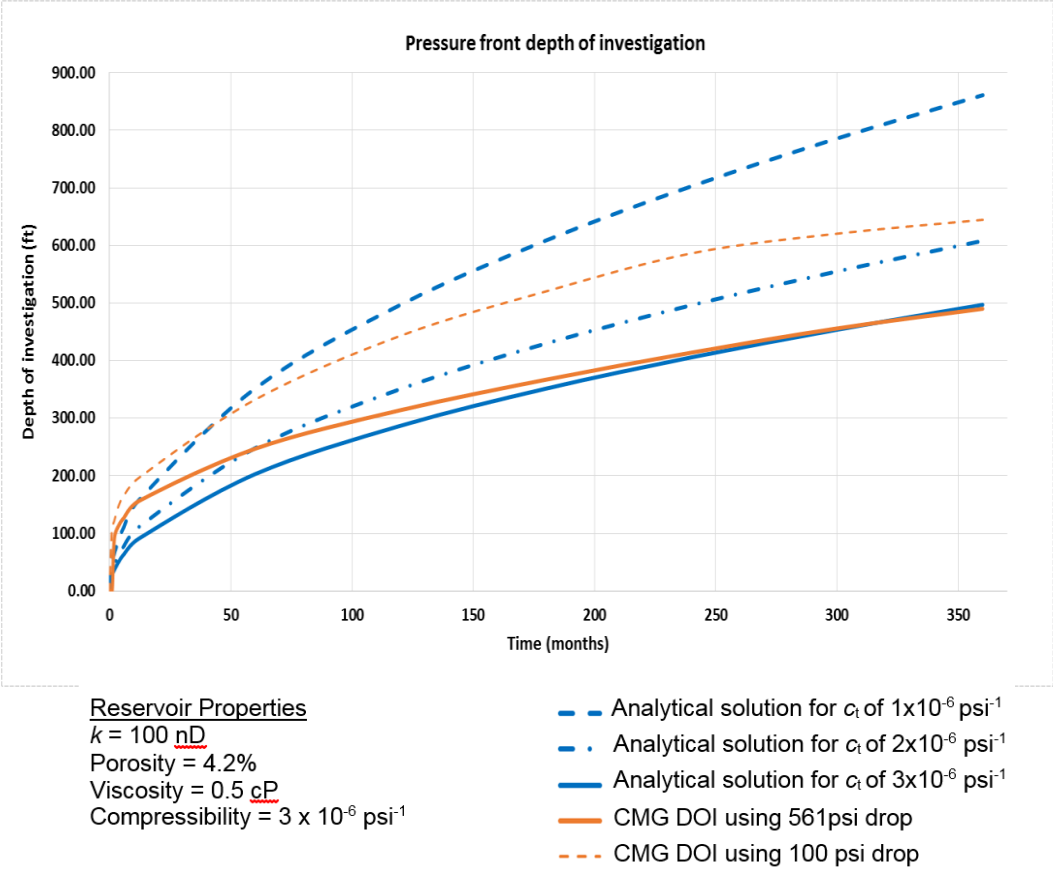

Figure 6-11 Depth of investigation (or pressure transient propagation) based on pressure front advancement normal to the well, based on CMG simulations for two pressure drops, compared to analytical solution using different compressibility factors (c_t)

6.3.2. Depth of investigation of tracer front

Here we distinguish between the time of flight due to the radius of investigation from a propagating pressure front in the reservoir (DTOF) and the tracer time of flight (TrTOF) due to the tracking of tracer particles released at the source/sink in the reservoir. Datta-Gupta and King (2007) used the term diffusive time of flight (see Appendix D for further deliberations) to represent the propagation of a front of maximum drawdown or buildup corresponding to an impulse source or sink. The DTOF is then compared to tracer front advance based on the (convective) tracer time of flight (TrTOF). Datta-Gupta and King (2007) showed that the pressure front propagates orders of magnitude faster than the tracer front. Evidently, there is a clear advantage of pressure interference tests as compared to tracer tests in terms of an early field response.

In the present study, the TrTOF is calculated based on the velocity field created due to the rate of withdrawal or injection of fluid at the well head. The velocity of the fluid particles in the reservoir traveling toward hydraulic fractures is modeled using history matched production rates. As shown before Complex analysis methods (CAM) represent the hydraulic fractures as an array of line sources and the velocity field near the fractures at any given time and is given by (Weijermars and van Harmelen, 2016):

$$V(z,t)=\sum_{k=1}^{N}\frac{m_k(t)}{2\pi L_k}e^{-i\beta_k}\cdot\left(\log\left[e^{-i\beta_k}\left(z-z_{c,k}\right)+0.5L_k\right]-\log\left[e^{-i\beta_k}\left(z-z_{c,k}\right)-0.5L_k\right]\right)$$

[ft.mth^{-1}] (6-4)

Eq. (6-4) shows that the velocity field is dependent of the flux strength, $m_k(t)$, allocated to a hydraulic fracture, which is scaled by the history-matched well rate q_k (with $q_k=q_{well}$ /number of fractures) (Khanal and Weijermars, 2019a):

$$m_k(t) = \frac{Bq_k(t)}{H_k n(1-R_s)} \qquad [\text{ft}^2.\text{mth}^{-1}] \text{ (6-5)}$$

Where B is the formation volume factor, $q_k(t)$ is wellhead production rate with time, arithmetically allocated to each fracture surface, H is the thickness of the reservoir, n is porosity, and R_s is the residual oil left behind after drainage. As the velocity field determines the propagation of the tracer front, we can now accurately define the progressive growth of the drained rock volume due to the porosity structure, accounting for any residual oil left behind. From the total velocity field, the velocities of all the fluid particles can be mapped in the x and y direction using the real and imaginary parts of the velocity potential:

$$V(z) = v_x - iv_y \qquad [\text{ft.mth}^{-1}] \text{ (6-6)}$$

A first order Eulerian scheme allows for the calculation of the streamline trajectories and particle flight time for a well-defined $V(z)$. The generalization of this Eulerian scheme specifies the new position of any particle after the time-step size Δt:

$$z_j(t_j) = z_{j-1}(t_{j-1}) + v(z_{j-1}(t_{j-1}))\Delta t \qquad [\text{ft}] \qquad \text{(6-7)}$$

The tracer front location $R_{i\,TR}$ after a certain time is given by integration of the particle paths over the changing velocity field over that time period. The traveled distance is equated to the typical distance $r_{i\,TR}$ of the actual drained region, now termed the drained rock volume (DRV).

$$r_i(t)_{Tr} = v_n(t).TrTOF \qquad \text{[ft]} \qquad (6\text{-}8)$$

Where TrTOF is simply given by:

$$TrTOF = number\ of\ \ timesteps \times \Delta t \qquad \text{[months]} \qquad (6\text{-}9)$$

Taking the distance traveled in the x-direction we are able to determine the maximum depth of investigation perpendicular to a hydraulic fracture, or the distance in the y-direction normal to Neal 346AH, based on the tracer front expression of Eq. (6-8) (Fig. 6-12).

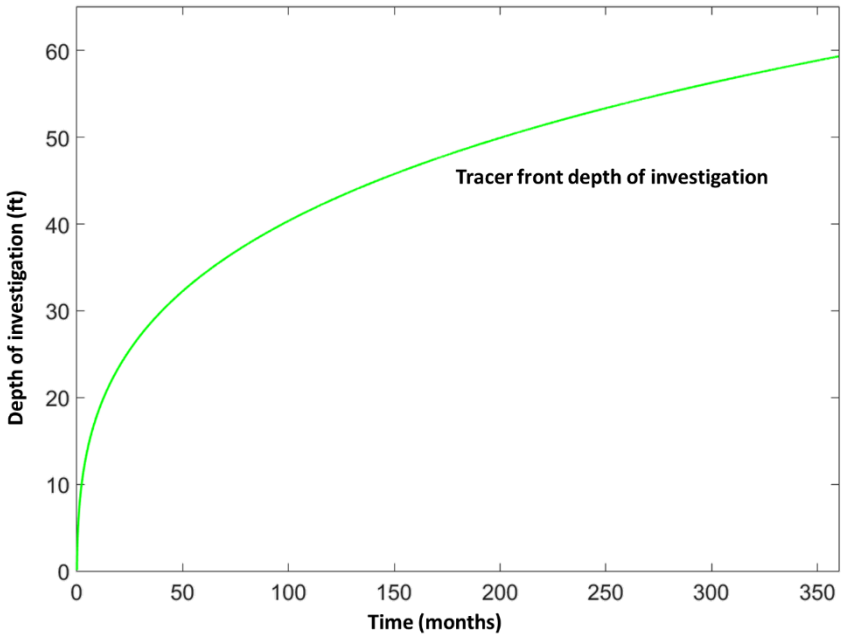

Figure 6-12 Depth of investigation calculated from $r_{i\,TR}$ based on velocity field from history-matched production date of Neal 346AH.

6.3.3. Comparison of DOI and DRV propagation rates

The question now becomes: *How do we relate the DOI of the pressure front to that of the DRV?* The main issue is how to relate a front based on permeability and porosity to one determined from production. To reconcile this, we use history matching based on the well production data to determine the effective permeability of the reservoir. Using the CMG numerical simulator with reservoir data from Table 6-1, we obtain a history matched reservoir permeability of 100 nD. With this history matched permeability and known reservoir porosity we are able to calculate the DTOF for a well with a given production. The difference in depth of investigation due to differences in DTOF and the TrTOF is shown in Fig. 6-13.

Table 6-1 History matched reservoir properties based on field data from Neal 346AH.

Parameters	**Values**	**Units**
TVD	8557	ft
Well Length	6524	ft
Number of Fractures	108	
Fracture Stages (no.)	27	
Fracture Width	0.01	ft
Fracture Spacing	60	ft
Fracture Height	220	ft
Fracture Half-length	105	ft
Fracture Permeability	6000	mD
Initial Reservoir Pressure	5134	psia
Reservoir Temperature	110	°F
Total Compressibility	$3x10^{-6}$	psi^{-1}
Permeability	100	nD
Porosity	4.2	%
Water cut (1/WOR)	0.15	
Residual oil and/or water	0.25	
Oil API	46.8	°API

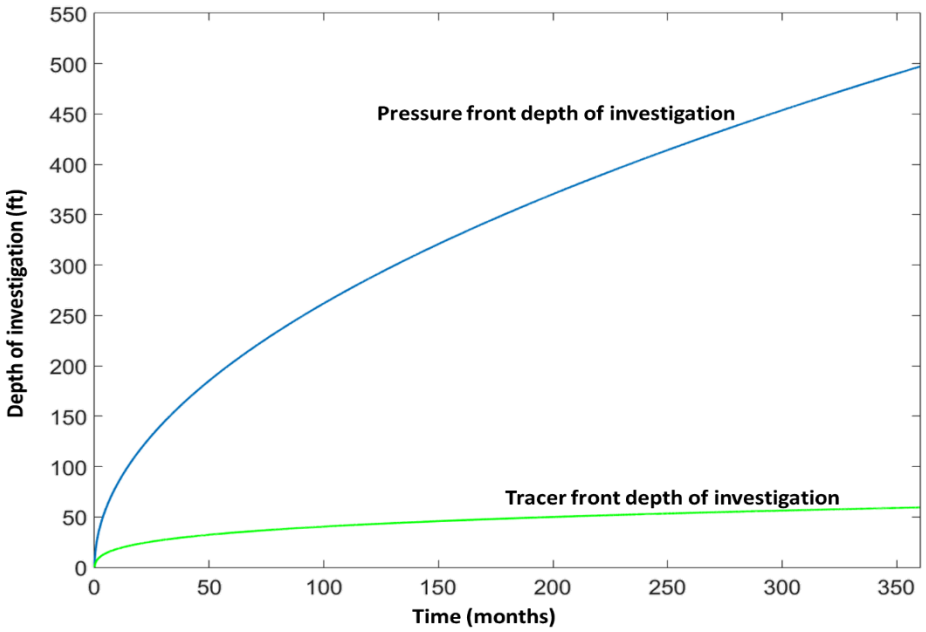

Figure 6-13 Difference in depth of investigation $r_{i\,,}$ calculated from DTOF for history matched reservoir permeability (k=100 nD), and $r_{i\,TR}$, due to the TrTOF using the CAM-based velocity field from history-matched production.

Fig. 6-14 shows the CAM model with the DRV after 30 years production. The DOI of the tracer front given in the plot of Fig. 6-13 is highlighted as the green arrow in Fig. 6-14. The total lag between the DOI of the pressure front and tracer front is given in Fig. 6-15. After a forecasted production time of 30 years (360 months) the tracer front lags behind the diffusive pressure front by approximately 438 ft.

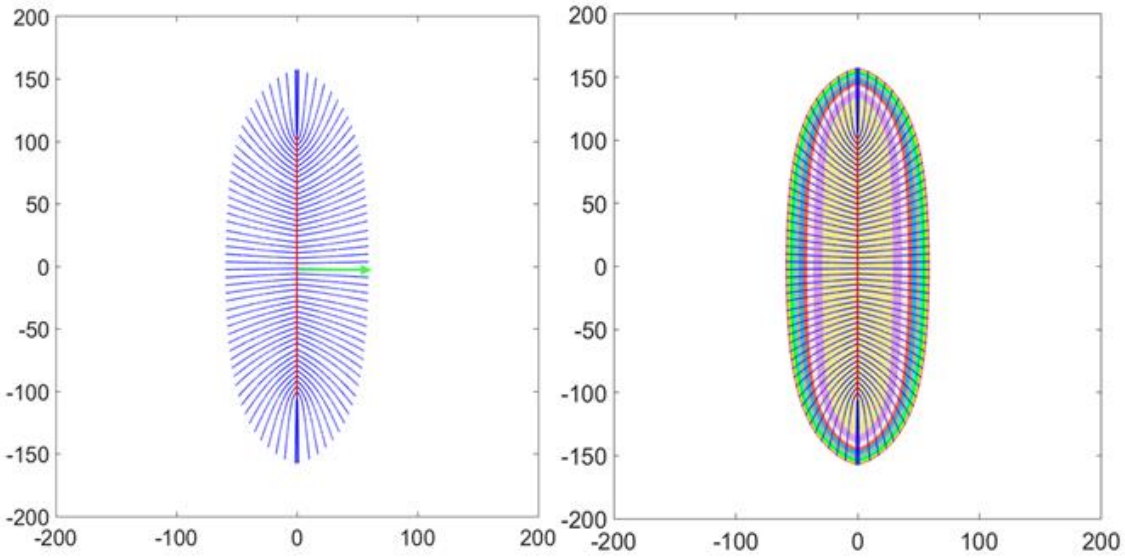

Figure 6-14 DRV after 30 years of production (data from the history-matched Neal 346AH well, Table 6-1) determined from CAM based tracer front model. a) Particle paths, b) Time-of-flight or fluid withdrawal contours. Each color band is for 3 years of production; the first three years are fastest (inner region) and the last 3 years are slowest (final red outline, with negligible surface area).

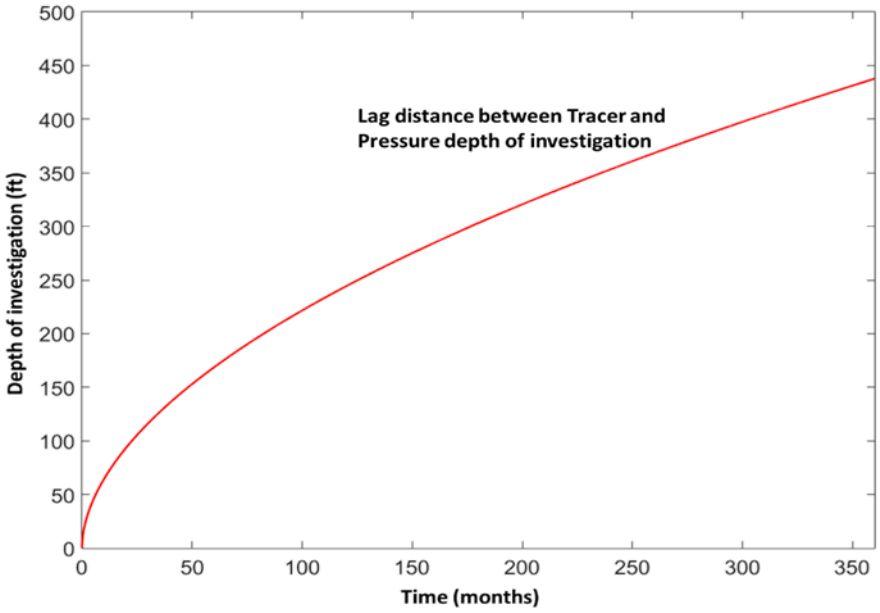

Figure 6-15 Lag in depth of investigation between r_i, due to the DTOF for history matched reservoir permeability (k=100 nD), and $r_{i\,TR}$, based on velocity field from production.

6.4. Discussion

6.4.1. Model strengths

The tracer time of flight requires the use of streamline simulations whereby neutral tracer particles are released at the pressure source/sink and travel based on the velocity field, commonly based on history-matched production data. Although the local velocity is partly controlled by the local pressure gradient, the actual velocity for a given fluid viscosity is inversely proportional to the permeability and linear proportional to the porosity in the simulation model. We make use of the Complex Analysis Method (CAM) to model the tracer time of flight, using real field production data from various hydraulically fractured wells. The results show that the pressure front moves several orders faster than the tracer front. The tracer front determined from actual well production will more accurately delineate the drained rock volume (DRV). By this method we can identify undrained rock volumes between the hydraulic fractures that will be ideal candidates for refracturing to help increase recovery rates from the reservoir. In this paper we showed that for unconventional reservoirs with ultra-low permeability, the pressure front does not actually correspond to the matrix volume where all hydrocarbons have been drained.

6.4.2. Model limitations

The depth of investigation can be calculated by both analytical and numerical methods with the analytical solutions being more apt for homogenous reservoirs. Our models for both the numerical and analytical calculations of DOI show slight

differences. These differences can be attributed to a couple of factors. Firstly the DOI calculated analytically is dependent on reservoir properties of porosity, permeability, compressibility and viscosity. There is a great impact on the DOI with any small changes in either compressibility or viscosity (Fig. 6-11) and these two values are often not reliably known. For the numerical simulation these two properties are also heavily pressure dependent (changing with corresponding pressure changes in the reservoir) while the analytical solution assumes constant values. The second reason to explain the slight discrepancy between the numerical and analytical DOI is the issue of numerical dispersion. The numerical simulation accuracy in terms of distance to a certain pressure drop is heavily dependent on the size of the grid blocks used in the model. This issue does not arise with the analytical solution. Nevertheless there was an overall good match between the numerical and analytical DOI solutions that were run for the Neal 346 case.

6.5. Conclusions

The research outlined in this chapter explains why mismatches evolve, in shale, between pressure depletion zones and the region where fluid recovered via hydraulically fractured wells originated from. An important distinction must be made between the diffusive time of flight, which quantifies the pressure front propagation distance over time, and the “tracer time of flight”, which shows the time of flight for fluid particles from certain reservoir regions to the well. The time required for the transient pressure front propagation to reach a certain location in the reservoir is known as the “diffusive time of flight”.

The distance to the concurrent pressure front location and the source of the pressure wave is commonly called the depth of investigation. The impact of the ultra-low permeability of shale on the Drained Rock Volume (DRV) appears to limit the DRV to only about 12% of the DOI established by the propagating pressure front. The lag between the DOI and the DRV perimeter is one of the principal reasons for the dismal recovery factors of shale oil and gas reservoirs, and is quantified here by simple analytical expressions for the first time.

Some major insights generated in the present study include:

1) New insight on hydrocarbon withdrawal rates in shale reservoirs
2) Drained rock volume in shale mismatches pressure depletion patterns
3) Pressure plots are a poor proxy for migration paths of hydrocarbons
4) Industry should not only resort to traditional pressure depletion simulators
5) CAM simulations provide unique information on drained rock volume

7. COMPARISON OF COMPLEX ANALYSIS METHOD (CAM) WITH FAST MARCHING METHOD (FMM): CONVECTIVE TIME OF FLIGHT VERSUS DIFFUSIVE TIME OF FLIGHT

7.1. Introduction

The CAM models presented in this dissertation visualize the DRV based on tracer front propagation calculated using a novel semi-analytical streamline simulator. The DRV plots shown are representations of the outlined contours of the convective time-of-flight. In comparison, the diffusive time-of-flight, which is not particle based, seeks to model the wave-like propagating pressure front. One method to determine this propagating pressure front and thus the diffusive time-of-flight is by use of the Fast Marching Method (FMM) which is an algorithm that is used to solve the Eikonal equation.

This chapter presents research on the comparison of the CAM model based on convective time-of-flight and the FMM model that uses the diffusive time-of-flight as a measure of the propagating pressure front. Chapter 6 showed the crucial insight of the difference in speed of the propagation of both these fronts. This section seeks to investigate the difference in the responses of the CAM and the FMM model and how this can be used to potentially optimize fracture cluster and well spacing decisions in future work to be performed beyond this dissertation.

7.2. The fast marching method (FMM)

Production from any sub-surface hydrocarbon reservoir requires the creation of a pressure differential between the wellbore and the reservoir. This pressure differential drives fluid movement toward the wellbore then onwards towards the surface. The pressure differential leads to the creation of a pressure front that moves throughout the reservoir. One way to represent this pressure front equation is by the use of a form of the Eikonal equation (King et al., 2016). The Eikonal equation represents a high frequency asymptotic solution of the diffusivity equation and can be solved in either homogenous or heterogeneous reservoirs using a class of solutions called the Fast Marching Method (FMM). This Eikonal equation is given as:

$$\nabla\tau(\vec{x}) \cdot \vec{\vec{\alpha}}(\vec{x}) \cdot \nabla\tau(\vec{x}) = 1 \tag{7-1}$$

Where α is known as the hydraulic diffusivity and is equal to:

$$\vec{\vec{\alpha}}(\vec{x}) = \frac{\vec{\vec{k}}(\vec{x})}{\phi(\vec{x})\mu c_t} \tag{7-2}$$

With k representing permeability, ϕ for porosity, μ representing fluid viscosity and c_t the total compressibility. The use of the FMM gives the diffusive time-of-flight (DTOF) which can then be used as a spatial coordinate to outline the movement of the propagating pressure front. The spatial coordinate that represents the DTOF is given the symbol $\boldsymbol{\tau}$ and can be thought of as the spatial coordinate along the modeled streamtube.

An example of the use of FMM to determine the propagating front can be seen in Fig. 7-1. This figure shows the propagating DTOF front around several hydraulic fractures in a horizontal well. It should be noted that for this homogenous reservoir, the

FMM model shows that as the τ contours evolve over time they approach elliptical shapes. Only after τ becomes greater than a year do the fronts from each individual hydraulic fracture overlap leading to interference effects.

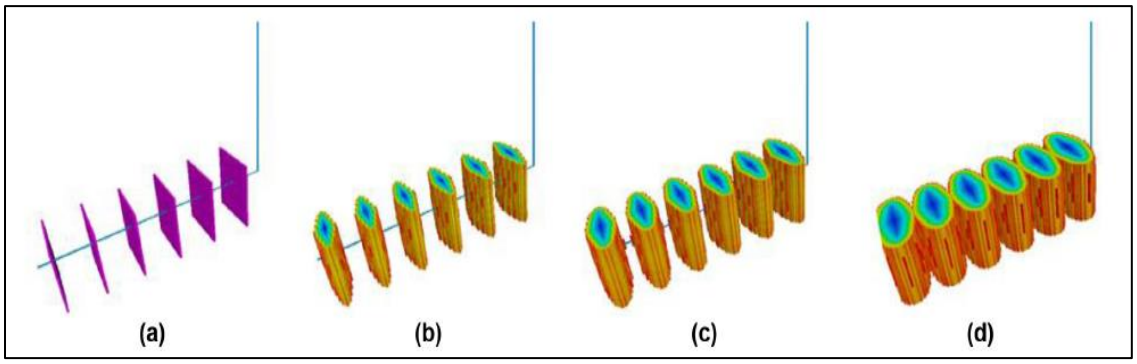

Figure 7-1 Visualization of the solution to the Eikonal equation for a hydraulically fractured well in a homogenous reservoir using FMM. a) Hydraulic fracture ($\tau \approx 0$) b) ($\tau^2/4$) ≤ 3 months c) ($\tau^2/4$) ≤ 6 months d) ($\tau^2/4$) ≤ 1 year.
(after Datta-Gupta et al., 2011)

By expansion of this asymptotic solution it is also possible to determine such quantities as drainage volumes and predicting pressure profiles using FMM (King et al., 2016).

7.3. Comparison between CAM and FMM

This section presents results from initial work to compare the CAM convective time-of-flight tracer front (CTOF) and the diffusive time-of-flight pressure front (DTOF). It should be noted that both methods have different formulations and approaches so simple REV models are used as a starting point to systematically investigate and compare the results from the CAM and FMM models.

7.3.1. CAM approach

The CAM approach is a grid-less, meshless analytical solution and can model fluid flow using either specified far-field or line source/sinks flows. We are able to specify natural fractures in the reservoir space as discrete elements and account for the effects of either enhanced permeability or porosity. Using Eulerian particle tracking in conjunction with the changing velocity field, the propagating CTOF can be visualized to determine the DRV.

7.3.2. FMM approach

This approach can be classified as a numerical method and requires gridding of a mesh, with the use of the mesh's corresponding nodes to calculate the propagating DTOF. Due to this gridding process, decisions have to be made on number of grid blocks, size of grid blocks and the assigning of reservoir properties to these grid blocks such as porosity and permeability. Heterogeneities such as natural fractures are

represented by local grid refinements with grid blocks given higher permeability or porosity.

7.4. Comparative solution results

Comparison of both methods starts with a simple REV model with five natural fractures. These natural fractures are assumed to have differing porosity to that of the reservoir matrix as given in Table 7-1. Assumed width of the natural fracture is 5ft with a length of 25ft. The assumed width, though unrealistic in nature, is used to better show the effects on flow of the natural fractures.

Table 7-1 Matrix and natural fracture porosity used for REV models

Matrix porosity	Natural fracture 1 porosity	Natural fracture 2 porosity	Natural fracture 3 porosity	Natural fracture 4 porosity	Natural fracture 5 porosity
5%	5%	6%	8%	10%	15%

Results from the CAM model using a constant far-field flow of 2.5 ft/yr and a run time of 30 years is shown in Fig. 7-2. As described in detail in Chapter 3, the impact in increased porosity is a slowdown in the CTOF contours leading to a smaller DRV.

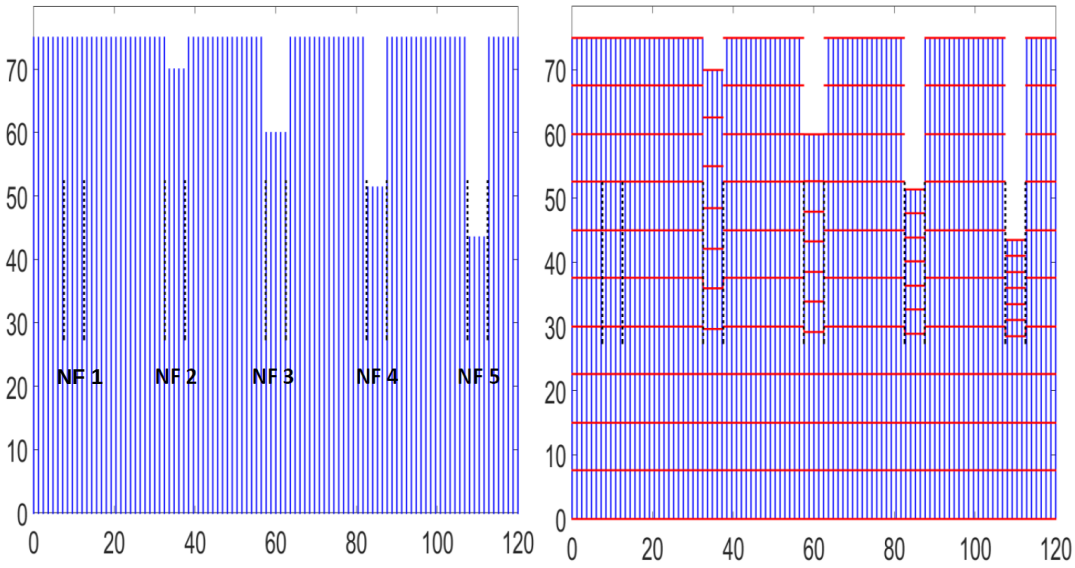

Figure 7-3 REV model showing impact of different natural fracture porosity on CTOF. Streamlines in blue (left side) and CTOF contours in red (right side) every 3 years.

The FMM model requires a gridded approach for creating an REV to compare to the CAM result in Fig. 7-2. The grid used in this model measures 120-ft in the x-direction and 80ft in the y-direction. Grid blocks used measure 1ft by 1ft in size and we use a unit reservoir height for simplicity. The natural fractures are represented by grid blocks of altered porosity and the coordinates (in *i* and *j* representations) of these blocks are given in Table 7-2.

Table 7-2 Definition of natural fractures in FMM grid

	Start block in x-direction	End block in x-direction	Start block in y-direction	End block in y-direction
NF 1	I1_nf1 = 9	I2_nf1 = 13	J1_nf1 = 28	J2_nf1 = 52
NF 2	I1_nf2 = 34	I2_nf2 = 38	J1_nf2 = 28	J2_nf2 = 52
NF 3	I1_nf3 = 58	I2_nf3 = 62	J1_nf3 = 28	J2_nf3 = 52
NF 4	I1_nf4 = 84	I2_nf4 = 88	J1_nf4 = 28	J2_nf4 = 52
NF 5	I1_nf5 = 108	I2_nf5 = 112	J1_nf5 = 28	J2_nf5 = 52

The results from the FMM model with five natural fracture with varying porosity is shown in Fig. 7-3. The FMM model gives the propagating pressure front in terms of the DTOF through the reservoir space with units of $\sqrt{time}$. What is important is that for both the CAM and FMM models, the increasing porosity in the natural fractures from left to right results in a decrease in both the CTOF and DTOF contours. The only aspect that needs reconciling between the models is the use of units of actual time in CAM and $\sqrt{time}$ in FMM.

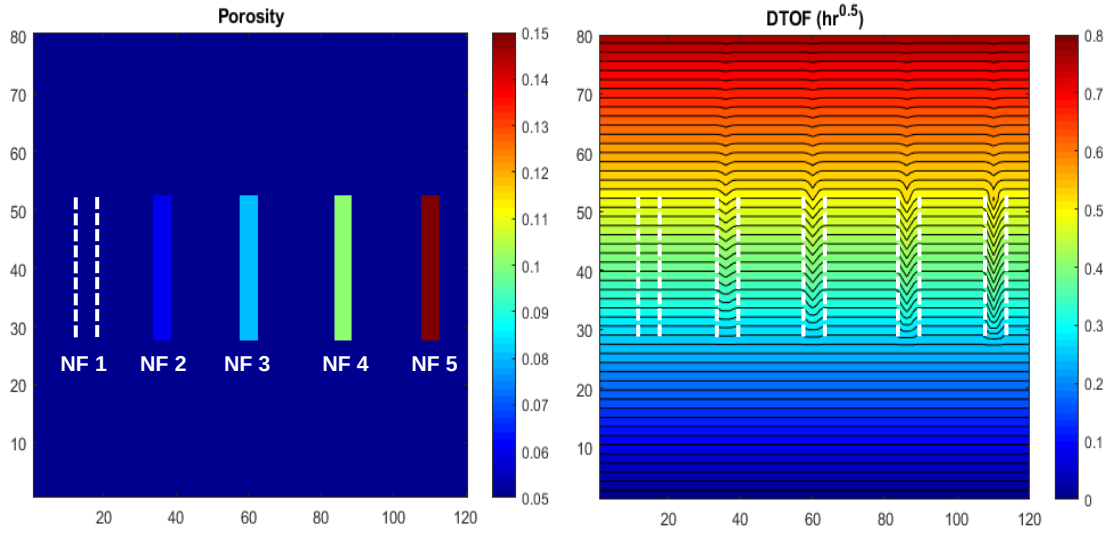

Figure 7-6 REV model showing impact of different natural fracture porosity using FMM. Porosity distribution for grid blocks in model (left side). DTOF contours showing impact of changing porosity in natural fracture (right side).

These initial results show a promising correlation between the CTOF plots realized from the CAM model with the results of DTOF from the FMM models. The CAM model due to being gridless has better resolution for the visualization of streamlines while the FMM when used with the expanded asymptotic solution can generate better visualizations of the propagating pressure front. What we put forward is that the CTOF visualized by CAM more accurately delineates the actual reservoir volume that is drained by wells (point source/sink) and hydraulic fractures (line source/sink).

7.5. Future work

The previous section shows initial results in comparing the CAM and FMM methods in a simple REV model with varying porosity in a simple natural fracture set. Future work will look at the effects of varying permeability in the models as well as comparison of the pressure fields generated. CAM generates an instantaneous snapshot of the pressure field at a given time of production while FMM can capture and visualize pressure transients throughout. This is one of the advantages of the FMM method as it allows the visualization of the changing pressure front in the reservoir as we move from transient flow to pseudo steady state. This future work will provide a more robust comparison between the methods and highlight in which situations the CAM method is better suited to be used.

One common realization between these two methods is the formation of stagnation zones in the reservoir due to flow interference between fracture clusters and also possibly between hydraulically fractured wells. The FMM method when used to model hydraulic fractures shows that as fracture drainage areas (denoted by the DTOF) begin to overlap, there is the creation of stagnation lines which are where fluid flux splits into one fracture or another (Malone et al., 2019).

The interaction between the pressure fronts and the drained rock volume delineated by the tracer front can potentially be used to determine optimum well spacing. We can quantify the DTOF propagation front and the relation of its propagation to the CTOF tracer front (Figs. 7-2 and 7-3). The interplay of the DTOF based on pressure and CTOF based on tracer front is a crucial factor in determining how to optimize

hydrocarbon recovery by the proper spacing of these hydraulically fractured wells. Results throughout this dissertation show that we cannot simply rely on any one propagating front as the basis for well spacing decisions. Use of the pressure front interference solely to determine well spacing leads to large undrained regions between the wells in the reservoir.

Utilizing our insight of the relation between DTOF and CTOF (Figs. 7-2 and 7-3), and the associated onset of well interference we will in future work devise an optimization strategy to determine the optimum well spacing. The anticipated outcome of future modeling work proposed in this last chapter will be to accurately delineate the right balance of DTOF and CTOF to determine the optimum well spacing in unconventional reservoirs, based on reservoir specific data and properties to maximize recovery factors.

8. CONCLUSIONS

8.1. Summary

The main aim of this research work was the creation of a method for high-resolution modeling of drained rock volumes around hydraulic fractures in heterogeneous unconventional reservoirs. This aim was achieved by the use of a novel semi-analytical streamline simulator based on complex analysis methods (CAM). The CAM models are the common theme that links the various chapters of this dissertation. Each chapter in this dissertation introduces new capabilities of the CAM tool ranging from modeling complex hydraulic fracture networks to the inclusion of reservoir heterogeneity in the form of natural fractures. These new and original capabilities are summarized below:

- Chapter 2: The ability to model hydraulic fractures as complex fractal networks.
- Chapter 3: Determining the impact of natural fracture enhanced permeability and storativity on drained rock volume and use of this model with field data from the Hydraulic Fracturing Test Site (HFTS) to determine undrained areas along the well.
- Chapter 4: Moving from 2D DRV representation to a 3D model via the use of physics driven hydraulic fracture conductivity maps.
- Chapter 5: Use of DRV calculation using field data from the Permian Basin to highlight the impact of natural fracture clusters on DRV as well as new insights on recovery factors.

- Chapter 6: Differentiation and insights into fundamental differences between pressure front and tracer front advance.
- Chapter 7: Comparison of CAM with FMM and the differences between Convective time of flight and Diffusive time of flight.

8.2. Conclusions

By the use of newly developed tools, methodologies and insights created over the course of this research, some key conclusions can be made about fluid flow and drained rock volume in hydraulically fractured, heterogeneous unconventional reservoirs:

1) The presence of a complex hydraulic fracture network enhances the drained rock volume via two mechanisms. The first is that with more complex networks, the overall fracture surface area increases resulting in larger access to fluid stored in the reservoir matrix rock. The second mechanism is the suppression of stagnant flow zones when the complexity of the hydraulic fracture network increases.
2) The introduction of hydraulic fracture complexity as fractal networks, and the creation of branching fractures, leads to suppression of the flow stagnation areas, allowing for more efficient drainage. Velocity plots for the fractal networks show a larger spread in the local variation of velocity than for the planar fractures.
3) Natural fractures can affect subsurface fluid flow through three major mechanisms: (i) by enhancing permeability, (ii) by altering the porosity in the fractures, leading to

increased storativity, and (iii) by becoming extensions of the hydraulic fracture network due to reactivation.

4) Natural fractures with an enhanced permeability to that of the matrix create high velocity flow zones which preferentially channel fluid flow through them. At high enough permeabilities (or natural fracture strengths as used in our models), this preferential pathway to flow leads to bypassed regions in the matrix blocks between the natural fractures, which are left undrained. These undrained matrix regions can then be targeted by refracturing to improve recovery factors from hydraulically fractured horizontal wells.
5) Altered porosity or enhanced storativity (due to natural fractures with a higher porosity than the reservoir matrix as investigated in synthetic models) leads to a decrease in the lateral extent of the DRV. The impact of both natural fracture storativity and permeability greatly affect the shape and extent of the DRV around the hydraulic fractures. However, results show that the enhanced flow due to increase natural fracture permeability far outweighs any storativity effects of said natural fractures.
6) Field data on in-situ natural fracture characteristics such as porosity and permeability is sparse and lacking in literature. Industry needs to ensure collection of such data for use in reservoir models to accurately determine subsurface flow and drainage volumes.

7) Based on results from 3D modeling of the hydraulic fracture propagation and CAM models, a significant section of the distal fracture length has hydraulic conductivity so low that no significant contribution is made to the DRV.
8) A major highlight is the difference between the depth of investigation due to the propagating pressure front and the depth of investigation from the tracer front, which is used to calculate the extent of the DRV.
9) The limited growth of DRVs in the shale wells studied here shows that there is considerable potential for undrained regions between the hydraulic fractures that can be accessed by either restimulating the existing hydraulic fracture or by creating new hydraulic fractures by refracturing.
10) New insight on hydrocarbon withdrawal rates in shale reservoirs show that the drained rock volume in shale mismatches pressure depletion patterns. As such pressure plots are a poor proxy for migration paths of hydrocarbons in ultra-low permeability shale reservoirs. Industry should not only resort to traditional pressure depletion simulators but other methods such as CAM simulations which provide unique information on drained rock volume.

REFERENCES

Aguilera, R., 2008. Effect of Fracture Dip and Fracture Tortuosity on Petrophysical Evaluation of Naturally Fractured Reservoirs. Petrol. Soc. Canada. https://doi.org/10.2118/2008-110.

Ajani, A.A. and Kelkar, M.G., 2012. Interference Study in Shale Plays, in: SPE Hydraulic Fracturing Technology Conference. Society of Petroleum Engineers. https://doi.org/10.2118/151045-MS

Al-Kobaisi, M., Ozkan, E., Kazemi, H., Ramirez, B., 2006. Pressure-Transient-Analysis of Horizontal Wells with Transverse, Finite-Conductivity Fractures, in: Canadian International Petroleum Conference. Petroleum Society of Canada. https://doi.org/10.2118/2006-162

Al-Obaidy, R. T. I., Gringarten, A. C., Sovetkin, V., 2014, October 27. Modeling of Induced Hydraulically Fractured Wells in Shale Reservoirs Using "Branched" Fractals. Society of Petroleum Engineers. doi:10.2118/170822-MS.

Andersson, J., and Dverstorp, B., 1987. Conditional Simulations of Fluid Flow in Three-Dimensional Networks of Discrete Fractures. Water Resources Research, 1987;23(10):1876–1886. doi:10.1029/WR023i010p01876

Arps, J.J., 1945. Analysis of Decline Curves. Trans. AIME. doi: 10.2118/945228-G.

Arshadi, M., Zolfaghari, A., Piri, M., Al-Muntasheri, G., Sayed, M., 2017, The Effect of Deformation on Two-phase Flow Through Proppant-packed Fractured Shale Samples: A Micro-scale Experimental Investigation. Advances in Water Resources,

Volume 105, Pages 108-131, ISSN 0309-1708, https://doi.org/10.1016/j.advwatres.2017.04.022.

Barree, R. D. and Miskimins, J. L., 2015, February 3. Calculation and Implications of Breakdown Pressures in Directional Wellbore Stimulation. Society of Petroleum Engineers. doi:10.2118/173356-MS.

Barree, R.D., Cox, S.A., Miskimins, J.L., Gilbert, J. V., Conway, M.W., 2015. Economic Optimization of Horizontal-Well Completions in Unconventional Reservoirs. SPE Prod. Oper. 30, 293–311. https://doi.org/10.2118/168612-PA

Batchelor, G. K., 1967. An Introduction to Fluid Mechanics, Cambridge Univ. Press, Cambridge, U. K.

Beggs, H.D. and Robinson, J.R., 1975. Estimating the Viscosity of Crude Oil Systems. SPE J. Pet. Technol. doi: 10.2118/5434-pa

Berkowitz, B., 2002. Characterizing Flow and Transport in Fractured Geological Media: A Review. Adv.Water Resources, 25, 861–884.

Berta, D., Hardy, H. H., Beier, R. A., 1994, January 1. Fractal Distributions of Reservoir Properties and Their Use in Reservoir Simulation. Society of Petroleum Engineers. doi:10.2118/28734-MS.

Blomquist, P.K., 2016. Wolfcamp Horizontal Play, Midland Basin, West Texas. American Association of Petroleum Geologists Search and Discovery Article #10890, Nov. 28, 2016.

Brown, M., Ozkan, E., Raghavan, R., Kazemi, H., 2011. Practical Solutions for Pressure-Transient Responses of Fractured Horizontal Wells in Unconventional Shale Reservoirs. Society of Petroleum Engineers. doi:10.2118/125043-PA

Cai, L., Ding, D.-Y., Wang, C., Wu, Y.-S., 2015. Accurate and Efficient Simulation of Fracture–Matrix Interaction in Shale Gas Reservoirs. Transp. Porous Media 107, 305–320.

Chen, C.C., and Raghavan, R., 1997. A Multiply-Fractured Horizontal Well in a Rectangular Drainage Region. Society of Petroleum Engineers. doi:10.2118/37072-PA

Chen, T., Clauser, C., Marquart, G., Willbrand, K., Mottaghy, D., 2015. A New Upscaling Method for Fractured Porous Media. Adv. Water Resour. 80, 60–68.

Chen T, Clauser C, Marquart G, Willbrand K, Büsing H, 2016. Modeling Anisotropic Flow and Heat Transport by Using Mimetic Finite Differences. Adv Water Resour 94:441–456. https://doi.org/10.1016/j.advwatres.2016.06.006

Cipolla, C.L., Lewis, R.E., Maxwell, S.C. et al. 2011. Appraising Unconventional Resource Plays: Separating Reservoir Quality from Completion Effectiveness. The International Petroleum Technology Conference, SPE-14677. doi: 10.2523/14677-ms.

Cossio, M., Moridis, G. J., Blasingame, T. A., 2012, January 1. A Semi-Analytic Solution for Flow in Finite-Conductivity Vertical Fractures Using Fractal Theory. Society of Petroleum Engineers. doi:10.2118/153715-MS.

Da Costa, J.A. and Bennett, R.R., 1960. The Pattern of Flow in the Vicinity of a Recharging and Discharging Pair of Wells in an Aquifer Having Areal Parallel Flow, Int. Ass. Sci. Hydrol. Publ., **52,** 524–536.

Dahi-Taleghani, A. and Olson, J. E., 2013, February 1. How Natural Fractures Could Affect Hydraulic-Fracture Geometry. Society of Petroleum Engineers. doi:10.2118/167608-PA

Daneshy, A. A., 2005, January 1. Pressure Variations Inside the Hydraulic Fracture and Its Impact on Fracture Propagation, Conductivity, and Screen-out. Society of Petroleum Engineers. doi:10.2118/95355-MS

Datta-Gupta, A. and King, M.J., 2007. Streamline simulation: theory and practice. Society of Petroleum Engineers.

Datta-Gupta, A., Xie, J., Gupta, N., King, M., Lee, J., 2011, July. Radius of Investigation and its Generalization to Unconventional Reservoirs. Journal of Petroleum Technology, pp. 52-55.

Dershowitz, W. S. and Einstein, H. H., 1987. Three-dimensional Flow Modelling in Jointed Rock Masses. International Society for Rock Mechanics and Rock Engineering Proc. of 6th Cong. ISRM, Vol. 1, pp. 87–92, 1987. doi: ISRM-6CONGRESS-1987-016

Dershowitz W.S., Ambrose, R., Lim, D.H., Cottrell, M.G., 2011. Hydraulic Fracture and Natural Fracture Simulation for Improved Shale Gas Development. American Association of Petroleum Geologists (AAPG) Annual Conference and Exhibition Houston.

Doe, T., Lacazette, A., Dershowitz, W., Knitter, C., 2013. Evaluating the Effect of Natural Fractures on Production from Hydraulically Fractured Wells using Discrete Fracture Network Models. In Proceedings of the First Unconventional Resources Technology Conference, Society of Petroleum Engineers, Denver, Colorado. Paper SPE 168823/URTeC 1581931.

Drillinginfo, Well Card details for several wells. Accessed March 4, 2019.

Du, S., Yoshida, N., Liang, B., Chen, J., 2016. Dynamic Modeling of Hydraulic Fractures Using Multisegment Wells. SPE J. 21, doi:10.2118/175540-MS.

Duda, A., Koza, Z., Matyka, M., 2011. Hydraulic Tortuosity in Arbitrary Porous Media Flow. Phys. Rev. E 84, 036319

Duong, A.N., 1989. A New Approach for Decline-Curve Analysis, in: SPE Production Operations Symposium. Society of Petroleum Engineers. https://doi.org/10.2118/18859-MS

Duong, A.N., 2011. Rate-Decline Analysis for Fracture-Dominated Shale Reservoirs. SPE Reserv. Eval. Eng. 14, 377–387. doi : 10.2118/137748-PA

EIA, 2018, U.S. Crude Oil and Natural Gas Proved Reserves, Year-end 2016, U.S. Energy Information Publication report, https://www.eia.gov/naturalgas/crudeoilreserves/pdf/usreserves.pdf , Accessed on April 26, 2019.

Elsworth, D., 1986. A Hybrid Boundary-Finite Element Analysis Procedure for Fluid Flow Simulation in Fractured Rock Masses. International Journal for Numerical and

Analytical Methods in Geomechanics,1986;10(6):569–584. doi: 10.1002/nag.1610100603

Fisher, M. K., Wright, C. A., Davidson, B. M., Goodwin, A. K., Fielder, E. O., Buckler, W. S., Steinsberger, N. P., 2002, January 1. Integrating Fracture Mapping Technologies to Optimize Stimulations in the Barnett Shale. Society of Petroleum Engineers. doi:10.2118/77441-MS.

Flemisch, B., Berre, I., Boon, W., Fumagalli, A., Schwenck, N., Scotti, A, Stefanson, I., Tatomir, A., 2018.Benchmarks for Single-phase Flow in Fractured Porous Media. Advances in Water Resources, 111, 239-258. doi:10.1016/j.advwatres.2017.10.036

Forand, D., Heesakkers, V., Schwartz, K., 2017, July 24. Constraints on Natural Fracture and In-situ Stress Trends of Unconventional Reservoirs in the Permian Basin, USA. Unconventional Resources Technology Conference. doi:10.15530/URTEC-2017-2669208

Frame, M., Manna, S., Novak, M., 2012. Fractals: Complex Geometry, Patterns, and Scaling in Nature and Society. World Scientific Publishing Company Journal. http://www.worldscinet.com/fractals/mkt/aims_scope.shtml.

Gale, J.F.W., Reed, R.M., Holder, J. 2007. Natural Fractures in the Barnett Shale and Their Importance for Hydraulic Fracture Treatments. AAPGBull. **91:** 603-622.

Gale, J., Laubach, S., Olson, J., Eichhubl, P., Fall, A., 2014. Natural Fractures in Shale: A Review and New Observations. AAPG Bulletin, Volume 98, No. 11, Pages 2165-2216. doi: 10.1306/08121413151.

Gale, J. F. W., Elliott, S. J., Laubach, S. E., 2018, August 9. Hydraulic Fractures in Core from Stimulated Reservoirs: Core Fracture Description of HFTS Slant Core, Midland Basin, West Texas. Unconventional Resources Technology Conference. doi:10.15530/URTEC-2018-2902624

Gardiner, W. B., 1990. Fault fabric and Structural Subprovinces of the Central basin Platform: A model for strike - slip movement, in Flis, J. E., and Price. R. C., eds., Permian basin Oil and Gas Fields: Innovative Ideas in Exploration and Development: Mid land. West Tex.as Geological Society, 90-87, p. 15-27.

Gaswirth, S.B., 2017. Assessment of Undiscovered Continuous Oil Resources in the Wolfcamp Shale of the Midland basin, West Texas, AAPG ACE proceeding, April 2017.

Grechka V, Li Z, Howell R, Vavrycuk V., 2017. Single-well Moment Tensor Inversion of Tensile Microseismic Events. In: 2017 SEG international exposition and annual meeting, 24–29 September. Houston; SEG-2017-16890707.

Gutierrez, M., Øino, L.E., Nygård, R., 2000. Stress-Dependent Permeability of a De-Mineralised Fracture in Shale. Mar.Petrol. Geol. **17** (8): 895-907. http://dx.doi.org/10.16/S0264-8172(00)00027-1.

Hamlin, H. S. and Baumgardner, R. W., 2012, May. Wolfberry play, Midland Basin, West Texas. AAPG Southwest Section Meeting, USA.

Han, G., 2017. Highlights from Hydraulic Fracturing Community: From Physics to Modelling, URTeC 2768686.

Han, J., 2007 Plant Simulation Based on Fusion of L-system and IFS. Computational

Science-ICCS, 1091-1098.

Holzbecher, E., 2005. Analytical Solution for Two-dimensional Groundwater Flow in Presence of Two Isopotential Lines, Water Resour. Res., **41**(12), 1–7.

Holzbecher, E. and Sauter, M., 2010. The Doublet System Simulator, in Proceedings of the World Geothermal Congress 2010, Bali, Indonesia, 2010 April 25–29 April.

Holzbecher, E., Oberdorfer, P., Maier, F., Jin, Y., Sauter, M., 2011. Simulation of Deep Geothermal Heat Production, in Proceedings of the 2011 COMSOL Conference 2011, Stuttgart, Germany, 26–28 October.

Huang J. and Kim K., 1993. Fracture Process Zone Development During Hydraulic Fracturing. Int J Rock Mech Min Sci Geomech Abstr.;30(7):1295–8. https://doi.org/10.1016/0148-9062(93)90111-P.

Huang, T., Guo, X., Chen, F., 2015. Modeling Transient Flow Behavior of a Multiscale Triple Porosity Model for Shale Gas Reservoirs. Journal of Natural Gas Science and Engineering, Volume 23, Pages 33-46, https://doi.org/10.1016/j.jngse.2015.01.022.

Izadi, G., Moos, D., Cruz, L., Gaither, M., Chiaramonte, L., Johnson, S., 2017. Fully Coupled 3-D Hydraulic Fracture Growth in the Presence of Weak Horizontal Interfaces, in: SPE Hydraulic Fracturing Technology Conference and Exhibition. Society of Petroleum Engineers. https://doi.org/10.2118/184854-MS

Jing, L. and Stephansson, O., 2007. Fundamentals of Discrete Element Methods for Rock Engineering. Developments in Geotechnical Engineering, Elsevier, Volume 85, https://doi.org/10.1016/S0165-1250(07)85010-3.

Jones, J. R., Volz, R., Djasmari, W., 2013, November 5. Fracture Complexity Impacts on Pressure Transient Responses From Horizontal Wells Completed With Multiple Hydraulic Fracture Stages. Society of Petroleum Engineers. doi:10.2118/167120-MS.

Kang, S., Datta-gupta, A., Lee, W.J.J., 2011. Impact of Natural Fractures in Drainage Volume Calculations and Optimal Well Placement in Tight Gas Reservoirs. North American Unconventional Gas 134 Conference and Exhibition, SPE-144338. doi: 10.2118/144338-ms

Katz, A. and Thompson A.H., 1985. Fractal Sandstone Pores: Implications for Conductivity and Pore Formation. Physical Review Letters, 54, 1325.

Kazemi, H., Merrill Jr., L.S., Porterfield, K.L, Zeman P.R., 1976. Numerical Simulation of Water-Oil Flow in Naturally Fractured Reservoirs. SPE Journal 6: 317-326. doi: 10.2118/5719-pa.

Khanal, A., Khoshghadam, M., Lee, W.J., 2015a. Optimal Decline Curve Analysis (DCA) Models for Liquid Rich Shale (LRS) Gas Condensate Reservoirs, in: SPE Liquids-Rich Basins Conference - North America. Society of Petroleum Engineers. doi: 10.2118/175530-MS

Khanal, A., Khoshghadam, M., Makinde, I., Lee, W. J., 2015b. Modeling Production Decline in Liquid Rich Shale (LRS) Gas Condensate Reservoirs. Society of Petroleum Engineers. doi:10.2118/175913-MS

Khanal, A., Nandlal, K., Weijermars, R., 2019. Impact of Natural Fractures on the Shape and Location of Drained Rock Volumes in Unconventional Reservoirs: Case Studies from the Permian Basin. SPE URTeC 2019 Denver Colorado 22-24 July, URTeC 1082.

Khanal, A. and Weijermars, R., 2019a. Pressure Depletion and Drained Rock Volume near Hydraulically Fractured Parent and Child Wells. J. Pet. Sci. Eng. 172, 607–626. doi: 10.1016/j.petrol.2018.09.070.

Khanal, A. and Weijermars, R., 2019b. Visualization of Drained Rock Volume (DRV) in Hydraulically Fractured Reservoirs With and Without Natural Fractures Using Complex Analysis Methods (CAM). Pet. Sci. (2019). doi.org/10.1007/s12182-019-0315-9

Khanal, A. and Weijermars, R., 2019c. Modeling Flow and Pressure Fields in Porous Media with Discrete Fractures and Smart Placement of Branch Cuts for Variant and Invariant Complex Potentials Appl. Math. Model. In Review.

Khanal, A. and Weijermars, R., 2019d. Estimation of Drained Rock Volume (DRV) and Pressure Depletion using Discrete Fracture Model and Complex Analysis Methods SPE Europec featured at 81st EAGE Conference and Exhibition, SPE-195433-MS.

Khoshghadam, M., Khanal, A., Lee, W. J., 2015. Numerical Study of Impact of Nano-Pores on Gas-Oil Ratio and Production Mechanisms in Liquid-Rich Shale Oil Reservoirs. Unconventional Resources Technology Conference. doi:10.15530/URTEC-2015-2154191

Khoshghadam, M., Khanal, A., Rabinejadganji, N., Lee, W. J., 2016. How to Model and Improve Our Understanding of Liquid-Rich Shale Reservoirs with Complex

Organic/Inorganic Pore Network. Unconventional Resources Technology Conference. doi:10.15530/URTEC-2016-2459272

Khoshghadam, M., Khanal, A., Yu, C., Rabinejadganji, N., and Lee, W. J., 2017. Producing Gas-Oil Ratio Behavior of Unconventional Volatile-Oil Reservoirs, and Its Application in Production Diagnostics and Decline Curve Analysis. Unconventional Resources Technology Conference. doi:10.15530/URTEC-2017-2670925

Khristianovic, S.A. and Zheltov, Y.P., 1955. Formation of Vertical Fractures by Means of Highly Viscous Liquid. Proceeding 4th World Pet. Congr.

Kilaru, S., Goud, B.K., Rao, V.K., 2013. Crustal Structure of the Western Indian Shield: Model Based on Regional Gravity and Magnetic Data, Geoscience Frontiers 4 (06), 717 – 728. doi: 10.1016/j.gsf.2013.02.006.

Kim, B. Y., Akkutlu, I. Y., Martysevich, V., Dusterhoft, R., 2018, January 23. Laboratory Measurement of Microproppant Placement Quality using Split Core Plug Permeability under Stress. Society of Petroleum Engineers. doi:10.2118/189832-MS

Kim, J., Seo, Y., Wang, J., Lee, Y. 2019. History Matching and Forecast of Shale Gas Production Considering Hydraulic Fracture Closing. Energies, MDPI.

King, G.E. and Valencia, R.L., 2016. Well Integrity for Fracturing and Re-Fracturing: What Is Needed and Why?, in: SPE Hydraulic Fracturing Technology Conference. Society of Petroleum Engineers. https://doi.org/10.2118/179120-MS

King, M. J., Wang, Z., Datta-Gupta, A., 2016, May 30. Asymptotic Solutions of the Diffusivity Equation and Their Applications. Society of Petroleum Engineers. https://doi.org/10.2118/180149-MS.

Kresse, O., Cohen, C., Weng, X., Wu, R., Gu, H., 2011. Numerical Modeling of Hydraulic Fracturing in Naturally Fractured Formations, in: 45th US Rock Mechanics / Geomechanics Symposium. Society of Petroleum Engineers, pp. 61–68.

Kresse, O., Weng, X., Gu, H., Wu, R., 2013. Numerical Modeling of Hydraulic Fractures Interaction in Complex Naturally Fractured Formations. Rock Mech. Rock Eng. 46, 555–568. https://doi.org/10.1007/s00603-012-0359-2

Kumar, A., Shrivastava, K., Manchanda, R., Sharma, M., 2019, July 25. An Efficient Method for Modeling Discrete Fracture Networks in Geomechanical Reservoir Simulation. Unconventional Resources Technology Conference. doi:10.105530/urtec-2019-1083

Kundu, P. K. and Cohen, I. M., 2002. Fluid Mechanics, 2nd ed., Academic Press, San Diego, Calif.

Kurtoglu, B. and Salman, A., 2015. How to Utilize Hydraulic Fracture Interference to Improve Unconventional Development, in: Abu Dhabi International Petroleum Exhibition and Conference. Society of Petroleum Engineers. https://doi.org/10.2118/177953-MS

Kvale, E. P., and Rahman, M., 2016. Depositional Facies and Organic Content of Upper Wolfcamp Formation (Permian) Delaware Basin and Implications for Sequence Stratigraphy and Hydrocarbon Source. Unconventional Resources Technology Conference. doi:10.15530/URTEC-2016-2457495

Laubach, S. E., 2003. Practical Approaches to Identifying Sealed and Open Fractures: AAPG Bulletin, v. 87, no. 4, p. 561–579.

Lawal, H., Jackson, G., Abolo, N., Flores, C., 2013. A Novel Approach to Modeling and Forecasting Frac Hits in Shale Gas Wells, in: EAGE Annual Conference & Exhibition Incorporating SPE Europec. Society of Petroleum Engineers. https://doi.org/10.2118/164898-MS

Lee, D. S., Herman, J. D., Elsworth, D., Kim, H. T., Lee, H. S., 2011. A Critical Evaluation of Unconventional Gas Recovery from the Marcellus Shale, Northeastern United States. KSCE Journal of Civil Engineering, v. 15, no. 4, p. 679–687, doi:10.1007/s12205-011-0008-4.

Lee, S.H., Lough, M.F., Jensen, C.L., 2001. Hierarchical Modeling of Flow in Naturally Fractured Formations with Multiple Length Scales. Water Resour. Res. **37** (3): 443–455. http://dx.doi.org/10.1029/2000WR900340.

Li, J., Pei, Y., Jiang, H., Zhao, L., Li, L., Zhou, H., … Zhang, Z., 2016, November 7. Tracer Flowback Based Fracture Network Characterization in Hydraulic Fracturing. Society of Petroleum Engineers.doi:10.2118/183444-MS

Li, L. and Lee, S. H. 2008. Efficient Field-Scale Simulation of Black Oil in a Naturally Fractured Reservoir through Discrete Fracture Networks and Homogenized Media. SPE Reservoir Evaluation and Engineering, 11(04).

Lindenmayer, A., 1968. Mathematical Methods for Cellular Interactions in Development, II. Simple and Branching Filaments with Two-sided Inputs. Journal of Theoretical Biology, 18 (3), 300.

Long, J. C. S., Remer, J. S., Wilson, C. R., Witherspoon, P. A., 1982. Porous Media Equivalents for Networks of Discontinuous Fractures, Water Resour. Res., 18(3), 645-658.

Lorenz, J.C., Sterling, J.L., Schechter David S., Whigham, C.L., Jensen, J.L., 2002. Natural Fractures in the Spraberry Formation, Midland basin, Texas: The Effects of Mechanical Stratigraphy on Fracture Variability and Reservoir Behavior. Am. Assoc. Pet. Geol. Bull. 86, 505–524. https://doi.org/10.1306/61EEDB20-173E-11D7-8645000102C1865D

Loughry, D., Epps, D., Forrest, J., 2015. Using Pad ISIP, DFIT, and ESP Data to Generate a Pore Pressure Model for the Midland Basin, in: Proceedings of the 3rd Unconventional Resources Technology Conference. American Association of Petroleum Geologists, Tulsa, OK, USA. https://doi.org/10.15530/urtec-2015-2162973

Ma, Jianjun, 2015. Review of Permeability Evolution Model for Fractured Porous Media. Journal of Rock Mechanics and Geotechnical Engineering, Volume 7, Issue 3, Pages 351-357, https://doi.org/10.1016/j.jrmge.2014.12.003.

Malone, A., King, M. J., Wang, Z., 2019, June 3. Characterization of Multiple Transverse Fracture Wells Using the Asymptotic Approximation of the Diffusivity Equation. Society of Petroleum Engineers. doi:10.2118/195505-MS

Malpani, R., Sinha, S., Charry, L., Sinosic, B., Clark, B., Gakhar, K., 2015. Improving Hydrocarbon Recovery of Horizontal Shale Wells Through Refracturing, in:

SPE/CSUR Unconventional Resources Conference. Society of Petroleum Engineers. https://doi.org/10.2118/175920-MS

Mandelbrot, B.B., 1979. Fractals: Form, Chance and Dimension. San Francisco (CA, USA): WH Freeman and Co., 16+ 365 p.1.

Maxwell, S. C., Urbancic, T. I., Steinsberger, N., Zinno, R., 2002, January 1. Microseismic Imaging of Hydraulic Fracture Complexity in the Barnett Shale. Society of Petroleum Engineers. doi:10.2118/77440-MS.

McKenzie, N.R., Hughes, N.C., Myrow, P.M., Banerjee, D.M., Deb, M., Planavsky, N.J., 2013. New Age Constraints for the Proterozoic Aravalli-Delhi Successions of India and Their Implications, Precambrian Res. 238, 120 – 128. doi: 10.1016/j.precamres.2013.10.006.

Meyer, B. R. and Bazan, L. W., 2011, January 1. A Discrete Fracture Network Model for Hydraulically Induced Fractures - Theory, Parametric and Case Studies. Society of Petroleum Engineers. doi:10.2118/140514-MS.

Milne-Thomson, L.M., 1962. Theoretical Hydrodynamics, 4th edn, pp. 200 – 208, Macmillan and Co. Ltd.

Moinfar, A.; Varavei, A.; Sepehrnoori, K.; Johns, R. T., 2014. Development of an Efficient Embedded Discrete Fracture Model for 3D Compositional Reservoir Simulation in Fractured Reservoirs. SPE Journal 2014, 19, 289−303.

Mukhopadhyay, S. and Bhattacharya, A. K., 2009. Bidasar Ophiolite Suite in the Trans-Aravalli Region of Rajasthan; A New Discovery of Geotectonic Significance. Indian Journal of Geosciences 63(4): 345-350.

Muskat, M., 1937. Flow of Homogenous Fluids, International Human Resources Development Corporation, Boston, Massachusetts.

Muskat, M., 1949. The Theory of Potentiometric Models. Trans. AIME 179, 216–221. https://doi.org/10.2118/949216-G.

Nagel, N., Zhang, F., Sanchez-Nagel, M., Lee, B., Agharazi, A., 2013, November 5. Stress Shadow Evaluations for Completion Design in Unconventional Plays. Society of Petroleum Engineers. doi:10.2118/167128-MS

Nandlal, K. and Weijermars, R., 2019a. Drained Rock Volume around Hydraulic Fractures in Porous Media: Planar Fractures versus Fractal Networks. Springer Pet. Sci. https://doi.org/10.1007/s12182-019-0333-7

Nandlal, K. and Weijermars, R., 2019b. Impact on Drained Rock Volume (DRV) of Storativity and Enhanced Permeability in Naturally Fractured Reservoirs: Upscaled Field Case from Hydraulic Fracturing Test Site (HFTS), Wolfcamp Formation, Midland Badin, West Texas. MDPI Energies. 12(20), 3852, https://doi.org/10.3390/en12203852.

Nelson, R. A., 1985. Geologic Analysis of Naturally Fractured Reservoirs, Houston, Gulf Publishing, 320 p.

Nelson, R., 2001. Geological Analysis of Naturally Fractured Reservoirs, Gulf Professional Publishing 2nd Edition.

Nelson, R., Zuo, L., Weijermars, R. and Crowdy, D., 2018. Outer Boundary Effects in a Petroleum Reservoir (Quitman field, East Texas): Applying Improved Analytical

Methods for Modelling and Visualization of Flood Displacement Fronts, J. Pet. Sci. Eng., 166 (2018), pp. 1018-1041

Neuman, S.P., 2005. Trends, Prospects and Challenges in Quantifying Flow and Transport Through Fractured Rocks. Hydrogeol. J., 13, 124–147.

Niu, G., Sun, J., Parsegov, S., Schechter, D., 2017. Integration of Core Analysis, Pumping Schedule and Microseismicity to Reduce Uncertainties of Production Performance of Complex Fracture Networks for Multi-Stage Hydraulically Fractured Reservoirs, in: SPE Eastern Regional Meeting. Society of Petroleum Engineers, Lexington, Kentucky, USA. https://doi.org/10.2118/187524-MS

Olorode, O., Freeman, C.M., Moridis, G., and Blasingame, T.A., 2013. High-Resolution Numerical Modeling of Complex and Irregular Fracture Patterns in Shale-Gas Reservoirs and Tight Gas Reservoirs. SPE Reserv. Eval. Eng. 16, doi:10.2118/152482-PA.

Olson, Jon E., 1997. Natural Fracture Pattern Characterization Using a Mechanically-Based Model Constrained by Geologic Data—Moving Closer to a Predictive Tool. International Journal of Rock Mechanics and Mining Sciences, vol. 34, no. 3-4, 1997, doi: 10.1016/s1365-1609(97)00227-x.

Olson, J.E., 2008. Multi-Fracture Propagation Modeling: Applications to Hydraulic Fracturing in Shales and Tight Gas Sands. The 42nd U.S. Rock Mechanics Symposium (USRMS), Paper 08-327.

Pandey, C.S., Richards, L.E., Louat, N., Dempsey, B.D., Schwoeble, A.J., 1987. Fractal Characterization of Fractured Surfaces. Acta Metallurgica, 35 (7), 1633- 1637.

Pankaj, P., and Li J, 2018. Impact of Natural Fractures Beyond the Hydraulic Fracture Complexity in Unconventional Reservoirs – A Permian Case Study. Proceedings of the 6th Unconventional Resources Technology Conference. doi:10.15530/urtec-2018-2874839.

Parsegov, S.G., Schechter, D.S., 2017. Mudstone Nanoindentation — How Little Cuttings can Make a Big Difference, in: Gulf Coast Association of Geological Societies Transactions. Gulf Coast Association of Geological Societies (GCAGS) Transactions, San Antonio, TX, pp. 477–480.

Parsegov, S.G., Nandlal, K., Schechter, D.S., and Weijermars, R., 2018a. Physics-Driven Optimization of Drained Rock Volume for Multistage Fracturing: Field Example from the Wolfcamp Formation, Midland Basin. URTeC: 2879159. Unconventional Resources Technology Conference held in Houston, Texas, USA, 23-25 July 2018. DOI 10.15530/urtec-2018-2879159.

Parsegov, S.G., Niu, G., Schechter, D.S., Laprea-Bigott, M., 2018b. Benefits of Engineering Fracture Design. Lessons Learned from Underperformers in the Midland Basin., in: SPE Hydraulic Fracturing Technology Conference and Exhibition. Society of Petroleum Engineers, The Woodlands, Texas, USA. https://doi.org/10.2118/189859-MS

Perkins, T.K., Kern, L.R., 1961. Widths of Hydraulic Fractures. J. Pet. Technol. 13, 937–949. https://doi.org/10.2118/89-PA

Pólya, G., and G. Latta, 1974. Complex Variables, John Wiley & Sons, New York.

Potter, H.D.P., 2008. On Conformal Mappings and Vector Fields, Senior Thesis, Marietta College, Marietta, Ohio.

Pradhan, V.R., Meert, J.G., Pandit, M.K., Kamenov, G., Mondal, M.E.A., 2012. Paleomagnetic and Geochronological Studies of the Mafic Dyke Swarms of Bundelkhand Craton, Central India: Implications for the Tectonic Evolution and Paleogeographic Reconstructions. Precambrian Res.;198–199:51 76. https://doi.org/10.1016/j.precamres.2011.11.011.

Raterman, K. T., Farrell, H. E., Mora, O. S., Janssen, A. L., Gomez, G. A., Busetti, S., … Warren, M., 2017, July 24. Sampling a Stimulated Rock Volume: An Eagle Ford Example. Unconventional Resources Technology Conference. doi: 10.15530/URTEC-2017-2670034.

Rittenhouse, S., Currie, J., Blumstein, R., 2016. Using Mud Weights, DST, and DFIT Data to Generate a Regional Pore Pressure Model for the Delaware Basin, New Mexico and Texas. Unconventional Resources Technology Conference. URTEC_2450423-MS.

Robertson, S., 1988. Generalized Hyperbolic Equation. Society of Petroleum Engineers, SPE-18731.

Ruppel S.C., Jones R. H., Breton C.L., Kane J.A., 2005. Preparation of Maps Depicting Geothermal Gradient and Precambrian Structure in the Permian Basin. Contract report to USGS 04CRSA0834. Bureau of Economic Geology.

Sang G, Elsworth D, Miao X, Mao X, Wang J., 2016. Numerical Study of a Stress Dependent Triple Porosity Model for Shale Gas Reservoirs Accommodating Gas

Diffusion in Kerogen. J Nat Gas Sci Eng.; 32: 423–438. https://doi.org/10.1016/j.jngse.2016.04.044.

Sato, K., 2015. Complex Analysis for Practical Engineering. Springer International Publishing, Cham. https://doi.org/10.1007/978-3-319-13063-7.

Scanlon, B.R., Reedy, R.C., Male, F., Walsh, M., 2017. Water Issues Related to Transitioning from Conventional to Unconventional Oil Production in the Permian Basin. Environ. Sci. Technol. 51, 10903–10912. https://doi.org/10.1021/acs.est.7b02185

Shrivastava, K. and Sharma, M. M., 2018, January 23. Proppant Transport in Complex Fracture Networks. Society of Petroleum Engineers. doi:10.2118/189895-MS

Shrivastava, K., Hwang, J., Sharma, M., 2018, September 24. Formation of Complex Fracture Networks in the Wolfcamp Shale: Calibrating Model Predictions with Core Measurements from the Hydraulic Fracturing Test Site. Society of Petroleum Engineers. doi:10.2118/191630-MS

Sinha, S., Devegowda, D., Deka, B., 2017. Quantification of Recovery Factors in Downspaced Wells: Application to the Eagle Ford Shale. In: SPE Western Regional Meeting. Society of Petroleum Engineers. doi: 10.2118/185748-MS.

Smith, M.B., Bale, A.B., Britt, L.K., Klein, H.H., Siebrits, E., Dang, X., 2001. Layered Modulus Effects on Fracture Propagation, Proppant Placement, and Fracture Modeling, in: SPE Annual Technical Conference and Exhibition. Society of Petroleum Engineers, p. 14. https://doi.org/10.2118/71654-MS

Soeder, D.J., 1988. Porosity and Permeability of Eastern Devonian Gas Shale. Society of Petroleum Engineers, SPE Formation Evaluation, March, p. 116-124.

Stalgorova, K., and Mattar, L., 2013, July 31. Analytical Model for Unconventional Multifractured Composite Systems. Society of Petroleum Engineers. doi:10.2118/162516-PATRRC. 2019.

Strack, O. D. L., 1989. Groundwater Mechanics, Prentice-Hall, Englewood Cliffs, N.J.

Sun, J., and Schechter, D. S., 2014. Optimization-Based Unstructured Meshing Algorithms for Simulation of Hydraulically and Naturally Fractured Reservoirs with Variable Distribution of Fracture Aperture, Spacing, Length and Strike. Society of Petroleum Engineers. doi:10.2118/170703-MS

Texas Permian Basin Oil Production 2008 through January 2019. https://www.rrc.state.tx.us/oil-gas/major-oil-and-gas-formations/permian-basin-information/. Accessed on April 20, 2019.

Tiab, D., Restrepo, D. P., Igbokoyi, A. O., 2006, January 1. Fracture Porosity of Naturally Fractured Reservoirs. Society of Petroleum Engineers. doi:10.2118/104056-MS

Tinni, A., Sondergeld, C., Rai, C., 2014. Particle Size Effect on Porosity and Specific Surface Area Measurements of Shales. International Symposium of the Society of Core Analysts, Avignon, France, 8-11 September.

TRRC, 2014. Final Order Amending Field Rules for the Spraberry (Trend Area) Field Various Counties, Texas.

U.S. Energy Information Administration (EIA), 2018. Permian Basin, Wolfcamp Shale Play, Geology review.

Valko, P. P., and Amini, S., 2007. The Method of Distributed Volumetric Sources for Calculating the Transient and Pseudosteady-State Productivity of Complex Well-Fracture Configurations. Society of Petroleum Engineers. doi:10.2118/106279-MS

Van Harmelen, A. and Weijermars, R., 2018. Complex Analytical Solutions for Flow in Hydraulically Fractured Hydrocarbon Reservoirs With and Without Natural Fractures. Applied Mathematical Modelling, vol. 56, p. 137-157.

Vasco, D.W., Karasaki, K., and Keers, H., 2000. Estimation of Reservoir Properties using Transient Pressure Data: An Asymptotic Approach. Water Resources Res. 36, 3447-3465.

Walls J., Morcote A., Hintzman T., and Everts M., 2016. Comparative Core Analysis from a Wolfcamp Formation Well; A Case Study. International Symposium of the Society of Core Analysts in Snow Mass, Colorado. SCA2016-044.

Wang, J. and Weijermars, R., 2019. Expansion of Horizontal Wellbore Stability Model for Elastically Anisotropic Shale Formations with Anisotropic Failure Criteria: Permian Basin Case Study. American Rock Mechanics Association. ARMA 19–2062.

Wang, W., Su, Y., Sheng, G., Cossio, M., Shang, Y., 2015. A Mathematical Model Considering Complex Fractures and Fractal Flow for Pressure Transient Analysis of Fractured Horizontal Wells in Unconventional Reservoirs. Journal of Natural Gas Science and Engineering, 23, 139-147.

Wang, W., Su, Y., Zhou, Z., Sheng, G., Zhou, R., Tang, M., … An, J., 2017, October 17. Method of Characterization of Complex Fracture Network with Combination of

Microseismic using Fractal theory. Society of Petroleum Engineers. doi:10.2118/186209-MS.

Wang, WD., Su, YL., Zhang, Q. et al., 2018 Performance-based Fractal Fracture Network Model for Complex Fracture Network Simulation. Pet. Sci. 15: 126. https://doi.org/10.1007/s12182-017-0202-1.

Warpinski, N.R., Moschovidis, Z.A., Parker, C.D., Abou-Sayed, I.S., 1994. Comparison Study of Hydraulic Fracturing Models—Test Case: GRI Staged Field Experiment No. 3 (includes associated paper 28158). SPE Prod. Facil. 9, 7–16. https://doi.org/10.2118/25890-PA

Warren, J.E. and Root, P.J., 1963. The Behavior of Naturally Fractured Reservoirs. SPE J. 3, 245–255. https://doi.org/10.2118/426-PA.

Weber, K. J., and Bakker, M., 1981. Fracture and Vuggy Porosity. Society of Petroleum Engineers 56th Annual Fall Technical Conference, San Antonio, 11 p.

Weijermars, R., and Poliakov, A., 1993. Stream Functions and Complex Potentials: Implications for the Development of Rock Fabric and the Continuum Assumption, Tectonophysics, 220, 33–50.

Weijermars, R., 2014. Visualization of Space Competition and Plume Formation with Complex Potentials for Multiple Source Flows: Some Examples and Novel Application to Chao Lava Flow (Chile). Journal of Geophysical Research, Vol. 119, issue 3, p. 2397-2414.

Weijermars, R., Dooley, T.P., Jackson, M.P.A., Hudec, M.R., 2014. Rankine Models for Time-dependent Gravity Spreading of Terrestrial Source Flows over Sub-planar Slopes. J. Geophys. Res 119 (9), 7353–7388. https://doi.org/10.1002/2014JB011315.

Weijermars, R. and van Harmelen, A., 2016. Breakdown of Doublet Re-circulation and Direct Line Drives by Far-field Flow: Implications for Geothermal and Hydrocarbon Well Placement. Geophysical Journal International (GJIRAS), Vol. 206, p. 19-47.

Weijermars, R., van Harmelen, A., Zuo, L., 2016. Controlling Flood Displacement Fronts Using a Parallel Analytical Streamline Simulator. J. Petrol. Sci. Eng. 139, 23–42. https://doi.org/10.1016/j.petrol.2015.12.002

Weijermars, R. and van Harmelen, A., 2017. Advancement of Sweep Zones in Waterflooding: Conceptual Insight and Flow Visualizations of Oil-withdrawal Contours and Waterflood Time-of-Flight Contours using Complex Potentials. Journal of Petroleum Exploration and Production Technology.

Weijermars, R., van Harmelen, A., Zuo, L., Nascentes Alves, I., and Yu, W., 2017a. High-Resolution Visualization of Flow Interference Between Frac Clusters (Part 1): Model Verification and Basic Cases. SPE/AAPG/SEG Unconventional Resources Technology Conference. SPE, URTEC, 24-26 July 2017, Austin, Texas. SPE URTeC 2670073A. https://doi.org/10.15530/URTEC-2017-2670073.

Weijermars, R., van Harmelen, A., and Zuo, L., 2017b. Flow Interference between Frac Clusters (Part 2): Field Example from the Midland Basin (Wolfcamp Formation, Spraberry Trend Field) With Implications for Hydraulic Fracture Design.

Unconventional Resources Technology Conference doi: 10.15530/urtec-2017-2670073B.

Weijermars, R. and Nascentes Alves, I., 2018. High-resolution Visualization of Flow Velocities near Frac-tips and Flow Interference of Multi-fracked Eagle Ford Wells, Brazos County, Texas. J. Pet. Sci. Eng. 165, 946–961. https://doi.org/10.1016/j.petrol.2018.02.033.

Weijermars, R. and van Harmelen, A., 2018. Shale Reservoir Drainage Visualized for a Wolfcamp Well (Midland Basin, West Texas, USA). Energies, 11, 1665, https://doi.org/10.3390/en11071665.

Weijermars, R., van Harmelen, A., Zuo, L., Nascentes Alves, I., and Yu, W., 2018. Flow Interference between Hydraulic Fractures. SPE Reservoir Evaluation & Engineering, vol. 21, no. 4, p. 942-960 (Reservoir Engineering - Special Issue: Unconventionals), SPE-194196-PA. doi:10.2118/194196-PA.

Weijermars, R. and Khanal, A., 2019. High-resolution Streamline Models of Flow in Fractured Porous Media using Discrete Fractures: Implications for Upscaling of Permeability Anisotropy, Earth-Science Reviews, Volume 194, Pages 399-448, https://doi.org/10.1016/j.earscirev.2019.03.011.

Weijermars, R., Nandlal, K., Khanal, A., and Tugan, F.M., 2019. Comparison of Pressure Front with Tracer Front Advance and Principal Flow Regimes in Hydraulically Fractured Wells in Unconventional Reservoirs. Journal of Petroleum Science and Engineering, Vol. 183, 106407, https://doi.org/10.1016/j.petrol.2019.106407.

Weng, X., 2015. Modeling of Complex Hydraulic Fractures in Naturally Fractured Formation. J. Unconv. Oil Gas Resour. 9, 114–135. https://doi.org/10.1016/j.juogr.2014.07.001

Weng, X., Kresse, O., Cohen, C.-E., Wu, R., Gu, H., 2011. Modeling of Hydraulic-Fracture-Network Propagation in a Naturally Fractured Formation. SPE Prod. Oper. 26, 368–380. https://doi.org/10.2118/140253-PA

Wu, K. and Olson, J. E., 2014, August 25. Mechanics Analysis of Interaction Between Hydraulic and Natural Fractures in Shale Reservoirs. Unconventional Resources Technology Conference. doi:10.15530/URTEC-2014-1922946

Wu, K. and Olson, J. E., 2016, November 1. Numerical Investigation of Complex Hydraulic-Fracture Development in Naturally Fractured Reservoirs. Society of Petroleum Engineers. doi:10.2118/173326-PA

Xu, W., Thiercelin, M. J., Ganguly, U., Weng, X., Gu, H., Onda, H., … Le Calvez, J., 2010, January 1. Wiremesh: A Novel Shale Fracturing Simulator. Society of Petroleum Engineers. doi:10.2118/132218-MS.

Yaich, E., Diaz De Souza, O.C., Foster, R.A., Abou-sayed, I.S., 2014. A Methodology to Quantify the Impact of Well Interference and Optimize Well Spacing in the Marcellus Shale, in: SPE/CSUR Unconventional Resources Conference – Canada. Society of Petroleum Engineers. https://doi.org/10.2118/171578-MS

Yao, Y., et al., 2010. Cohesive Fracture Mechanics Based Analysis to Model Ductile Rock Fracture, in 44th U.S. Rock Mechanics Symposium and 5th U.S.-Canada Rock

Mechanics Symposium. American Rock Mechanics Association: Salt Lake City, Utah.

Yu, W., Wu, K., Zuo, L., Tan, X., Weijermars, R., 2016. Physical Models for Inter-Well Interference in Shale Reservoirs: Relative Impacts of Fracture Hits and Matrix Permeability, in: Proceedings of the 4th Unconventional Resources Technology Conference. American Association of Petroleum Geologists, Tulsa, OK, USA, pp. 1–3. https://doi.org/10.15530/urtec-2016-2457663

Yu, W., Xu, Y., Weijermars, R., Wu, K., Sepehrnoori, K., 2017a. A Numerical Model for Simulating Pressure Response of Well Interference and Well Performance in Tight Oil Reservoirs With Complex-Fracture Geometries Using the Fast Embedded-Discrete-Fracture-Model Method. SPE Reserv. Eval. Eng. https://doi.org/10.2118/184825-PA

Yu, W., Xu, Y., Weijermars, R., Wu, K., Sepehrnoori, K., 2017b. Impact of Well Interference on Shale Oil Production Performance: A Numerical Model for Analyzing Pressure Response of Fracture Hits with Complex Geometries, in: SPE Hydraulic Fracturing Technology Conference and Exhibition. Society of Petroleum Engineers. https://doi.org/10.2118/184825-MS

Yu, W. and Sepehrnoori, K., 2018, January. Embedded Discrete Fracture Model (EDFM) for Complex Fracture Geometry. Shale Gas and Tight Oil Reservoir Simulation (pp. 155-200). Cambridge, MA: Gulf Professional Publishing, an imprint of Elsevier

Yu, W., Zhang, Y., Varavei, A., Sepehrnoori, K., Zhang, T., Wu, K., Miao, J., 2018. Compositional Simulation of CO2 Huff-n-Puff in Eagle Ford Tight Oil Reservoirs

with CO2 Molecular Diffusion, Nanopore Confinement and Complex Natural Fractures, in: SPE Improved Oil Recovery Conference. Society of Petroleum Engineers. https://doi.org/10.2118/190325-MS

Zakhour, N., Shoemaker, M., and Lee, D., 2015. Integrated Workflow Using 3D Seismic and Geomechanical Properties with Microseismic and Stimulation Data to Optimize Completion Methodologies: Wolfcamp Shale-Oil Play Case Study in the Midland Basin. Society of Petroleum Engineers. doi:10.2118/177298-MS.

Zhang, X., Thiercelin, M. J., Jeffrey, R. G., 2007, January 1. Effects of Frictional Geological Discontinuities on Hydraulic Fracture Propagation. Society of Petroleum Engineers. doi:10.2118/106111-MS.

Zhou, W., Banerjee, R., Poe, B. D., Spath, J., Thambynayagam, M., 2012, January 1. Semi-Analytical Production Simulation of Complex Hydraulic Fracture Network. Society of Petroleum Engineers. doi:10.2118/157367-MS

Zolfaghari, A., Ghanbari, E., Dehghanpour, H., Bearinger, D., 2016, February. Fracture Characterization Using Flowback Salt-Concentration Transient. SPE Journal

Zolfaghari, A., Tang, Y., He, J., Dehghanpour, H., Bearinger, D., Virues, C., 2017, February 15. Fracture Network Characterization by Analyzing Flowback Salts: Scale-Up of Experimental Data. Society of Petroleum Engineers. doi:10.2118/185078-MS

Zuo, L. and Weijermars, R., 2017. Rules for Flight Paths and Time of Flight for Flows in Heterogeneous Isotropic and Anisotropic Porous Media. Geofluids 18. https://doi.org/10.1155/2017/5609571. 5609571. https://www.hindawi.com/journals/geofluids/2017/5609571

APPENDIX A

UPSCALING FOR FRACTURED POROUS MEDIA

Upscaling of fractured porous media using an object-based approach is first considered. The object-based upscaling involves no flow simulation and the elements of the equivalent permeability tensor are obtained from the spatial distribution of high permeability zones (Weijermars and Khanal, 2019). Assuming the natural fractures have a uniform width and conductivity simplified expressions for the principal components k_x* and k_y* when fractures are parallel to far field flow (Fig.A1a), using a 2D Cartesian grid with unit reservoir depth, are given as (Weijermars and Khanal, 2019):

$$k_x^* = \frac{N w_f k_f}{w_{REV}} \tag{A1}$$

$$k_y^* = k_m \frac{w_{REV}}{(N+1) w_m} \tag{A2}$$

With:
$$w_{REV} = N w_f + (N+1) w_m \tag{A3}$$

Where N is the number of fractures in the pre-determined representative elementary volume (REV), w_f the width of the fracture, k_f permeability of fracture, w_{REV} width of the REV in question, k_m permeability of the matrix and w_m the width of the matrix blocks between the fractures. Normalizing the length scale with respect to w_f and w_m gives:

$$w^*_{REV} = w^*_f + w^*_m = 1 \quad \text{(A4)} \quad \text{where} \quad w^*_f = \frac{N w_f}{w_{REV}} \quad \text{(A5)} \quad \text{and} \quad w^*_m = \frac{(N+1) w_m}{w_{REV}} \quad \text{(A6)}$$

When the natural fractures are oblique to the far-field flow (Fig. A1b), the equivalent permeability tensor can be expressed in terms of the normalized w^*_f as:

$$k(\theta) = \begin{bmatrix} w^*_f k_f \cos^2\theta + k_m \sin^2\theta & (w^*_f k_f - k_m)\cos\theta\sin\theta \\ (w^*_f k_f - k_m)\cos\theta\sin\theta & w^*_f k \sin^2\theta + k_m \cos^2\theta \end{bmatrix} = \begin{bmatrix} k_{xx} & k_{xy} \\ k_{yx} & k_{yy} \end{bmatrix} \quad \text{(A7)}$$

It is argued that the object-based method of upscaling cannot accurately capture the physics of flow in fractures porous media and that instead flow-based methods should be used (Chen et al., 2015; Weijermars and Khanal, 2019). Chen et al. (2016) propose solving the flow problem with a multi-boundary approach which commonly requires the use of numerical simulators. Weijermars and Khanal (2019) approached the flow based upscaling by looking at the ratio of the velocity of flow inside and outside of the fracture zones to determine the equivalent permeability for a REV model using CAM. This approach led to the formulation of the 2D equivalent permeability tensor ellipses based on directional flow rates measured in CAM models with the axial ratios given by:

$$\frac{k^*_x}{k_m} = \frac{\bar{v}_y + \bar{v}_x}{v_{y\_ff}} \quad \text{(A8)} \qquad \frac{k^*_y}{k_m} = \frac{\bar{v}_y - \bar{v}_x}{v_{y\_ff}} \quad \text{(A9)}$$

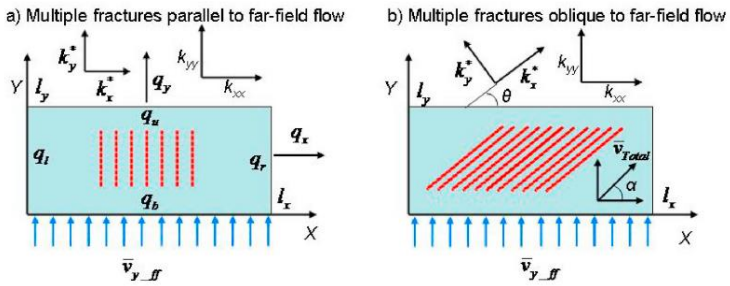

Fig. A1: Permeability tensor components for multiple fracture a) parallel and b) oblique to far-field flow (modified from Weijermars and Khanal, 2019).

$\bar{v}_y$ is the average velocity in the y direction while $\bar{v}_x$ is the average velocity in the x direction. The variable v_{y_ff} gives the velocity if the far field flow into the REV model.

Our present formulation for upscaling the permeability in fractured porous media is a hybrid between the object-based and flow-based upscaling methods. The object-based upscaling [Eqs. (A1) to (A7)] is first used to reduce the total number of natural fractures used in the model (essentially decreasing the natural fracture density). Next, the flow-based method [Eqs. (A8) and (A9)] is used with the upscaled fracture density to ensure the equivalent permeability for the REV of concern remains identical to the prototype.

Object-based upscaling step:

To demonstrate the proposed method we consider two similar REV's (Fig. A2).

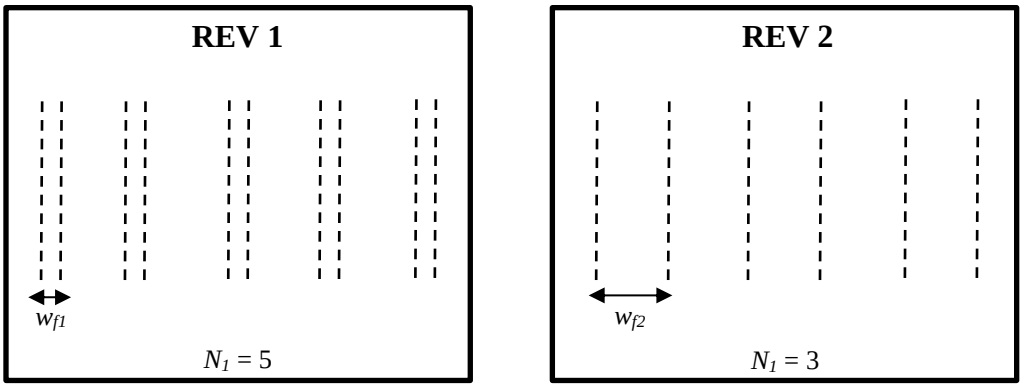

Fig. A2: Two equal REV's with different numbers of natural fractures

For REV 1: $k_x^* = \frac{N_1 w_{f1} k_f}{w_{REV}}$ (A10)

For REV 2: $k_x^* = \frac{N_2 w_{f2} k_f}{w_{REV}}$ (A11)

Assuming k_f and w_{REV} are constant and equating the equations for REV 1 and REV 2 we arrive at;

$$N_1 w_{f1} = N_2 w_{f2}$$

The number of fractures in REV 1 can be determined from the natural fracture density and REV width and length (L_{REV});

$$N_1 = NF_{density1} \times w_{REV} \times L_{REV}$$

Substituting for N_1;

$$N_2 = \frac{(NF_{density1} \times w_{REV} \times L_{REV}) w_{f1}}{w_{f2}} \quad \text{(A12)}$$

Based on a user defined value for a new natural fracture width we can upscale from N_1 fractures to a lower value of N_2 natural fractures which is more practical for use in discrete natural fracture models, including CAM used in our study

Validation of object-based upscaling step:

The proposed object-based upscaling (reduction) of the number of natural fractures in a given reservoir area was validated using the flow-based upscaling method. For the models with N_1 and N_2 fractures, the velocities are calculated in and outside of the natural fractures and the permeability tensor ellipses are generated. To properly account for the reduction of the number of fracture and equivalent upscaling, the assigned natural fracture permeabilities of the original prototype ($\upsilon_{f1} w_{f1}$) and upscaled models ($\upsilon_{f2} w_{f2}$) needed to maintain the same equivalent permeability are given by;

$$\upsilon_{f2}(t) = \frac{\upsilon_{f1}(t) w_{f2}}{w_{f1}} \tag{A13}$$

Where $\upsilon_{f1}(t)$ is the original strength prior to upscaling, and $\upsilon_{f2}(t)$ is the new strength (which are proxies to the permeability in our models) to be used after upscaling the number of natural fractures with the corresponding fracture width change. This procedure is demonstrated via the upscaling of natural fractures at an angle of 45^{O} to the far field flow starting with Fig. A3 and A4, up to the final upscaled REV in Fig. A5.

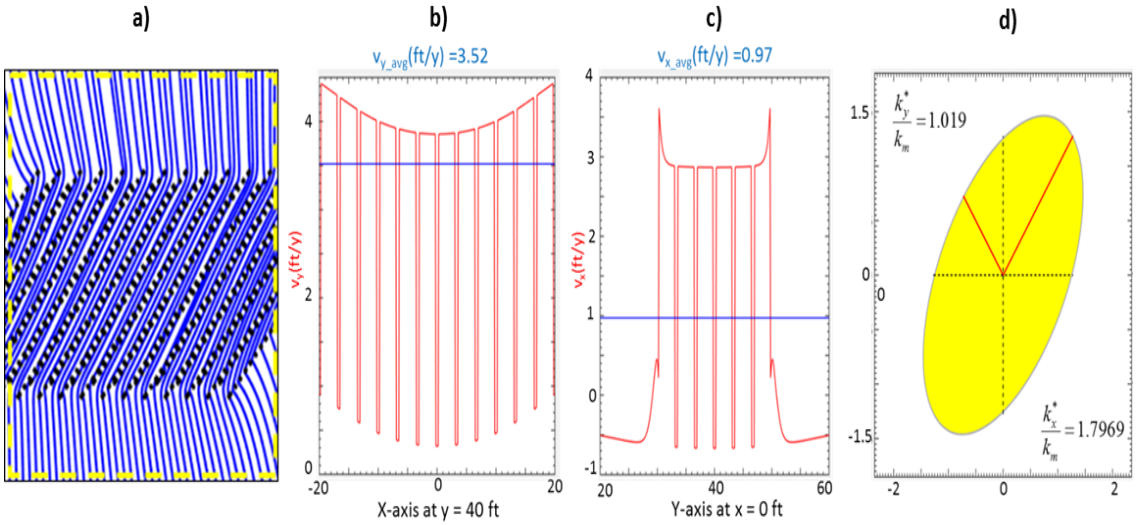

Fig. A3: a) Flow in a defined REV space with streamlines in blue and natural fractures (NF) in dashed black, **b&c)** Velocity profiles along cross-hairs at y= +40 and x = 0 respectively, **d)** Equivalent permeability ellipse based on Eqs. A8 and A9. Number of NF = 16; width of NF = 2ft; strength of NF = 120 ft^4/yr.

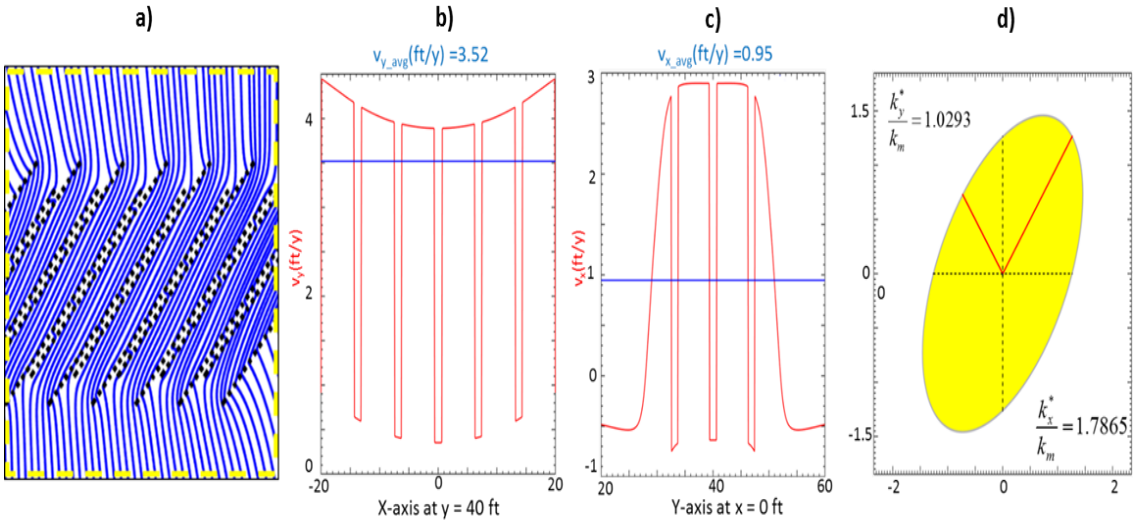

Fig. A4: a) Flow in a defined REV space with streamlines in blue and natural fractures (NF) in dashed black, **b&c)** Velocity profiles along cross-hairs at y= +40 and x = 0, respectively, **d)** Equivalent permeability ellipse based on Eqs. A8 and A9. Number of NF = 8; width of NF = 4ft; upscaled strength of NF = 240 ft^4/yr.

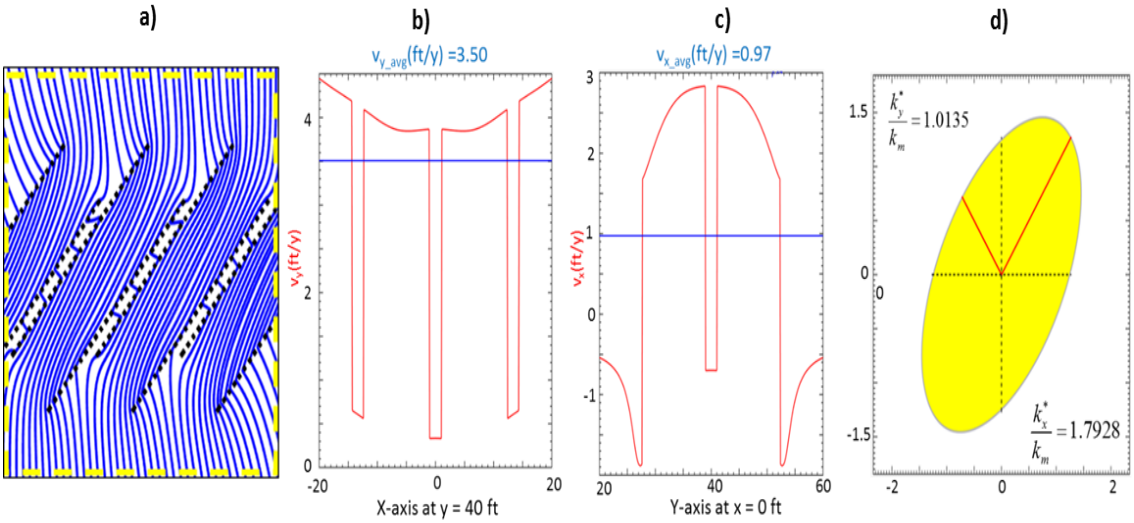

Fig. A5: a) Flow in a defined REV space with streamlines in blue and natural fractures (NF) in dashed black, **b&c)** Velocity profiles along cross-hairs at y= +40 and x = 0, respectively, **d)** Equivalent permeability ellipse based on Eqs. A8 and A9. Number of NF = 4; width of NF = 8ft; upscaled strength f NF = 480 ft^4/yr.

The above results show that with a reduction in the number of natural fractures by object-based upscaling within a defined REV, using the appropriate upscaling for fracture width and permeability in the natural fractures, the equivalent permeability remains constant. By using this method, we can upscale a realistic fracture density to a manageable number of natural fractures for use in the CAM models for DRV calculations. This upscaling methodology was applied in the next section to field data from the Hydraulic Fracturing Test Site (Midland Basin, West Texas, with completions in the Wolfcamp Formation).

Application of object-based and flow-based upscaling to HFTS field model:

This section makes use of the proposed combination of object-based and flow-based upscaling to reduce the natural fracture density used by Shrivastava et al. (2018) in their model to match the data from the HFTS. Selecting a REV located around a hydraulic fracture of 125 ft in length by 45 ft in height above the hydraulic fracture corresponds a true density of 210 natural fractures with an assumed width of 0.2 inches. The 210 fractures are reduced in the proposed upscaling procedure, making use of Eq. A12, and adopting an upscaled natural fracture width of 6 inches (based on object-based upscaling), results in 6 natural fractures of length 30 ft. These 6 natural fractures have fracture centers and angles (kept in range of HFTS data) that are stochastically generated within the specified REV both below and above the hydraulic fracture. This results in a total of 12 upscaled natural fractures that are used in the final HFTS field model (Fig.A6). The CK correlation was used with a final upscaled strength of 155 ft^4/yr, which gives a corresponding porosity of 7.32% within the natural fractures.

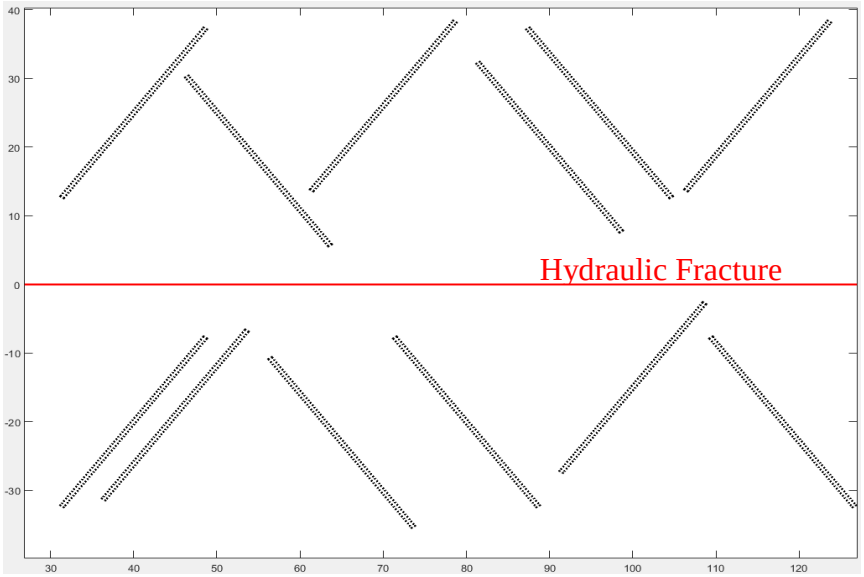

Fig. A6: REV near single hydraulic fracture (horizontal red line) with upscaled natural fractures (dashed black lines) based on HFTS field data.

APPENDIX B

CARMAN-KOZENY RELATION FOR ESTIMATING NATURAL FRACTURE PERMEABILITY FROM POROSITY

For the field models looking at use of the natural fracture data and its impact on DRV, the Carman-Kozeny correlation was used to determine an effective porosity-permeability relationship. The generic Carman-Kozeny correlation is given by (Duda et al., 2011):

$$k = \frac{\phi^3}{\beta T^2 S^2} \tag{B1}$$

This well-known correlation seeks to link the permeability of a porous medium (in our case natural fractures with a predetermined porosity) to the porosity along with other rock properties. β represents the shape factor of the rock and is a constant characteristic for a particular type of granular material, S is known as the specific surface area and is the ratio of the total interstitial surface area to the bulk volume (Duda et al., 2011). T is the hydraulic tortuosity defined as by the equation:

$$T = \frac{\langle \lambda \rangle}{\bar{L}} \tag{B2}$$

Where $\langle \lambda \rangle$ represents the mean length of fluid particle paths and the variable $\bar{L}$ gives the straight-line distance through the medium in the direction of macroscopic flow. We adopted a T value of 1.41 (Duda et al., 2011) and a β of 3 for the pore shape coefficient

for thin cracks (Jianjun Ma, 2015). The specific surface area by volume (*S*) is calculated from the specific surface area by weight and the average density using data from Wolfcamp formation samples. Specific surface areas are given by Tinni et al. (2014) for various particle sizes in the Wolfcamp formation with an average specific surface area of 9.36 m^2/g. Using this value in conjunction with the average Wolfcamp formation density of 2.73 g/cm^3 (EIA report, 2018), *S* is calculated at $2.55x10^7$ m^{-1}. Using these values with a given natural fracture porosity, natural fracture permeability is then calculated and converted to the equivalent strength using Equation (3-11) for use in the CAM models. An example of the correlation is given in Table B1 with the first row values used for Fig. 3-11b.

Table B1: Natural fracture strength from Carman-Kozeny correlation

Natural fracture porosity (%)	Natural fracture permeability (nD)	Rk	Matrix velocity (ft/day)	Natural fracture width (ft)	Natural fracture length (ft)	Natural fracture height (ft)	Natural fracture strength (ft^4/day)
8.4	152.6	1.53	0.169	0.5	20	60	**155**
9.8	246.1	2.46	0.169	0.5	20	60	**250**

APPENDIX C

WATER CUT FOR MODELED WELLS IN MIDLAND AND DELAWARE BASIN

Water and gas production data for the wells considered for the study are shown below (Fig. C1). Well 346AH from the Midland Basin shows considerable water production, which is accounted for in the DRV calculated Wells Neal 322H (Midland Basin) and Autobahn 34-117 1H (Delaware Basin) show negligible water production mostly towards the early life of the well.

a)

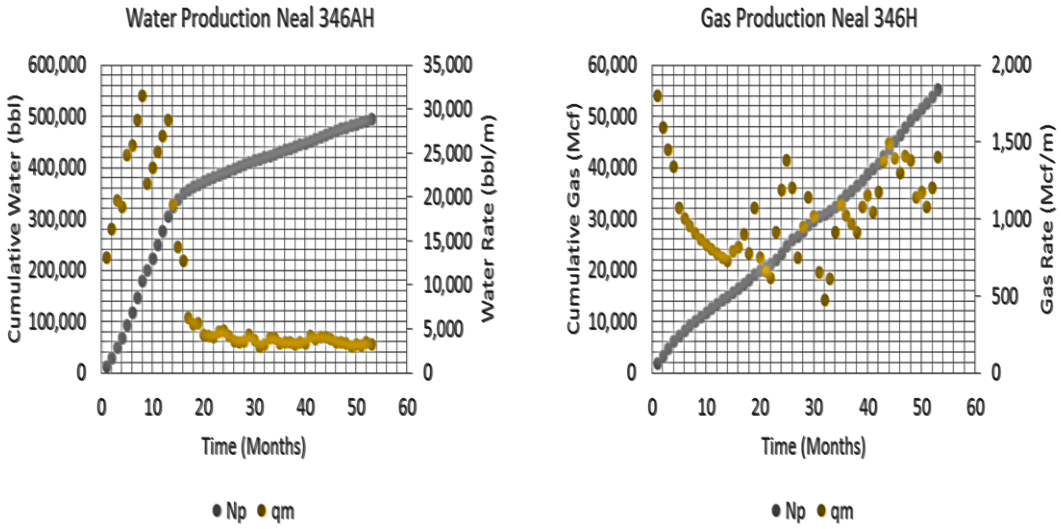

Fig. C1. Water and gas production data for a) Neal 346AH (Midland Basin) b) Neal 322H (Midland Basin), and c) Autobahn 34-117 1H.

b)

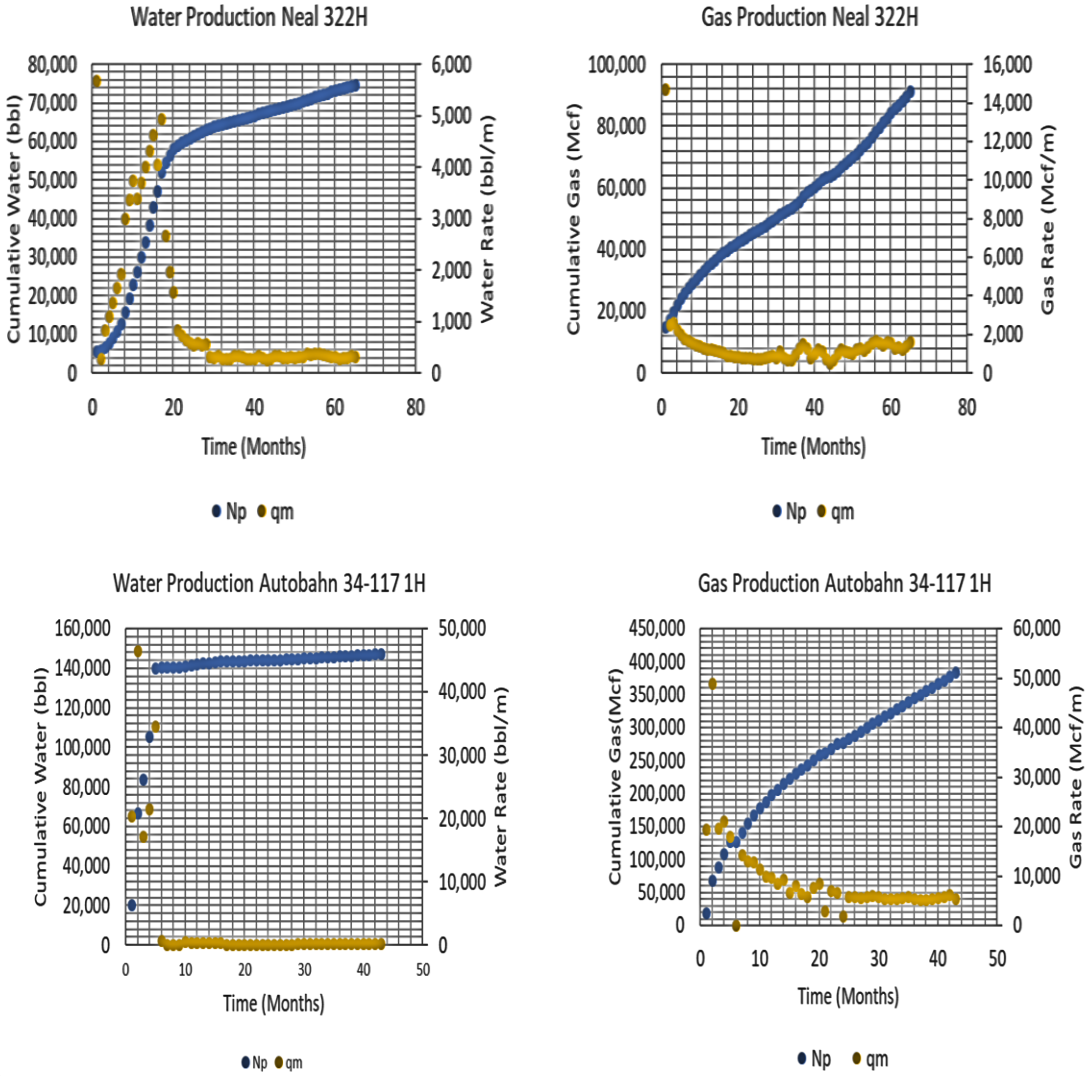

c)

Fig. C1. Continued

APPENDIX D

DIFFUSIVE TIME OF FLIGHT (DTOF) CALCULATIONS

The diffusive time of flight refers to the distance traveled by the pressure front and the terminology was first applied to simple homogenous problems. The introduction of the time of flight measure as a spatial coordinate effectively allows for the decoupling of pressure from saturation and concentration calculations during flow simulations (Data-Gupta and King, 2007). The diffusive time of flight, τ, is originally defined as:

$$\tau(\mathbf{x}) = \int_{\psi} \frac{ds}{\| \mathbf{v}(\mathbf{x}) \|} \tag{D1}$$

Where **v(x)** represents the interstitial velocity of a neutral tracer along streamlines ψ.

For a heterogeneous permeable medium governed by the diffusivity equation, this method was expanded upon to define a time of flight for diffusive or compressible flow, hereafter referred to as the diffusive time of flight (King et al., 2016). The diffusive time of flight accounts for transient, compressible fluid flow:

$$\tau(\mathbf{x}) = \int_{\psi} \frac{ds}{\sqrt{\alpha(\mathbf{x})}} \tag{D2}$$

We can now relate the time, *t*, required for the DOI to reach a given location (Eq. (D2)) to the diffusive time of flight, τ, (Eq. (D4)):

$$\tau = \sqrt{t} = r_i \sqrt{\frac{1688.7}{\alpha}}, \quad [\text{hours}^{1/2}] \tag{D3}$$

Replacing back the constituents for the hydraulic diffusivity term we have for diffusive TOF (τ):

$$\tau = r_i \sqrt{\frac{1688.7\, n\mu c_t}{k}} \tag{D4}$$